New Developments in Open System Quantum Dynamics

Lachlan P. J. Lindoy

Magdalen College

University of Oxford

A thesis submitted for the degree of

Doctor of Philosophy

Michaelmas 2019

New Developments in Open System Quantum Dynamics

Lachlan P. J. Lindoy

Magdalen College
University of Oxford

A thesis submitted for the degree of
Doctor of Philosophy

Michaelmas 2019

Abstract

The dynamics of many chemical systems can be influenced significantly by interactions with their environment (bath). An exact treatment of this is often infeasible due to the exponential scaling of Hilbert space with the number of degrees of freedom. In this thesis, dynamical methods, which overcome this difficulty, are considered for spin systems coupled to spin baths as well as systems coupled to harmonic oscillator baths.

The thesis begins by considering recombination reactions of radical pairs, in which two electron spins interact with baths of nuclear spins. Motivated by inaccuracies observed in semiclassical treatments of the dynamics of a series of cryptochrome-based radical pairs, a new approach capable of treating the quantum dynamics of spin systems coupled to large baths of spins is presented. This method is validated for a series of central spin models, and is found to correctly describe the quantum dynamics of spin systems containing up to 1000 spins.

Following this, the validity of the conventional treatment of radical pair recombination reactions is explored by considering the coupled electronic, nuclear and spin dynamics of a model radical ion pair. The dynamics of this model is treated using the hierarchical equations of motion (HEOM) formalism, and the results obtained are used to validate a recently proposed series of master equations. The HEOM formalism exactly captures the quantum dynamics of systems that are coupled to harmonic baths. However, due to the scaling of its computational cost with the strength of the coupling, it often becomes impractical. To overcome this difficulty, an efficient tree tensor network-based approach is presented and valided by treating a series of simple models. Following this, it is applied to the calculation of electron transfer rates for a series of models spanning a wide range of physical regimes in order to validate a recently proposed interpolation formula for the calculation of electron transfer rates.

Acknowledgements

First, I would like to thank my supervisor, Prof. David Manolopoulos, for his invaluable insight and guidance throughout the past 4 years. It has been a really enjoyable few years, particularly the time spent discussing ideas at the board.

Secondly, I would like to thank Prof. Peter Hore for his suggestions and his support over the past year.

I'd also really like to thank Joe Lawrence, Thomas Fay, and Theo Fletcher. It's been great collaborating with you three. The discussions about work and otherwise have been great fun.

Thanks to my friends, both at college and in the department, who have helped keep me sane over the past four years. The tea-time chat has been a surprisingly important part of that.

Finally, a massive thanks to my family for their love and encouragement over the years. In particular, thank you Granddad for your very helpful proofreading of my thesis.

List of Publications

Chapter 2

- Reference [89]: T. P. Fay, L. P. Lindoy, D. E. Manolopoulos and P. J. Hore, *How quantum is radical pair magnetoreception?*, *Faraday Discuss.*, 2020, **221**, 77–91.

Chapter 3

- Reference [137]: L. P. Lindoy and D. E. Manolopoulos, *Simple and accurate method for central spin problems*, *Phys. Rev. Lett.*, 2018, **120**, 220604.
- In Preparation: L. P. Lindoy, T. P. Fay and D. E. Manolopoulos, *Quantum dynamics of a molecular magnetoreceptor*.

Chapter 4

- Reference [33]: T. P. Fay, L. P. Lindoy and D. E. Manolopoulos, *Spin-selective electron transfer reactions of radical pairs: beyond the Haberkorn master equation*, *J. Chem. Phys*, 2018, **149**, 064107.

Chapter 5

- Reference [181]: J. E. Lawrence, T. Fletcher, L. P. Lindoy and D. E. Manolopoulos, *On the calculation of quantum mechanical electron transfer rates*, *J. Chem. Phys*, 2019, **151**, 114119.
- In Preparation: L. P. Lindoy and D. E. Manolopoulos, *HEOM-TN: tree-tensor network state solver for the hierarchical equations of motion*.

Contents

1 Introduction

The dynamics of many chemical systems can be fully captured through the use of the Liouville-von Neumann equation,[1]

$$\frac{\mathrm{d}}{\mathrm{d}t}\hat{\rho}(t) = -\frac{i}{\hbar}\left[\hat{H}, \hat{\rho}(t)\right], \tag{1.1}$$

which describes the unitary evolution of the density operator, $\hat{\rho}(t)$, under the Hermitian Hamiltonian operator, $\hat{H}$, that accounts for all interactions present in the system (and has been assumed to be independent of time). The density operator, which represents an ensemble of states in the Hilbert space of the system, fully characterises the state of the system at time t and from it all physically properties of interest can be obtained.[2,3] For small and isolated systems, such as those arising in the gas-phase, a direct solution to equation 1.1 is often practical and, as such, the dynamics of such systems can be readily described. In the condensed-phase, interactions between the system and its environment can significantly influence the dynamics of both. In order to accurately capture these effects it is, in general, necessary to include the degrees of freedom for both the system and environment in the description of the dynamics. As condensed-phase environments often contain a very large number of degrees of freedom,[4,5] a direct solution of equation 1.1 is typically intractable. Due to the exponential scaling of Hilbert space with the

number of degrees of freedom, the density operator for the combined system-environment degrees of freedom may contain too many elements to be able to be practically evaluated.

In many situations, the only observables of interest depend solely on the state of the system. In such a case, the state of the environment is unimportant, it is only its influence on the system dynamics that matters. As such, the full density operator, $\hat{\rho}(t)$, for both the system and environment (bath) degrees of freedom contains much unnecessary information. It is possible to work with a simpler object: the system reduced density operator, $\hat{\rho}_S(t)$, which only describes the state of the system. The system reduced density operator may be obtained from the full density operator as[4–6]

$$\hat{\rho}_S(t) = \mathrm{tr}\left[\hat{\rho}(t)\right]_B, \tag{1.2}$$

where $\mathrm{tr}\left[\cdot\right]_B$ denotes the partial trace over the degrees of freedom of the environment, B. When treating the dynamics of the system reduced density operator, it is often useful to decompose the Hamiltonian into contributions that only act on the system, $\hat{H}_S$, or environment, $\hat{H}_B$, degrees of freedom, and a term describing the coupling between them, $\hat{H}_{SB}$, as

$$\hat{H} = \hat{H}_S + \hat{H}_{SB} + \hat{H}_B. \tag{1.3}$$

An equation of motion for the system reduced density operator may be obtained from equation 1.1 by taking a partial trace over the environment degrees of freedom,[5]

$$\frac{\mathrm{d}}{\mathrm{d}t}\hat{\rho}_S(t) = -\frac{i}{\hbar}\mathrm{tr}\left(\left[\hat{H}, \hat{\rho}(t)\right]\right)_B \tag{1.4}$$

$$= -\frac{i}{\hbar}\left[\hat{H}_S, \hat{\rho}_S(t)\right] - \frac{i}{\hbar}\mathrm{tr}\left(\left[\hat{H}_{SB} + \hat{H}_B, \hat{\rho}(t)\right]\right)_B. \tag{1.5}$$

In addition to the standard coherent evolution that arises from the first term, a term that describes the influence of the environment on the system and gives rise to non-unitary evolution is also present. This "open quantum system" is appropriate for treating many different types of system interacting with varying environments. In this thesis, two cases will be considered. The first is a spin system that interacts with

an environment of spins, as arises in the description of radical pair recombination dynamics and in the hyperfine-induced decoherence of electron spins confined within quantum dots. This will be considered in Chapters 2 and 3. The second is a two-level system interacting with an environment of harmonic oscillators, as arises in models of electron transfer reactions. This is discussed in Chapters 4 and 5.

1.1 Outline of this Thesis

Standard quantum mechanical and semiclassical treatments of radical pair recombination reactions are discussed in Chapter 2. The chapter begins with a description of the radical pair mechanism and the standard master equation used to treat its spin dynamics. This is followed by a discussion of how experimentally observable quantities may be obtained quantum mechanically for moderate size radical pairs ($\lesssim$30 spins), and how semiclassical approaches can be used to obtain approximations to these quantities for significantly larger radical pairs. Finally, the chapter is concluded with discussion of an application of the semiclassical and quantum mechanical theories to a series of model cryptochrome-based radical pairs, with the aim of assessing the accuracy of the semiclassical treatment of radical pair recombination.

In Chapter 3, building on the results obtained in Chapter 2, a new quantum mechanical method is described for treating the dynamics of central spin and radical pair models with considerably more spins than are feasible using standard approaches. The chapter begins with an overview of the central spin model. Following this, two numerically exact methods that have previously been applied to central spin models, again with considerably more spins than can be treated using standard quantum mechanical approaches, are discussed. Motivated by two special cases of the central spin model for which quantum mechanical treatments are trivial, a new method is then presented for treating the central spin dynamics of the general central spin model. While this approach works in the full Hilbert space of the central spin model (the central spin and its environment) it employs ideas from "open quantum system"

dynamics. Rather than attempting to treat the environment exactly, it employs an approximate description of the environment spins that can be systematically improved to capture their influence on the central spin dynamics more accurately. This new method is validated against previously obtained numerically exact results for a set of central spin problems containing between 48 and 999 nuclear spins. It is then applied to assess the validity of semiclassical treatments of the asymmetric recombination dynamics of a prototypical magnetoreceptor: a cartoneid-porphyrin-fullerene triad radical pair which contains 45 nuclear spins.

The hierarchical equations of motion (HEOM) formalism[7,8] is discussed in the context of the condensed-phase electron transfer reactions arising in radical ion pairs in Chapter 4. This formalism, which has emerged as one of the most powerful approaches to open quantum system dynamics, gives rise to a non-perturbative system of equations describing the time-evolution of the reduced density operator of a system linearly coupled to an infinite bath of harmonic oscillators. The basic theory of nonadiabatic electron transfer reactions will be presented, following which the spin-boson model, a commonly employed model for treating such reactions, will be covered. This model takes the form of a two-level system coupled to an infinite bath of harmonic oscillators, and its dynamics may be obtained exactly using the HEOM approach. A derivation of the relevant equations of motion, and a discussion of some of the implementation details necessary to obtain an efficient numerical method, are then presented. The chapter concludes with an application of the HEOM to a model radical ion pair recombination reaction, with the aim of exploring the validity of a recently proposed set of quantum master equations for the dynamics of the radical pair spin system.

Motivated by some of the difficulties arising in the solution of the hierarchical equations of motion, a new approach for solving these equations of motion is presented in Chapter 5. This chapter begins by discussing an alternative representation of the HEOM that is entirely analogous to the equations of motion

for a wavefunction evolving under a non-Hermitian Hamiltonian. Following this, the structure of tree tensor network states is described, and by applying the time-dependent variational principle, a set of equations describing the evolution of tree tensor network states is obtained. These equations are the multilayer-multiconfigurational time-dependent Hartree (ML-MCTDH) equations of motion. The main difficulty associated with integrating these equations, and two recently proposed methods for overcoming this difficulty, are then outlined. This is followed by discussion of some implementation details that are necessary to obtain an efficient method. The method is then applied to obtain solutions of the HEOM for a set of model problems. Finally, the method is used to validate a simple approach for computing electron transfer rates in a wide variety of condensed phase regimes, that range from the nonadiabatic to the adiabatic limits.

2

Radical Pair Recombination Dynamics

Contents

2.1 Introduction

Magnetic interactions play a significant role in the reactions of many biological and chemical systems.[9–13] The application of weak magnetic fields[14,15] or substitution of isotopes with different nuclear spin[16] can dramatically alter the rates and product yields of these reactions. These effects can often be explained with the radical pair mechanism in which a transient radical pair is formed with two electron spins that interact with the local magnetic environment.

2.1.1 The Radical Pair Mechanism

In the idealised radical pair model shown in figure 2.1, a spin correlated radical pair is initially formed (e.g. via photoexcitation) in a singlet electron spin state. Interactions between the electron and nuclear spins in each radical lead to the singlet electronic spin state not being a stationary state; these potentially weak magnetic interactions result in an oscillatory interconversion between singlet and triplet electronic spin states. When in the singlet state, the radical pair recombines with rate k_S to reform the ground state, whereas the triplet state recombines to form a possibly distinct triplet product at a different rate, k_T. The interplay between the coherent evolution and the incoherent, spin-selective recombination process, gives rise to a magnetic field effect. Small magnetic fields with interaction energies that are orders of magnitude smaller than the thermal energy can dramatically influence the resultant dynamics.

In what follows, a description of how these reactions can be modelled is presented. First, the property of spin is discussed. This is followed by a description of the standard master equation used to treat the dynamics of these systems, in which the Hamiltonian accounting for the magnetic interactions that give rise to the coherent spin dynamics and two superoperators that account for the dynamics of the recombination process will be introduced. How experimentally observable quantities can be obtained quantum mechanically for moderate size radical pairs ($\lesssim 30$ spins) is then described, before semiclassical approximations, which allow

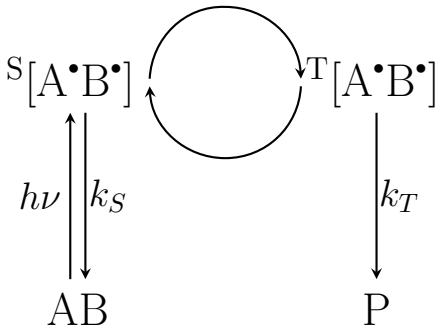

Figure 2.1: An idealised radical pair recombination reaction. An initial ground state precursor is excited to form a radical pair initially in a singlet state. This radical pair undergoes coherent spin evolution, interconverting between singlet and triplet states. The singlet and triplet states of the radical pair each can recombine to form their respective products (AB and P) with rates k_S and k_T, respectively.

significantly larger radical pairs to be treated, are discussed. Finally, the chapter is concluded with an application of the semiclassical and quantum mechanical theories to a series of model cryptochrome-based radical pairs, with the aim of assessing the accuracy of semiclassical treatments of radical pair recombination.

2.1.2 Spin

Spin is an intrinsic property of particles. It is a purely quantum mechanical phenomenon, there is no classical analogue.[2,17] It takes the form of an intrinsic angular momentum and, as such, can be parameterised by two quantum numbers: the spin quantum number, $S = \frac{n}{2}$ (where n can be any non-negative integer), and the spin projection quantum number, M_S, defined with respect to an arbitrary direction (this is the quantisation axis which, by convention, is denoted by z).[18] The projection quantum number can take values ranging from $-S$ to S in steps of 1; for a particle with spin quantum number S there are $2S + 1$ unique projection states. Being an angular momentum, spin can be accounted for using the vector operator $\hat{\boldsymbol{S}} = (\hat{S}_x, \hat{S}_y, \hat{S}_z)$, with each component operator satisfying the commutation relation[18]

$$\left[\hat{S}_\alpha, \hat{S}_\beta\right] = i\hbar\epsilon_{\alpha\beta\gamma}\hat{S}_\gamma. \tag{2.1}$$

In this equation, $\epsilon_{\alpha\beta\gamma}$ is the Levi-Civita symbol defined by

$$\epsilon_{\alpha\beta\gamma} = \begin{cases} 1 & (\alpha,\beta,\gamma) \in \{\text{cyclic permutations of}(x,y,z)\} \\ -1 & (\alpha,\beta,\gamma) \in \{\text{cyclic permutations of}(x,z,y)\} \\ 0 & \text{otherwise} \end{cases}, \tag{2.2}$$

where the Einstein summation convention (a sum over all repeated indices, here $\gamma = \{x, y, z\}$) has been adopted. The square of the magnitude of the angular momentum vector operator,

$$\hat{\boldsymbol{S}}^2 = \hat{S}_x^2 + \hat{S}_y^2 + \hat{S}_z^2, \tag{2.3}$$

commutes with each of the component operators

$$\left[\hat{\boldsymbol{S}}^2, S_\alpha\right] = 0. \tag{2.4}$$

As such, it is possible to construct states that are simultaneous eigenstates of $\hat{\boldsymbol{S}}^2$ and any of the component operators. For a spin-S particle, the $2S+1$ mutual eigenstates of $\hat{\boldsymbol{S}}^2$ and $\hat{S}_z$ ($|S, M_S\rangle$) satisfy

$$\hat{\boldsymbol{S}}^2 |S, M_S\rangle = \hbar^2 S(S+1) |S, M_S\rangle \tag{2.5}$$

$$\hat{S}_z |S, M_S\rangle = \hbar M_S |S, M_S\rangle . \tag{2.6}$$

For a set of spin-$\frac{1}{2}$ particles there are two such eigenstates,

$$|\alpha\rangle \equiv \left|\frac{1}{2}, \frac{1}{2}\right\rangle \qquad \text{and} \qquad |\beta\rangle \equiv \left|\frac{1}{2}, -\frac{1}{2}\right\rangle. \tag{2.7}$$

The spin-$\frac{1}{2}$ operators can be represented, with respect to these states, in terms of the Pauli spin matrices[2]

$$\hat{S}_x = \frac{\hbar}{2}\hat{\sigma}_x = \frac{\hbar}{2}\begin{pmatrix} 0 & 1 \\ 1 & 0 \end{pmatrix} \quad \hat{S}_y = \frac{\hbar}{2}\hat{\sigma}_y = \frac{\hbar}{2}\begin{pmatrix} 0 & -i \\ i & 0 \end{pmatrix} \quad \hat{S}_z = \frac{\hbar}{2}\hat{\sigma}_z = \frac{\hbar}{2}\begin{pmatrix} 1 & 0 \\ 0 & -1 \end{pmatrix}. \tag{2.8}$$

At this stage it is useful to introduce the raising and lowering operators,

$$\hat{S}_\pm = \hat{S}_x \pm i\hat{S}_y. \tag{2.9}$$

These operators act on a state, $|S, M_S\rangle$, raising or lowering its spin angular momentum projection quantum number, M_S, that is[2]

$$\hat{S}_{\pm} |S, M_S\rangle = \hbar\sqrt{S(S+1) - M_S(M_S \pm 1)}\, |S, M_S \pm 1\rangle \,. \tag{2.10}$$

For a spin-$\frac{1}{2}$ particle these operators have the matrix representations

$$\hat{S}_{+} = \hbar \begin{pmatrix} 0 & 1 \\ 0 & 0 \end{pmatrix} \qquad\qquad \hat{S}_{-} = \hbar \begin{pmatrix} 0 & 0 \\ 1 & 0 \end{pmatrix}, \tag{2.11}$$

with respect to the $|\alpha\rangle$, $|\beta\rangle$ basis.

In the radical pairs of interest here, there are typically many interacting spins. The unpaired electrons in each radical have spin $S = \frac{1}{2}$. These two electron spins can interact with any nuclei that possess non-zero spin angular momentum. To differentiate between electron and nuclear spins, I is used to refer to the spin quantum number of the nuclear spins (and $\hat{\boldsymbol{I}}$ is used to represent their vector spin operator). For the organic radicals considered in the next two chapters, the important nuclei are ^{1}H and ^{14}N with spin quantum numbers of $I = \frac{1}{2}$ and 1, respectively. Typically all carbon nuclei can be ignored. ^{12}C nuclei have spin $I = 0$ and so do not interact with the electron spins. The ^{13}C isotope has $I = \frac{1}{2}$, however, due to its naturally low abundance ($\sim 1\%$),[19] the possibility of it being present is ignored.

The spin angular momenta (S_1 and S_2) of two particles can couple. The sum of two vector spin operators,

$$\hat{\boldsymbol{S}} = \hat{\boldsymbol{S}}_1 + \hat{\boldsymbol{S}}_2, \tag{2.12}$$

has components satisfying the commutation relations given in equation 2.1 and, as such, is another angular momentum operator.[18] There are two particularly useful ways of representing the states of the two-spin system. As the spin operators for each spin act on a different Hilbert space, they commute. The set of operators $\hat{\boldsymbol{S}}_1^2$, $\hat{S}_{1z}$, $\hat{\boldsymbol{S}}_2^2$, $\hat{S}_{2z}$ therefore all mutually commute and hence share a set of simultaneous eigenstates,

$$|S_1, M_{S_1}, S_2, M_{S_2}\rangle = |S_1, M_{S_1}\rangle\, |S_2, M_{S_2}\rangle \,, \tag{2.13}$$

that span the two-spin Hilbert space. This set of $(2S_1 + 1)(2S_2 + 1)$ states is a direct product of the states, $|S, M_S\rangle$, spanning each of the two single-spin Hilbert spaces. This representation is often referred to as the uncoupled representation, and throughout the remainder of this chapter will be the primary representation employed.

An alternative complete set of commuting operators for this two-spin space is $\hat{\boldsymbol{S}}_1^2$, $\hat{\boldsymbol{S}}_2^2$, $\hat{\boldsymbol{S}}^2 = (\hat{\boldsymbol{S}}_1 + \hat{\boldsymbol{S}}_2)^2$, and $\hat{S}_z = \hat{S}_{1z} + \hat{S}_{2z}$. In addition to the square of the magnitude of the spin angular momentum of each spin, this set of operators contains the square of the magnitude of the spin angular momentum of the coupled spin operator and its projection onto the z axis. Here, the $(2S_1+1)(2S_2+1)$ simultaneous eigenstates of these operators will be denoted by $|SM_S\rangle$. These states can take any spin quantum number S in the range $|S_1 - S_2| \leq S \leq S_1 + S_2$, and for a given S there are $2S + 1$ functions with different projection quantum numbers. The states $|SM_S\rangle$ satisfy the relations

$$\hat{\boldsymbol{S}}^2 \, |S, M_S\rangle = \hbar^2 S(S+1) \, |S, M_S\rangle \qquad \hat{S}_z \, |S, M_S\rangle = \hbar M_S \, |S, M_S\rangle \, . \tag{2.14}$$

This is referred to as the coupled representation. For a set of two spin-$\frac{1}{2}$ particles the four coupled representation states are

$$\begin{aligned} |0,0\rangle \equiv |S\rangle &= \frac{1}{\sqrt{2}}\Big(|\alpha\beta\rangle - |\beta\alpha\rangle \Big) \quad & |1,0\rangle \equiv |T_0\rangle &= \frac{1}{\sqrt{2}}\Big(|\alpha\beta\rangle + |\beta\alpha\rangle \Big) \\ |1,1\rangle \equiv |T_+\rangle &= |\alpha\alpha\rangle & |1,-1\rangle \equiv |T_-\rangle &= |\beta\beta\rangle \, , \end{aligned} \tag{2.15}$$

where $|S\rangle$ is the singlet state while $|T_+\rangle$, $|T_0\rangle$, and $|T_-\rangle$ are the three triplet states. For the radical pair considered here, the reactivity of the system depends on whether the two electron spins are in a singlet or triplet state. In Chapter 3, this coupled representation will be employed to develop an alternative approach for treating the dynamics of large spin systems.

2.2 Quantum Dynamics

2.2.1 Spin Dynamics

The quantum dynamics of radical pair reactions can be described in terms of the density operator for the spin degrees of freedom of the radical pair, $\hat{\rho}$. The time evolution of this density operator is typically described by a master equation of the form[20]

$$\frac{\mathrm{d}}{\mathrm{d}t}\hat{\rho}(t) = -\frac{i}{\hbar}\left[\hat{H}, \hat{\rho}(t)\right] - \mathcal{K}\hat{\rho}(t). \tag{2.16}$$

The unitary evolution of the density operator due to the interactions present in the spin Hamiltonian, $\hat{H}$, is given by the first term. The second term describes the incoherent recombination process, here modelled using the Liouville space superoperator $\mathcal{K}$.

2.2.2 Radical Pair Hamiltonian

The spin Hamiltonian for the radical pair system can be written as a sum of Hamiltonians for each radical and an electron spin-spin coupling term

$$\hat{H} = \hat{H}_1 + \hat{H}_2 + \hat{H}_{12}. \tag{2.17}$$

The single radical Hamiltonians, $\hat{H}_i$, include the Zeeman interaction between the radical's unpaired electron spin and an applied magnetic field, $\boldsymbol{B}$, and the hyperfine interactions between the electron spin and each of the nuclear spins in the radical. For a radical containing N_i nuclear spins this Hamiltonian is

$$\hat{H}_i = \boldsymbol{\omega}_i \cdot \hat{\boldsymbol{S}}_i + \sum_{k=1}^{N_i} \hat{\boldsymbol{S}}_i \cdot \mathbf{A}_{ik} \cdot \hat{\boldsymbol{I}}_{ik}, \tag{2.18}$$

where $\boldsymbol{\omega}_i = \mu_B \mathbf{g}_i \cdot \boldsymbol{B}/\hbar$, μ_B is the Bohr magneton, $\mathbf{g}_i$ is the g-tensor of the i-th radical electron, $\mathbf{A}_{ik}$ is the hyperfine coupling tensor between this electron spin and the k-th nuclear spin, and $\hat{\boldsymbol{I}}_{ik}$ and $\hat{\boldsymbol{S}}_i$ are the vector spin operators corresponding to this nuclear spin and electron spin i, respectively.

Zeeman Interactions

The magnetic dipole moment associated with the spin of each unpaired electron in the radical pair can interact with an applied magnetic field. For an electron with no orbital angular momentum and in the absence of spin-orbit coupling, the magnetic dipole moment operator is[19]

$$\hat{\boldsymbol{\mu}}_i = \gamma_e \hat{\boldsymbol{S}}_i, \tag{2.19}$$

where $\gamma_e = -\mu_B g_e/\hbar$ is the gyromagnetic ratio of a free electron. The interaction between an applied magnetic field, $\boldsymbol{B}$, and the electron's magnetic moment is[19]

$$\hat{H}_{\mathrm{Z},i} = -\hat{\boldsymbol{\mu}}_i \cdot \boldsymbol{B} = \frac{g_e \mu_B}{\hbar} \hat{\boldsymbol{S}}_i \cdot \boldsymbol{B}. \tag{2.20}$$

where μ_B is the Bohr magneton and g_e is the free electron g-factor. Without loss of generality the spin operators can be defined so that the z axis points along the axis of the applied magnetic field. On doing so the contribution to the Zeeman interaction becomes

$$\hat{H}_{\mathrm{Z},i} = \frac{g_e \mu_B}{\hbar} \hat{S}_{iz} B. \tag{2.21}$$

As such, the Zeeman interaction splits the energy of the $|\alpha\rangle$, $|\beta\rangle$ electron spin states by

$$\Delta E = g_e \mu_B B. \tag{2.22}$$

For a radical pair, with each radical electron spin experiencing the same electron Zeeman interaction, the Zeeman interaction provides a non-zero contribution to the energy of any electron spin state with non-zero magnetisation. As such, the Zeeman interaction does not influence the energy of the $|S\rangle$ and $|T_0\rangle$ states while the energies of the $|T_+\rangle$ and $|T_-\rangle$ triplet states become

$$\langle T_+| \hat{H}_{\mathrm{Z}} |T_+\rangle = g_e \mu_B B \qquad \langle T_-| \hat{H}_{\mathrm{Z}} |T_-\rangle = -g_e \mu_B B, \tag{2.23}$$

where $\hat{H}_{\mathrm{Z}} = \hat{H}_{\mathrm{Z},1} + \hat{H}_{\mathrm{Z},2}$ is the total Zeeman interaction contribution to the radical pair Hamiltonian.

The presence of spin-orbit coupling can lead to the g-factor deviating from the free electron value.[19,21,22] Including the spin-orbit coupling to second order in perturbation theory leads to an electron g-factor given by[19,22,23]

$$\mathbf{g}_{\alpha\beta} = g_e\delta_{\alpha\beta} - 2\lambda\sum_n \frac{\langle\Psi_0|\,\hat{L}_\alpha\,|\Psi_n\rangle\,\langle\Psi_n|\,\hat{L}_\beta\,|\Psi_0\rangle}{E_n - E_0}, \tag{2.24}$$

where $\hat{L}_\alpha$ is the α-th component of the orbital angular momentum operator, λ is the spin orbit coupling parameter, and $|\Psi_n\rangle$ is a spatial component of the n-th electronic wavefunction. For the conjugated organic radicals considered throughout this thesis spin-orbit coupling is typically small[24] and can be ignored. However, for a large applied magnetic field, the spin-orbit contribution to the g-factor can significantly influence the dynamics of radical pairs. Differences in the g-factor between the two electron spins in a radical pair can introduce magnetic field dependent transitions between singlet and triplet states, which at high fields can significantly influence radical pair reaction yields.[25]

The magnetic moments of nuclei can likewise interact with an applied magnetic field. Throughout this thesis, these nuclear Zeeman interactions will be ignored. The gyromagnetic ratio of a particle is inversely proportional to its mass[22] and so the nuclear Zeeman interactions are at least 3 orders of magnitude smaller than the electronic Zeeman interaction. These interactions are unlikely to play a significant role in the spin dynamics of radical pair until after a very long time.

Electron Spin Coupling Interactions

The electron spin coupling Hamiltonian is[19]

$$\hat{H}_{12} = \hat{\boldsymbol{S}}_1 \cdot \mathbf{M} \cdot \hat{\boldsymbol{S}}_2 \tag{2.25}$$

$$= -2J\hat{\boldsymbol{S}}_1 \cdot \hat{\boldsymbol{S}}_2 + \hat{\boldsymbol{S}}_1 \cdot \mathbf{D} \cdot \hat{\boldsymbol{S}}_2 \tag{2.26}$$

where $\mathbf{M} = -2J\mathbf{1} + \mathbf{D}$ is the total electron spin coupling tensor, J is the scalar exchange coupling and $\mathbf{D}$ is the dipolar coupling tensor. The dipolar coupling between the two electron spins is analogous to the coupling arising between two

classical magnetic dipoles. The magnetic field at a point $\boldsymbol{r}$ away from a classical point magnetic dipole, with dipole moment $\boldsymbol{\mu}_{e1}$, is

$$\boldsymbol{B}(\boldsymbol{r}) = \frac{\mu_0}{4\pi r^3}\left(\frac{3(\boldsymbol{\mu}_{e1}\cdot\boldsymbol{r})\boldsymbol{r}}{r^2} - \boldsymbol{\mu}_{e1}\right). \tag{2.27}$$

where μ_0 is the permeability of free space and $r = \|\boldsymbol{r}\|$ is the distance between the point $\boldsymbol{r}$ and the location of the magnetic dipole (here taken to be the origin). A second magnetic dipole will interact with this field. If this second dipole is located at point $\boldsymbol{r}$ and has dipole moment $\boldsymbol{\mu}_{e2}$, then the interaction energy between these two classical magnetic dipoles is

$$E(\boldsymbol{r}) = -\boldsymbol{B}(\boldsymbol{r})\cdot\boldsymbol{\mu}_{e2} \tag{2.28}$$

$$= \frac{\mu_0}{4\pi r^3}\left(\boldsymbol{\mu}_{e1}\cdot\boldsymbol{\mu}_{e2} - \frac{3(\boldsymbol{\mu}_{e2}\cdot\boldsymbol{r})(\boldsymbol{\mu}_{e1}\cdot\boldsymbol{r})}{r^2}\right). \tag{2.29}$$

Quantum mechanically this interaction is represented by the Hamiltonian[22]

$$\hat{H}_{\text{dip}}(\boldsymbol{r}) = \frac{\mu_0}{4\pi r^3}\left(\hat{\boldsymbol{\mu}}_{e1}\cdot\hat{\boldsymbol{\mu}}_{e2} - \frac{3(\hat{\boldsymbol{\mu}}_{e2}\cdot\boldsymbol{r})(\hat{\boldsymbol{\mu}}_{e1}\cdot\boldsymbol{r})}{r^2}\right) \tag{2.30}$$

$$= \frac{\mu_0\gamma_1\gamma_2}{4\pi r^3}\left(\hat{\boldsymbol{S}}_1\cdot\hat{\boldsymbol{S}}_2 - \frac{3(\hat{\boldsymbol{S}}_2\cdot\boldsymbol{r})(\hat{\boldsymbol{S}}_1\cdot\boldsymbol{r})}{r^2}\right) \tag{2.31}$$

where the definition of the dipole moment operators for two electron spins with gyromagnetic ratios γ_1 and γ_2, respectively, have been inserted. Factorising out the spin operators, this expression may be rewritten as

$$\hat{H}_{\text{dip}}(\boldsymbol{r}) = \hat{\boldsymbol{S}}_1\cdot\left[\frac{\mu_0\gamma_1\gamma_2}{4\pi r^3}\left(\mathbf{1} - \frac{3\boldsymbol{r}\otimes\boldsymbol{r}}{r^2}\right)\right]\cdot\hat{\boldsymbol{S}}_2 \tag{2.32}$$

$$= \hat{\boldsymbol{S}}_1\cdot\mathbf{D}(\boldsymbol{r})\cdot\hat{\boldsymbol{S}}_2 \tag{2.33}$$

where $\otimes$ denotes an outer product of two vectors, $\mathbf{1}$ is the 3×3 identity matrix and $\mathbf{D}(\boldsymbol{r})$ is a position dependent dipolar coupling tensor. Evaluating the average of the dipolar coupling Hamiltonian over the electron spin density removes the spatial dependence and gives an effective spin Hamiltonian. On doing so the anisotropic dipolar coupling tensor is obtained[19,22]:

$$D_{\alpha\beta} = \frac{\mu_0\gamma_1\gamma_2}{4\pi}\left\langle\frac{r^2\delta_{\alpha\beta} - 3r_\alpha r_\beta}{r^5}\right\rangle, \tag{2.34}$$

where $\alpha, \beta \in \{x, y, z\}$, and $\langle \cdot \rangle$ denotes the average over the electron spin density. This tensor is symmetric and its trace is

$$\mathrm{tr}\,[\mathbf{D}] = \frac{\mu_0 \gamma_1 \gamma_2}{4\pi} \sum_{\alpha} \left\langle \frac{r^2 - 3r_\alpha^2}{r^5} \right\rangle = 0, \tag{2.35}$$

as expected.

It is often convenient to define the spin operators with respect to the eigenframe of this dipolar coupling operator. On doing so the Hamiltonian becomes

$$\hat{H}_{\mathrm{dip}} = \hat{\boldsymbol{S}}_1 \cdot \mathbf{D} \cdot \hat{\boldsymbol{S}}_2 \tag{2.36}$$

where the dipolar coupling tensor is now diagonal,

$$\mathbf{D} = \begin{pmatrix} D_x & 0 & 0 \\ 0 & D_y & 0 \\ 0 & 0 & D_z \end{pmatrix}, \tag{2.37}$$

and by convention $|D_z| \geq |D_y| \geq |D_x|$. As the dipolar coupling tensor is traceless $D_x + D_y + D_z = 0$, and so the quantities D_x, D_y, and D_z can be uniquely specified by two parameters. By convention, the two parameters chosen are the axiality, D, and rhombicity, E, given by[19]

$$D = \frac{3}{2} D_z \qquad\qquad E = \frac{1}{2}(D_x - D_y). \tag{2.38}$$

The importance of these parameters becomes apparent when the dipolar coupling interaction is written in terms of the coupled representation spin operators as

$$\hat{H}_{\mathrm{dip}} = D\left(\hat{S}_z^2 - \frac{1}{3}\hat{\boldsymbol{S}}^2\right) + E(\hat{S}_x^2 - \hat{S}_y^2), \tag{2.39}$$

where $\hat{\boldsymbol{S}} = \hat{\boldsymbol{S}}_1 + \hat{\boldsymbol{S}}_2$. This is commonly referred to as the zero field splitting Hamiltonian. Even in the absence of an applied magnetic field it splits the energy levels of the singlet and triplet electronic spin states. If the rhombicity is non-zero, the $|T_+\rangle$ and $|T_-\rangle$ states are not eigenstates of the electron spin coupling and the final term in equation 2.39 introduces a coherent oscillation between them. From the two parameters (D and E) and the eigenframe of this tensor the full dipolar coupling tensor may be reconstructed. The dipolar coupling constant depends on

the separation, r, of the radical pairs, and for sufficiently well separated radical pairs the axiality is well described by[26]

$$D(r) \propto r^{-3}. \tag{2.40}$$

In addition to the anisotropic dipolar coupling, an isotropic exchange coupling interaction exists between the two electron spins. This isotropic exchange coupling, parameterised by the constant J, arises due to correlations between electrons in the radical pair system and can be written as a sum of contributions from direct exchange and superexchange interactions. The direct exchange interaction arises due to the fermionic nature of electrons. By the Pauli exclusion principle the total electronic wavefunction must be antisymmetric under exchange of any two electrons. The origin of this effect for a two electron system is briefly discussed next[27,28].

First consider two non-interacting electrons (ignoring all spin degrees of freedom) with each electron experiencing the same potential. The Schrödinger equation for this system is,

$$\left[\frac{\hat{\boldsymbol{p}}_1^2}{2m_e} + \frac{\hat{\boldsymbol{p}}_2^2}{2m_e} + (V(\hat{\boldsymbol{r}}_1) + V(\hat{\boldsymbol{r}}_2))\right]\Psi = E_0\Psi, \tag{2.41}$$

where $\hat{\boldsymbol{r}}_i$ and $\hat{\boldsymbol{p}}_i$ are the position and momentum operators for the the i-th electron, V is the describes the potential energy, and E_0 is the energy of the system. This equation is separable and so its solutions can be written as a direct product of solutions of the Schrödinger equation for each electron independently. Two solutions to equation 2.41 are

$$\Psi_I(\boldsymbol{r}_1, \boldsymbol{r}_2) = \psi_a(\boldsymbol{r}_1)\psi_b(\boldsymbol{r}_2) \qquad \Psi_{II}(\boldsymbol{r}_1, \boldsymbol{r}_2) = \psi_b(\boldsymbol{r}_1)\psi_a(\boldsymbol{r}_2), \tag{2.42}$$

both with energy $E_0 = E_a + E_b$. ψ_a and ψ_b are solutions to the single electron problem, which here (for simplicity) are assumed to be orthonormal, and E_a and E_b are the energies associated with these two states.[28] Introducing the Coulomb interaction between the two electrons as a perturbation, the degeneracy between

these two states is broken. To first order, the energies of the two non-degenerate states are given by the solutions of the secular equations[17,27]

$$\det\begin{pmatrix} E_0 + K - E & J_{ex} \\ J_{ex} & E_0 + K - E \end{pmatrix} = 0, \tag{2.43}$$

where the Coulomb

$$K = \frac{e^2}{4\pi\epsilon_0} \langle \Psi_I(\boldsymbol{r}_1, \boldsymbol{r}_2) | \frac{1}{|\boldsymbol{r}_1 - \boldsymbol{r}_2|} | \Psi_I(\boldsymbol{r}_1, \boldsymbol{r}_2) \rangle \tag{2.44}$$

$$= \frac{e^2}{4\pi\epsilon_0} \langle \Psi_{II}(\boldsymbol{r}_1, \boldsymbol{r}_2) | \frac{1}{|\boldsymbol{r}_1 - \boldsymbol{r}_2|} | \Psi_{II}(\boldsymbol{r}_1, \boldsymbol{r}_2) \rangle \tag{2.45}$$

$$\tag{2.46}$$

and exchange integrals[19]

$$J_{ex} = \frac{e^2}{4\pi\epsilon_0} \langle \psi_a(\boldsymbol{r}_1)\psi_b(\boldsymbol{r}_2) | \frac{1}{|\boldsymbol{r}_1 - \boldsymbol{r}_2|} | \psi_b(\boldsymbol{r}_1)\psi_a(\boldsymbol{r}_2) \rangle \tag{2.47}$$

have been introduced. Equation 2.43 has two solutions,

$$E_+ = E_0 + K + J_{ex} \qquad\qquad E_- = E_0 + K - J_{ex}, \tag{2.48}$$

which are the energies of the symmetric and antisymmetric combinations of the spatial wavefunctions (orbitals) Ψ_I and Ψ_{II},[28]

$$\begin{aligned} \Psi_+(\boldsymbol{r}_1, \boldsymbol{r}_2) &= \frac{1}{\sqrt{2}}(\psi_a(\boldsymbol{r}_1)\psi_b(\boldsymbol{r}_2) + \psi_b(\boldsymbol{r}_1)\psi_a(\boldsymbol{r}_2)) \\ \Psi_-(\boldsymbol{r}_1, \boldsymbol{r}_2) &= \frac{1}{\sqrt{2}}(\psi_a(\boldsymbol{r}_1)\psi_b(\boldsymbol{r}_2) - \psi_b(\boldsymbol{r}_1)\psi_a(\boldsymbol{r}_2)). \end{aligned} \tag{2.49}$$

In the absence of any spin-orbit coupling the total electronic wavefunction can be written as a product of a spatial component (equation 2.49) and a spin component (equation 2.15). By the Pauli exclusion principle the total electronic wavefunction must be antisymmetric with respect to exchange of the two electrons. When the spin wavefunction is antisymmetric it must therefore be paired with a symmetric spatial wavefunction and vice versa. The singlet spin state is therefore paired with Ψ_+ while the triplet spin states are paired with Ψ_-. As such, there is a difference in the energy of singlet and triplet spin states of

$$E_S - E_T = 2J_{ex}. \tag{2.50}$$

This exchange interaction introduces a Heisenberg exchange Hamiltonian term to the spin Hamiltonian of the form[19,28]

$$\hat{H}_{ex} = -2J\hat{\boldsymbol{S}}_1 \cdot \hat{\boldsymbol{S}}_2, \tag{2.51}$$

where $J = J_{ex}/\hbar^2$ is the exchange coupling constant.

The antisymmetric spatial wavefunction, Ψ_-, vanishes when $\boldsymbol{r}_1 = \boldsymbol{r}_2$ while there is a corresponding increase in probability density associated with the symmetric wavefunction, Ψ_+.[17] That is, there is a reduced probability of observing the two electrons nearby in the Ψ_- state compared to the Ψ_+ state and so the electron electron repulsion energy is lower for Ψ_-. Therefore, J is typically positive and the direct exchange coupling lowers the energy of the triplet states with respect to the singlet state.

The overall J coupling constant, however, is not necessarily always positive. In addition to this direct mechanism, there is an indirect superexchange contribution to the exchange coupling.[22] This superexchange interaction accounts for exchange interactions in excited states of the molecule,[29,30] and is mediated by the electrons in orbitals bridging the two radicals. This term arises as a higher order correction to the interaction energy,[29,31] and depends on the overlap of the occupied orbitals of the radical pair and the bridging orbitals and can be strongly influenced by interactions between the radical pair and its environment.[32] This interaction can provide either positive or negative contributions to the exchange coupling constant, J, depending on the orbitals involved.[30] Both of these exchange interactions depend on the separation between the radicals forming the radical pair.[32] Often, within the spin chemistry literature, it is assumed that the overall exchange interaction decreases exponentially with the separation, r, of the two radicals

$$J(r) = J_0 e^{-\beta r} \tag{2.52}$$

and is independent of the orientation of the system.[20,26] For a well-separated radical pair, this exchange interaction is often weak and the dipolar coupling interaction

(which has a much less rapid decay with seperation) is the dominant contribution to the electron spin coupling.

Recently, Fay *et al.* have proposed that radical pairs undergoing spin selective recombination reactions will experience an additional exchange coupling originating from the recombination reaction.[33] This reactive exchange coupling arises due to the coupling between the spin, electronic, and nuclear degrees of freedom in the full system. The coupling between radical pair and product states gives rise to shifts in the radical pair energy levels, which to lowest order depends on the square of the diabatic coupling between the states. If the shifts for singlet and triplet radical pair states are different then this introduces is a further contribution to the difference in the singlet and triplet energy levels. This effect is expected to be most important when the recombination rates for singlet and triplet states are significantly different.[33]

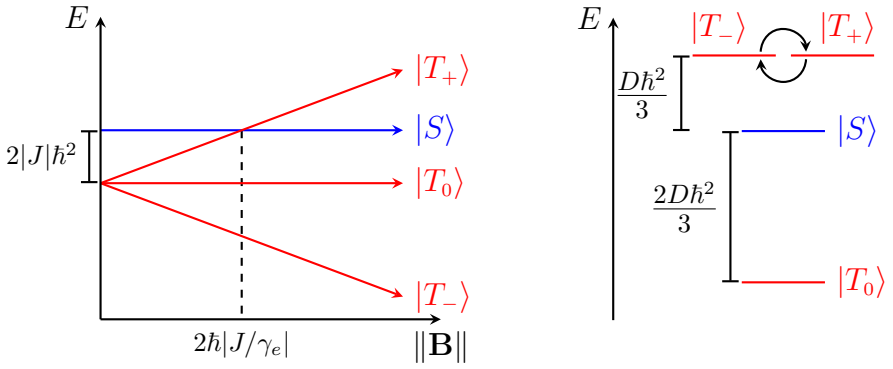

Figure 2.2: (left) The energy of singlet and triplet spin states in the presence of scalar electron exchange and electron Zeeman interactions for different values of the applied magnetic field $\boldsymbol{B}$. The projection quantum numbers are defined with respect to the magnetic field direction. (right) The energy of singlet and triplet states in the presence of dipolar coupling with $D > 0$. If the rhombicity of the dipolar coupling is non-zero, the $|T_+\rangle$ and $|T_-\rangle$ states are not eigenstates of the dipolar coupling Hamiltonian and interconversion between these two states occurs.

The effects of the Zeeman and spin coupling terms on the energies of the singlet and triplet states are shown in figure 2.2. In the presence of an applied magnetic field, there is a splitting of the energy levels of the triplet states due to the Zeeman

interaction. For $B = 2\hbar|J/\gamma_e|$ the energies of the $|S\rangle$ and $|T_-\rangle$ states cross. Provided a transition between these two states is spin allowed (e.g., as a result of hyperfine interactions) it will be most efficient for this value of the applied magnetic field. This leads to an increase in the percentage of singlet-born radical pairs that convert to a triplet state, and is one of the dominant mechanisms by which magnetic fields can influence the outcomes of radical pair recombination reactions. As the strength of the applied magnetic field increases, the $|T_+\rangle$ and $|T_-\rangle$ states become energetically separated from the singlet state, and conversion between these states becomes less efficient. Singlet states will only interconvert significantly with $|T_0\rangle$ states, leading to a decrease in the percentage of singlet-born radical pairs that convert to a triplet state. In the absence of any additional spin-spin interactions these transitions are forbidden by conservation of spin angular momentum. It is the presence of interactions of the electron spins with the nuclear spins in each radical that allow for these transitions.

Hyperfine Interactions

The hyperfine term in the Hamiltonian arises from the interaction of the electron spin with the magnetic field induced by the nuclear spins. This interaction can be decomposed into two components: an isotropic Fermi contact interaction and an anisotropic dipole-dipole interaction. That is,

$$\hat{H}_{\mathrm{hyp},ik} = a_{ik}\hat{\boldsymbol{S}}_i \cdot \hat{\boldsymbol{I}}_{ik} + \hat{\boldsymbol{S}}_i \cdot \mathbf{A}'_{ik} \cdot \hat{\boldsymbol{I}}_{ik}, \tag{2.53}$$

where $a_{ik} = \frac{1}{3}\mathrm{tr}\left[\mathbf{A}_{ik}\right]$ accounts for the Fermi contact interactions and $\mathbf{A}'_{ik} = \mathbf{A}_{ik} - a_{ik}\mathbf{1}$ is the traceless part of the hyperfine coupling tensor arising from the dipole-dipole interaction.

The dipolar coupling between electron and nuclear spins is analogous to the dipolar coupling between two electron spins. A nuclear spin with dipole moment operator, $\hat{\boldsymbol{\mu}}_{nik} = \gamma_{ik}\hat{\boldsymbol{I}}_{ik}$ will interact with the magnetic field arising from the

electron spins in the radical. The dipolar coupling tensor between the nuclear spin and electron spin[19] is

$$A'_{ik\alpha\beta}(\boldsymbol{r}) = \frac{\mu_0\gamma_i\gamma_{ik}}{4\pi}\left\langle\frac{r^2\delta_{\alpha\beta} - 3r_\alpha r_\beta}{r^5}\right\rangle, \tag{2.54}$$

where γ_i is the gyromagnetic ratio of electron i, γ_{ik} is the gyromagnetic ratio of nucleus ik, $\boldsymbol{r}$ is the separation between the electron and nuclear spins, and $\langle\cdot\rangle$ denotes an average over the electron spin density.

The point dipole approximation holds when the electron and nuclear spins are well separated. For a system with non-zero electron spin density at the nucleus, the point dipole approximation is no longer sufficient. In this case it becomes necessary to include an additional contribution accounting for the non-zero probability of finding the electron spin at the nucleus, the Fermi contact interaction.[34,35] In the limit of a magnetic dipole, $\boldsymbol{\mu}$, with zero size, the resultant magnetic field includes a delta function correction at the dipole in addition to the dipolar coupling term in equation 2.27,[36]

$$\mathbf{B}(\boldsymbol{r}) = \frac{2}{3}\mu_0\boldsymbol{\mu}\delta(\boldsymbol{r} - \boldsymbol{r}_\mu) \tag{2.55}$$

where $\boldsymbol{r}_\mu$ is the position of the dipole. The electron spins in the radical pair interact with the field associated with each nuclear spin dipole. Averaging over the electron spin density, one obtains the isotropic contribution to the hyperfine coupling constant[19,22,23,37]

$$a_{ik} = -\frac{2}{3}\mu_0\gamma_e\gamma_{ik}\rho_S(\boldsymbol{r}_{ik}), \tag{2.56}$$

where $\boldsymbol{r}_{ik}$ is the position of the k-th nuclear spin in radical i, and $\rho_S(\boldsymbol{r}_{ik})$ is the unpaired electron density at this nucleus, which can be defined in terms of the full many-electron wavefunction, $|\Psi\rangle$, and the positions of each of the electrons $\boldsymbol{r}_k$ by[22]

$$\rho_S(\boldsymbol{r}_{ik}) = \frac{1}{\hbar}\langle\Psi|\sum_k 2\hat{S}_{zk}\delta(\boldsymbol{r}_k - \boldsymbol{r}_{ik})|\Psi\rangle. \tag{2.57}$$

An analogous contact interaction exists between two electron spins.[19] This provides an additional contribution to the exchange interaction, although typically this term is very small.[38]

Isotropic Hamiltonian

For radical pair recombination reactions in solution, rapid tumbling of the radical pairs may lead to anisotropic effects becoming unimportant. Provided the tumbling motion is sufficiently rapid (compared to the timescale of the spin dynamics) the spin system will evolve under a rotationally averaged Hamiltonian. The rotational averages of the anisotropic hyperfine and electron spin coupling interaction terms are zero, and so the spin Hamiltonian reduces to

$$\hat{H} = \hat{H}_1 + \hat{H}_2 - 2J\hat{\boldsymbol{S}}_1 \cdot \hat{\boldsymbol{S}}_2. \tag{2.58}$$

Provided the spin-orbit coupling contributions to the electron g-factors are negligible, the isotropic single radical Hamiltonians may be written as

$$\hat{H}_i = \omega \hat{S}_{iz} + \sum_{k=1}^{N_i} a_{ik} \hat{\boldsymbol{S}}_i \cdot \hat{\boldsymbol{I}}_{ik}, \tag{2.59}$$

where the quantisation axes for the spins have been selected to point along the magnetic field direction. If the tumbling motion occurs on a comparable timescale to the spin dynamics this no longer holds. The modulation of the anisotropic interactions induces relaxation of the spin system. In this case the treatment that is presented below is no longer valid, and it is necessary to use an alternative approach that explicitly accounts for the spin-lattice relaxation.[39–44]

Sparsity of the Hamiltonian

In the quantum mechanical calculations that follow it is necessary to construct a matrix representation of the Hamiltonian using some basis. One convenient basis for doing so is the direct product basis of uncoupled states for each spin,

$$\{\mathcal{B}\} = \{\bigotimes_{i=1}^{2} |S_i, M_{S_i}\rangle \bigotimes_{k=1}^{N_i} |I_{ik}, M_{I_{ik}}\rangle\}. \tag{2.60}$$

This basis provides one significant advantage over other possible choices for the radical pair simulations considered here: the matrix representation of the Hamiltonian is sparse.

For a radical pair system containing N total nuclear spins (and $Z = \mathcal{O}(2^N)$ nuclear spin states), the radical pair Hamiltonian is a sum of $9(N+1)+6$ terms, each of which contains an operator with one of the following forms:

$$\hat{S}_{i\alpha} \qquad \hat{S}_{1\alpha}\hat{S}_{2\beta} \qquad \hat{S}_{i\alpha}\hat{I}_{ik\beta}. \tag{2.61}$$

For a given state each of the above terms has a non-zero matrix element between this state and, at most, four other states. Importantly, this number does not depend on the number of spins present in the system. As there are $\mathcal{O}(N = \log(Z))$ such terms, each of the $\mathcal{O}(Z)$ states of the radical pair spin system has a non-zero Hamiltonian matrix element with only $\mathcal{O}(N)$ other states. The Hamiltonian therefore contains $\mathcal{O}(Z\log(Z))$ non-zero elements, compared to the $\mathcal{O}(Z^2)$ elements of a dense Hamiltonian. Exploiting this sparsity reduces the effort required to evaluate the action of the Hamiltonian on an arbitrary spin state to $\mathcal{O}(Z\log(Z))$ operations compared to the standard $\mathcal{O}(Z^2)$ operations required for dense matrix-vector products. For a radical pair with N spin-$\frac{1}{2}$ nuclei ($Z = 2^N$) the total number of non-zero elements is $16Z + 8Z\log_2(Z)$.

This sparsity becomes particularly important when treating a radical pair system with a large total number of spins. For a system containing $N = 20$ spin-$\frac{1}{2}$ nuclei the Hamiltonian contains $\mathcal{O}(10^5)$ times more elements than there are non-zero elements. The sparsity gives an $\mathcal{O}(10^5)$ reduction in the memory requirements and number of operations required to calculate matrix vector products between the Hamiltonian and a wavefunction.

2.2.3 Recombination Operator

In order to describe the spin selective recombination reaction of a radical pair, in which the singlet electron spin states recombine with rate k_S and the triplet rates recombine with a rate k_T, it is necessary to introduce an additional non-unitary contribution to the dynamics of the spin density operator. Over the years, a range of forms for the recombination superoperator, $\mathcal{K}$, have been proposed.[45–48] In this

section two will be discussed: the Haberkorn[45] and Jones-Hore[46,47] recombination superoperators. These two approaches for including recombination only differ in their treatment of coherences between singlet and triplet states of the radical pair.

The Haberkorn Recombination Operator

The conventional approach for including spin-selective recombination, originally presented in reference [45], includes recombination using the superoperator

$$\mathcal{K}\hat{\rho}(t) = \left\{\hat{K}, \hat{\rho}(t)\right\}, \tag{2.62}$$

where $\{\cdot,\cdot\}$ indicates an anticommutator. The Haberkorn recombination operator, $\hat{K}$, is given by

$$\hat{K} = \frac{k_S}{2}\hat{P}_S + \frac{k_T}{2}\hat{P}_T, \tag{2.63}$$

where $\hat{P}_S$ and $\hat{P}_T$ are projection operators onto the singlet and triplet electron spin subspaces and are given by

$$P_S = \frac{1}{4} - \frac{1}{\hbar^2}\hat{\boldsymbol{S}}_1 \cdot \hat{\boldsymbol{S}}_2 \tag{2.64}$$

$$P_T = \frac{3}{4} + \frac{1}{\hbar^2}\hat{\boldsymbol{S}}_1 \cdot \hat{\boldsymbol{S}}_2, \tag{2.65}$$

respectively. In the absence of any coherent terms, the Haberkorn master equation, which can be obtained by inserting equation 2.62 into equation 2.16, can be solved analytically. In the coupled electron spin basis, the equations of motion for the elements of the density operator are given by

$$\begin{aligned} \frac{\mathrm{d}}{\mathrm{d}t}\rho_{SS}(t) &= -k_S\rho_{SS}(t) & \frac{\mathrm{d}}{\mathrm{d}t}\rho_{ST_\beta}(t) &= -\left(\frac{k_S+k_T}{2}\right)\rho_{ST_\beta}(t) \\ \frac{\mathrm{d}}{\mathrm{d}t}\rho_{T_\alpha S}(t) &= -\left(\frac{k_S+k_T}{2}\right)\rho_{T_\alpha S}(t) & \frac{\mathrm{d}}{\mathrm{d}t}\rho_{T_\alpha T_\beta}(t) &= -k_T\rho_{T_\alpha T_\beta}(t). \end{aligned} \tag{2.66}$$

Within the Haberkorn treatment of recombination, the singlet and triplet states decay with rate constants k_S and k_T as required, while coherences between singlet and triplet states decay with rate $k_{ST} = (k_S + k_T)/2$.

Since its introduction, this master equation has been widely used to explain the

dynamics of radical pairs and has become the standard approach for treating the recombination of radical pairs.[20] Recently, however, a number of alternative master equations have been proposed.[46–49] This has lead to some debate in the spin chemistry literature as to which master equation is best for modelling the recombination process.[33,47–52]

Jones-Hore Recombination

In recent years, a number of alternative forms for the recombination superoperator have been proposed based on quantum measurement theory arguments. Here the recombination superoperator proposed by Jones and Hore[46,47] will be considered. Within their approach, during a time step, dt, a fraction $k_S dt$ of radical pairs have a chance of undergoing singlet recombination, a fraction $k_T dt$ may undergo triplet recombination, while the remaining $1 - k_S dt - k_T dt$ have no chance of undergoing a reaction.[46] The fraction of radical pairs which can undergo a singlet (triplet) reaction will react if they are currently in a singlet (triplet) state. The radical pairs which had a chance to react but did not must therefore be in a triplet (singlet) state.[46] The recombination reaction acts as a projective quantum measurement: failure to undergo a singlet (triplet) reaction projects the unreacted component of the density operator onto the triplet (singlet) subspace. After a time step this recombination process leads to a radical pair spin density operator given by

$$\hat{\rho}(t+dt) = (1 - k_S dt - k_T dt)\hat{\rho}(t) + k_S dt \hat{P}_T \hat{\rho}(t) \hat{P}_T + k_T dt \hat{P}_S \hat{\rho}(t) \hat{P}_S. \tag{2.67}$$

The first term accounts for the fraction of radical pairs which had no chance of undergoing a reaction. The second and third terms account for the fraction of radical pairs which failed to undergo a singlet or triplet reaction and are therefore projected onto the triplet or singlet subspaces, respectively. From this, the Jones-Hore form for the recombination superoperator[46,47] is obtained as

$$\mathcal{K}\hat{\rho}(t) = \left\{\hat{K}, \hat{\rho}(t)\right\} + \frac{k_S + k_T}{2}\left[\hat{P}_S \hat{\rho}(t) \hat{P}_T + \hat{P}_T \hat{\rho}(t) \hat{P}_S\right], \tag{2.68}$$

where $\hat{K}$ is once again the Haberkorn recombination operator but now the recombination superoperator includes an additional singlet-triplet dephasing contribution.

The Jones-Hore treatment of recombination leads to singlet-triplet coherences dephasing at a rate of $k_{ST} = k_S + k_T$, twice that of the Haberkorn treatment. This difference in recombination-induced singlet-triplet dephasing rates provides a means for experimentally testing these master equations.

Maeda *et al.*[53] have used this difference in dephasing rates to experimentally examine the treatment of recombination for a carotenoid-porphyrin-fullerine (cpf) triad radical pair. This is complicated by the fact that the addition dephasing in the Jones-Hore master equation is indistinguishable from other sources such as those arising from spin-lattice relaxation.[53] The singlet-triplet dephasing rate arising from the treatment of recombination is therefore a lower limit for the decoherence rate.[50] Maeda *et al.*[53] found that the singlet-triplet decoherence rate of the cpf triad radical pair was incompatible with the Jones-Hore master equation, because the Jones-Hore dephasing rate was larger than that obtained experimentally. In contrast, the theoretical dephasing rate obtained within the Haberkorn treatment was consistent with the experiment. This does not necessarily imply that the Haberkorn recombination operator is correct. In principle, the true master equation could include additional sources of singlet-triplet dephasing that are just smaller than those predicted using the Jones-Hore approach.

Recently, Fay *et al.*[33] have derived a series of quantum master equations describing the evolution of the radical pair spin density operator starting from a microscopic model for the recombination process. Treating the coupling between radical pair and product states in the nonadiabatic limit (second order in perturbation theory), the Haberkorn master equation (with an additional reactive exchange coupling term) was recovered. Higher order corrections introduce an additional singlet-triplet dephasing term as found in the Jones-Hore form of the recombination superoperator (equation 2.68); however, unlike the Jones-Hore approach, the dephasing rate is not necessarily $(k_S + k_T)/2$ and instead depends on the details of the system.[33] This will be discussed further in Chapter 4. In the following two chapters, however,

the Haberkorn master equation will be used to treat the recombination of radical pairs. Further, in order to simplify the following discussion a unit system where $\hbar = 1$ will be used throughout the remainder of this chapter.

2.2.4 Time Dependent Observables

For the model recombination reaction depicted in figure 2.1, the radical pair is initially prepared in a singlet state. The density operator for the spin system is initially

$$\hat{\rho}(0) = \frac{1}{Z_1 Z_2}\hat{P}_S, \tag{2.69}$$

where $Z_i = \prod_{k=1}^{N_i}(2I_{ik}+1)$ is the total number of nuclear spin states in radical i, and $Z = Z_1 Z_2$ is the total number of nuclear spin states. This corresponds to an infinite temperature distribution of the nuclear spins that is initially uncorrelated with the system. For radical pairs at room temperature, this approximation is often valid. As the typical spin interaction energies are between $\sim 10^{-4}$ and $\sim 10^{-6}$ $k_B T$, the Boltzmann distribution for the nuclear spin bath is well approximated by a uniform distribution. The typical spin interaction energies so the identity operator is a very good approximation to the Boltzmann distribution for the nuclear spin bath. The density operator evolves according to the Haberkorn master equation[20,45]

$$\frac{\mathrm{d}}{\mathrm{d}t}\hat{\rho}(t) = -i\left[\hat{H}, \hat{\rho}(t)\right] - \left\{\hat{K}, \hat{\rho}(t)\right\}, \tag{2.70}$$

whose solution gives the density operator at time t,

$$\hat{\rho}(t) = e^{-i\hat{H}t - \hat{K}t}\hat{\rho}(0)e^{+i\hat{H}t - \hat{K}t}. \tag{2.71}$$

From the time-evolved density operator, the ensemble averages of observables can be obtained as

$$O(t) = \mathrm{tr}\left[\hat{O}\hat{\rho}(t)\right], \tag{2.72}$$

where the trace is evaluated over the full spin Hilbert space and $\hat{O}$ is the Hermitian operator corresponding to the observable quantity, O. Inserting the Hermitian operators $\hat{\mathbf{1}}$, $\hat{P}_S$ and $\hat{P}_T$ gives the time-dependent probabilities of observing the

system in a radical pair state ($P(t)$), singlet radical pair state ($P_S(t)$) and triplet pair states ($P_T(t)$), respectively. These survival probabilities and the related singlet and triplet quantum yields,

$$\Phi_S = k_S \int_0^\infty P_S(t)\mathrm{d}t \qquad \Phi_T = k_T \int_0^\infty P_T(t)\mathrm{d}t, \tag{2.73}$$

are the key observables of interest in radical pair recombination reactions.

If the radical pair recombines from singlet and triplet states at the same rate $k = k_S = k_T$ (symmetric recombination) then these expressions simplify considerably. For symmetric recombination, the Haberkorn operator reduces to

$$\hat{K} = \frac{k}{2}(\hat{P}_S + \hat{P}_T) = \frac{k}{2}, \tag{2.74}$$

and thus commutes with all operators. Factorising out the recombination operator, equation 2.71 becomes

$$\hat{\rho}(t) = e^{-kt}e^{-i\hat{H}t}\hat{\rho}(0)e^{+i\hat{H}t} = e^{-kt}\hat{\rho}'(t), \tag{2.75}$$

where $\hat{\rho}'(t)$ corresponds to the density operator obtained in the absence of recombination. Inserting this into equation 2.77 gives

$$O(t) = e^{-kt}\mathrm{tr}\left[\hat{O}\hat{\rho}'(t)\right]. \tag{2.76}$$

Expectation values of observables can be evaluated by performing unitary time evolution of the spin density operator under the radical pair Hamiltonian. The recombination process simply introduces an exponential decay of these time-dependent quantities.

In order to obtain the ensemble average of time-dependent observables, it is necessary to evaluate equation 2.71. Using the sparsity of the system Hamiltonian this can be done in time scaling as $\mathcal{O}(\log(Z)Z^2)$ and using memory scaling as $\mathcal{O}(Z^2)$. As Z scales exponentially with the number of spins, memory requirements typically restrict this treatment to $\lesssim$15 spins. For larger systems an alternative approach for

evaluating these averages is needed.

By exploiting the invariance of the trace to cyclic permutations the operators in equation 2.77 can be transformed into the Heisenberg picture to

$$O(t) = \mathrm{tr}\left[\hat{O}(t)\hat{\rho}(0)\right] \tag{2.77}$$

where

$$\hat{O}(t) = e^{+i\hat{H}t-\hat{K}t}\hat{O}e^{-i\hat{H}t-\hat{K}t}, \tag{2.78}$$

evolves according to the Heisenberg equation of motion

$$\frac{\mathrm{d}}{\mathrm{d}t}\hat{O}(t) = i\left[\hat{H},\hat{O}(t)\right] - \left\{\hat{K},\hat{O}(t)\right\}. \tag{2.79}$$

Inserting the initial density operator (equation 2.69) into equation 2.77 gives

$$O(t) = \frac{1}{Z_1 Z_2}\mathrm{tr}\left[\hat{O}(t)\hat{P}_S\right]. \tag{2.80}$$

The trace can now be expanded with respect to any complete set of states. Expanding the trace in equation 2.80 with respect to the basis

$$\{|\mathcal{B}\rangle\} = \{|\Theta\rangle \otimes |\mathbf{m}_1\rangle \otimes |\mathbf{m}_2\rangle\}, \tag{2.81}$$

formed by taking a direct product of the coupled basis for the electronic spin states $|\Theta\rangle \in \{|S\rangle, |T_0\rangle, |T_+\rangle, |T_-\rangle\}$ and the uncoupled basis for each of the nuclear spins,

$$|\mathbf{m}_i\rangle = \bigotimes_{k=1}^{N_i} |m_{ik}\rangle, \tag{2.82}$$

gives

$$O(t) = \frac{1}{Z_1 Z_2}\sum_{\{\mathbf{m}_1\}}\sum_{\{\mathbf{m}_2\}} \langle S,\mathbf{m}_1,\mathbf{m}_2|\,\hat{O}(t)\,|S,\mathbf{m}_1,\mathbf{m}_2\rangle \tag{2.83}$$

$$= \frac{1}{Z_1 Z_2}\sum_{\{\mathbf{m}_1\}}\sum_{\{\mathbf{m}_2\}} \langle S,\mathbf{m}_1,\mathbf{m}_2|\,e^{+i\hat{H}t-\hat{K}t}\hat{O}e^{-i\hat{H}t-\hat{K}t}\,|S,\mathbf{m}_1,\mathbf{m}_2\rangle \tag{2.84}$$

$$= \frac{1}{Z_1 Z_2}\sum_{\{\mathbf{m}_1\}}\sum_{\{\mathbf{m}_2\}} \langle S,\mathbf{m}_1,\mathbf{m}_2;t|\,\hat{O}\,|S,\mathbf{m}_1,\mathbf{m}_2;t\rangle. \tag{2.85}$$

In equation 2.85, the notation

$$\sum_{\{\mathbf{m}_i\}} = \sum_{m_{i1}=-I_{i1}}^{I_{i1}} \cdots \sum_{m_{iN_i}=-I_{iN_i}}^{I_{iN_i}} \tag{2.86}$$

has been introduced to denote the sum over all nuclear spin basis states. The time-dependent expectation values of an operator can be evaluated by evolving Z wavefunctions, each with a different initial nuclear spin state, and averaging the expectation values obtained for each one. The time evolved wavefunction

$$|S, \mathbf{m}_1, \mathbf{m}_2; t\rangle = e^{-i\hat{H}t-\hat{K}t} |S, \mathbf{m}_1, \mathbf{m}_2\rangle \tag{2.87}$$

can be evaluated with time requirements scaling as $\mathcal{O}(\log(Z)Z)$ and memory requirements scaling as $\mathcal{O}(Z)$. This approach allows ensemble averages to be evaluated (numerically) exactly in time scaling as $\mathcal{O}(\log(Z)Z^2)$ and storage scaling as $\mathcal{O}(Z)$, allowing larger spin system ($\lesssim 20$ spins) to be treated. The need to propagate Z independent wavefunctions prevents this approach from being practical for larger spin systems. If, however, some uncertainty in the ensemble averages can be tolerated, this exponential scaling can be avoided by performing a Monte Carlo sampling over randomly chosen initial states. Such an approach has proven useful when evaluating traces of time-independent properties.[54] In this application, the sampling of arbitrary superpositions of basis states can allow rapid convergence of expectation values with the number of sampled states and with the number of states required not scaling (or even decreasing) with the size of the Hilbert space.[54] Here the approach in reference [55] is followed and the trace in equation 2.80 is stochastically evaluated using randomly sampled spin coherent states.

2.2.5 Coherent Spin States Sampling

The coherent states of a spin with quantum number I, $|\Omega_I\rangle = |\theta_I, \phi_I\rangle$ are defined by[56,57]

$$|\Omega_I\rangle = \cos\left(\frac{\theta_I}{2}\right)^{2I} \exp\left[\tan\left(\frac{\theta_I}{2}\right) e^{i\phi_I} \hat{I}_-\right] |I, I\rangle \tag{2.88}$$

$$= \sum_{m_I=-I}^{I} \sqrt{\binom{2I}{m_I+I}} \cos\left(\frac{\theta_I}{2}\right)^{I+m_I} \sin\left(\frac{\theta_I}{2}\right)^{I-m_I} e^{i(I-m_I)\phi_I} |I, m_I\rangle \tag{2.89}$$

where $0 \leq \theta_I \leq \pi$ and $0 \leq \phi_I < 2\pi$. The set of all coherent spin states $\{|\Omega_I\rangle\}$, span the Hilbert space of this spin. Two general spin coherent states ($|\Omega_I'\rangle$ and

$|\Omega_I\rangle$) are not orthogonal, having overlap[57]

$$\langle\Omega'_I|\Omega_I\rangle = \left[\cos\left(\frac{\theta_I}{2}\right)\cos\left(\frac{\theta'_I}{2}\right) + e^{i(\phi_I-\phi'_I)}\sin\left(\frac{\theta_I}{2}\right)\sin\left(\frac{\theta'_I}{2}\right)\right]^{2I}, \tag{2.90}$$

and so the set of all spin coherent states is overcomplete. These states satisfy the completeness relation

$$\hat{1}_I = \frac{2I+1}{4\pi}\int_0^{2\pi} \mathrm{d}\phi_I \int_0^{\pi} \mathrm{d}\theta_I \sin\theta_I \left|\Omega_{ik}\right\rangle \left\langle\Omega_{ik}\right|. \tag{2.91}$$

Expanding the trace in equation 2.80 with respect to the overcomplete set of states

$$\{\mathcal{B}'\} = \{|\Theta\rangle \otimes |\mathbf{\Omega}_1\rangle \otimes |\mathbf{\Omega}_2\rangle\}, \tag{2.92}$$

gives[55]

$$O(t) = \frac{1}{(4\pi)^{N_1+N_2}}\int \mathrm{d}\mathbf{\Omega}_1\mathrm{d}\mathbf{\Omega}_2 \left\langle S, \mathbf{\Omega}_1, \mathbf{\Omega}_2; t\right| \hat{O} \left|S, \mathbf{\Omega}_1, \mathbf{\Omega}_2; t\right\rangle. \tag{2.93}$$

$|S, \mathbf{\Omega}_1, \mathbf{\Omega}_2; t\rangle$ is the time-evolved state initially prepared in a singlet electronic spin state and a coherent spin state for each of the nuclear spins,

$$|\mathbf{\Omega}_i\rangle = \bigotimes_{k=1}^{N_i} |\Omega_{I_{ik}}\rangle, \tag{2.94}$$

and the notation

$$\int \mathrm{d}\mathbf{\Omega}_i = \int_0^{\pi} \mathrm{d}\theta_{I_{ik}} \sin\theta_{I_{ik}} \int_0^{2\pi} \mathrm{d}\phi_{I_{ik}} \cdots \int_0^{\pi} \mathrm{d}\theta_{I_{iN_i}} \sin\theta_{I_{iN_i}} \int_0^{2\pi} \mathrm{d}\phi_{I_{iN_i}} \tag{2.95}$$

has been introduced to denote the integral over all possible coherent spin states.

The integral in equation 2.93 can be evaluated by Monte Carlo sampling of the spin coherent states for the nuclear spins. The initial orientation ($\theta_{I_{ik}}$, $\phi_{I_{ik}}$) of each nuclear spin is uniformly sampled from the surface of a sphere. An approximation to the ensemble average is obtained by time evolving M such states and averaging the time dependent expectation values obtained for each state. This process has the same memory requirements as equation 2.85, however only requires $\mathcal{O}(M\log(Z)Z)$ operations. If sufficiently converged results can be obtained with $M \ll Z$ this dramatically reduces the cost associated with evaluating ensemble averages. As the value of $O(\mathbf{\Omega}_1, \mathbf{\Omega}_2; t) = \langle S, \mathbf{\Omega}_1, \mathbf{\Omega}_2; t| \hat{O} |S, \mathbf{\Omega}_1, \mathbf{\Omega}_2; t\rangle$ for each spin coherent state

sample is bounded between 0 and 1 for all of the operator ($\hat{O}(t) = \hat{P}_S(t)$, $\hat{P}_T(t)$, and $\hat{\mathbf{1}}(t)$) of interest here, the distribution of $O(\mathbf{\Omega}_1, \mathbf{\Omega}_2; t)$ has maximum possible standard deviation $\sigma = 1/2$.[55] The standard error, ϵ, in an unbiased Monte Carlo approximation to an integral is[58]

$$\epsilon = \frac{\sigma}{\sqrt{M}} \tag{2.96}$$

where M is the number of Monte Carlo samples. As such, provide the number of nuclear spin states, $Z_1 Z_2$, is greater than

$$M = \frac{1}{4\epsilon_{\max}^2}, \tag{2.97}$$

where $\epsilon_{\max}$ is the maximum acceptable error, this approach is expected to reduce the number of wavefunction propagations required. In reference [55] it was shown that this approach can lead to 3 orders of magnitude reduction in the number of trajectories required to evaluate the singlet yield for a model radical pair. So depending on the number of trajectories necessary for convergence, this approach allows ensemble properties to be obtained for radical pairs containing up to ~ 30 spins.

2.2.6 Independent Radicals

For a radical pair with no electron spin coupling ($\hat{H} = \hat{H}_1 + \hat{H}_2$) that is undergoing symmetric recombination, the calculation of survival probabilities simplifies significantly. To see this, consider the singlet survival probability of a radical pair,

$$P_S(t) = \frac{1}{Z}\mathrm{tr}\left[\hat{P}_S e^{i\hat{H}t - \hat{K}t}\hat{P}_S e^{-i\hat{H}t - \hat{K}t}\right]. \tag{2.98}$$

Inserting the definition of the singlet projection operator (equation 2.64) gives

$$P_S(t) = \frac{e^{-kt}}{Z}\mathrm{tr}\left[\left(\frac{1}{4} - \sum_{\alpha=\{x,y,z\}} \hat{S}_{1\alpha}\hat{S}_{2\alpha}\right)e^{i\hat{H}t}\left(\frac{1}{4} - \sum_{\beta=\{x,y,z\}} \hat{S}_{1\beta}\hat{S}_{2\beta}\right)e^{-i\hat{H}t}\right]. \tag{2.99}$$

$\hat{H}_1$ and $\hat{H}_2$ act on different spin degrees of freedom and therefore commute. Using this the evolution operator in equation 2.99 can be simplified to give

$$P_S(t) = \frac{e^{-kt}}{Z_1 Z_2}\mathrm{tr}\left[\left(\frac{1}{4} - \sum_{\alpha} \hat{S}_{1\alpha}\hat{S}_{2\alpha}\right)\left(\frac{1}{4} - \sum_{\beta} e^{i\hat{H}_1 t}\hat{S}_{1\beta}e^{-i\hat{H}_1 t}e^{i\hat{H}_2 t}\hat{S}_{2\beta}e^{-i\hat{H}_2 t}\right)\right] \tag{2.100}$$

$$= \frac{e^{-kt}}{Z_1 Z_2}\mathrm{tr}\left[\left(\frac{1}{4} - \sum_{\alpha} \hat{S}_{1\alpha}\hat{S}_{2\alpha}\right)\left(\frac{1}{4} - \sum_{\beta} \hat{S}_{1\beta}(t)\hat{S}_{2\beta}(t)\right)\right], \tag{2.101}$$

where $\hat{S}_{i\alpha}(t)$ is time evolved with respect to the single radical Hamiltonian, $\hat{H}_i$. Rearranging this expression gives

$$P_S(t) = e^{-kt}\Bigg\{\frac{1}{4} - \frac{1}{4Z_1Z_2}\sum_{\alpha}\mathrm{tr}\left[\left(\hat{S}_{1\alpha}\hat{S}_{2\alpha} + \hat{S}_{1\alpha}(t)\hat{S}_{2\alpha}(t)\right)\right] + \frac{1}{Z_1Z_2}\sum_{\alpha\beta}\mathrm{tr}\left[\hat{S}_{1\alpha}\hat{S}_{1\beta}(t)\hat{S}_{2\alpha}\hat{S}_{2\beta}(t)\right]\Bigg\}, \tag{2.102}$$

which simplifies to

$$P_S(t) = e^{-kt}\left\{\frac{1}{4} + \sum_{\alpha\beta}R^{(1)}_{\alpha\beta}(t)R^{(2)}_{\alpha\beta}(t)\right\}. \tag{2.103}$$

Here the electron spin correlation tensor for radical i,

$$R^{(i)}_{\alpha\beta}(t) = \frac{1}{Z_i}\mathrm{tr}\left[\hat{S}_{i\alpha}e^{i\hat{H}_it}\hat{S}_{i\beta}e^{-i\hat{H}_it}\right], \tag{2.104}$$

has been introduced. Similarly, the triplet survival probability can be evaluated in this manner giving

$$P_T(t) = e^{-kt}\left\{\frac{3}{4} - \sum_{\alpha\beta}R^{(1)}_{\alpha\beta}(t)R^{(2)}_{\alpha\beta}(t)\right\}. \tag{2.105}$$

The electron spin correlation tensors for each radical are independent of each other, and so can be evaluated independently.

To allow for efficient calculation of these electron spin correlation tensors it is useful to express the electron spin operators for radical i as $\hat{S}_{i\alpha} = |\psi_{i\alpha}\rangle\langle\psi_{i\alpha}| - \frac{1}{2}$ with

$$|\psi_{ix}\rangle = \frac{1}{\sqrt{2}}(|\alpha_i\rangle + |\beta_i\rangle) \quad |\psi_{iy}\rangle = \frac{1}{\sqrt{2}}(|\alpha_i\rangle + i\,|\beta_i\rangle) \quad |\psi_{iz}\rangle = |\alpha_i\rangle\,. \tag{2.106}$$

Inserting these expressions into equation 2.104 and expanding the trace with respect to the direct product basis of electron spin states ($|\alpha\rangle$, $|\beta\rangle$) and spin coherent states for the nuclear spins gives

$$R^{(i)}_{\alpha\beta}(t) = \int \mathrm{d}\mathbf{\Omega}_i\,\langle\psi_{i\alpha},\mathbf{\Omega}_i;t|\,\hat{S}_{i\beta}\,|\psi_{i\alpha},\mathbf{\Omega}_i;t\rangle\,. \tag{2.107}$$

All nine elements of the electron spin correlation tensor can be evaluated by performing $3M$ independent wave packet evolutions where M is the number

of spin coherent state samples required. For the special case of indepedent radicals, the singlet survival probability can be evaluated with memory requirements scaling as $\mathcal{O}(\max(Z_1, Z_2))$ and time scaling as $\mathcal{O}(3M(Z_1 \log(Z_1) + Z_2 \log(Z_2)))$. For large radical pairs, this is significantly more efficient than the calculation in the full Hilbert space.

2.2.7 Quantum Yields

Given the singlet and triplet survival probabilities, the relative yields of singlet and triplet products can be obtained by evaluating the integrals in equation 2.73 numerically. In doing so it is necessary to truncate the integral at some finite maximum time t_f. However, for small recombination rates the t_f required to obtain an accurate approximation may become infeasibly large. In such a case, it is beneficial to evaluate the integral in equation 2.73 analytically.

The singlet ($X = S$) or triplet ($X = T$) quantum yields,

$$\Phi_X = \frac{k_X}{Z} \int_0^\infty \mathrm{tr}\left[e^{+i\hat{H}t-\hat{K}t}\hat{P}_X e^{-i\hat{H}t-\hat{K}t}\hat{P}_S\right] \mathrm{d}t, \tag{2.108}$$

can be expressed as

$$\Phi_X = \frac{k_X}{Z} \int_0^\infty \mathrm{tr}\left[e^{+i\hat{W}^\dagger t}\hat{P}_X e^{-i\hat{W}t}\hat{P}_S\right] \mathrm{d}t \tag{2.109}$$

where the effective Hamiltonian $\hat{W} = \hat{H} - i\hat{K}$ has been introduced. The $(4Z \times 4Z)$ matrix representation of this operator, $\mathbf{W}$, can be diagonalised to give

$$\mathbf{X}_L \mathbf{W} \mathbf{X}_R = \mathbf{w} \tag{2.110}$$

where $\mathbf{w}$ is the diagonal matrix of eigenvalues of $\mathbf{W}$ and $\mathbf{X}_L$ and $\mathbf{X}_R$ are the left and right eigenvectors, respectively, and satisfy

$$\mathbf{X}_L = \mathbf{X}_R^{-1}. \tag{2.111}$$

Inserting this matrix representation into equation 2.108 gives

$$\Phi_X = \frac{k_X}{Z} \int_0^\infty \mathrm{tr}\left[e^{+i\mathbf{w}^\dagger t}\mathbf{X}_R^\dagger \mathbf{P}_X \mathbf{X}_R e^{-i\mathbf{w}t}\mathbf{X}_L \mathbf{P}_S \mathbf{X}_L^\dagger\right] \mathrm{d}t \tag{2.112}$$

$$\Phi_X = \frac{k_X}{Z} \int_0^\infty \mathrm{tr}\left[e^{+i\mathbf{w}^\dagger t}\mathbf{A} e^{-i\mathbf{w}t}\mathbf{B}\right] \mathrm{d}t, \tag{2.113}$$

where the two new matrices are $\mathbf{A} = \mathbf{X}_R^\dagger \mathbf{P}_X \mathbf{X}_R$ and $\mathbf{B} = \mathbf{X}_L \mathbf{P}_S \mathbf{X}_L^\dagger$. The integral over time can be evaluated to give

$$\Phi_X = \frac{k_X}{Z} \int_0^\infty \sum_{n,m}^{4Z} e^{-i(w_m - w_n^*)t} A_{nm} B_{mn} \mathrm{d}t \tag{2.114}$$

$$= \frac{ik_X}{Z} \sum_{n,m}^{4Z} \frac{A_{nm} B_{mn}}{(w_n^* - w_m)} \tag{2.115}$$

where w_n is the n-th eigenvalue of $\hat{W}$ and B_{mn} corresponds to the (m, n) element of matrix $\mathbf{B}$.

In the case of symmetric recombination, the recombination term can be factorised out allowing the trace to be evaluated in terms of the eigenstates of the Hamiltonian, $\hat{H}$, giving

$$\Phi_X = \frac{k^2}{4Z} \sum_{n,m=1}^{Z} \frac{\langle n| \hat{P}_X |m\rangle \langle m| \hat{P}_S |n\rangle}{[(\epsilon_n - \epsilon_m)]^2 + k^2}, \tag{2.116}$$

where $|n\rangle$ is the eigenstate of $\hat{H}$ with eigenvalue ϵ_n. By explicitly evaluating the integral the need to evolve wave packets over arbitrarily long timescales is removed. This allows radical pair recombination reactions with arbitrarily slow recombination rates to be treated. However, as the diagonalisation of the matrix $\hat{W}$ scales as $\mathcal{O}(Z^3)$, this approach is only practical for systems with $\lesssim 10$ spins.

2.3 Semiclassical Dynamics

The exponential scaling of exact quantum mechanical methods with the number of spins severely restricts the size of the system which can be treated. Many of the radical pairs of interest in chemistry have > 30 spins, and are therefore inaccessible to direct quantum mechanical treatments. Other spin systems with closely related Hamiltonians can have considerably more spins. The central spin model, which arises when describing the decoherence of an electron spin confined within a semiconductor quantum dot, is typically described by a Hamiltonian with the form given in equation 2.59.[59] These system can have anywhere up to $\mathcal{O}(10^6)$ spins that are important to the dynamics,[59] beyond that which is possible to treat

quantum mechanically. To avoid the scaling issue associated with exact quantum mechanical approaches, and to allow for the dynamics of larger spin systems, a number of semiclassical methods have been developed.[60–65] In the following, two are described: Schulten-Wolynes theory[60] and an improved semiclassical theory[61,62] that removes an approximation made in Schulten-Wolynes theory.

2.3.1 Schulten-Wolynes Theory

Schulten-Wolynes theory, originally presented in 1978,[60] is based on the observation that the total hyperfine field

$$\hat{\boldsymbol{K}}_i = \sum_{k=1}^{N_i} \mathbf{A}_{ik} \hat{\boldsymbol{I}}_{ik}, \tag{2.117}$$

will evolve on a timescale significantly slower than the electron spin if there are a sufficiently large number of nuclear spins. If this timescale is sufficiently slow then the total hyperfine field may be approximated by a constant classical vector that is not effected by the electron-nuclear spin interactions.[60] That is, the nuclear spin operators may be replaced by a set of time-independent classical vectors,

$$\hat{\boldsymbol{K}}_i \rightarrow \boldsymbol{K}_i = \sum_{k=1}^{N_i} \mathbf{A}_{ik} \boldsymbol{I}_{ik}, \tag{2.118}$$

where $\boldsymbol{I}_{ik}$ is a classical spin vector with orientation $\Omega_{ik} = (\theta_{ik}, \phi_{ik})$, given by

$$\boldsymbol{I}_{ik}^T = \sqrt{I_{ik}(I_{ik}+1)}\Big(\sin(\theta_{ik})\cos(\phi_{ik}), \sin(\theta_{ik})\sin(\phi_{ik}), \cos(\theta_{ik})\Big). \tag{2.119}$$

The radical pair Hamiltonian can be written in terms of the total hyperfine field operator as

$$\hat{H} = \sum_{i=1}^{2} \Big(\boldsymbol{\omega}_i \cdot \hat{\boldsymbol{S}}_i + \hat{\boldsymbol{K}}_i \cdot \hat{\boldsymbol{S}}_i \Big) + \hat{\boldsymbol{S}}_1 \cdot \mathbf{M} \cdot \hat{\boldsymbol{S}}_2. \tag{2.120}$$

and on making the Schulten-Wolynes theory approximation, this becomes

$$\hat{H}_{SW}(\boldsymbol{\Omega}_1, \boldsymbol{\Omega}_2) = \sum_{i=1}^{2} \Big(\boldsymbol{\omega}_i \cdot \hat{\boldsymbol{S}}_i + \boldsymbol{K}_i(\boldsymbol{\Omega}_i) \cdot \hat{\boldsymbol{S}}_i \Big) + \hat{\boldsymbol{S}}_1 \cdot \mathbf{M} \cdot \hat{\boldsymbol{S}}_2 \tag{2.121}$$

$$= \sum_{i=1}^{2} \boldsymbol{\omega}_i' \cdot \hat{\boldsymbol{S}}_i + \hat{\boldsymbol{S}}_1 \cdot \mathbf{M} \cdot \hat{\boldsymbol{S}}_2, \tag{2.122}$$

where $\mathbf{\Omega}_i$ represents the orientations of all nuclear spins in radical i. The nuclear spins now only introduce a Zeeman term to the Hamiltonian governing the dynamics of the electron spins as opposed to the hyperfine coupling term present in a fully quantum mechanical treatment.

For each realisation of the total hyperfine field the Schulten-Wolynes Hamiltonian, and therefore the dynamics, is different. In order to evaluate ensemble average properties of the electron spin system, it is necessary to average over all possible nuclear spin orientations. In particular, the electron spin density operator $\hat{\sigma}(t) = \mathrm{tr}\left[\hat{\rho}(t)\right]_N$ (where $\mathrm{tr}\left[\cdot\right]_N$ denotes the partial trace over all nuclear spins) may be obtained by replacing the quantum mechanical trace over nuclear spin states with an integral over the possible nuclear spin orientations

$$\mathrm{tr}_{I_{ik}} \rightarrow \frac{2I_{ik}+1}{4\pi}\int \mathrm{d}\Omega_{ik} = \frac{2I_{ik}+1}{4\pi}\int_0^{2\pi}\mathrm{d}\phi_{ik}\int_0^{\pi}\mathrm{d}\theta_{ik}\sin\theta_{ik}. \tag{2.123}$$

giving

$$\hat{\sigma}_{SW}(t) = \frac{1}{(4\pi)^{N_1+N_2}}\int\int \hat{\sigma}_{SW}(\mathbf{\Omega}_1,\mathbf{\Omega}_2,t)\mathrm{d}\mathbf{\Omega}_1\mathrm{d}\mathbf{\Omega}_2. \tag{2.124}$$

Here $\hat{\sigma}_{SW}(\mathbf{\Omega}_1,\mathbf{\Omega}_2,t)$ is the electron spin density operator for a given realisation, which evolves according to the master equation

$$\frac{\mathrm{d}}{\mathrm{d}t}\hat{\sigma}_{SW}(\mathbf{\Omega}_1,\mathbf{\Omega}_2,t) = -i\left[\hat{H}_{SW}(\mathbf{\Omega}_1,\mathbf{\Omega}_2),\hat{\sigma}_{SW}(\mathbf{\Omega}_1,\mathbf{\Omega}_2,t)\right] - \left\{\hat{K},\hat{\sigma}_{SW}(\mathbf{\Omega}_1,\mathbf{\Omega}_2,t)\right\}. \tag{2.125}$$

All properties of the two-electron spin system can be obtained from this electron spin density operator. For example, within the Schulten-Wolynes approximation the singlet survival probability of the radical pair is

$$P_S(t) = \mathrm{tr}\left[\hat{P}_S\hat{\sigma}_{SW}(t)\right]_S = \left(\frac{1}{4\pi}\right)^{N_1+N_2}\int\int \mathrm{tr}\left[\hat{P}_S\hat{\sigma}_{SW}(\mathbf{\Omega}_1,\mathbf{\Omega}_2,t)\right]_S \mathrm{d}\mathbf{\Omega}_1\mathrm{d}\mathbf{\Omega}_2, \tag{2.126}$$

where $\mathrm{tr}\left[\cdot\right]_S$ is the partial trace over the two-electron spin Hilbert space.

In general, the integrals in equation 2.126 cannot be evaluated analytically and it is necessary to sample configurations of the total hyperfine field by sampling each of the nuclear spin vectors from the surface of a sphere with the correct

radius. These integrals correspond to an average over the distribution of hyperfine fields, which, for a system with only isotropic hyperfine interaction and in the large N_i limit, can be replaced with

$$\int \mathrm{d}\boldsymbol{\Omega}_i \rightarrow \int \mathrm{d}\boldsymbol{K}_i P(\boldsymbol{K}_i). \tag{2.127}$$

Here $P(\boldsymbol{K}_i)$, is the asymptotic distribution of end-to-end distances of a random flight polymer with segment lengths of $a_{ik}\sqrt{I_{ik}(I_{ik}+1)}$,[60,61]

$$P(\boldsymbol{K}_i) = \left(\frac{\tau_i^2}{4\pi}\right)^{3/2} e^{-K_i^2\tau_i^2/4}, \tag{2.128}$$

where $K_i = \|\boldsymbol{K}_i\|$ is the length of the classical vector and

$$\tau_i^{-2} = \frac{1}{6}\sum_{k=1}^{N_i} a_{ik}^2 I_{ik}(I_{ik}+1). \tag{2.129}$$

For a general radical pair system it is still necessary to evaluate these expressions using a Monte Carlo sampling scheme of the initial hyperfine fields from the distribution in equation 2.128. However, for a number of special cases explicit expressions for the singlet survival probability may be obtained.[66]

For radicals containing $10-100$ nuclear spins, as is typical for the organic radical pairs of interest here, it is not clear whether the fixed bath approximation of Schulten-Wolynes will be valid.[61] By assuming a static nuclear spin bath, Schulten-Wolynes theory cannot capture effects arising from the relaxation of the nuclear spin bath. In order to overcome this limitation, Manolopoulos and Hore suggested an alternative semiclassical theory that does not make this assumption and is therefore is valid for a radical pair undergoing symmetric recombination at a rate k.[61]

2.3.2 The Improved Semiclassical Theory

The total survival probability of a radical pair undergoing symmetric recombination is

$$P_S(t) = \frac{1}{Z}\mathrm{tr}\left[\hat{P}_S(t)\hat{P}_S(0)\right]e^{-kt} \tag{2.130}$$

$$= \left(\frac{1}{4} + \frac{1}{Z}\mathrm{tr}\left[\hat{\boldsymbol{S}}_1(t)\cdot\hat{\boldsymbol{S}}_2(t)\hat{\boldsymbol{S}}_1(0)\cdot\hat{\boldsymbol{S}}_2(0)\right]\right)e^{-kt}. \tag{2.131}$$

The electron spin operators at time t evolve according to the Heisenberg equation of motion

$$\frac{\mathrm{d}}{\mathrm{d}t}\hat{\boldsymbol{S}}_i(t) = i\left[\hat{H}, \hat{\boldsymbol{S}}_i(t)\right]. \tag{2.132}$$

Inserting the radical pair Hamiltonian and expanding the commutators gives the equations of motion for the electron spin operators:

$$\frac{\mathrm{d}}{\mathrm{d}t}\hat{\boldsymbol{S}}_1(t) = \boldsymbol{\omega}_1 \times \hat{\boldsymbol{S}}_1(t) + \sum_{k=1}^{N_1}\left(\mathbf{A}_{1k}\cdot\hat{\boldsymbol{I}}_{1k}(t)\right)\times\hat{\boldsymbol{S}}_1(t) + \left(\mathbf{M}\cdot\hat{\boldsymbol{S}}_2(t)\right)\times\hat{\boldsymbol{S}}_1(t) \tag{2.133}$$

$$\frac{\mathrm{d}}{\mathrm{d}t}\hat{\boldsymbol{S}}_2(t) = \boldsymbol{\omega}_2 \times \hat{\boldsymbol{S}}_2(t) + \sum_{k=1}^{N_2}\left(\mathbf{A}_{2k}\cdot\hat{\boldsymbol{I}}_{2k}(t)\right)\times\hat{\boldsymbol{S}}_2(t) + \left(\mathbf{M}\cdot\hat{\boldsymbol{S}}_1(t)\right)\times\hat{\boldsymbol{S}}_2(t), \tag{2.134}$$

where $\mathbf{A}_{ik}$ is the hyperfine coupling tensor between electron spin i and its k-th nuclear spin, and $\mathbf{M}$ is the electron spin coupling tensor. Similarly, the nuclear spin operators evolve according to

$$\frac{\mathrm{d}}{\mathrm{d}t}\hat{\boldsymbol{I}}_{ik}(t) = \left(\mathbf{A}_{ik}\cdot\hat{\boldsymbol{S}}_i(t)\right)\times\hat{\boldsymbol{I}}_{ik}(t). \tag{2.135}$$

Making a semiclassical approximation at this stage, namely replacing the electron and nuclear spin vector operators with the corresponding classical vectors

$$\hat{\boldsymbol{S}}_i \rightarrow \boldsymbol{S}_i \qquad\qquad \hat{\boldsymbol{I}}_{ik} \rightarrow \boldsymbol{I}_{ik}, \tag{2.136}$$

with $\|\hat{\boldsymbol{S}}_i\| = \sqrt{S_i(S_i+1)} = \sqrt{3}/2$, and the traces over the electronic and nuclear spin states with integrals over the orientations of the corresponding classical vectors

$$\mathrm{tr}_{S_i} \rightarrow \frac{2}{4\pi}\int \mathrm{d}\Omega_i \qquad\qquad \mathrm{tr}_{I_{ik}} \rightarrow \frac{2I_{ik}+1}{4\pi}\int \mathrm{d}\Omega_{ik} \tag{2.137}$$

gives[61]

$$P_S(t) \approx \left(\frac{1}{2\pi}\right)^2\left(\frac{1}{4\pi}\right)^{N_1+N_2}\int e^{-kt}P_S(\boldsymbol{\Omega},t)P_S(\boldsymbol{\Omega},0)\mathrm{d}\boldsymbol{\Omega}. \tag{2.138}$$

Here, $P_S(\boldsymbol{\Omega},t) = \frac{1}{4} - \boldsymbol{S}_1(\boldsymbol{\Omega}_1,t)\cdot\boldsymbol{S}_2(\boldsymbol{\Omega}_2,t)$ is the semiclassical approximation to the singlet survival probability for a given orientation of the electron and nuclear spin vectors, $\boldsymbol{\Omega}$. To evaluate this expression, each nuclear and electron spin vector is sampled from the surface of a sphere of the correct radius, following which they are evolved according to the Heisenberg equations of motion (equations

2.133 - 2.135) with quantum mechanical operators replaced by the corresponding semiclassical variables.[61] By averaging the correlation function $P_S(\mathbf{\Omega}, t)P_S(\mathbf{\Omega}, 0)$ over many realisations of the initial spin vectors the semiclassical approximation to the singlet survival probability is obtained. In the following, this will be referred to as the one-spin variable semiclassical approximation (SC1).

In the absence of any electron spin coupling, the dynamics of the spin vectors in each radical decouple. This was the situation initially considered by Hore and Manolopoulos,[61] where the approach was found to perform well for predicting the triplet survival probabilities for a set of model radical pairs. In this case the method has a number of nice properties. First, if there are no hyperfine coupled nuclear spins in either radical the method becomes exact as it correctly describes the precession of the electron spins around a fixed magnetic field. As such, in the fixed bath limit where

$$\frac{\mathrm{d}}{\mathrm{d}t}\hat{\boldsymbol{I}}_{ik}(t) = 0, \tag{2.139}$$

this approach reduces to Schulten-Wolynes theory. This method is able to capture the Schulten-Wolynes theory limit in cases where Schulten-Wolynes becomes valid; however, by allowing for the evolution of the nuclear spins it can capture relaxation of the nuclear spin bath due to interactions with the electron spin.

In the presence of electron spin coupling, SC1 no longer has these nice properties; it is no longer exact in the no nuclei limit and it no longer reduces to Schulten-Wolynes theory. It is necessary to introduce an additional set of semiclassical variables for the two-electron spin operator terms in order to make the method exact in the absence of any nuclear spins.[62]

2.3.3 Two Electron Spin Variables

The Heisenberg equations of motion for the single electron spin variables (equations 2.133 as 2.134) can be rewritten in terms of in terms of the two-spin operators,

$$\hat{T}_{\alpha\beta} = \hat{S}_{1\alpha}\hat{S}_{2\beta}, \tag{2.140}$$

as

$$\frac{\mathrm{d}}{\mathrm{d}t}\hat{S}_{1\alpha}(t) = \sum_{\gamma}\varepsilon_{\alpha\beta\gamma}\left\{\left[\omega_{1\beta} + \sum_{k=1}^{N_1}\left(\mathbf{A}_{1k}\cdot\hat{\boldsymbol{I}}_{1k}(t)\right)_{\beta}\right]\hat{S}_{1\gamma}(t) + M_{\beta\delta}\hat{T}_{\gamma\delta}(t)\right\} \tag{2.141}$$

$$\frac{\mathrm{d}}{\mathrm{d}t}\hat{S}_{2\alpha}(t) = \sum_{\gamma}\varepsilon_{\alpha\beta\gamma}\left\{\left[\omega_{2\beta} + \sum_{k=1}^{N_1}\left(\mathbf{A}_{2k}\cdot\hat{\boldsymbol{I}}_{2k}(t)\right)_{\beta}\right]\hat{S}_{2\gamma}(t) - M_{\beta\delta}\hat{T}_{\gamma\delta}(t)\right\}. \tag{2.142}$$

These two-spin variables likewise evolve according to the Heisenberg equation of motion, which become

$$\begin{aligned}\frac{\mathrm{d}}{\mathrm{d}t}\hat{T}_{\alpha\beta}(t) = &\sum_{\gamma\delta}\varepsilon_{\alpha\gamma\delta}\left\{\left[\omega_{1\gamma} + \sum_{k=1}^{N_1}\left(\mathbf{A}_{1k}\cdot\hat{\boldsymbol{I}}_{1k}(t)\right)_{\gamma}\right]\hat{T}_{\delta\beta}(t) - \frac{1}{4}M_{\delta\beta}\hat{S}_{1\gamma}(t)\right\}\\ &+\sum_{\gamma\delta}\varepsilon_{\beta\gamma\delta}\left\{\left[\omega_{2\gamma} + \sum_{k=1}^{N_2}\left(\mathbf{A}_{2k}\cdot\hat{\boldsymbol{I}}_{2k}(t)\right)_{\gamma}\right]\hat{T}_{\alpha\delta}(t) - \frac{1}{4}M_{\alpha\delta}\hat{S}_{2\gamma}(t)\right\}.\end{aligned} \tag{2.143}$$

The Heisenberg equation of motion for the nuclear spin operators does not depend on the values of the two-spin operators and can be left unchanged. If each of the single-spin operators are now replaced with their corresponding classical vector, and the matrix containing the nine two-electron spin operators replaced with a matrix of classical variables $\hat{\boldsymbol{T}} = \hat{\boldsymbol{S}}_1 \otimes \hat{\boldsymbol{S}}_2 \rightarrow \mathbf{T}$, the two-spin variable semiclassical approximation (SC2) is obtained. Within this approximation the singlet survival probability may be evaluated from

$$P_S(t) \approx \left(\frac{1}{2\pi}\right)^2\left(\frac{1}{4\pi}\right)^{N_1+N_2}\int e^{-kt}P_S(\boldsymbol{\Omega},t)P_S(\boldsymbol{\Omega},0)\mathrm{d}\boldsymbol{\Omega} \tag{2.144}$$

where $P_S(\boldsymbol{\Omega},t) = \frac{1}{4} - \mathrm{tr}\left[\mathbf{T}\right]$ is the new semiclassical approximation to the singlet probability obtained by evolving the spin vectors and two-spin variable matrix.[62] In order to evaluate the total singlet survival probability, the electron and nuclear spin vectors are once again sampled from the surface of their respective spheres while the two-spin variable matrix is initially

$$T_{\alpha\beta}(0) = S_{1\alpha}(0)S_{2\beta}(0). \tag{2.145}$$

The semiclassical variables each evolve according to their Heisenberg equation of motion (equations 2.141 - 2.143 and equation 2.135) with quantum mechanical operators replaced with the corresponding semiclassical variables. In the absence of electron spin coupling the two semiclassical approximations (SC1 and SC2) are identical as $T_{\alpha\beta}(t) = S_{1\alpha}(t)S_{2\beta}(t)$ for all time. However, in the presence of electron spin coupling this is no longer true. By introducing the two electron spin variables, this semiclassical approximation becomes exact in the absence of any hyperfine coupled nuclear spins, regardless of the value of the electron spin coupling.[62]

2.3.4 Asymmetric Recombination

In the previous section, only the case of symmetric recombination, where the non-unitary contribution to the dynamics solely introduces an exponential decay which can be factorised out, was considered. For a radical pair undergoing asymmetric recombination, it is no longer possible to factor out the non-unitary dynamics. The recombination process must be included in the evolution of the semiclassical variables. In reference [62], Lewis *et al.* presented such a method. The semiclassical electron spin variables have equations of motion with the same form as those obtained for SC2 (equations 2.141 - 2.143), however, with the following additional terms that account for the recombination process[62]

$$\frac{\mathrm{d}}{\mathrm{d}t}S_{1\alpha}(t) = -\overline{k}S_{1\alpha}(t) + \Delta k S_{2\alpha}(t) \tag{2.146}$$

$$\frac{\mathrm{d}}{\mathrm{d}t}S_{2\alpha}(t) = -\overline{k}S_{2\alpha}(t) + \Delta k S_{1\alpha}(t) \tag{2.147}$$

$$\frac{\mathrm{d}}{\mathrm{d}t}T_{\alpha\beta}(t) = -\overline{k}T_{\alpha\beta}(t) + \Delta k T_{\beta\alpha}(t) + \delta_{\alpha\beta}\Delta k\Big(\frac{1}{4}\mathbf{1}(t) - \sum_{\gamma} T_{\gamma\gamma}(t)\Big). \tag{2.148}$$

Here $\overline{k} = (k_S + 3k_T)/4$, $\Delta k = (k_S - k_T)/4$, and $\mathbf{1}$ is an additional semiclassical variable representing the identity operator which, due to the non-unitary recombination dynamics, evolves according to the equation of motion

$$\frac{\mathrm{d}}{\mathrm{d}t}\mathbf{1} = -\overline{k}\mathbf{1} + 4\Delta k \sum_{\gamma} T_{\gamma\gamma}(t). \tag{2.149}$$

Within this approach the semiclassical nuclear spin variables evolve according to

$$\frac{\mathrm{d}}{\mathrm{d}t}\boldsymbol{I}_{ik}(t) = \frac{\sqrt{S_i(S_i+1)}}{\|\boldsymbol{S}_i\|}\Big(\mathbf{A}_{ik}\cdot\boldsymbol{S}_i(t)\Big)\times\boldsymbol{I}_{ik}(t), \tag{2.150}$$

for reasons explored in reference [62]. From these variables an approximation to the singlet survival probability is obtained using equation 2.144, with P_S given by

$$P_S(\boldsymbol{\Omega},t) = \frac{1}{4}\mathbf{1}(t) - \sum_{\gamma} T_{\gamma\gamma}(t). \tag{2.151}$$

Ensemble averages are computed as described above for the SC2 method, however the semiclassical variables are evolved according to these modified equations of motion.

This method has a number of properties that make it potentially useful for describing radical pairs undergoing asymmetric recombination. In the absence of any nuclear spins this method is exact.[62] Additionally, for symmetric recombination it reduces to the SC2 theory presented above. However, in arriving at the final equations of motion a number of ad hoc assumptions were necessary.[62,67] In obtaining the equations of motion for the single electron spin operators, equations 2.143, and nuclear spin operators, equation 2.135, it was necessary to insert an identity operator, $\hat{\mathbf{1}}$, expressed as a product of the evolution operator and its conjugate transpose,

$$\hat{\mathbf{1}} = e^{-i\hat{H}t}e^{i\hat{H}t}, \tag{2.152}$$

between the electron spin and nuclear spin operators in order to obtain both operators in the Heisenberg picture at time t. In the asymmetric recombination case the equivalent object,

$$e^{-i\hat{H}t-\hat{K}t}e^{i\hat{H}t-\hat{K}t}, \tag{2.153}$$

is not the identity operator, and so proceeding as above introduces an ad hoc approximation to the true equations of motion. To remedy this Lewis *et al.*, replaced the equations of motion for the nuclear spin varibles with equation 2.150.[62] However, it is not immediately clear that this fixes the issue and, as a result, what

effects this has on the dynamics obtained for radical pairs. As such, it is unclear whether this method is suitable for treating the dynamics of radical pairs undergoing strongly asymmetric recombination reactions. This aspect will be further discussed in Chapter 3.

Having presented the above quantum mechanical and semiclassical methods, magnetic field effects on the reaction yields of radical pairs can now be considered. In the following section the dynamics of a set of model radical pairs based on the photochemistry of cryptochrome proteins is discussed.

2.4 Application: Cryptochrome Radical Pairs

The potential for very weak magnetic fields to dramatically influence the yields of recombination reactions has led to the proposal that radical pair reactions may be central to magnetoreception in birds.[68,69] In 2008 Maeda *et al.* showed, for the first time, that an Earth strength magnetic field ($\sim 50\ \mu$T) could lead to observable differences in the dynamics of a radical pair.[9] While it was necessary to apply considerably larger magnetic fields (~ 3.1mT) to produce an observable orientation depedent magnetic field effect[9] (as required for the avian magnetoreception hypothesis) this proof-of-principle experiment demonstrated that this proposal was experimentally plausible. Since this proposal, the radical pair mechanism has become one of the leading hypotheses for avian magnetoreception.[70] A number of key features of the avian magnetic compass have been identified that have been suggested to be consistent with this hypothesis:

1. The avian magnetic compass is an inclination compass. It does not use the polarity of an applied magnetic field, instead it only uses the inclination of magnetic field lines[71]. At the equator (where the magnetic field lines are horizontal) such a compass is unable to provide any orientational information. In a horizontal magnetic field, European Robins were observed to be disoriented.[71] This observation is consistent with the radical pair mechanism.

By using the time-reversal symmetry of the radical pair Hamiltonian, it can be shown that the singlet (and triplet) survival probability and corresponding yields are invariant under changing the polarity of the magnetic field ($P_S(\boldsymbol{B}, t) = P_S(-\boldsymbol{B}, t)$ and $\Phi_S(\boldsymbol{B}) = \Phi_S(-\boldsymbol{B})$).[67]

2. The avian magnetic compass is highly sensitive to the strength of the applied magnetic field; small changes in the strength of the field can prevent birds from orienting with it.[72] This can again be explained using the radical pair mechanism The magnetic field effect observed for a radical pair depends on the intensity of an applied magnetic field, changing the strength of this alters the relative energy levels of the spin Hamiltonian. As a consequence, the form of anisotropic magnetic field effects can be significantly altered,[66] and it may take some time for birds to become accustomed to this new pattern.[10]

3. The application of weak, time-dependent magnetic fields can prevent birds from orienting with an applied magnetic field.[73–75] Incredibly weak magnetic fields oscillating at the Larmor frequency of the electron spins have been observed to significantly impact on the ability for birds to orient.[74] This observation is thought to rule out other alternative mechanisms that may give rise to magnetic sensing, and provide the most convincing evidence for the radical pair mechanism.[10,76] However, these behavioural experiments are somewhat controversial. Other such studies have obtained conflicting results as to whether birds are more sensitive to single frequency or broadband noise.[77] Additionally, recent theoretical studies of this phenomenon have failed to account for the experimental results; significantly larger field strengths and infeasibly long spin-coherence lifetimes were required to observe significant changes in reaction yields.[78]

4. The ability of birds to detect an applied magnetic field is dependent on the frequency of the ambient light. When exposed solely to red light birds are unable to orient themselves with an applied magnetic field, while under to blue or green light they are able to do so.[79,80] This observation is readily

explained with the radical pair hypothesis; photoexcited radical pairs will only be formed if incoming photons have sufficient energy.[81]

These observations have led to the proposal that cryptochrome proteins, found in the retinas of birds, are responsible for avian magnetoreception.[68] It has been proposed that photoexcitation of flavin adenine dinucleotide (FAD) chromophores by blue or green light induces a series of intra-protein electron transfers between a chain of three or four tryptophan residues within the protein that ultimately form a spin correlated radical pair.[82] This radical pair is immobilised in the protein and so anisotropic hyperfine interactions between the electron and nuclear spins or dipolar interactions between the electron spins, can lead to magnetic field effects being dependent on the orientation of an applied magnetic field. This hypothesis has some experimental support as cryptochrome proteins have been shown to exhibit magnetic field effects in solution.[82]

Quantum mechanical simulations of models for the $FAD^{\bullet-}TrpH^{\bullet+}$ radical pair have found a sharp peak in the orientation dependence of the singlet yield.[83] This "quantum needle" effect arises from avoided crossings in the radical pair spin Hamiltonian and is therefore an intrinsically quantum mechanical effect.[83] However, it is a small absolute effect and is only observed when considering radical pair lifetimes longer than those which are thought to be feasible.[76] Additionally, in the presence of electron spin coupling between the two radicals this effect vanishes.[78]

Quantum mechanical simulations performed for an alternative hypothetical radical pair, in which the tryptophan is replaced with a radical with no hyperfine coupled nuclear spins, predict anisotropic magnetic field effects up to two orders of magnitude larger than those observed for $FAD^{\bullet-}TrpH^{\bullet+}$.[84] This has lead to speculation that a radical pair containing flavin and an alternative partner radical may be responsible for the magnetic sensitivity of cryptochromes.[74,84] Superoxide, $O_2^{\bullet-}$, has been proposed as an alternative radical containing no nuclear spins,[85,86] however the strong spin-orbit coupling is expected to lead to extremely rapid electron spin

relaxation that will quench the anisotropic magnetic field effects.[84] Alternatively, the ascorbyl radical has been proposed as a candidate with fewer hyperfine coupled nuclear spins than tryptophan. This is not expected to produce as substantial magnetic field effects as $FAD^{\bullet-}Z^{\bullet}$, although it is still expected to be $\sim$50 times more sensitive than $FAD^{\bullet-}TrpH^{\bullet+}$.[84] While an alternative radical pair may dramatically increase the singlet yield anisotropies, whether such radical pairs form *in vivo* is unknown.

Recently, it has been proposed that a slightly modified mechanism may dramatically amplify the singlet yield anisotropies of these radical pairs.[87] Within this model, an additional scanvenger radical interacts with the radical pair forming a radical triad. This triad can undergo two recombination reactions: the standard radical pair recombination reaction or a recombination reaction involving the scavenger radical and one of the radicals in the radical pair. This mechanism is predicted to dramatically enhance the anisotropic magnetic field effects of the $FAD^{\bullet-}TrpH^{\bullet+}$radical pair[87] and be robust against spin relaxation effects.[88] While it is uncertain whether such a mechanism is present *in vivo*, it is a promising candidate for understanding the magnetic sensitity of cryptochrome proteins.

In the next section, the question of the identity of an alternative radical (or whether the magnetic sensitivity of cryptochrome is based on a radical pair at all) will be ignored. Instead two model radical pairs will be considered: $FAD^{\bullet-}TrpH^{\bullet+}$ and $FAD^{\bullet-}Z^{\bullet}$, a hypothetical radical pair where the $Z^{\bullet}$ radical is coupled to no nuclear spins. By comparing quantum mechanical and semiclassical simulations of these two radical pairs the aim is to assess whether semiclassical methods could provide a useful tool for understanding the magnetic sensitivity of cryptochrome proteins.

2.4.1 Model Systems

Here, simplified models of the $FAD^{\bullet-}TrpH^{\bullet+}$ and $FAD^{\bullet-}Z^{\bullet}$ radical pairs discussed above will be considered (which will be referred to as FAD-Trp and FAD-Z,

respectively, throughout).[89] For each of these radical pairs four distinct models will be considered, each with varying numbers of nuclear spins and electron spin coupling interactions. The first two of the four model radical pair systems includes only the 7 most strongly coupled nuclear spins in each radical while the remaining models increase the number of included spins in each radical to 11. The different FAD-Trp models therefore contain 14 or 22 nuclear spins, while the absence of any nuclear spins in the $Z^{\bullet}$ radical means that the FAD-Z models contain 7 or 11 nuclear spins. The hyperfine coupling constants for each of these nuclear spins (provided in appendix A) were taken from reference [83]. For the flavin radical the set of 7 most strongly coupled spins were the N5, N10, H6, 3×H8, and 1×Hβ (see figure 2.3), with 1×Hβ and 3×H7 added to the 11 spin model. The 7 spin model of the Trp included the N1, H1, H2, H4, H5, H7, and 1×Hβ spins, with H6, Hα, Hβ2 and the NH_2 nitrogen added to make 11 spins.

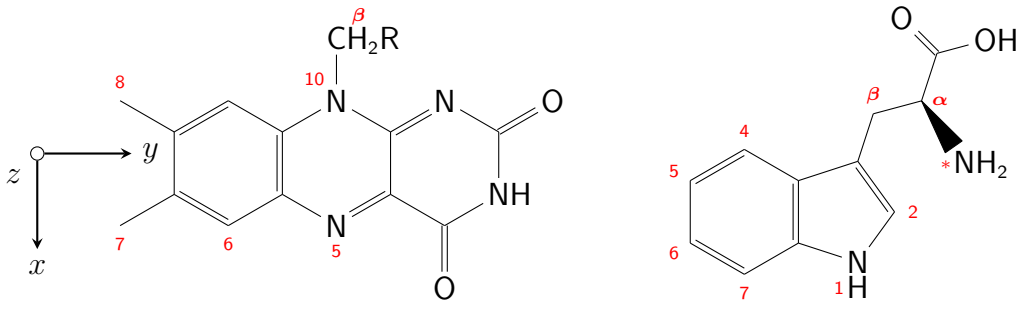

Figure 2.3: Structures of (left) flavin adenine dinucleotide (FAD) and (right) tryptophan (Trp), these are the two radicals which form the $FAD^{\bullet-}TrpH^{\bullet+}$ radical pair. All hyperfine coupling constants, the electron spin coupling constant, and magnetic field are defined with respect to the axis system shown which, itself, is defined with respect to the orientation of the FAD structure. In the models considered below, the tryptophan residue is not oriented along this axis.

The recombination rates, electron spin coupling tensor and a number of other properties of the FAD-Trp radical pair are not known *in vivo*. As such, it is necessary to make a number of assumptions about the interactions present. First spin relaxation arising from the coupling between the dynamics of the protein environment and the spin system will be ignored. This neglects additional dephasing

effects which will reduce the importance of quantum mechanical coherences in the spin dynamics. Secondly, the recombination of these radical pairs will be treated using a symmetric recombination reaction of $k_S = k_T = k = 10^6$ s^{-1}. This recombination rate is too large to observe the "chemical needle" that has previously been observed in quantum mechanical simulations of $FAD^{\bullet-}TrpH^{\bullet+}$ with sufficiently long-lived spin coherence.[83] Since this is a purely quantum mechanical effect, arising from avoided crossings in the energy levels of the spin Hamiltonian of the radical pairs,[83] it would not be captured by any of the semiclassical methods.

Two different values for the electron spin coupling interaction are considered. First, all electron spin coupling is ignored allowing for each radical to be treated independently, while in the second case contributions from both exchange and dipolar coupling interactions are included. Here the dipolar coupling parameters $D\hbar/|\gamma_e| = -0.38$mT and $E = 0$, which were calculated from the relative positions of the FAD and TrpC in the *Drosophila* (fruit fly) cryptochrome, and an exchange coupling constant of $J\hbar/|\gamma_e| = 0.224$ mT are used.[90] The overall electron spin coupling tensor, $\mathbf{M} = \mathbf{D} - 2J\mathbf{1}$, is

$$\mathbf{M} = \begin{pmatrix} -0.382276 & 0.292979 & -0.147696 \\ 0.292979 & -0.652196 & 0.229243 \\ -0.147696 & 0.229243 & -0.309528 \end{pmatrix} \text{mT}. \tag{2.154}$$

The same electron-spin coupling and recombination rate is used for the hypothetical FAD-Z radical pair for which all of these parameters are unknown.

For both FAD-Z and FAD-Trp the g-values for both electron spins are treated as isotropic and equal to the free-electron g-value, $g_1 = g_2 = g_e$. The electron spins interact with an applied magnetic field

$$\boldsymbol{B}(\theta)^T = B(\sin(\theta), 0, \cos(\theta)) \tag{2.155}$$

defined with respect to the coordinate system depicted in figure 2.3, and here $B = 1$ mT. This magnetic field is $\sim$20 times larger than the Earth's magnetic field and will therefore result in considerably larger anisotropic effects. This stronger field is

used as it considerably improves the convergence (with respect to the number of initial configurations sampled) of all semiclassical calculations and any quantum mechanical calculations that employ spin coherent state initial conditions. Although this field is significantly larger than the Earth's magnetic field it is still small enough that all interactions in the radical pair Hamiltonian are non perturbative. By varying the angle, θ the single yield will vary. By comparing the orientation dependent single yields obtained from semiclassical and quantum mechanical simulations, whether or not these semiclassical methods are suitable for exploring the mechanism of avian magnetoreception can be assessed.

2.4.2 Computational Details

Quantum Dynamics

In order to efficiently compute the singlet yields quantum mechanically, it was necessary to employ a number of different approaches dependeding on the model being treated. For all FAD-Z models it was practical to numerically diagonalise the radical pair Hamiltonian. Having computed the eigenvalues and eigenvectors, the singlet yield was then obtained using equation 2.116.

For the two FAD-Trp radical pair models including 14 and 22 nuclear spins, the Hilbert spaces contained 221,184 and 84,934,656 states, respectively. In both cases, this is too large for exact diagonalisation of the radical pair Hamiltonian. All calculations for FAD-Trp were performed using one of the time evolution schemes described previously, with the singlet survival probability computed up to a maximum time of $t_{max} = 11.5$ μs. The singlet yields were then obtained by numerically integrating the singlet survival probability (equation 2.73).

For FAD-Trp with no electron spin coupling, the separability of the dynamics of each radical, described in Section 2.2.6, could be exploited. While this makes the diagonalisation of each radical Hamiltonian possible, evaluating equation 2.116 is still impractical as it requires the evaluation of a double sum over all radical pair

states. As such, the singlet yields were computed by evaluating the electron spin correlation tensors for each radical independently. In order to evaluate the spin correlation tensors a series of 3 sets of Z_i wave packets were propagated for each radical (where Z_i is the number of nuclear spin states in the radical). For each of the 3 sets a different inital state for the electron spin state was used (equation 2.106), and the trace over nuclear spin states was evaluated exactly by considering each of the Z_i distinct nuclear spin configurations.

In the presence of electron spin coupling it is no longer possible to treat the evolution of each radical independently. Evaluation of the singlet yields for the 22 nuclear spin model for FAD-Trp with electron spin coupling was infeasible; the larger Hilbert space, with 84,934,656 states, the long time period for the evolution, and large number of different field orientations required made these calculations impractical. For the 14 nuclear spin model, results were obtained using the spin coherent state sampling procedure described in Section 2.2.5. The singlet survival probabilities presented below were obtained using 1280 samples of the initial coherent spin states. The reported error bars correspond to two standard errors in the mean of the singlet yields computed this way.

Semiclassical Dynamics

For each of the models considered here, semiclassical results were obtained using Schulten-Wolynes (SW) theory and both the one (SC1) and two (SC2) electron spin operator forms of the improved semiclassical theory. In the absence of electron spin coupling SC1 and SC2 are identitical, so only one set of results will be shown. All of the semiclassical results presented in this section were obtained by Thomas Fay.[89]

2.4.3 Results

Fad-Z

The dependence of the FAD-Z radical pair singlet quantum yield on the orientation of the applied magnetic field is shown in figure 2.4. In the absence of electron

spin coupling the semiclassical methods agree well with the quantum results. The improved semiclassical method agrees almost quantitatively except that it fails to capture the sharp peaks arising from avoided energy level crossings that are observed in the quantum mechanical results. As the number of nuclear spins increases, this fine structure is washed out and the semiclassical methods become more accurate. The SW theory captures the θ dependence of the singlet yield well, however it performs noticeably poorer than the SC method and systematically overestimates the singlet yields at all orientations. The SW theory fails to capture the effect of the relaxation of the nuclear spin bath which for this problem drives conversion from singlet to triplet states.

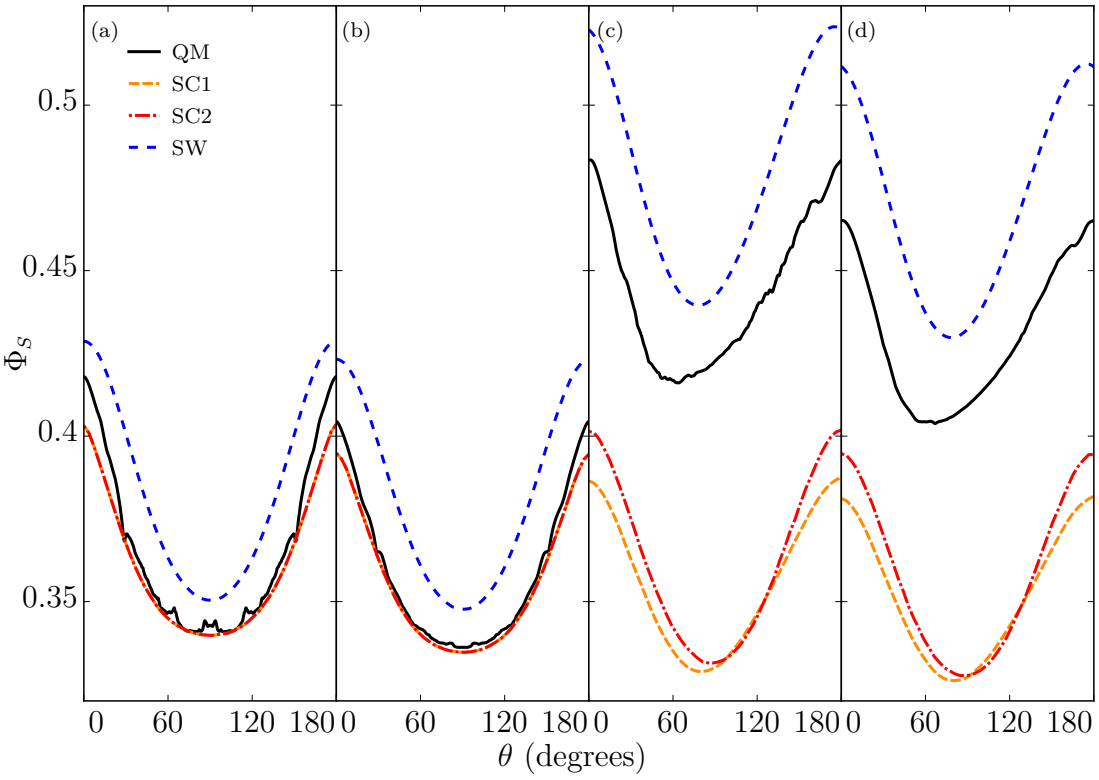

Figure 2.4: Singlet Yield anisotropy as a function of the orientation (θ) of an applied magnetic field for the four models of the FAD-Z radical pair: without exchange coupling (a, b) or with exchange coupling (c, d), and with 7 (a, c) or 11 (b, d) hyperfine-coupled nuclear spins in the flavin radical.

In the presence of exchange coupling none of the semiclassical methods is accurate. As expected, SC1 and SC2 provide different results; however, neither captures the

θ dependence of the singlet yield correctly. All three semiclassical methods predict a minimum in the singlet yield at an incorrect value of θ. For the 7 spin model this minimum is observed at $\theta \sim 60°$ quantum mechanically. Schulten-Wolynes theory predicts this minimum at $\theta \sim 77°$, while SC1 and SC2 predict $\theta \sim 80°$ and $\theta \sim 87°$. If this radical pair were to form the basis of a magnetic compass, the semiclassical theories would lead to a $\sim 15 - 30°$ error in the orientation. Additionally, none of the semiclassical methods is able to predict the value of the singlet quantum yield at any θ. The SC1 and SC2 methods systematically underestimate the yield while SW theory provides a systematic overestimation. Increasing the number of nuclear spins does not significantly improve the results, which suggests that increasing the number of nuclear spins may not be enough to make the semiclassical theory accurate in this regime.

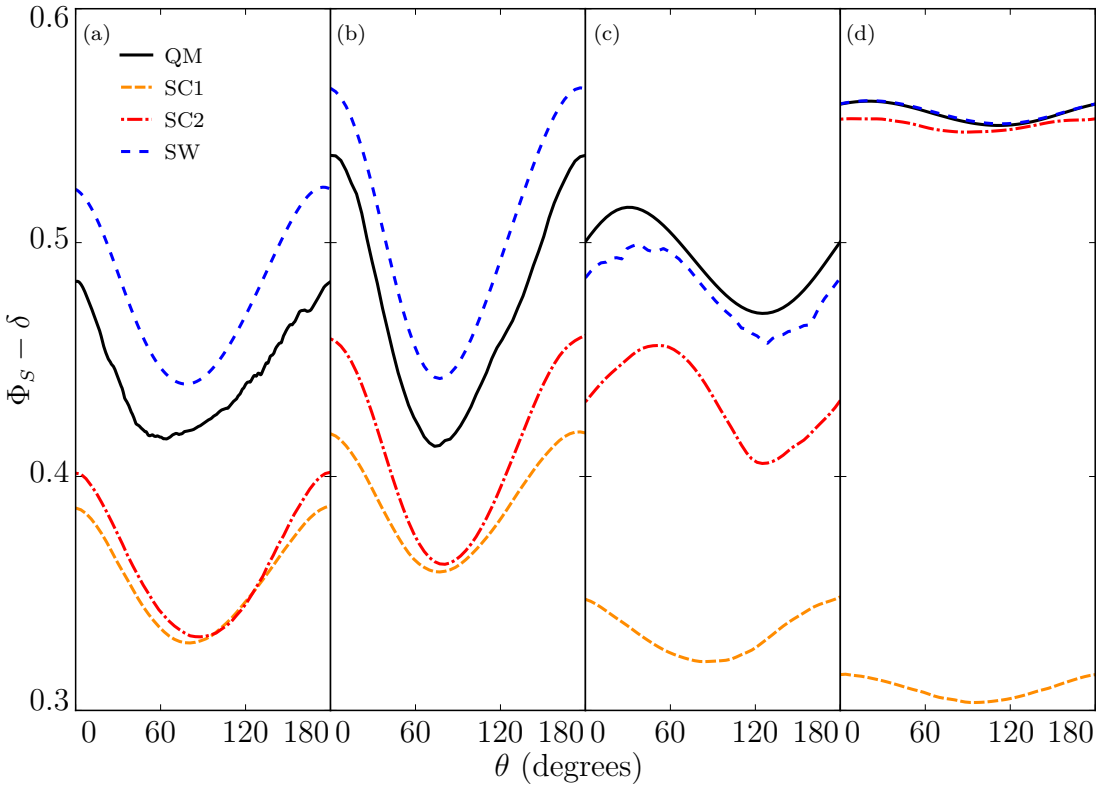

Figure 2.5: Singlet Yield anisotropy as a function of the orientation (θ) of an applied magnetic field for the 11 hyperfine-coupled nuclear spin model of FAD-Z for differing strengths of the electron spin coupling. In each panel the electron spin coupling tensor **M** was scaled by a factor of: 1 (a), 2 (b), 5 (c), and 10 (d). In order to allow easier comparisons between the results the y-axis has been shifted ($\Phi_S \rightarrow \Phi_S - \delta$) by: (a) and (b) $\delta = 0$, (c) $\delta = 0.2$, and (d) $\delta = 0.35$.

In figure 2.5 the effect of stronger electron spin coupling interactions on the singlet yield anisotropy ($\mathbf{M}$, $2\mathbf{M}$, $5\mathbf{M}$, and $10\mathbf{M}$, where $\mathbf{M}$ is the matrix defined in equation 2.154) is illustrated. As the strength of the electron spin coupling increases, the anisotropy in the singlet yield decreases significantly. Both the SW and SC2 methods approach the quantum mechanical results for increased coupling. For the largest electron spin coupling considered here, the SW theory agrees exceptionally well with the quantum results. In contrast, the SC1 method completely fails to describe the effects of increasing the electron spin coupling. As the electron spin coupling increases, this method performs worse and fails to capture the change in shape of the singlet yield anisotropy (this is most evident in panel (c) of figure 2.5). This suggests that as the electron spin coupling increases in strength it dominates the dynamics of the spin system. Correctly treating the dynamics of coherences between the two electron spins becomes more important than capturing the evolution of the nuclear spin bath. In the absence of any nuclear spins both the SW and SC2 methods are exact for the two electron spin system, they both treat this subsystem exactly quantum mechanically. In contrast, the SC1 method employs a semiclassical approximation to the dynamics of this subsystem and so is not able to describe coherences. Even in the presence of nuclear spins SW and SC2 are able to describe coherences between the two electron spins well, while the SC1 method completely fails to capture any such effects leading to its incredibly poor performance.

Fad-Trp

The θ dependent singlet quantum yield anisotropies for the FAD-Trp models are shown in figure 2.6. A similar pattern to the FAD-Z models is observed here. In the absence of any electron spin coupling the semiclassical methods generally perform well in describing the relative θ dependence, capturing the broad shape but failing to reproduce the sharp peaks arising from avoided level crossings in the spin Hamiltonian. Increasing the number of nuclear spins from 7 in each radical to 11 washes out this fine structure, and the SC method becomes more accurately once

again. The singlet yield anisotropy has a much flatter minimum compared to the FAD-Z model, which is well described using the SC method. SW theory provides a poorer description of this relative θ dependence, suggesting that the motion of the nuclear spins is more important in the FAD-Z case.

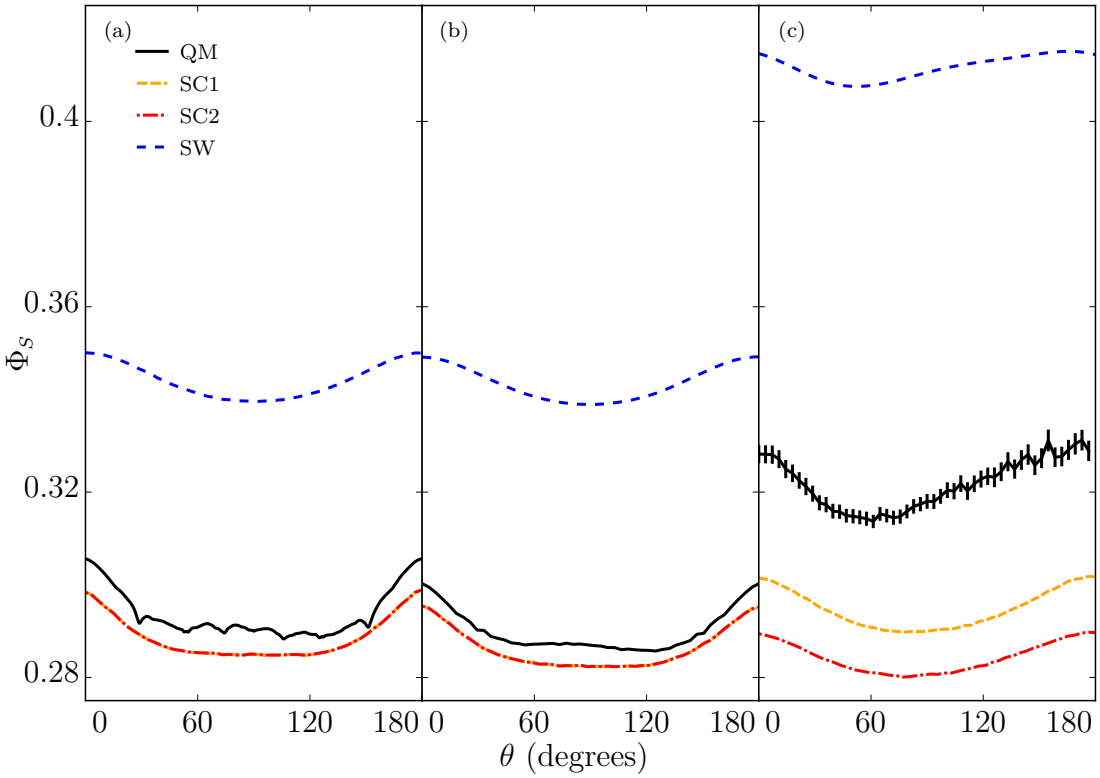

Figure 2.6: Singlet Yield anisotropy as a function of the orientation (θ) of an applied magnetic field for the three models of the FAD-Trp radical pair: without exchange coupling (a, b) or with exchange coupling (c), and with 7 (a, c) or 11 (b) hyperfine-coupled nuclear spins in each radical. The error bars obtained for QM results in panel (c) correspond to 2 standard errors in the mean arising from Monte-Carlo sampling over 1280 nuclear spins states.

The semiclassical methods perform noticeably worse for the FAD-Trp radical pair in comparison to FAD-Z. In the absence of electron spin coupling all semiclassical methods exactly capture the dynamics of one of the radicals ($Z^\bullet$) for the FAD-Z radical pair. For FAD-Trp, the dynamics of both radicals are captured approximately and as a result larger deviations are observed.

When electron spin coupling is included, none of the semiclassical methods is

accurate. The SC1 and SC2 methods are better than SW for the average singlet yield, however they completely fail to capture the θ dependence of the singlet yield. SW theory is able to reproduce the relative θ dependence, capturing the shift in the θ value at the minimum singlet yield, however it significantly overestimates the average singlet yield. For this problem, an accurate description of the electron spin dynamics is necessary to capture the relative shape, while the dynamics of the nuclear spin bath appears to be important for capturing the average singlet yield.

2.4.4 Discussion

From the results presented above, it is expected that there are a number of situations in which existing semiclassical approximations may be inaccurate:

1. When the interaction between the two electron spins is of comparable strength to the hyperfine interactions present. In this regime, coherences between the electronic and nuclear spin may become important. Semiclassical methods are unable to capture these coherences and, as illustrated above, may lead to qualitatively incorrect results. For very weak electron spin coupling other contributions to the dynamics dominate and it is likely that that semiclassical methods are able to capture the dynamics accurately. When the electron spin coupling is dominant semiclassical methods are likely to be accurate provided they correctly describe the dynamics of the two electron spin system (SW and SC2). It is at intermediate coupling strengths that semiclassical methods are expected to have the most difficulty.

   This situation may also arise whenever the radical pair recombines with two significantly different rates from the singlet (k_S) and triplet (k_T) states. For a system with asymmetric recombination, the Haberkorn recombination operator provides a direct coupling between the electron spins of each radical. This becomes clear when the Haberkorn recombination operator is written as:

$$-i\hat{K} = -\frac{i(k_S + 3k_T)}{8}\hat{\mathbf{1}} + \frac{i(k_S - k_T)}{2}\hat{\boldsymbol{S}}_1 \cdot \hat{\boldsymbol{S}}_2. \tag{2.156}$$

The second term is an electron spin coupling term with an imaginary coupling constant that depends on how asymmetric the reaction is. The dynamics of the two radicals is now no longer uncoupled and it is unclear whether the semiclassical theories will be accurate.

2. If the spin coherence lifetime of the radical pair is very large. For the $FAD^{\bullet-}TrpH^{\bullet+}$ model a sharp spike in the single yield anisotropy is observed when the lifetime is very large, which arises due to avoided level crossings associated with the anisotopic hyperfine tensors for the N5 and N10 nitrogen atoms in the flavin radical.[83] This is a purely quantum mechanical phenomenon that cannot be captured by semiclassical methods.

3. When the number of nuclear spins in one (or both) of the radicals is small but non-zero. In this regime the dynamics of the radical pair is dominated by coherences between the spins. As the number of spins increase, these coherences are rapidly quenched and the resultant dynamics can be captured by semiclassical methods.[61]

If none of these hold for a radical pair, semiclassical approaches may be able to accurately describe the dynamics of the system. However, for cryptochrome based radical pairs, this seems unlikely.

The electron spin coupling interactions depend on the seperation between the radical pairs (equations 2.40 and 2.52). In order for these interactions to be negligible, and semiclassical approaches to be suitable, the two radicals must be sufficiently well separated. For the *Drosophila* cryptochrome, the flavin and tryptophan radicals are separated by either 1.91 nm or 2.21 nm giving rise to dipolar coupling constants of $D\hbar/|\gamma_e| \sim -400$ or ~ -260 μT, respectively, depending on which tryptophan is involved.[90] In order for the dipolar coupling to be smaller than the Earth's magnetic field (and unlikely to contribute significantly to the dynamics) the two radicals would need to be separated by $\gtrsim 3.82$ nm. This seems infeasible as the recombination rate of the radical pair decreases approximately exponentially with

the separation of the radical pair, and would be unrealistically slow for such a large separation.[89,91]

All simulations presented here have been restricted to the case of symmetric recombination $k_S = k_T$. This is again unlikely to be the case for the FAD-Trp radical pair. When in the singlet state the FAD-Trp radical pair is free to recombine to give the ground state, however, there are no triplet product states energetically accessible from the radical pair state. The recombination from the singlet state competes against a non-spin selective (de)protonation of one or both of the radicals to form a long-lived state.[82] As this process is independent of the spin state, and the singlet state can undergo an additional recombination process, $k_S \neq k_T$. Whether or not semiclassical methods are suitable for modelling this reaction will depend on how asymmetric the reaction is.

2.5 Conclusion

In this chapter the standard quantum mechanical and semiclassical treatments of the dynamics of radical pair recombination reactions have been presented. By considering two model radical pairs ($FAD^{\bullet -}Z^{\bullet}$ and $FAD^{\bullet -}TrpH^{\bullet +}$) based on the photochemistry of cryptochrome proteins, the accuracy of these semiclassical methods has been assessed. For two non-interacting radicals, both the improved semiclassical and Schulten-Wolynes theories accurately captured orientation dependent magnetic field effects on the singlet yield, with the improved semiclassical theory providing good agreement with the quantum results. But once interactions between the electron spins were introduced (comparable in strength to the hyperfine interactions) none of the semiclassical methods is accurate. As the strength of the electron spin interaction is increased, Schulten-Wolynes theory and the improved two-spin variable variant of the improved semiclassical theory become more accurate. In contrast, the performance of the one-spin variable variant of the improved semiclassical theory deteriorates. These results suggest that even with a relatively large number of nuclear spins it is not immediately obvious if the semiclassical methods will be

accurate. For large radical pair systems ($\gtrsim 30$ spins) in which all spin interactions are non-perturbative, there is a need to develop either more accurate semiclassical methods or more efficient quantum mechanical methods. The second of these options will be explored in the next chapter.

3

Quantum Dynamics of Large Spin Systems

Contents

3.1 Introduction

In the previous chapter, the standard quantum mechanical treatment of radical pair recombination reactions was described. For relatively small spin systems, such an approach provides an exact treatment of the dynamics. However, as the number of hyperfine coupled nuclear spins increases, the exponential scaling of the Hilbert space dimension quickly leads to these methods becoming infeasible. To avoid this scaling issue, semiclassical approaches are commonly utilised.

The semiclassical methods commonly used in spin dynamics rely upon mapping quantum dynamics onto the evolution of a set of classical vectors.[60,61,92] The numerical cost associated with these methods may be independent of the number of nuclear spins, as is the case for Schulten-Wolynes theory, or scale linearly with the number, as is the case for the improved semiclassical theories.[61] As a result, considerably larger spin systems can be treated. However, whether or not the semiclassical approximation is valid for a given system is not always clear. This was illustrated in the previous chapter for a set of cryptochrome-based radical pairs. Even when semiclassical methods could accurately predict the singlet yield for a radical pair without electron spin coupling interactions, the inclusion of such interactions resulted in a failure of the semiclassical approximation. While semiclassical methods typically become more accurate as the number of nuclear spins increases,[61,62] it is not obvious *a priori* when this occurs for a given spin system. For relatively small spin systems, as considered in the last chapter, the semiclassical approximation can be validated through comparison with exact quantum mechanical simulations — for larger systems this is no longer possible. Thus, there is a need for quantum mechanical methods that can efficiently treat the dynamics of larger spin systems.

The key challenge in applying quantum mechanical methods to the dynamics

of radical pairs arises from the large number of hyperfine-coupled nuclear spins. In what follows, the central spin model is considered. This is a simpler, yet related, model that suffers from the same scaling issues but does not include some of the complexities of the radical pair model (such as the non-unitary dynamics arising from the recombination process). First, the Hamiltonian for this model, along with some of its potential applications, and methods that have been previously developed for treating its dynamics are described. Following this, a new method, motivated by two special cases for which evaluation of the dynamics does not scale exponentially, will be presented and validated using a series of central spin models. The chapter concluded by an application of this method to a radical pair recombination reaction.

3.2 The Central Spin Model

In addition to being an important component of the isotropic radical pair Hamiltonian (equations 2.58 and 2.59) that governs the dynamics of the spins in radical pairs of chemical and biological interest, the central spin Hamiltonian,[14,20,93]

$$\hat{H} = \omega \hat{S}_z + \sum_{k=1}^{N} a_k \hat{\boldsymbol{S}} \cdot \hat{\boldsymbol{I}}_k, \tag{3.1}$$

arises when describing the hyperfine induced decoherence of the spin of an electron (or hole) trapped within a semiconductor quantum dot.[92,94–101] In this context, the first term in the central spin Hamiltonian accounts for the Zeeman interaction between the central electron spin and an external magnetic field applied along the z-axis (see Section 2.2.2). The second term accounts for the Fermi contact interactions between the electron spin and the bath of N nuclei with non-zero magnetic moments in the quantum dot. The latter's strength depends on the electron spin density at the nucleus[34,35,37] (see Section 2.2.2). A schematic illustrating the star-shaped topology of the interactions present in the central spin model is shown in figure 3.1 .

Contributions from the Zeeman interactions between the nuclear spins and the

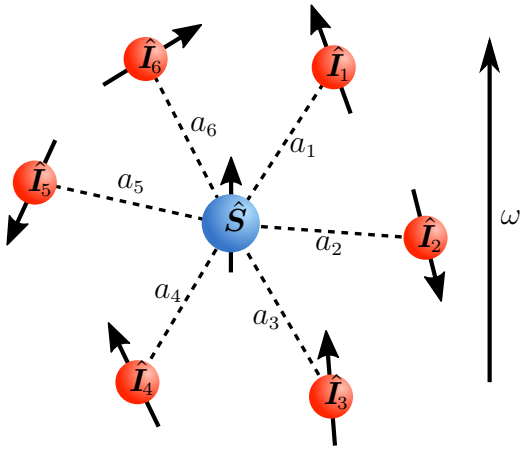

Figure 3.1: An illustration of the central spin Hamiltonian. The central spin (blue) interacts with a set of coupled bath spins (red) through the isotropic interaction a_k (e.g. Fermi contract interactions between electron spins and nuclear spins) and an applied magnetic field with magnitude ω.

applied magnetic field have been excluded in equation 3.1. If all nuclear spins have the same g-factor, g_b, the nuclear Zeeman interaction Hamiltonian is

$$\hat{H}_n = -\frac{g_b \mu_b B}{\hbar} \sum_{k=1}^{N} \hat{I}_{kz}, \tag{3.2}$$

where B is the strength of the applied field. As was the case for the radical pair Hamiltonian, this term is typically considerably smaller than the other spin interactions present. Moreover, it can be eliminated entirely from the Hamiltonian by defining $\omega = (g_c - g_b)B$, where g_c is the g-factor of the central spin. Since the z component of the total spin operator $\hat{J}_z = \hat{S}_z + \sum_{k=1}^{N} \hat{I}_{kz}$ commutes with the central spin Hamiltonian, the difference between equation 3.1 and the central spin Hamiltonian (including nuclear Zeeman interactions) is a trivial energy shift within each symmetry block of the $\hat{J}_z$ operator.[102] In addition, dipolar interactions between the bath spins have also been ignored in equation 3.1. While these terms will induce additional decoherence of the central spin, they are typically much weaker than the Zeeman and hyperfine interactions and so only influence the central spin dynamics significantly on very long timescales.[103]

Due to the ease with which the spins of electrons confined within quantum dots can be manipulated[104–106] and their spin states probed,[104,105,107] as well as the long

coherence times of these states,[104,105,108–110] quantum dots have been proposed as candidates for the realisation of a quantum bit that may form the basis of a universal quantum computer.[105,111–113] One of the key challenges with respect to this goal is the decoherence of the spin of the electron due to interactions with its environment.[114] For a quantum bit to be useful, the decoherence of its state due to interactions with its environment must occur on a timescale considerably longer than that which is required to perform the operations necessary for computations.[113] At low applied magnetic field strengths, the dominant mechanism for the decoherence of quantum dots is the hyperfine interactions arising from the nuclear spins.[98,105,108,115,116] This decoherence can be quantified using three lifetimes: the relaxation time (T_1), the decoherence time (T_2), and the dephasing time (T_2^*).[114] These lifetimes quantify the rates of various transitions of the quantum bit, which arise due to interactions with its environment. For the quantum dot, T_1 and T_2 can be extracted from time-dependent expectation values of the central spin (assuming exponential decay of these expectation values),[114] as summarised in table 3.1. Hence, there is considerable interest in being able to predict the dynamics of the central spin arising from this Hamiltonian.

	Transition	Expecation Value	Correlation Tensors
T_1	$\|\uparrow\rangle \rightarrow \|\downarrow\rangle$	$\langle\uparrow\| S_z(t) \|\uparrow\rangle$	$R_{zz}(t)$
T_2	$\|\psi\rangle = \frac{1}{\sqrt{2}}(\|\uparrow\rangle + \|\downarrow\rangle) \rightarrow \|\uparrow\rangle$ or $\|\downarrow\rangle$	$\left\| \langle\psi\| (S_x(t) + iS_y(t)) \|\psi\rangle \right\|$	$\left\|R_{xx}(t) + iR_{xy}(t)\right\|$

Table 3.1: Lifetimes describing the decoherence of a quantum bit due to interaction with its environment. The second and third columns present the transition of the quantum bit that this lifetime describes and the expectation value of the central spin that captures this.[114] In the fourth column, these expectation values are expressed in terms of components of the central spin correlation tensor introduced previously in equation 2.104.

For central spin problems containing few bath spins this is straightforward. The quantum mechanical treatment of independent radicals discussed in the previous chapter (Section 2.2.6) can be applied directly to this system. Many of the approximations made for the radical pair system hold here; the hyperfine interactions present in a quantum dot are extremely weak and so under typical experimental conditions ($\sim$5 K) can be assumed to have an initial thermal equilibrium at infinite

temperature.[59,117,118] The central spin correlation tensor, $R_{\alpha\beta}(t)$, introduced in equation 2.104, can be evaluated as outlined in Section 2.2.6. For the Hamiltonian considered here (corresponding to an isotropic single radical) the elements of the spin correlation can be shown to be real and to satsify

$$R_{xx}(t) = R_{yy}(t) \tag{3.3}$$

$$R_{xy}(t) = -R_{yx}(t) \tag{3.4}$$

$$R_{xz}(t) = R_{zx}(t) = R_{yz}(t) = R_{zy}(t) = 0. \tag{3.5}$$

In the following discussion, $R_{xx}(t)$, $R_{xy}(t)$ and $R_{zz}(t)$ (from which the full spin correlation tensor can be constructed) will be the primary variables of interest. From the central spin correlation tensor, additional time-dependent properties of the central spin can be constructed (see table 3.1).

The main difficulty in computing the dynamics of the central spin lies in the exponential scaling of Hilbert space dimension with the number of nuclear spins, N. For a system with N nuclear spins each having $I = 1/2$, the Hilbert space has dimension 2^{N+1}, and so methods based on exact diagonalisation are impractical for $N \gtrsim 20$. For semiconductor quantum dots containing anywhere between $\mathcal{O}(10^4)$ and $\mathcal{O}(10^6)$ hyperfine coupled nuclear spins,[59] such calculations are clearly infeasible. Over the years a wide range of methods have been developed in an effort to overcome this limitation. These range from those based on semiclassical approximations,[60,61,94,99,100,119] large N approximations,[117] perturbative approximations,[95] non-Markovian master equations using perturbative expansions,[97,120,121] short time approximations[101] or approximate bath correlation functions,[122] as well as efficient methods of evaluating the exact dynamics.[96,102,103,123,124] While approximate methods can provide insight into the dynamics of the central spin model, they are often limited in applicability and may only be accurate: for short time frames,[120] for specific distributions of hyperfine coupling constants,[60,94] and/or in the presence of large magnetic fields.[97]

Semiclassical and numerically exact approaches will be the focus of the remainder

of this chapter. In the next section, two numerically exact approaches that have been successfully applied for central spin models, with considerably more spins than are practical for exact diagonalisation, are described.

3.3 Beyond Exact Diagonalisation

3.3.1 Algebraic Bethe Ansatz

One of the more elegant techniques that has been developed to overcome the exponential scaling with the number of bath spins exploits the fact that the central spin problem has the form of a Gaudin magnet in an external magnetic field. This is well known to be an integrable problem, and so there exists a set of $N+1$ conserved quantities (including the Hamiltonian, $\hat{H}$, and the z component of the total spin operator, $\hat{J}_z$).[125,126] The eigenvalues and eigenstates of all $N+1$ conserved quantities can be obtained by solving a system of $N+1$ coupled algebraic Bethe equations.[127,128] In the limit that $1/B \to 0$, the coupled system of equations may be solved analytically, which can then be extended numerically to obtain solutions at finite values of B.[102,124]

Having done the above, it is still necessary to evaluate a double sum over the eigenstates to calculate the correlation tensor of the central spin. Once again, this requires numerical effort that scales exponentially with N, and thereby rapidly becomes infeasible. Faribault and Schuricht[124] proposed using a Metropolis Monte Carlo algorithm to overcome this issue. They considered evaluating the real part of the coherence factor,

$$\mathrm{Re}\left(\left\langle \hat{S}_+(t)\right\rangle\right) = \mathrm{Re}\left(\frac{1}{2}\Big[\,\langle\uparrow| + \langle\downarrow|\,\Big]\hat{S}_+(t)\Big[\,|\uparrow\rangle + |\downarrow\rangle\,\Big]\right) \tag{3.6}$$

which, when expressed in terms of the eigenstates $|n\rangle, |m\rangle$ and corresponding eigenvalues ω_n, ω_m of the central spin Hamiltonian, is

$$\mathrm{Re}\left(\left\langle \hat{S}_+(t)\right\rangle\right) = \sum_{nm}\left|\langle n|\,\hat{S}_+\,|m\rangle\right|^2 e^{i(\omega_n-\omega_m)t}. \tag{3.7}$$

By treating $P_{mn} = |\langle n|\hat{S}_+|m\rangle|^2$ as a probability distribution, they developed a Metropolis update scheme to efficiently generate pairs of eigenstates consistent with this distribution. The approach corresponds to sampling the Fourier transform of the correlation function, then obtaining the time evolution by inverting the transform. The quantity P_{mn} describes the relative importance of the Fourier component $(\omega_n - \omega_m)$ to the correlation function. In principle, this allows the approach to be applied over arbitrarily long timescales.

This implementation of the algebraic Bethe ansatz has been applied to evaluate the coherence factor for central spin problems with up to $N = 48$ nuclear spins to arbitrarily long times.[124] However, owing to the Monte carlo sampling of the double sum, significant statistical errors were observed in the results. Although this sampling scheme is rapidly able to determine the frequencies contributing to the correlation function, there are errors in the relative importance of each component thereby leading to unphysical oscillations in the correlation function. As the number of nuclear spins increases, it would be expected that, for a fixed number of Monte Carlo samples, the statistical errors would increase due to a smaller fraction of terms in the double sum being sampled.

For other correlation functions, the statistical errors associated with this method are likely to be far more significant. Within the method of Faribault and Schuricht, an arbitrary component of the spin correlation tensor, $R_{\alpha\beta}(t)$, can be evaluated as

$$R_{\alpha\beta}(t) = \sum_{m,n}^{2Z} \langle m|\hat{S}_\alpha|n\rangle \langle n|\hat{S}_\beta|m\rangle e^{i(\omega_m-\omega_n)t}. \tag{3.8}$$

The Metropolis sampling of the coherence factor exploited that $P_{mn} = |\langle n|\hat{S}_+|m\rangle|^2$ is a well-defined probability distribution function defining the importance of each Fourier component. The analogous quantity for $R_{\alpha\beta}(t)$, $\langle m|\hat{S}_\alpha|n\rangle\langle n|\hat{S}_\beta|m\rangle$, is only a well-defined (positive definite) probability distribution if $\alpha = \beta$. For $\alpha \neq \beta$, it may take arbitrary complex values. Monte Carlo evaluation of the above double sum therefore has an associated sign problem. Algorithms exist for sampling from

such distributions, however they are typically associated with significantly less rapid convergence.[129]

Finally, the integrability of the central spin model is key to the success of this method as, without it, elements of the double sum in equation 3.7 cannot be evaluated efficiently. If additional interactions are introduced to the model, the resultant problem is not necessarily integrable. As such, while this approach has found success for the central spin problem, it cannot be readily transferred to other models such as radical pair recombination.

3.3.2 t-DMRG

A contrasting approach is based on applying the time-dependent density matrix renormalisation group (t-DMRG) method[130] to the star-shaped topology of the central spin[103,123] (see figure 3.1). As the t-DMRG method is typically formulated for one-dimensional problems,[131,132] this requires some modification of the underlying algorithm.[103,133] As shown by Uhrig *et al.*, the resultant approach can provide well converged results for the short-time dynamics of central spin models with up to 999 hyperfine-coupled nuclear spins,[103,123] and at arbitrary magnetic field strengths.[123] However, this method suffers from one serious limitation, a rapid growth of errors with time.[123,133]

The t-DMRG method avoids the exponential growth of Hilbert space with the number of spins by restricting the solution to a subset of Hilbert space parameterised by matrix product states (a special case of the tensor networks that will be discussed in Chapter 5).[132] Matrix product states can provide a compact representation of the ground state of a one-dimensional system with nearest neighbour coupling.[132] This representation can become less efficient for time-dependent states of these systems, and a larger matrix product state representation may become necessary to accurately address the problem. This is a consequence of an increase in the entanglement of a quantum state, which for such a one-dimensional system can grow up to linearly in

time.[132,134] For a fixed-sized matrix product state representation, this can lead to a truncation error in the solution that grows exponentially with time.[135] For the star-shaped topology of the central spin model, any two of the bath spins are coupled by two successive applications of the Hamiltonian. This implies that the entanglement of the exact wavefunction will grow rapidly with time, leading to the matrix product form becoming less efficient. Uhrig *et al.* have shown that the truncation error becomes unacceptable for $t > 40\tau$ for a problem with $N = 99$ bath spins, where

$$\tau = \sqrt{\sum_{j=1}^{N} a_j^2} \tag{3.9}$$

is the characteristic timescale of the electron spin precession in the total hyperfine field. For a fixed-sized matrix product state, the truncation error at a given time increases with N and it is necessary to exponentially increase the size of the matrix product state in order to obtain a linear increase in the time for which results are accurate.[123,133] As such, while this t-DMRG method does remove the exponential scaling with the number of nuclear spins, it is replaced with an exponential scaling with time. Consequently this method is only suitable for short time dynamics.

Although these two methods (the algebraic Bethe ansatz and t-DMRG) do partially overcome the exponential scaling issue associated with quantum mechanical approaches, they have a number of shortcomings that restrict their usefulness. Two special cases of the central spin model, for which the spin correlation tensor can be evaluated efficiently, will now be described. These special cases will form the basis of a new method for treating the quantum dynamics of general central spin models.

3.4 Special Cases

The two special cases considered here are the case of homogeneous coupling and a limiting case in which Schulten-Wolynes theory becomes exact.

3.4.1 Homogeneous Coupling

If all nuclear spins couple to the central spin with the same hyperfine coupling constant, the Hamiltonian becomes

$$\hat{H} = \omega \hat{S}_z + a \sum_{k=1}^{N} \hat{\boldsymbol{S}} \cdot \hat{\boldsymbol{I}}_k \tag{3.10}$$

$$= \omega \hat{S}_z + a \hat{\boldsymbol{S}} \cdot \hat{\boldsymbol{I}}, \tag{3.11}$$

where $\hat{\boldsymbol{I}}$ is the total spin angular momentum of the N bath spins. This expression can be simplified by performing a Clebsch-Gordan decomposition of the resultant total spin angular momentum, which transforms it into the coupled representation.[18] The number of ways of coupling the angular momentum of the bath spins to obtain a resultant spin quantum number, I, depends on the spin quantum number of each of the bath spins. For a bath with N nuclear spins, each with spin quantum numbers $I = 1/2$, the number of ways of obtaining a total spin angular momentum I is given by

$$W(N, I) = \binom{N}{N/2 + I} \frac{(2I + 1)}{(N/2 + I + 1)}, \tag{3.12}$$

some values of which are shown in table 3.2. It is straightforward to show that

$$\sum_{I} W(N, I)(2I + 1) = 2^N. \tag{3.13}$$

That is, the 2^N uncoupled states $|\sigma_1, \cdots, \sigma_N\rangle$ (where $\sigma_i = \pm 1/2$ is the projection of the i-th nuclear spin on the z axis) can be combined to give the same number of states, $|I, M_I\rangle$, in the coupled representation.

Transforming to the coupled representation block-diagonalises the homogeneous coupling Hamiltonian, with each symmetry block accounting for the interaction of the central spin with a single spin with a particular value of the spin quantum number I. For every I there are $W(N, I)$ blocks, each corresponding to a different way of obtaining this spin quantum number. The central spin Hamiltonian in this basis becomes

$$\hat{H} = \omega \hat{S}_z + a \sum_{\alpha} \hat{S}_\alpha \Big[\bigoplus_{I=I_{\min}}^{I_{\max}} \Big(\bigoplus_{p=1}^{W(N,I)} \hat{I}_\alpha^{(I,p)} \Big) \Big], \tag{3.14}$$

N	$I=0$	$\frac{1}{2}$	1	$\frac{3}{2}$	2	$\frac{5}{2}$	3	$\frac{7}{2}$	4	
1		1								
2	1		1							
3		2		1						
4	2		3		1					
5		5		4		1				
6	5		9		5		1			
7		14		14		6		1		
8	14		28		20		7		1	
⋮										⋱

Table 3.2: The possible number of ways of coupling N individual spin-$\frac{1}{2}$ angular momenta to produce an overall angular momentum with quantum number I.

where $I_{\min} = (2I \bmod 2)/2$ and $I_{\max} = \sum_{i=1}^{N} I_i = N/2$ are the minimum and maximum possible spin quantum numbers, respectively. $\hat{I}_{\alpha}^{(I,p)}$ is the α-th component of a vector spin operator with spin quantum number I, arising from the p-th way of combining the bath spins to obtain this angular momentum. Introducing the Hamiltonian for each block

$$\hat{H}^{(I,p)} = \omega \hat{S}_z \otimes \mathbf{1}^{(I,p)} + a \sum_{\alpha} \hat{S}_{\alpha} \hat{I}_{\alpha}^{(I,p)}, \tag{3.15}$$

where $\mathbf{1}^{(I,p)}$ corresponds to the identity operator acting on the region of Hilbert space associated with this block, the total Hamiltonian becomes

$$\hat{H} = \bigoplus_{I=I_{\min}}^{I_{\max}} \bigoplus_{p=1}^{W(N,I)} \hat{H}^{(I,p)}. \tag{3.16}$$

The application of the unitary transform ($\hat{X}$) from the uncoupled basis to the coupled basis leaves the initial bath density operator, $\hat{\rho}_B(0) = \frac{1}{Z}\mathbf{1}$, unchanged (as $\hat{X}^{\dagger}\hat{X} = \mathbf{1}$). As such, the central spin correlation tensors may be written as

$$R_{\alpha\beta}(t) = \frac{1}{Z}\mathrm{tr}\left[\hat{S}_{\alpha}(0)e^{i\hat{H}t/\hbar}\hat{S}_{\beta}(0)e^{-i\hat{H}t/\hbar}\right] \tag{3.17}$$

$$= \frac{1}{Z}\mathrm{tr}\left[\bigoplus_{I=I_{\min}}^{I_{\max}} \bigoplus_{p=1}^{W(N,I)} \left(\hat{S}_{\alpha}(0)\otimes\mathbf{1}^{(I,p)}\right)e^{i\hat{H}^{(I,p)}t/\hbar}\left(\hat{S}_{\beta}(0)\otimes\mathbf{1}^{(I,p)}\right)e^{-i\hat{H}^{(I,p)}t/\hbar}\right] \tag{3.18}$$

$$= \sum_{I=I_{\min}}^{I_{\max}} \sum_{p=1}^{W(N,I)} \frac{2I+1}{Z} R_{\alpha\beta}^{(I,p)}(t) \tag{3.19}$$

where $R_{\alpha\beta}^{(I,p)}(t)$ is the central spin correlation tensor calculated for the (I,p)-th symmetry block. For a given I, the Hamiltonian for each of the $W(N,I)$ possible

ways, p, of obtaining this total spin number simply describes the central spin interacting with a single nuclear spin, of length I, with hyperfine interaction a. The dynamics of such a Hamiltonian is clearly independent of p, and for the initial condition considered here, the spin correlation tensor for the block is therefore also independent of p. As such, the ensemble-averaged spin correlation tensor may be written as

$$R_{\alpha\beta}(t) = \sum_{I=I_{\min}}^{I_{\max}} \frac{(2I+1)W(N,I)}{Z} R_{\alpha\beta}^{(I)}(t). \tag{3.20}$$

The problem of computing the central spin correlation tensor, which normally scales as $\mathcal{O}(2^N)$, here requires the evaluation of spin correlation tensors for $\mathcal{O}(N)$ different spin systems, each with Hilbert space dimension scaling as $\mathcal{O}(N)$. As the spin correlation tensor for each block can be evaluated exactly in $\mathcal{O}(Z^2 = N^2)$ operations, the total cost of this approach is reduced to $\mathcal{O}(N^3)$. By exploiting the conservation of the spin projection quantum number, each block can be further decomposed into $\mathcal{O}(N)$ 2×2 blocks, reducing the computation effort to $\mathcal{O}(N^2)$.

The use of the symmetry of the homogeneous coupling Hamiltonian makes it trivial to obtain the central spin correlation tensors for a system including $\mathcal{O}(10^6)$ nuclear spins. However, this is a rather restricted case. In the $N \to \infty$ limit, it becomes possible to evaluate the dynamics of central spin problems with more general hyperfine distributions.

3.4.2 Schulten-Wolynes Theory: An Exact Limit

In the previous chapter, the semiclassical theory presented by Schulten-Wolynes theory was discussed in the context of radical pairs. This theory is based on the assumption that when there are a sufficiently large number of bath spins, the details of the dynamics of the bath spins are unimportant.[60] The influence of the bath on the central spin can be accounted for by treating the hyperfine-weighted sum of nuclear spin operators,

$$\hat{\boldsymbol{K}} = \sum_{k=1}^{N} a_k \hat{\boldsymbol{I}}_k, \tag{3.21}$$

as a constant vector, $\boldsymbol{K}$, which will be referred to as the total hyperfine field. This theory becomes exact in the limit of an infinite number of bath spins, N. This can be shown by considering a central spin problem containing N bath spins each coupled to the central spin with a hyperfine coupling constant, $a_k(N)$, that is a function of N, provided the hyperfine coupling constants satisfy

$$\lim_{N\to\infty} \sqrt{N} a_k(N) = \widetilde{a}_k, \tag{3.22}$$

where each $\widetilde{a}_k$ is independent of N. A proof of this is given in appendix B. The constraint given in equation 3.22 ensures that the second moment of the hyperfine field,

$$A_N^2 = \sum_{k=1}^{N} a_k^2 I_k(I_k+1), \tag{3.23}$$

remains constant in the $N \to \infty$ limit and fixes the characteristic timescale, τ, of the electron spin precession due to the total hyperfine field (which for a bath of spin-$\frac{1}{2}$s is given by equation 3.9).

On making the Schulten-Wolynes theory approximation, the Hamiltonian governing the dynamics of the central spin becomes

$$\hat{H}_{SW}(\Omega) = \omega \hat{S}_z + \boldsymbol{K}(\boldsymbol{\Omega}) \cdot \hat{\boldsymbol{S}}, \tag{3.24}$$

where $\boldsymbol{K}(\boldsymbol{\Omega})$ depends on the orientations of all nuclear spin vectors, $\boldsymbol{\Omega}$. The Schulten-Wolynes theory approximation to the central spin operators at time t evolve according to the Heisenberg equation of motion

$$\frac{\mathrm{d}}{\mathrm{d}t}\hat{\boldsymbol{S}}(t) = \frac{i}{\hbar}\left[\hat{H}_{SW}, \hat{\boldsymbol{S}}(t)\right] \tag{3.25}$$

$$= \tilde{\boldsymbol{\omega}}(\boldsymbol{\Omega}) \times \hat{\boldsymbol{S}}(t), \tag{3.26}$$

where the vector $\tilde{\boldsymbol{\omega}}(\boldsymbol{\Omega}) = (0,0,\omega)^T + \boldsymbol{K}(\boldsymbol{\Omega})$ has been introduced. This coupled system of equations can be solved analytically and the spin correlation tensor, for a given orientation of the nuclear spins, can be obtained as[61]

$$R_{\alpha\beta}(\boldsymbol{\Omega},t) = \mathrm{tr}\left[\hat{\boldsymbol{S}}_\beta(\boldsymbol{\Omega},0)\hat{\boldsymbol{S}}_\beta(\boldsymbol{\Omega},t)\right] \tag{3.27}$$

$$= \frac{S(S+1)(2S+1)}{3}\left[\hat{\tilde{\omega}}_\alpha\hat{\tilde{\omega}}_\beta + (\delta_{\alpha\beta} - \hat{\tilde{\omega}}_\alpha\hat{\tilde{\omega}}_\beta)\cos(\tilde{\omega}t) + \epsilon_{\alpha\beta\gamma}\hat{\tilde{\omega}}_\gamma \sin(\tilde{\omega}t)\right], \tag{3.28}$$

where $\tilde{\omega} = |\tilde{\boldsymbol{\omega}}(\boldsymbol{\Omega})|$ and $\hat{\tilde{\omega}}_\alpha$ is the α-th component of the unit vector $\hat{\tilde{\boldsymbol{\omega}}} = \tilde{\boldsymbol{\omega}}/\tilde{\omega}$. In order to obtain the ensemble average of the components of the spin correlation tensor, this expression must be averaged over the distribution of the total hyperfine field given by[60] (see appendix B)

$$P(\boldsymbol{K}) = \frac{1}{(2\pi)^{3/2}\sigma^3} e^{-\boldsymbol{K}^2/(2\sigma^2)}, \tag{3.29}$$

where $\sigma = A_N^2/3$. This average can be evaluated analytically to give,[66]

$$R_{xx}(t) = \left[\omega_*\left(2 + e^{-t_*^2}[(\omega_*^2 - 2)\cos(\omega t) - 2\omega t \sin(\omega t)]\right) - 4f(\omega_*, t_*)\right]/2\omega_*^3 \tag{3.30}$$

$$R_{xy}(t) = e^{-t_*^2}(2\omega t\cos(\omega t) + (\omega_s^2 - 2)\sin(\omega t))/2\omega_*^3 \tag{3.31}$$

$$R_{zz}(t) = \left[\omega_*\left(\omega_*^2 + 4e^{-t_*^2}\cos(\omega t) - 4\right) + 8f(\omega_*, t_*)\right]/2\omega_*^3 \tag{3.32}$$

where $\omega_* = \sqrt{2}\omega/\sigma$, $t_* = t\sigma/\sqrt{2}$, and

$$f(\omega_*, t_*) = \int_0^{t_*} e^{-\tau_*^2}\sin(\omega_*\tau_*)\mathrm{d}\tau_* \tag{3.33}$$

can be expressed as a sum of four complex error functions. In the absence of an external magnetic field, these expressions reduce to

$$R_{xx}(t) = R_{zz}(t) = \frac{1}{6}\left(1 + 2e^{-t_*^2}(1 - 2t_*^2)\right) \tag{3.34}$$

$$R_{xy}(t) = 0. \tag{3.35}$$

The $R_{xx}(t)$ spin correlation functions obtained using quantum mechanical (QM) calculations and Schulten-Wolynes (SW) theory for a series of central spin models with homogeneous hyperfine couplings are shown in figure 3.2. The Hamiltonian for these systems takes the form

$$\hat{H}_N = \omega\hat{S}_z + \frac{\widetilde{a}}{\sqrt{N}}\hat{\boldsymbol{S}}\cdot\sum_{k=1}^{N}\hat{\boldsymbol{I}}_k, \tag{3.36}$$

where $N = 10$, 10^2, 10^3, and 10^6, $\widetilde{a}\hbar/|\gamma_e| = 1.0$ mT, and $\omega\hbar/|\gamma_e| = 0$ mT (first row) or $\omega\hbar/|\gamma_e| = 0.5$ mT (second row). The hyperfine coupling constant $a \propto 1/\sqrt{N}$ satisfies equation 3.22, and ensures that the characteristic timescale of the electron spin dynamics, τ, (defined in equation 3.9) is the same for all N.

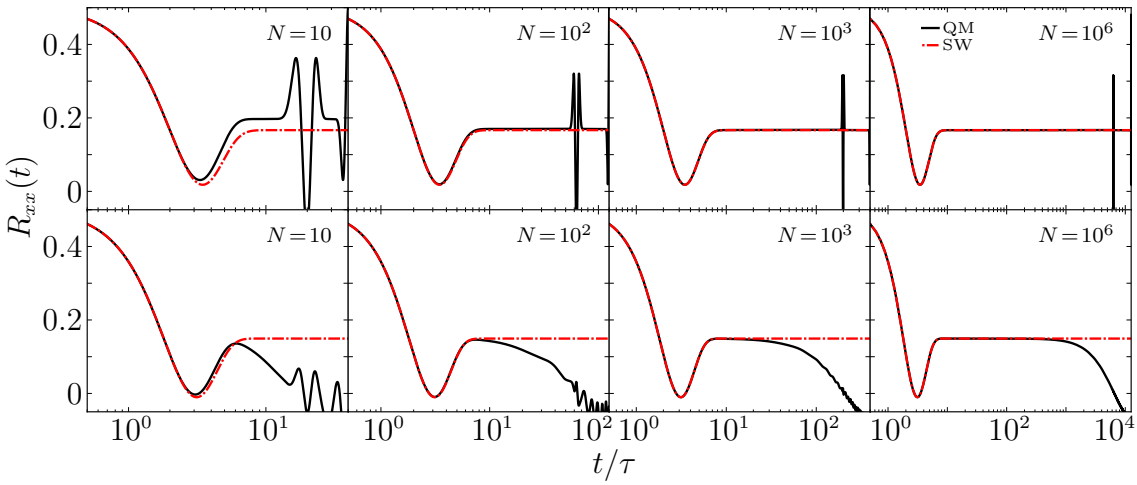

Figure 3.2: The $R_{xx}(t)$ component of the spin correlation for a series of central spin models with homogeneous hyperfine couplings obtained using exact dynamics (black) and Schulten-Wolynes theory (red). The system evolves under the Hamiltonian given in equation 3.36 with N nuclear spins with $\omega\hbar/|\gamma_e| = 0$ mT (first row) or $\omega\hbar/|\gamma_e| = 0.5$ mT (second row).

In the absence of an applied field, both approaches predict an initial short time decay in $R_{xx}(t)$, however for $N = 10$ the Schulten-Wolynes theory results deviate noticeably from the quantum mechanical results. Following this initial decay, $R_{xx}(t)$ increases until reaching a plateau at $t \sim 5\tau$. For small N, the two methods predict different plateau values, SW theory predicts a plateau value of 1/6 independent of N, while the QM plateau value is observed to decrease with N tending towards 1/6. In contrast to SW theory, which predicts that this plateau continues for all time, the QM correlation function is observed to recur for $t \propto \sqrt{N}\tau$.[136] On these timescales the error associated with SW theory is of order $\mathcal{O}(1)$ and it therefore fails to capture the dynamics here. As $N \to \infty$ the recurrences are pushed to $t \to \infty$, and SW theory becomes exact for any finite time.

In the presence of an applied magnetic field, the quantum mechanical correlation function no longer recurs. Instead, a slow decay is observed at long times and is associated with decoherence of the central spin arising from the evolution of the bath spins. SW theory fails to capture this effect due to the assumption of a static bath. For $N = 10^3$ and 10^6, a long-lived plateau is observed before the onset of

this decay. As N increases, the onset of this decay is pushed to later time and SW theory becomes more accurate. In the $N \to \infty$ limit, the decay will be pushed to $t \to \infty$ and SW theory will become exact.

Although neither the homogeneous coupling nor Schulten-Wolynes limit are physically realistic models for describing quantum dots (or individual radicals in radical pair recombination reactions), they provide useful limiting cases for validating more general methods. Additionally, these two limits motivate the following method for treating the dynamics of the central spin problem with generic hyperfine coupling constants.

3.5 A Simple and Accurate Method

Motivated by the issues with existing approaches and the two special cases discussed above, an alternative approach to the general central spin problem will now be presented. Rather than attempting to calculate the exact dynamics of the central spin evolving under the Hamiltonian in equation 3.1, the dynamics arising due to a series of simpler Hamiltonians, $\hat{H}_M$ for $M = 1, 2, \ldots$ will be considered instead.

The Hamiltonians, $\hat{H}_M$, considered here,[137]

$$\hat{H}_M = \omega \hat{S}_z + \sum_{j=1}^{M} \sum_{k=1}^{N_j} \alpha_j \hat{\boldsymbol{S}} \cdot \hat{\boldsymbol{I}}_{jk}, \tag{3.37}$$

describe a central spin interacting with M groups of bath spins, where each of the N_j spins in group j interact with the central spin through a Fermi contact interaction with a hyperfine coupling constant, α_j. A schematic representation of such a Hamiltonian is shown in figure 3.3. The parameters α_j and N_j are chosen so that as M increases, the resultant Hamiltonian is better able to capture the influence of the bath on the central spin. This is done by selecting the N_j's and α_j's such that the first $M + 1$ moments of the modified hyperfine distribution

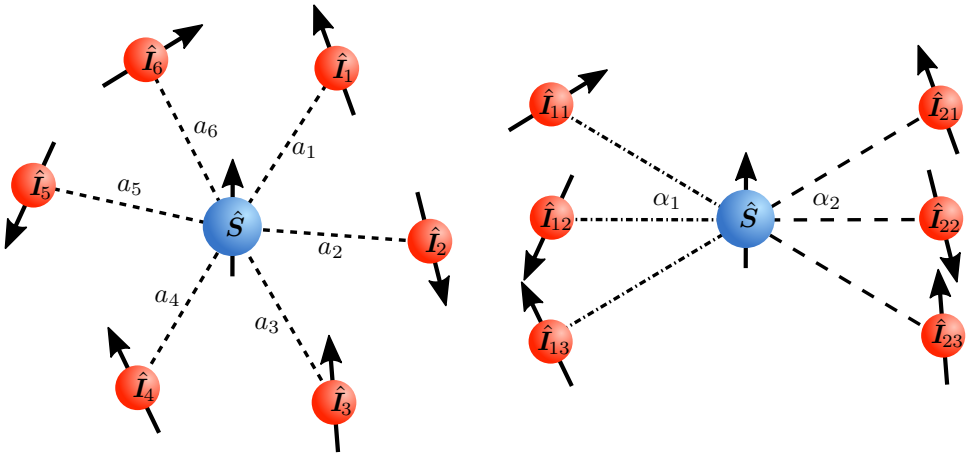

Figure 3.3: (left) An illustration of a central spin Hamiltonian representing a central spin interacting with 6 bath spins. The central spin (blue) interacts with a set of coupled bath spins (red) through the isotropic interaction a_k (e.g. Fermi contract interactions between electron spins and nuclear spins). (right) A simplified Hamiltonian obtained with $M = 2$ groups of 3 bath spins. Each of the 3 bath spins in each group interacts with the central spin through a hyperfine interaction with the same hyperfine coupling constant α_i. The number of spins, $N_j = 3$, in each group and the hyperfine coupling constant associated with that group are chosen so that the modified hyperfine distribution captures the first $M = 2$ moments of the original hyperfine distribution.

coincide with those of the original distribution:

$$\mu_n = \sum_{j=1}^{N} a_j^n = \sum_{j=1}^{M} N_j \alpha_j^n \qquad \text{for } n = 0, 1, \ldots, M. \tag{3.38}$$

This process is not unique, for a given M there are a large number of sets of N_js and α_js which can satisfy these conditions. Here a heuristic scheme is employed that allows for a specific choice of the N_js and α_js to be made efficiently.

For a given M, the distribution of the modified hyperfine coupling constants is selected by first generating a gaussian quadrature rule, defined by the weights, w_j, and nodes, $\widetilde{\alpha}_j$, using the discrete procedure of Stieltjes.[138] The quadrature rule exactly integrates the product of all polynomials with order less than $2M$ and the original hyperfine distribution function. As such, the nodes and weights exactly reproduce the first $2M - 1$ moments of the original hyperfine distribution:

$$\mu_n = \sum_{j=1}^{N} a_j^n = \sum_{j=1}^{M} w_j \widetilde{\alpha}_j^n \qquad \text{for } n = 0, 1, \ldots, 2M - 1. \tag{3.39}$$

The weights correspond to the number of spins in each group while the nodes correspond to the hyperfine coupling constants. Although as the weights are, in general, not integers they cannot represent the number of spins in a group. So instead, all possible sets of integers obtained by taking the floor and ceiling of the Stieltjes weights ($N_j = \lfloor w_j \rfloor$ or $\lceil w_j \rceil$) such that,

$$\sum_{j=1}^{M} N_j = N, \tag{3.40}$$

are considered. For each set of integers, a set of hyperfine coefficients, $\{\alpha_j\}$, is obtained by solving the nonlinear system of equations defining the M moments of the distribution

$$\mu_1 = \sum_{j=1}^{M} N_j \alpha_j \tag{3.41}$$

$$\vdots \tag{3.42}$$

$$\mu_M = \sum_{j=1}^{M} N_j \alpha_j^M \tag{3.43}$$

using Newton's method with an initial guess of $\{\alpha_j\} = \{\widetilde{\alpha}_j\}$. Finally, from all $< 2^M$ possible sets of $\{N_j\}$ and $\{\alpha_j\}$ the final distribution is selected as the one that minimises the absolute error in the next moment, μ_{M+1}. It is possible that an alternative approach for selecting the modified hyperfine distribution may provide better results; however, this scheme allows for rapid construction of the new hyperfine distribution and, as will be shown below, leads to rapid convergence (with respect to M) of the central spin dynamics for a number of different models.

The simplified Hamiltonians defined in equation 3.37 still act on the full Hilbert space of the system. As such, a naive treatment of the dynamics suffers from exponential scaling with the number of spins. However, for a given M, the Hamiltonian can be rewritten as

$$\hat{H}_M = \omega \hat{S}_z + \sum_{j=1}^{M} \alpha_j \hat{\boldsymbol{S}} \cdot \hat{\tilde{\boldsymbol{I}}}_j, \tag{3.44}$$

where $\hat{\tilde{\boldsymbol{I}}}_j = \sum_{k=1}^{N_j} \hat{\boldsymbol{I}}_{jk}$ is the total angular momentum operator for j-th group of bath spins. Performing a Clebsch-Gordan decomposition on each of these total spin

angular momentum operators, $\hat{\tilde{\boldsymbol{I}}}_j$, results in block diagonalisation of this modified Hamiltonian. Each of the non-interacting blocks of the Hamiltonian describe a central spin interacting with M bath spins with varying spin quantum numbers. As was the case for homogeneous coupling, the central spin correlations tensors can be evaluated through a weighted sum over this quantity obtained for each block. Exploiting the symmetry of the simplified Hamiltonian, $\hat{H}_M$, can dramatically reduce the computation effort to obtain the central spin correlation tensors. For example, a calculation with $M = 1$ and $N_1 = 100$ equivalent spin-$\frac{1}{2}$ nuclei is reduced to 51 separate calculations, with the largest having a Hilbert space dimension of 202, as opposed to 2^{101} if the symmetry is not exploited. For $M = 2$ and $N_1 = N_2 = 50$, the calculation is reduced to $26 \times 26 = 676$ separate calculations with I_1 and I_2 between 0 and 25. The largest Hilbert space dimension of any of these calculations is then $5,202$. While the effort increases with M, if $M \ll N$ then the total effort required remains many orders of magnitude less than that for a full calculation. In what follows, the method based on the use of these simplified Hamiltonians will be referred to as the moment-fitting method.

There are a number of features of these simplified Hamiltonians which suggest that this approach may provide an efficient way of treating the dynamics of a general central spin problem. For a central spin problem with homogeneous coupling, this method is exact for all $M \geq 1$. For $M = 1$ this approach fully uses the symmetry associated with the homogeneous coupling, while for larger M it only partially exploits this. In the Schulten-Wolynes limit, the second moment of the hyperfine field (μ_2) uniquely determines the dynamics of the system. By construction, the approximate Hamiltonians described above capture the correct dynamics in the large N limit for any $M \geq 2$. Additionally, as equation 3.37 reduces to the full Hamiltonian when $M = N$ the correct result in the small N limit will be obtained when the exact calculation is feasible. What remains to be determined is how well this method works for intermediate numbers of spins that are away from either of

these two limits. Before this is tested, it is necessary to discuss some implementation details that dramatically improve the efficiency of this method.

3.5.1 Implementation Details

Truncation of Blocks

Following the approximation of the Hamiltonian by M sets of equivalent spins, the central spin correlation functions for the full system can be obtained by taking a weighted sum of those for each symmetry block. In practice, it is both inefficient and unnecessary to evaluate the contribution arising from all blocks. To illustrate this, consider a central spin problem with a bath of $N = 100$ spin-$\frac{1}{2}$s. If the approximate Hamiltonian obtained for $M = 5$ groups has each group containing $N_j = 20$ spins, then, in order to obtain the central spin correlation function, it is necessary to perform a series of simulations of a central spin interacting with 5 bath spins where each one can independently have any spin quantum number $I_j \in \{0, 1, 2, \ldots, 10\}$. It is therefore necessary to evaluate the dynamics of $11^5 = 161,051$ distinct spin systems. The spin correlation tensor is then obtained as

$$R_{\alpha\beta}(t) = \sum_{I_1=0}^{10} \cdots \sum_{I_5=0}^{10} w_{I_1 \ldots I_5} R_{\alpha\beta}^{(I_1 \ldots I_5)}(t), \tag{3.45}$$

where the weight of each term is

$$w_{I_1 \ldots I_5} = \frac{1}{Z} \prod_{i=1}^{5} (2I_i + 1) W(N_i, I_i), \tag{3.46}$$

with $Z = 2^{100}$, the nuclear Hilbert space dimension. The most expensive individual step of this calculation is the evaluation of the correlation function $R_{\alpha\beta}^{10 \ldots 10}(t)$. This spin system has a total Hilbert space dimension of $2 \times 21^5 = 8,168,202$. While possible, this is an expensive calculation. However, $0 \leq |R_{\alpha\beta}^{(I_1 \ldots I_5)}(t)| \leq 1$ for all time. As such, each term in equation 3.45 can contribute at most $w_{I_1 \ldots I_5}$ to the total correlation function. The maximum contribution of the $R_{\alpha\beta}^{10 \ldots 10}(t)$ correlation function is therefore

$$w_{10 \ldots 10} = \frac{21^5}{2^{100}} \approx 3.2 \times 10^{-24}, \tag{3.47}$$

well below the machine epsilon associated with double precision numbers.[138] Other blocks with similar Hilbert space dimension likewise contribute little to the total correlation function. This suggests that significantly improved performance may be obtained, without significant loss in accuracy, by only including terms in the sum in equation 3.45 with a Hilbert space dimension ($Z_{1\ldots M} = (2I_1+1)(2I_2+1)\ldots(2I_M+1)$) smaller than some maximum. The spin correlation function can be approximated by

$$R_{\alpha\beta}(t) \approx R^{\epsilon}_{\alpha\beta}(t) = \sum_{\substack{I_1,I_2,\ldots I_M \\ Z_{1\ldots M}<N_{hmax}}} w_{I_1\ldots I_M} R^{(I_1\ldots I_M)}_{\alpha\beta}(t), \tag{3.48}$$

where the maximum nuclear spin Hilbert space dimension, $N_{\max}$, is taken as the smallest value satisfying

$$\epsilon < 1 - \sum_{\substack{I_1,I_2,\ldots I_M \\ Z_{1\ldots M}>N_{\max}}} w_{I_1\ldots I_M}, \tag{3.49}$$

for some predefined error tolerance, ϵ. This guarantees a maximum error in the central spin correlation function of

$$|R^{\epsilon}_{\alpha\beta}(t) - R_{\alpha\beta}(t)| < \epsilon \tag{3.50}$$

for all time. This truncation can dramatically reduce the computational effort required. For the example of a central spin with $N = 100$ spin-$\frac{1}{2}$s decomposed into the $M = 5$ groups considered above, using a tolerance of $\epsilon = 10^{-6}$ reduces the total number of correlation functions that must be evaluated from $161,051$ to $132,270$. More significantly, the largest symmetry block included has a Hilbert space dimension of $266,175$; this is $\sim$30 times smaller than the largest block which would be included using equation 3.45. In the discussion below, all results were obtained using equation 3.48 with a tolerance parameter selected to ensure convergence.

Evaluation of Correlation Functions

The spin correlation tensors for each symmetry block of the Hamiltonian must be evaluated in order to obtain the ensemble average spin correlation tensor. For symmetry blocks with small Hilbert space dimensions (~ 1000) it is practical to exactly evaluate the trace using a sum over the uncoupled basis states (analogous to

equation 2.85). As the Hilbert space dimension grows, this becomes impractical and it becomes necessary to employ the coherent spin state sampling scheme discussed in Section 2.2.5. While in practice this could be used for evaluating the dynamics of small and large blocks, it is inefficient for the smaller blocks, for which, it is often necessary to use more coherent spin state samples than there are states in the Hilbert space in order to obtain well converged results. As such, here a hybrid scheme is employed. For blocks with more bath states than some cutoff value, N_{css}, the spin correlation function is evaluated using N_{css} coherent spin state samples. Correlation functions of all blocks with fewer bath states are evaluated using an exact evaluation of the trace.

3.6 Application: Dynamics of Model Quantum Dots

As a first application and a validation of this method, the $R_{xx}(t)$ component of the central spin correlation tensor is calculated for two central spin models, for which numerically exact results are available. The first of these models (model 1) describes a central spin coupled to N spin-$\frac{1}{2}$ nuclei with hyperfine coupling constants obtained from the uniform distribution[103]:

$$a_j\tau = \sqrt{\frac{6N}{2N^2+3N+1}}\frac{N+1-j}{N}. \tag{3.51}$$

This model is unlikely to represent any real world problems, however, the $R_{xx}(t)$ component of the central spin correlation tensor has previously been obtained for $N = 49$, 99, and 999 using the t-DMRG approach of Uhrig *et al.*.[103,123] It provides a convenient test problem for exploring the convergence of the moment-fitting method as the number of bath spins is increased. In the $N \to \infty$ limit this distribution satisfies equation 3.22, and the dynamics of this system will be captured by Schulten-Wolynes theory.

The second model (model 2) again treats a central spin coupled to a bath of N spin-$\frac{1}{2}$ nuclei. However, except now with a hyperfine distribution,

$$a_j\tau = \sqrt{\frac{1-e^{-2/(N_0-1)}}{1-e^{-2N/(N_0-1)}}}e^{-(j-1)/(N_0-1)}, \tag{3.52}$$

arising from Fermi contact interactions present in a simple model of a two-dimensional quantum dot with a Gaussian electronic wavefunction.[97] N_0 corresponds to the number of nuclear spins found within one standard deviation of the maximum of the Gaussian wavefunction[97] and significantly influences the distribution of the hyperfine coupling constants. For $N_0 \gg N$, the distribution tends towards the uniform distribution considered in model 1, while for $N_0 \ll N$ there are a few spins with dominant hyperfines and a large number of spins which couple weakly to the central spin. In the limit that $N \to \infty$ and with N_0 held fixed, this distribution does not satisfy equation 3.22, and hence Schulten-Wolynes theory does not provide an accurate description of the dynamics. This model should, therefore, provide a challenging test for the moment-fitting method. The central spin dynamics for this model have previously been obtained for $N = 48$ and $N_0 = 24$ and 36 using the algebraic Bethe Ansatz approach of Faribault and Schuricht.[124]

3.6.1 Convergence with M

Model 1: Varying N

The convergence of the moment-fitting method for model 1 with $N = 49$ is shown in figure 3.4. Here the $R_{xx}(t)$ central spin correlation function obtained for varying values of M is compared against the converged result obtained with $M = 7$. For all values of M, the initial short time precession of the electron spin around the total hyperfine field is captured accurately. Over this short time period, the nuclear spin bath does not have enough time to evolve significantly and so the Schulten-Wolynes theory approximation of a fixed bath is accurate. Schulten-Wolynes theory depends solely on the second moment of the hyperfine distribution, which all Hamiltonians with $M \geq 2$ capture exactly. Due to this connection with Schulten-Wolynes theory, the short time dynamics obtained using the moment-fitting method is expected to

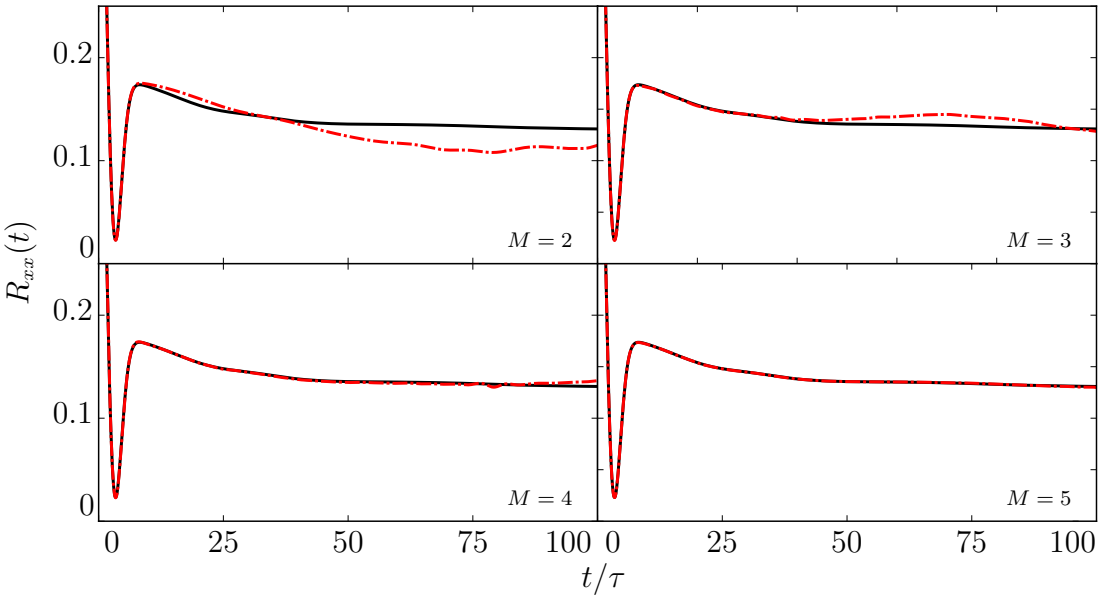

Figure 3.4: The $R_{xx}(t)$ component of the spin correlation tensor obtained using the moment-fitting method for Model 1 with $N = 49$ bath spins. The red curves are obtained with the value of M shown in each panel, while the black curve corresponds to the converged result obtained with $M = 7$.

converge rapidly with M. At longer times, the $M = 2$ results deviate significantly from the converged results. In this case, decoherence of the central spin arising from the evolution of the nuclear spin bath, which is not captured by Schulten-Wolynes theory, becomes important. As M increases this is captured rapidly and for $M = 3$ the effect of the nuclear bath is described well out to times of $t \sim 30\tau$. Increasing M to 4 this is extended to $t \sim 70\tau$. Finally, for $M = 5$ the dynamics of the central spin has converged for all $t < 100\tau$; further increasing M to 7 does not alter $R_{xx}(t)$ over this time frame.

Figure 3.5 shows the convergence of $R_{xx}(t)$ obtained using the moment-fitting method with increasing M for model 1 with $N = 99$ nuclear spins. Similar convergence behaviour to the $N = 49$ case is observed; however, as M increases the central spin dynamics converges more rapidly. Significant deviations from the exact results are observed for $M = 2$ and $M = 3$ after $t \sim 10\tau$ and $t \sim 50\tau$, respectively. By $M = 4$, the results agree with the converged $M = 5$ results over the entire time period considered. This improved convergence can be understood

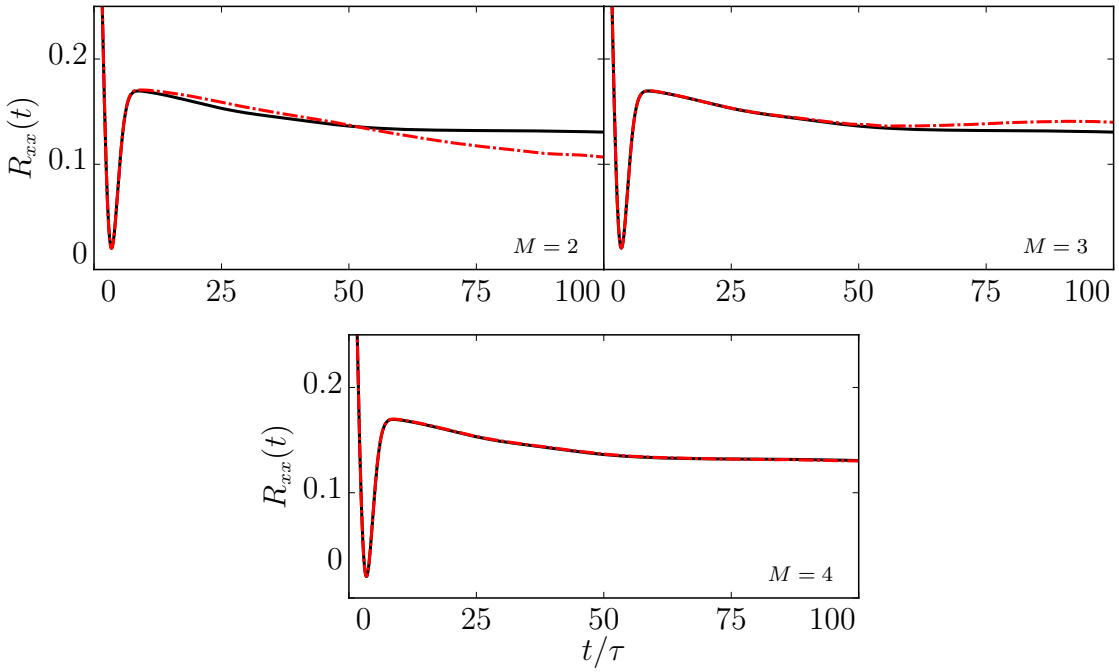

Figure 3.5: The $R_{xx}(t)$ component of the spin correlation tensor obtained using the moment-fitting method for Model 1 with $N = 99$ bath spins. The red curves are obtained with the value of M shown in each panel, while the black curve corresponds to the converged result obtained with $M = 5$.

through the connection with Schulten-Wolynes theory. As the hyperfine distribution for this model (equation 3.51) satisfies equation 3.22, in the $N \to \infty$ limit the second moment of the hyperfine distribution solely determines the dynamics. As the number of spins increases, higher order moments of the hyperfine distribution become less important for this model and converged results can be obtained with smaller M. This improved convergence continues for $N = 999$ where the converged results are obtained for $M = 3$.

Model 2: Varying the Distribution

The convergence of $R_{xx}(t)$ as a function of M is shown for model 2, with $N = 48$ nuclear spins and $N_0 = 12$, in figure 3.6. In this case, considerably slower convergence with M is observed than for model 1. For $M = 2$, only the short time dynamics is captured accurately. At longer times, high frequency, large amplitude oscillations that are not present in the converged ($M = 9$) results are observed. When M is increased to 4, the central spin dynamics is accurately captured until $t \sim 50\tau$. Past

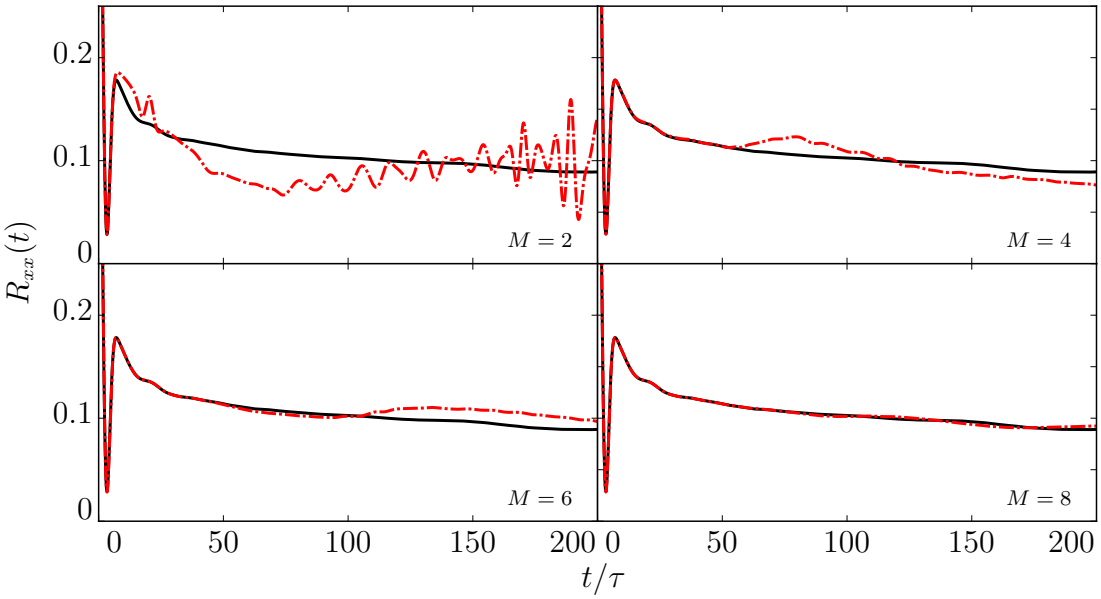

Figure 3.6: The $R_{xx}(t)$ component of the spin correlation tensor obtained using the moment-fitting method for Model 2 with $N = 48$ bath spins and $N_0 = 12$. The red curves are obtained with the value of M shown in each panel, while the black curve corresponds to the converged result obtained with the $M = 9$.

this time, significant deviations are still observed. Further increasing M to 6 does not significantly extend the time over which the correlation function is accurate, although the deviations observed between $t = 50\tau$ and 100τ are considerably reduced. Finally, for $M = 8$, the results agree well with the $M = 9$ results except at long times small where small oscillation are observed around the $M = 9$ results.

The convergence of $R_{xx}(t)$ with M for model 2 with $N_0 = 36$ is shown in figure 3.7. Once again, the results for $M = 2$ fail to describe the long-time behaviour of $R_{xx}(t)$. Significant high frequency oscillations are observed at long times, however, in contrast to the results with $N_0 = 12$, these oscillations occur around the converged result obtained with $M = 7$. The $M = 4$ results agree to graphical accuracy with the $M = 7$ results to times of $t \sim 100\tau$, following which there are small amplitude deviations. As M increases further, significantly smaller changes in the correlation function are observed. Results obtained with $M = 5$ deviate only slightly from the $M = 7$ results, showing small amplitude, large frequency oscillations at long times. For $M = 6$, the results have converged over the timescale considered.

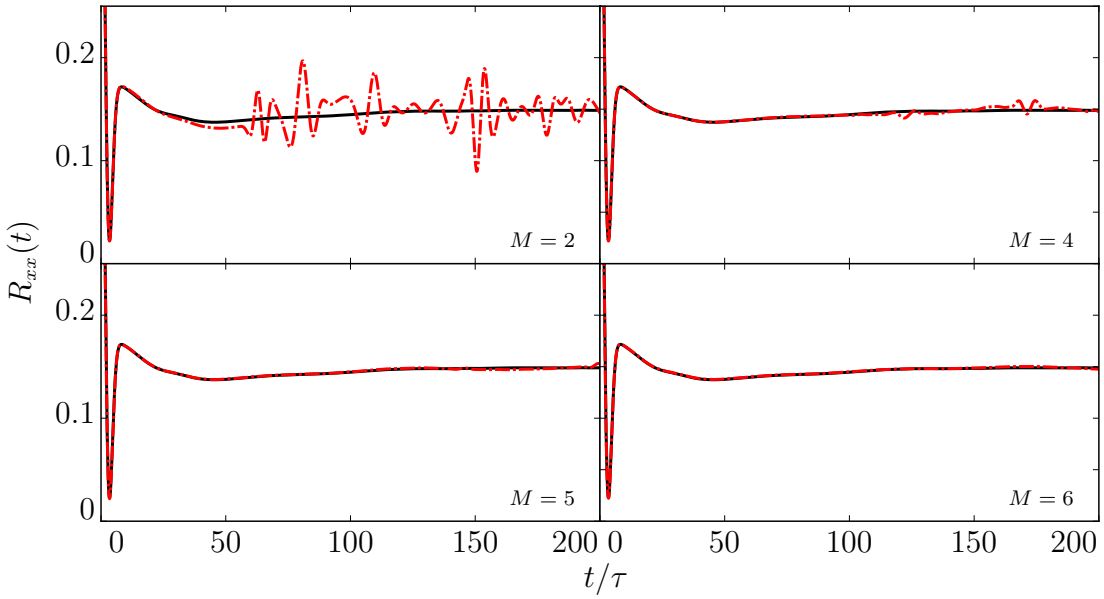

Figure 3.7: The $R_{xx}(t)$ component of the spin correlation tensor obtained using the moment-fitting method for model 2 with $N = 48$ bath spins and $N_0 = 36$. The red curves are obtained with the value of M shown in each panel, while the black curve corresponds to the converged result obtained with $M = 7$.

These results show that as N_0 increases the moment-fitting method converges more rapidly with M. For small N_0, there are a few bath spins with dominant hyperfines, while a considerably larger number of bath spins have very small hyperfines. The few spins with larger hyperfines allow for rapid exchange of energy between the central spin and nuclear spin bath, and at short times contribute most significantly to the decoherence of the central spin. The weakly coupled spins facilitate energy exchange between the central and spin bath on considerably longer timescales, and only contribute significantly to the decoherence of the central spin over longer times[100]. For the moment-fitting approach to be successful, the modified Hamiltonian needs to be able to describe the dynamics occurring on both the short and long timescales involved in the full problem. As the moments of the hyperfine distribution are considerably less sensitive to the small hyperfine coupling constants of weakly coupled spins, a larger M value is required before the modified Hamiltonian will capture their dynamics. For $N_0 = 36$, the spin with the largest hyperfine coupling constant evolves on a timescale ~ 4 times faster than that of the weakest coupled

spin. For $N_0 = 12$ this factor increases to ~ 70. The modified Hamiltonian must be able to capture the decoherence of the central spin arising due to nuclear spins precessing over a considerably larger range of timescales, and this requires a larger M.

The results presented in this section have demonstrated that the central spin dynamics arising from the Hamiltonians $\hat{H}_M$ converges as M increases. All that remains to be seen is whether they have converged to the correct value.

3.6.2 Exact Dynamics

The converged dynamics obtained with the moment-fitting method for model 1 is compared with the t-DMRG results presented by Uhrig *et al.* in figure 3.8.[103,123] The good agreement over the timescales for which the t-DMRG results are available confirms that the moment-fitting method converges to the correct quantum mechanical central spin dynamics for this model. It also avoids the growth of the error with time that is observed in the t-DMRG results. For $N = 49$ and $N = 99$, the correlation functions obtained using the two approaches agree until $t =\sim 30\tau$ and 20τ, respectively. For $N = 49$, the two results still agree qualitatively at longer times but for $N = 99$ significant deviations are observed. This can be attributed to the truncation error associated with the t-DMRG calculation, which for $N = 99$ is expected to be $\sim 10\%$ for $t \geq 40\tau$.[123,133] The t-DMRG results for $N = 999$ are only available up to $t = 10\tau$ as the truncation error increases with increasing N.

The converged correlation functions obtained with the moment-fitting method for model 2 are compared in figure 3.9 with those obtained by Faribault and Schuricht using the algebraic Bethe ansatz (ABA) approach.[124] Here, once again, the agreement between the two methods is excellent over the entire time period shown, and confirms that the moment-fitting method is able to capture the central spin dynamics accurately even for this more challenging model. The two methods capture the same long timescale behaviour; however, the moment-fitting results are smoother than those obtained with the ABA approach. The high frequency

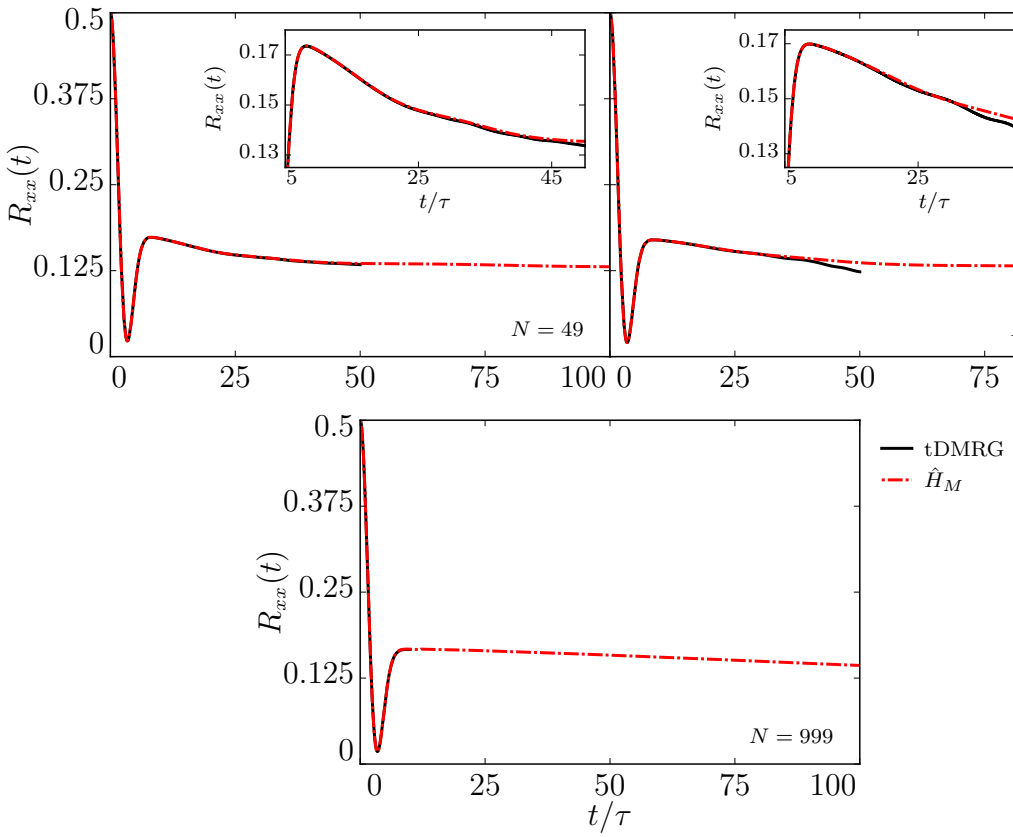

Figure 3.8: Comparison of the converged results (red dashed lines) for model 1 with the t-DMRG results of Uhrig *et al.*[103,123] (black solid lines) obtained for $N = 49$, 99, and 999.

oscillation observed in the ABA approach (see the insets in figure 3.9) can be attributed to statistical errors associated with the incomplete Monte Carlo sampling of pairs of eigenstates in equation 3.7. As discussed above these stochastic errors are likely to become more pronounced for larger N.

The results presented in the past two sections demonstrate that the moment-fitting method provides an efficient approach for obtaining the exact quantum dynamics of central spin models for large nuclear spin baths and over long timescales. The quantum mechanical results obtained using this approach are sufficiently well converged over sufficiently long times that they can provide a stringent test of the semiclassical methods that were discussed in Section 2.3.

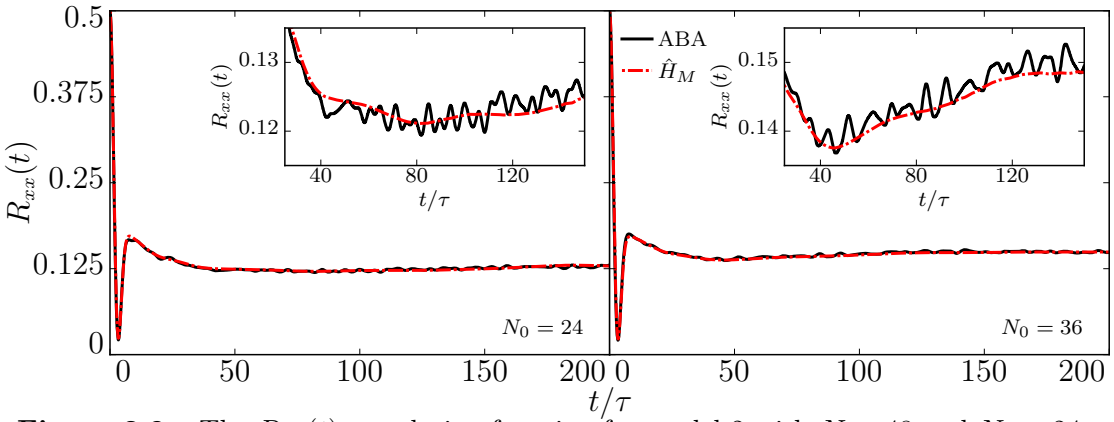

Figure 3.9: The $R_{xx}(t)$ correlation function for model 2 with $N = 48$ and $N_0 = 24$ and 36. Here the converged results obtained using the moment-fitting method (red dashed lines) are compared against the results obtained by Faribault and Schuricht using the algebraic Bethe ansatz (black solid lines).[124]

3.6.3 Semiclassical Dynamics

The central spin correlation functions, $R_{xx}(t)$, for model 1 with $N = 49$, 99, and 999 that were obtained using: the moment-fitting method, Schulten-Wolynes theory (SW), and the improved semiclassical theory (SC) of Manolopoulos and Hore[61] (the central spin variant of the theory described in Section 2.3.2) are shown in figure 3.10. The semiclassical theories qualitatively capture the dynamics, however, neither the SW nor the SC theory is quantitatively accurate, even for $N = 999$. SW theory fails to capture the long-time decay of the central spin correlation function arising from the evolution of the nuclear spin bath. In contrast, the improved semiclassical theory predicts too rapid a decay. This is most apparent in the insets of figure 3.10. As N increases, the decay of the correlation function occurs on a considerably longer timescale. As a result, both semiclassical methods become more accurate.

The $R_{xx}(t)$ correlation functions obtained using the semiclassical methods are compared with the quantum mechanical results for model 2 with $N_0 = 12$, 24, and 36, in figure 3.11 . As the value of N_0 decreases, the spin correlation function predicted using SW theory deviates further from the QM results. For all values of N_0, SW theory predicts that $R_{xx}(t)$ will plateau at 1/6, while the QM correlation functions are observed to decay. SW theory is based on the assumption that,

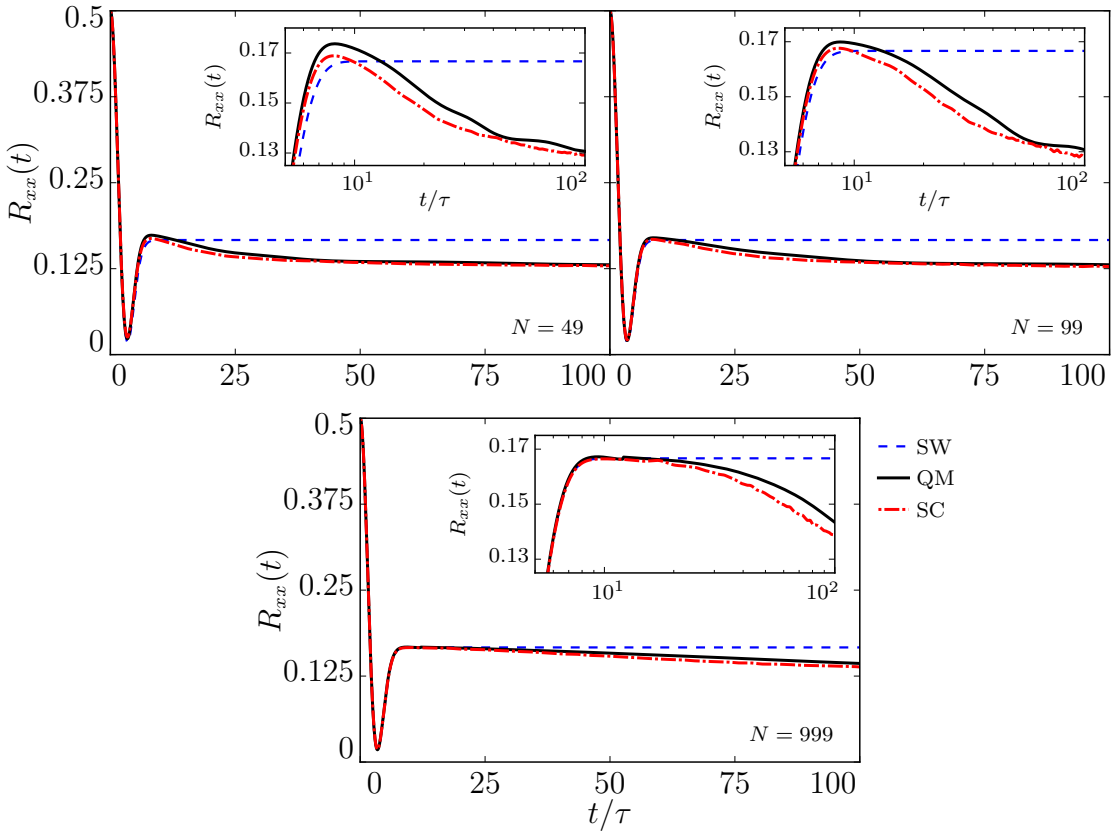

Figure 3.10: Comparison of the converged quantum mechanical (QM) results for model 1 for varying values of N (as shown) with the results of the semiclassical theory of Schulten and Wolynes (SW),[60] and the semiclassical theory of Manolopoulos and Hore (SC).[61] The insets show the long-time decay of these correlation functions on a semi-log plot ($R_{xx}(t)$ verus $\log t$) in order to emphasise the long-time behaviour of the three correlation functions.

for a large number of nuclear spins, each individual bath spin does not evolve substantially on the timescale of the electron spin dynamics (determined by the strength of the total hyperfine field). As N_0 decreases, this assumption becomes less valid. The total hyperfine field becomes dominated by a few strongly coupled bath spins. While there may be a large total number of spins, the strongly coupled spins will evolve on a rapid timescale (comparable to the electron spin dynamics).

The SC theory agrees well with QM for all values of N_0; however, as was observed for model 1, it significantly overestimates the rate of decay of the correlation function due to the rearrangement of the bath. This is most evident in the $N_0 = 36$ result.

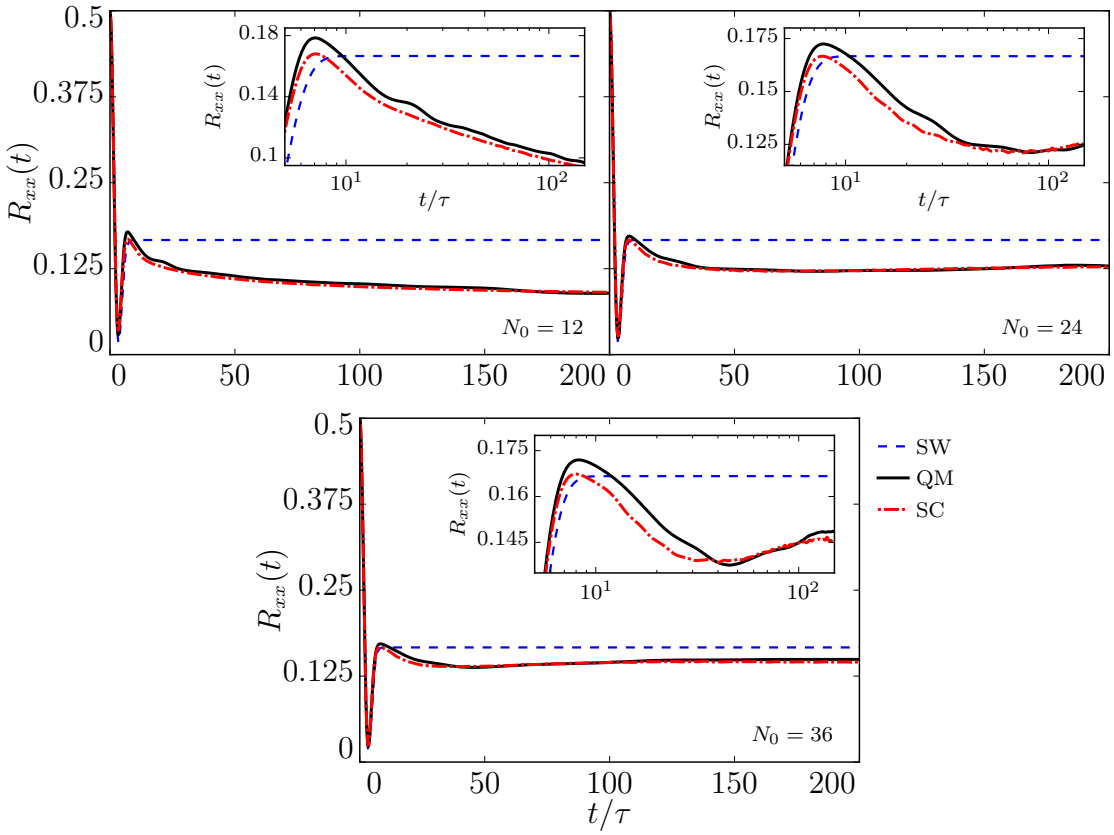

Figure 3.11: Comparison of the converged quantum mechanical (QM) results for model 2 with the results of the semiclassical theory of Schulten and Wolynes (SW), and the improved semiclassical theory of Manolopoulos and Hore (SC). The insets show the long-time decay of these correlation functions on a semi-log plot ($R_{xx}(t)$ versus $\log t$) to emphasise the long-time behaviour of the three correlation functions.

Following the initial short time dynamics, the spin correlation function decays towards a local minimum that is observed at $t \sim 30\tau$. Quantum mechanically this minimum is observed at $t \sim 45\tau$. As N_0 decreases, this minimum is observed at longer times. Quantum mechanically, it is observed at $t \sim 90\tau$ for $N_0 = 24$ and is not seen over the timescale considered for $N_0 = 12$. The differences in the decay of the correlation functions can be understood by considering the different hyperfine coupling constant distributions present for each problem. For $N_0 = 36$, the largest hyperfine coupling constant is only ~ 4 times larger than the smallest and each spin will contribute to the decoherence of the central spin over similar timescales. Once these spins have relaxed, they will no longer contribute to the decoherence and the spin correlation tensor will begin to plateau. For $N_0 = 12$, the largest hyperfine

is ~ 72 times larger than the smallest, resulting in a considerably wider range of timescales over which individual bath spins contribute to the decoherence of the central spin. For both cases the total hyperfine field is the same and the initial spin dynamics occurs on the same timescale. As a consequence, the wider range of timescales for the dynamics in the bath for the $N_0 = 12$ case leads to a considerably longer lived decay.

Additionally, for $N_0 = 12$ the quantum mechanical correlation function shows a significantly higher peak at $t \sim 10\tau$ and a pronounced shoulder at $t \sim 20\tau$. This is not observed semiclassically, and is likely caused by quantum mechanical coherence effects. These coherences are expected to be quenched for system containing large numbers of spins, as is the case for $N_0 = 24$ and 36. However, for $N_0 = 12$, a small set of spins with larger hyperfine coupling constants dominate this short time dynamics. The other bath spins do not evolve over this timescale, and so while there are a large number of total spins, only a small number contribute to the dynamics over this timescale. As a consequence, these quantum mechanical coherence effects are not fully quenched at short times.

3.6.4 Summary

In this section, the moment-fitting method has been shown to be able to accurately compute the quantum dynamics of a central spin interacting with a large bath of spins. Here, it was shown that this new approach provides an efficient scheme for computing the exact central spin dynamics of system containing up to 1000 spins. Following this, results obtained using the moment-fitting method were used to test the accuracy of two semiclassical methods (Schulten-Wolynes theory and the improved semiclassical method) for large spin systems. Neither Schulten-Wolynes theory nor the improved semiclassical theory were able to accurately describe the long-time decay of the spin correlation tensor due to the relaxation of the bath spins. Schulten-Wolynes theory does not capture this decay at all, while the improved semiclassical theory predicts too rapid a decay, even for a system containing $N = 999$

spins. In view of this, it would be interesting to apply the moment-fitting method to a variety of problems that have previously only been studied semiclassically. In the next section, the moment-fitting method is applied to one such problem, the recombination of a carotenoid-porphyrin-fullerene triad radical pair.

3.7 Application: The CPF Radical Pair

As mentioned in Chapter 2, in 2008 Maeda *et al.* provided the first experimental evidence that an Earth strength magnetic field could influence the outcome of the recombination reaction of a radical pair.[9] The proof-of-principle magnetoreceptor molecule considered in these experiments was a carotenoid-porphyrin-fullerene (CPF) triad composed of a porphyrin linked to both a fullerene electron acceptor and a carotenoid electron donor.[139] Exposure to green light induces a series of electron transfers within the triad, initially from the porphyrin to the fullerene and then from the carotenoid to the porphyrin.[139] The final spin correlated radical pair, $C^{\bullet+}PF^{\bullet-}$ is formed predominately in a singlet state.[140] When in a singlet state the radical pair is free to either undergo a reverse electron transfer back to the ground state with rate k_S, or coherently interconvert to a triplet radical pair state that can then undergo recombination to an excited triplet state with rate k_T.[9,139] The reaction scheme and structure of this triad are shown in figure 3.12.

The coherent interconversion between singlet and triplet states is sensitive to the application of magnetic fields. For the $C^{\bullet+}PF^{\bullet-}$ radical pair, the application of a weak field (39 μT) hase been shown to give rise to detectable differences in the time-dependent survival probability of the radical pair.[9] These differences manifested themselves as biphasic behaviour in the time-dependent difference in radical pair survival probabilities in the presence and absence of a field, $\Delta P(B,t) = \mathbf{1}(B,t) - \mathbf{1}(0,t)$. For stronger fields, the magnetic field effects were observed to depend on the orientation of the applied field, demonstrating that the $C^{\bullet+}PF^{\bullet-}$ radical could in principle act as a magnetic compass.[9] More recent experiments have shown that these orientation-dependent magnetic field effects are present at weaker

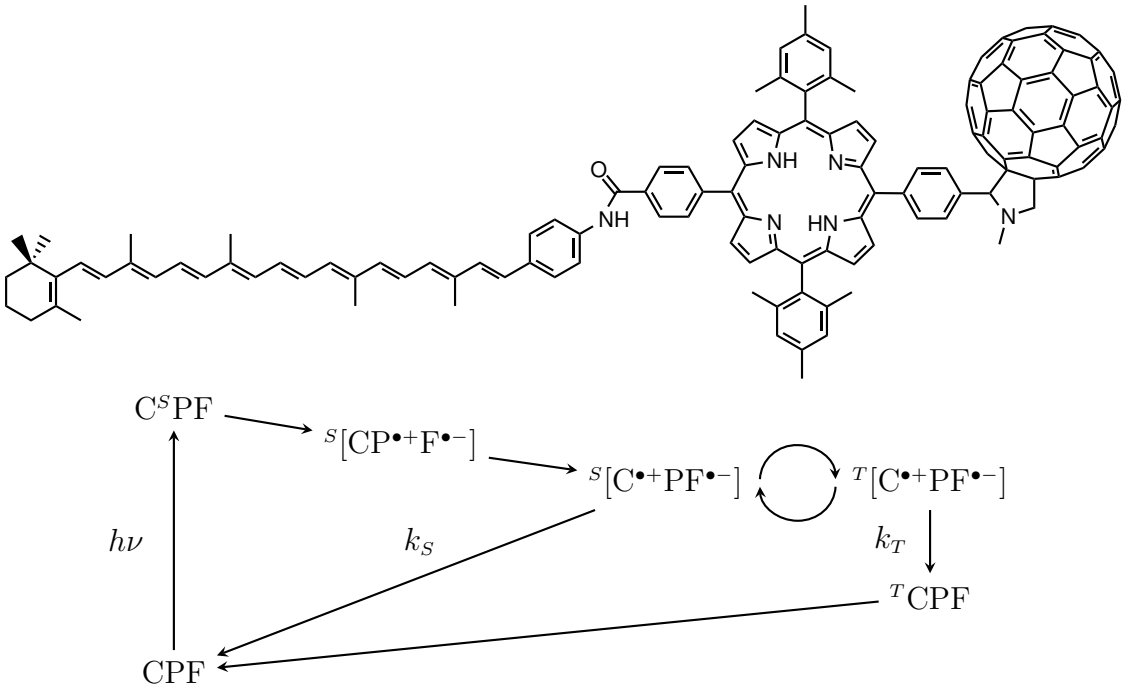

Figure 3.12: Structure (top) and reaction scheme (bottom) of the CPF triad. After photoexcitation by green light, a series of intramolecular electron transfers leads to the formation of the $C^{\bullet+}PF^{\bullet-}$ radical pair, predominantely in a singlet state. The radical pair is free to interconvert between singlet and triplet states due to the magnetic interactions present in the system, in particular the 45 hydrogens present on the carotenoid. The radical pair states can then undergo a spin selective recombination reaction, recombining with rate k_S from the singlet state to form the ground state and rate k_T from the triplet state to form an excited triplet state.[9]

fields (100 μT) thus providing evidence that, in principle, such a magnetic compass could be sensitive to the Earth's magnetic field.[141] Due to the possibility that radical pairs may be responsible for avian magnetoreception, there has been interest in understanding what features of this radical pair give rise to the high magnetic sensitivity of this radical pair.[48,62,140] However, the large number of nuclear spins present in this molecule again make full quantum mechanical calculations impractical. Previous theoretical treatments of this system have relied upon reduced dimensional simulations containing very few spins,[48,140] or semiclassical approximations of the spin dynamics.[62,142]

Semiclassical simulations have previously been used to study the magnetic field effects arising in the $C^{\bullet+}PF^{\bullet-}$ radical pair.[62,142] For Earth-strength magnetic fields,

the semiclassical theory was able to fit the time-dependent magnetic field effects ($\Delta P(B,t)$) observed in the $C^{\bullet+}PF^{\bullet-}$ radical.[62] At stronger fields, the semiclassical theory provides a qualitative description of the dynamics.[142] In view of the results obtained in the previous section, the accuracy of these semiclassical approximations will be explored here. In the following discussion, $\Delta P(B,t)$ will be computed both semiclassically and quantum mechanically (using the moment-fitting method) for the $C^{\bullet+}PF^{\bullet-}$ radical pair at a range of applied magnetic fields.

3.7.1 Model Parameters

The key difficulty in obtaining quantum mechanical results for this radical pair is the large number of magnetic nuclei in this molecule. The carotenoid contains 45 hydrogen nuclei, while the porphyrin linker contains 4 nitrogens and a number of hydrogens. If the natural $\sim 1\%$ abundance of ^{13}C is ignored, then these are the only magnetic nuclei present. Following the approach taken in references [62] and [142], all hyperfine coupling constants between the electron spins and the magnetic nuclei on the porphyrin linker will be ignored. On doing so, the resultant radical pair model consists of a carotenoid radical where the electron spin interacts with 45 hyperfine-coupled spin-$\frac{1}{2}$s and a fullerene radical with no nuclear spins.

k	$a_{1k}\hbar/\lvert\gamma_e\rvert$(mT)	k	$a_{1k}\hbar/\lvert\gamma_e\rvert$(mT)	k	$a_{1k}\hbar/\lvert\gamma_e\rvert$(mT)	k	$a_{1k}\hbar/\lvert\gamma_e\rvert$(mT)	k	$a_{1k}\hbar/\lvert\gamma_e\rvert$(mT)
1	0.048790	10	-0.021817	19	0.329013	28	0.304986	37	0.018443
2	0.046328	11	-0.140593	20	0.329013	29	0.304986	38	0.001563
3	-0.115098	12	-0.087963	21	0.329013	30	0.304986	39	-0.017735
4	-0.111317	13	-0.071456	22	0.216954	31	0.173690	40	0.014287
5	-0.361254	14	0.050581	23	0.216954	32	0.579152	41	-0.028314
6	0.130081	15	-0.275215	24	0.216954	33	0.057321	42	0.003183
7	0.094903	16	0.056448	25	0.170627	34	0.006161	43	0.238826
8	-0.316911	17	0.111917	26	0.170627	35	-0.005099	44	0.238826
9	0.094676	18	-0.385563	27	0.170627	36	-0.003271	45	0.238826

Table 3.3: The isotropic hyperfine coupling constants of the magnetic nuclei in the carotenoid radical cation. These values are based on the values in reference [62] which were obtained using density functional theory with the B3LYP functional and EPR-II basis set. The hyperfine coupling constants for the methyl group hydrogens have been averaged to account for the rapid internal rotation of these groups.

The hyperfine coupling constants used below are based on those provided in reference

[62] for the carotenoid cation. However, the hyperfine coupling constant for each hydrogen on the methyl groups of the carotenoid have been averaged. On the timescale of the electron spin dynamics, these methyl groups are freely rotating and the electron spin will experience an averaged hyperfine coupling constant. The resultant isotropic hyperfine coupling constants are given in table 3.3. Following reference [62], it is assumed that exchange and dipolar coupling can be neglected, and that the singlet and triplet states recombine with rates $k_S = 1.8 \times 10^7$ s^{-1} and $k_T = 7.1 \times 10^4$ s^{-1}, respectively.

3.7.2 Moment Fitting Method for Radical Pairs

The moment-fitting method for the central spin problem treats the dynamics of the central spin by considering a series of simpler Hamiltonians that approximate the influence of the bath spins. Importantly, no approximations are made regarding operators acting on the central spin Hilbert space within this method. In principle, an arbitrary system can be considered instead of the central spin. The moment-fitting method can be trivially generalised to radical pair recombination reactions described by the Hamiltonian,

$$\hat{H} = \sum_{i=1}^{2} \left(\boldsymbol{\omega}_i \cdot \hat{\boldsymbol{S}}_i + \sum_{k=1}^{N_i} a_{ik} \hat{\boldsymbol{S}}_i \cdot \hat{\boldsymbol{I}}_{ik} \right) + \hat{\boldsymbol{S}}_1 \cdot \mathbf{M} \cdot \hat{\boldsymbol{S}}_2. \tag{3.53}$$

Once again, a series of approximate Hamiltonians are considered but are now given by

$$\hat{H}_{M_1 M_2} = \sum_{i=1}^{2} \left(\boldsymbol{\omega}_i \cdot \hat{\boldsymbol{S}}_i + \sum_{j=1}^{M_i} \alpha_{ij} \sum_{k=1}^{N_{ij}} \hat{\boldsymbol{S}}_i \cdot \hat{\boldsymbol{I}}_{ijk} \right) + \hat{\boldsymbol{S}}_1 \cdot \mathbf{M} \cdot \hat{\boldsymbol{S}}_2 \tag{3.54}$$

where the two sets $\{\{\alpha_{1j}\}, \{N_{1j}\}\}$ and $\{\{\alpha_{2j}\}, \{N_{2j}\}\}$ are each independently selected according to the procedure described in Section 3.5. The Haberkorn recombination operator, acting only on the electron spin subspace, does not introduce any further complications to this process. For the CPF radical pair, there are no nuclear spins in one of the radicals and so it is only necessary to perform the moment-fitting procedure for the carotenoid radical pair.

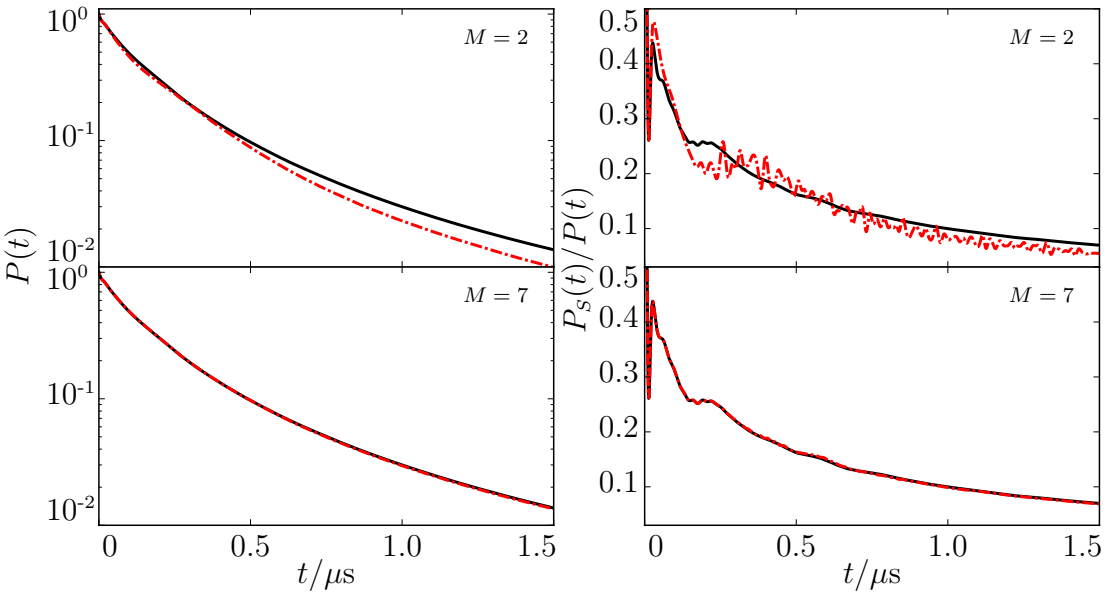

Figure 3.13: Convergence (with M) of the radical pair survival probability (left) and singlet fraction (right) for the $C^{\bullet+}PF^{\bullet-}$radical pair in the absence of an external magnetic field. The solid black curve in each panel shows the fully converged result obtained with $M = 9$, and the dashed red curve shows the value obtained for the specified value of M.

3.7.3 Convergence with M

In order to demonstrate the convergence of the electron spin dynamics of this radical pair with M, the time-dependent radical pair survival probability ($P(t) = P_S(t) + P_T(t)$) and singlet radical pair fraction ($P_S(t)/P(t)$), obtained in the absence of a magnetic field, are shown in figure 3.13. For $M = 2$, the total survival probability is reasonably well captured, however it deviates from the converged result, obtained with $M = 9$, at long times. In contrast, significant errors are observed in the singlet fraction, indicating that with $M = 2$ this method is unable to capture the interconversion between singlet and triplet states correctly. These results significantly overestimate the peak in the singlet fraction observed at short times, and exhibit considerable oscillations at longer times. As M increases, these deviations disappear and for $M = 7$ the results have converged onto the results obtained for $M = 9$ over all times considered here.

The convergence, with M, of the time-dependent survival probability and singlet fraction of the $C^{\bullet+}PF^{\bullet-}$ radical pair is shown in figure 3.14 for a 1.6 mT applied

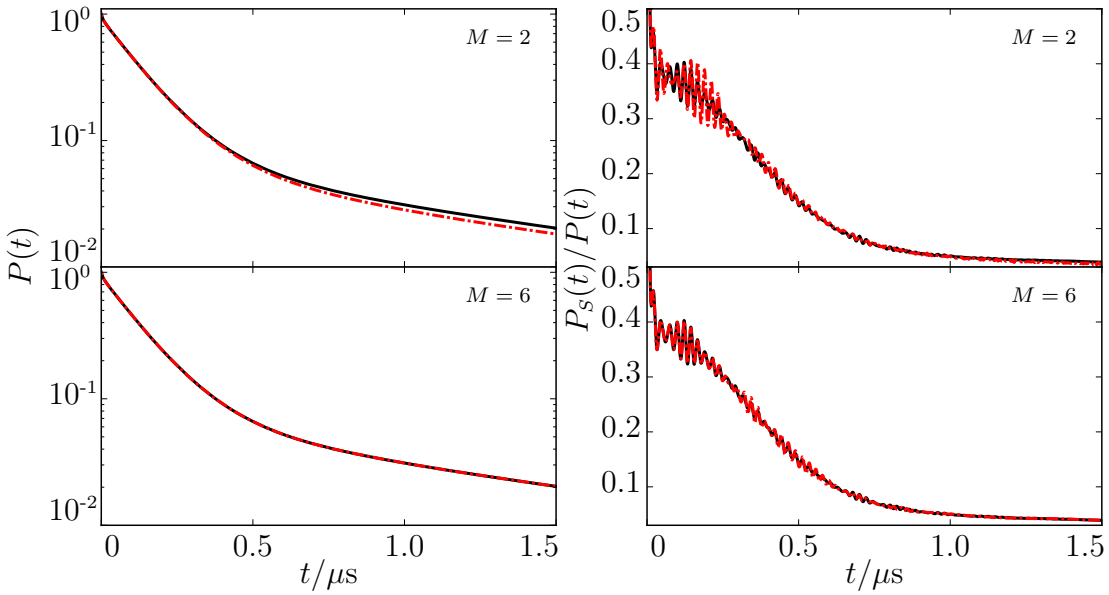

Figure 3.14: Convergence (with M) of the radical pair survival probability (left) and singlet fraction (right) for the $C^{\bullet+}PF^{\bullet-}$radical pair in a 1.6 mT external magnetic field. The solid black curve in each panel shows the fully converged result obtained with $M = 7$, while the dashed red curve shows the value obtained for the specified value of M.

magnetic field. In this case, more rapid convergence with M is observed than that for no applied magnetic field. For $M = 2$, the total survival probability is well converged up to $t \approx 0.5$ μs following which a small deviation from the converged $M = 7$ results is observed. In contrast, the singlet fraction is less well captured. While the $M = 2$ result captures the decay of the singlet fraction correctly, it overestimates the amplitude of the high frequency oscillations arising due to the Zeeman interaction with the applied magnetic field. For $M = 6$, both quantities are converged to match the final results obtained with $M = 7$.

3.7.4 Semiclassical Dynamics

The magnetic field effect curves ($\Delta P(B, t)$) obtained for the $C^{\bullet+}PF^{\bullet-}$ radical pair using Schulten-Wolynes theory (SW), the improved semiclassical theory (SC) of Lewis *et al.*,[62] and the moment-fitting approach (QM) are shown in figure 3.15. The SW theory fails to capture these magnetic field effects for all magnetic field considered, predicting qualitatively incorrect behaviour at all times. At short times, the SC theory describes the magnetic field effects well, however, at longer times

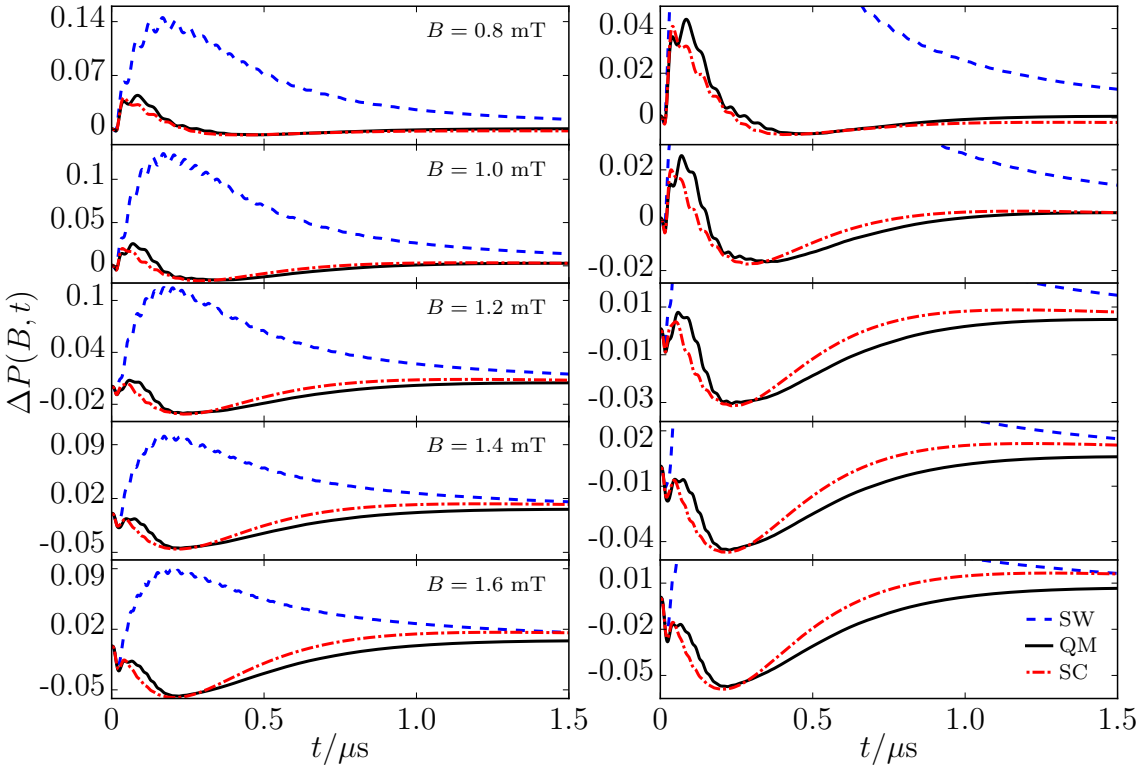

Figure 3.15: Comparison of the magnetic field effect on the radical pair survival probability ($\Delta P(B,t)$) for the $C^{\bullet+}PF^{\bullet-}$radical pair obtained using the semiclassical theory of Schulten and Wolynes (SW), Lewis *et al.* (SC), and quantum dynamics (QM) for the $C^{\bullet+}PF^{\bullet-}$radical pair at different strengths of an applied magnetic field. The panels on the right present the same data, however, using a smaller scale in order to focus on the difference between the SC and QM results.

larger deviations are observed. The SC theory predicts a considerably more rapid and larger increase in the field effect after ~ 0.2 μs for $B \geq 1.2$ mT than in the exact QM case. While this deviation only corresponds to an absolute error of ~ 0.01, it is worth noting that on this timescale a significant portion of radical pairs will have recombined. Past $t = 1.0$ μs the QM simulations predict a total radical pair survival probability of $\lesssim 0.02$. As the values of $P(B,t)$ and $P(0,t)$ are comparable to the error in $\Delta P(B,t)$, this constitutes a large relative error.

In order to explore the origin of this deviation, the total survival probabilities of the $C^{\bullet+}PF^{\bullet-}$ radical obtained using the quantum mechanical and two semiclassical methods are shown in figure 3.16 for a range of applied magnetic fields, $B = 0.0$, 0.8, 1.2, and 1.6 mT. For $B = 0.0$ mT, SW theory deviates significantly from the QM

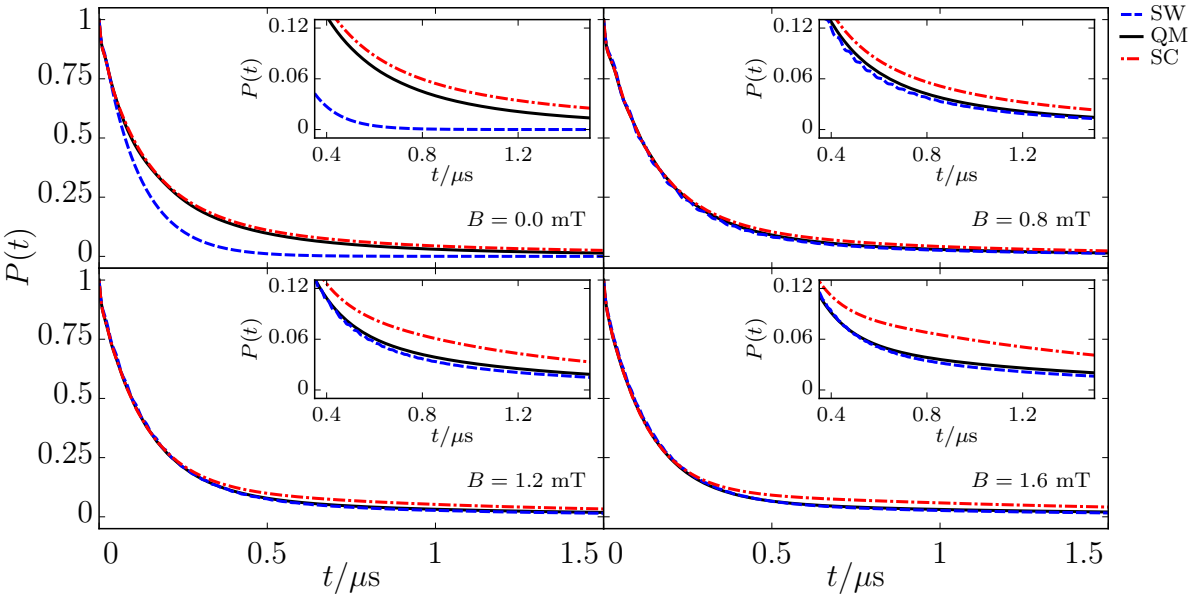

Figure 3.16: Comparison of the time-dependent radical pair survival probability obtained using the semiclassical theory of Schulten and Wolynes (SW), Lewis *et al.* (SC), and quantum dynamics (QM) for the $C^{\bullet+}PF^{\bullet-}$radical pair at different strengths of an applied magnetic field.

result, predicting much too rapid a decay of the radical pair states. As the magnetic field increases SW theory becomes considerably more accurate, with only small deviations observed at long times. These results demonstrate that the failure of SW theory in capturing the magnetic field effect in the radical pair survival probability, as shown in figure 3.15, is entirely due to its failure to describe the zero field results. In comparison, the SC theory does not suffer from such a dramatic failure, instead it systematically overestimates the radical pair survival probability at long time. This overestimation becomes more significant as the magnetic field strength is increased, as illustrated in the insets of this figure. For all fields presented here, except $B = 0.0$ mT, the SC method performs worse than SW theory. Given the results observed here, the relatively good performance of the SC theory for $\Delta P(B, t)$, particularly for weaker magnetic fields, can in part be attributed to a cancellation of errors. Each of the singlet survival probabilities obtained semiclassically is significantly larger than the corresponding quantum mechanical result but these overestimations partly cancel when calculating the magnetic field effect.

As an aid for determining the causes of the deviations discussed above, the fraction of radical pairs found in a singlet state, as a function of time and obtained using the three methods, are shown in figure 3.17. For all magnetic fields considered the SC theory accurately captures the short-time oscillations in the singlet fraction, and for small fields it provides a reasonable estimate of the long time behaviour. However, as the magnetic field increases it significantly overestimates the decay of the singlet fraction at longer times. It therefore predicts that, at longer times, a significantly larger fraction of the radical pairs are found in the slowly decaying triplet state than is observed quantum mechanically and, as such, the total radical pair population decays more slowly.

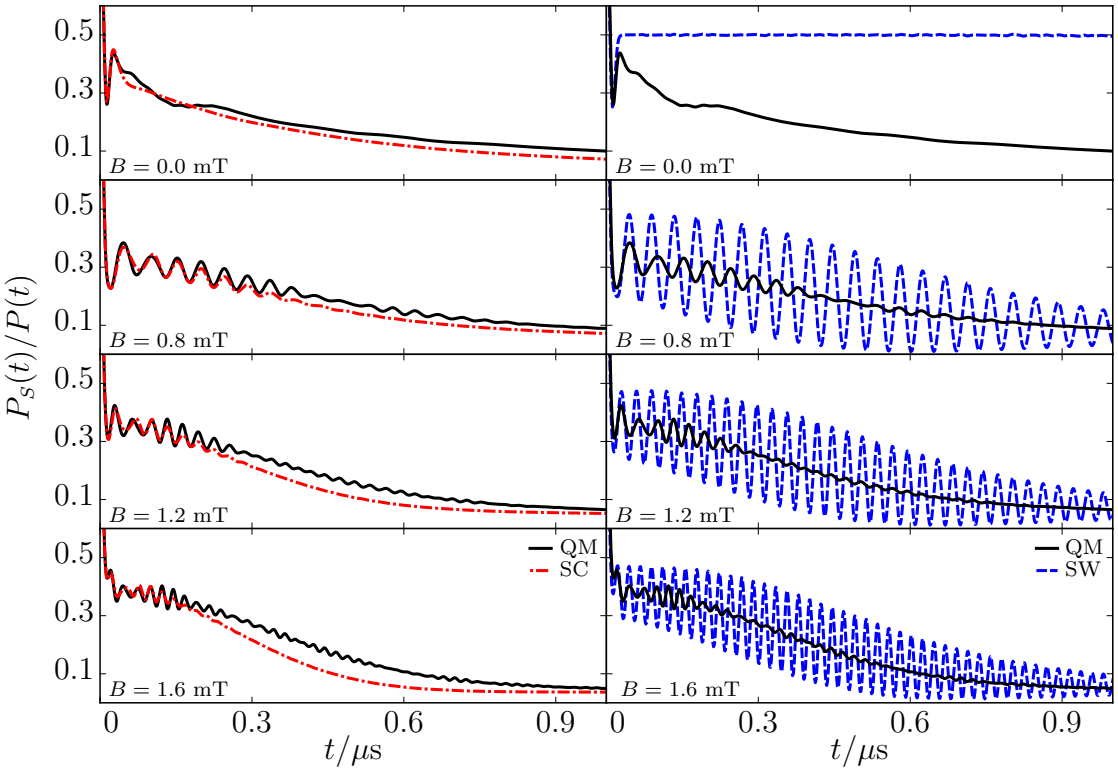

Figure 3.17: Comparison of the time-dependent singlet fraction obtained using the semiclassical theory of Schulten and Wolynes (SW), Lewis *et al.* (SC), and quantum dynamics (QM) for the $C^{\bullet+}PF^{\bullet-}$radical pair at different strengths of an applied magnetic field.

In the absence of an applied magnetic field, SW theory significantly overestimates the singlet fraction for times $t > 0.05$ μs, predicting a value of 0.5. As the singlet

state radical pairs are considerably shorter lived than the triplet state radical pairs($k_S \gg k_T$), this leads to a significant overestimation of the decay rate of the radical pair. When a magnetic field is applied, SW theory predicts significant oscillations in the singlet fraction. These oscillations occur with a period of $2\pi/|B\gamma_e|$ and arise from the Zeeman interaction term in the Hamiltonian.[62] In both the SC and QM simulations these oscillations are observed at short time. They are rapidly damped at longer times in the QM and SC simulations due to interactions with the nuclear spin bath. As SW theory treats the bath as static, the method is unable to capture the damping of the oscillations and so they are observed out to long times. Despite these osillations, however, SW theory correctly captures the decay of the singlet fraction. The SW theory results are seen to oscillate around the quantum mechanical results. While at any given time SW theory may significantly over or underestimate the singlet fraction on average it performs well.

The improved convergence (with M) of the moment-fitting method in the presence of an applied magnetic field can be understood by considering the results presented in figure 3.17. When no field is applied, the failure of SW theory suggest that the fluctuations of the bath spins play a significant role in the interconversion between singlet and triplet states. However, when a moderate strength magnetic field is applied, the key features of this interconversion are captured within the SW theory, which depends on only the second moment of the hyperfine distribution. In this case, the dynamics of the bath primarily influences the central spin by damping the Zeeman oscillations, it does not significantly influence the decay in the singlet population. As a result, for small M the interconversion is captured well; however, significantly larger oscillations are observed as this damping effect is not accurately captured.

The results obtained in figure 3.17 suggest that in the presence of a moderate strength magnetic field, accurately describing the dynamics of the bath is less important than a consistent description of the electron spin dynamics. As discussed

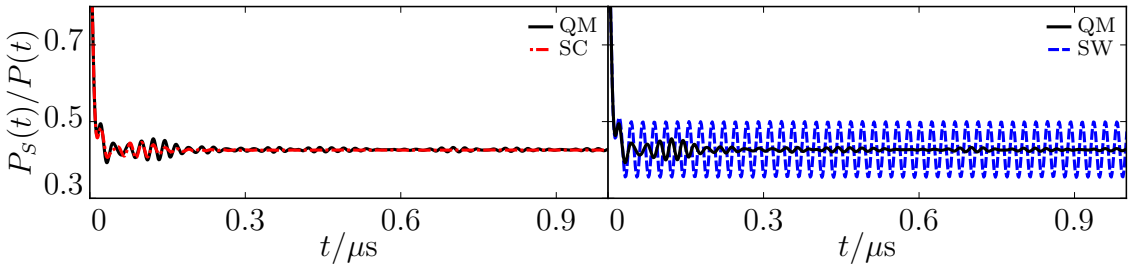

Figure 3.18: Comparison of the time-dependent singlet fraction obtained using the semiclassical theory of Schulten and Wolynes (SW), Lewis *et al.* (SC), and quantum dynamics (QM) for the $C^{\bullet+}PF^{\bullet-}$radical pair undergoing no recombination reaction and in an applied magnetic field of $B = 1.6$ mT.

before, the improved semiclassical theory for asymmetric recombination introduces some ad hoc assumptions. As an aid in probing whether it is this incorrect treatment of the recombination process that leads to inaccuracies in the semiclassical method, the singlet fraction obtained using the three different methods in the absence of any recombination is presented figure 3.18. In the absence of recombination the improved semiclassical theory reduces to the one-spin variable semiclassical theory for this system, and as observed here performs exceptionally well. It is able to accurately capture the long time limit of the singlet fraction and provides a good description of the spin-spin relaxation process. Here Schulten-Wolynes theory, once again, gives results that oscillate around the quantum results. In the absence of any asymmetric recombination, the improved semiclassical theory is accurate, suggesting that it is indeed the treatment of asymmetric recombination that leads to the inaccuracies noted above.

3.8 Conclusion and Future Work

This chapter began with an introduction to the central spin model, a model which has been widely studied in the condensed matter physics literature because of its relevance to the decoherence of electron spins confined in quantum dots. This model is closely related to the radical pair model of interest in the previous section. Following this introduction, two special cases of the central spin model for which the exact dynamics can be obtained, without running into the exponential scaling

problem, were discussed: the case of homogeneous coupling and the Schulten-Wolynes theory limit. Motivated by these two special cases, a new method, the moment-fitting method, was introduced that treats the dynamics of large central spin problems by considering a series of simpler problems, designed to capture the influence of the bath spins on the central spin. As the complexity of these simpler Hamiltonians was increased, this method was shown to converge onto the exact dynamics for two model central spin problems by comparing to results that had previously been obtained using the t-DMRG and ABA methods.

The moment-fitting method was then used to provide a series of benchmark results against which approximate methods could be tested. Comparisons of the quantum dynamics against two semiclassical methods (the Schulten-Wolynes theory[60] and the improved semiclassical theory of Hore and Manolopoulos[61]) demonstrated that, even for a large nuclear spin bath containing $N = 999$ nuclear spins, neither of the semiclassical methods could quantitatively describe the dynamics of these central spin systems. Schulten-Wolynes theory does not capture long time decay of correlations of the central spin arising from the rearrangement of the bath, while the improved semiclassical theory overestimates the rate of this decay.

Motivated by this difference between semiclassical and quantum results, the moment-fitting method was applied to the radical pair recombination dynamics of a model magnetoreceptor that had previously only been studied (in its full dimensionality) using semiclassical techniques. While the generalisation of the improved semiclassical method to allow for asymmetric recombination by Lewis *et al.*[62] was able to qualitatively capture the magnetic field effects in the radical pair survival probability observed for this radical pair, it was found to significantly and systematically overestimate long time magnetic field effects. Additionally, the semiclassical theory also consistently overestimated the proportion of radical pairs that survive at long times. These deviations of the semiclassical theory disappear in the case of symmetric recombination, suggesting that this issue arises from an

incorrect treatment of the asymmetric recombination process. For this problem with asymmetric recombination, Schulten-Wolynes theory provided a significantly better estimate of the radical pair survival probability for non-zero applied magnetic fields but it completely failed in the zero field case. When taken in combination with the results presented in the previous chapter, these results suggest that until more generally applicable methods have been developed, caution should be used when applying semiclassical methods to study the dynamics of radical pairs that involve electron spin coupling and asymmetric recombination. The results presented in this chapter may serve as useful benchmarks against which new semiclassical methods may be validated.

Finally, while the results in this chapter show that the moment-fitting method is able to provide numerically exact results for central spin problems and for the recombination dynamics of the $C^{\bullet+}PF^{\bullet-}$ radical pair, it is still yet to be seen whether it can provide accurate results for more general radical pair recombination reactions. Based on the results presented in this chapter, it appears likely that this method may be able to successfully describe the recombination dynamics of radical pairs where one radical has a large number of hyperfine coupled nuclear spins and the other only a few. For radical pairs with considerable numbers of nuclear spins in each radical, it is necessary to perform the moment-fitting procedure for each radical independently. Whether it is possible to converge the dynamics of the resultant approximate Hamiltonians is yet to be seen. Additionally, at present, this scheme can only be applied to systems with isotropic hyperfine distributions. In the case of a distribution of anisotropic hyperfine coupling tensors, it is not as clear which properties of the hyperfine distribution are most important for describing the dynamics, and whether an analogous method could be developed in such a case remains to be seen.

4

Open System Quantum Dynamics

Contents

In the previous two chapters, the dynamics of radical pair recombination reactions was treated using the Haberkorn master equation (equation 2.70). Over the past 40 years, this master equation has been successfully applied to explain magnetic field effects in radical pairs, and has become the standard approach for treating such systems.[15] In recent years, however, a number of alternative master equations have been proposed,[46–49] leading to debate in the spin chemistry literature as to which of them correctly describes the radical pair mechanism.[33,47–52]

In this chapter, this question is explored for an important subset of radical pair recombination reactions, namely those involving electron transfers within the radical ion pairs. The discussion begins with an overview of the basic theory of electron transfer reactions, after which the spin-boson model, a simple model that is commonly used to describe electron transfer reactions in condensed phase environments, will be discussed. Following this the hierarchical equations of motion (HEOM) method, a numerically exact approach for simulating arbitrary quantum mechanical systems coupled to harmonic baths, will be discussed and a derivation provided. This chapter concludes with an application of the HEOM to a model for a radical ion pair recombination reaction that is closely related to the spin-boson model, with the aim of exploring the validity of a recently proposed series of master equations for treating these reactions.[33]

4.1 Electron Transfer Dynamics

Electron transfer processes play a significant role in the recombination reactions of many radical ion pairs.[14,15,143] As an example, two of the model radical pairs considered thus far in this thesis, $FAD^{\bullet-}TrpH^{\bullet+}$ and $C^{\bullet+}PF^{\bullet-}$ undergo spin selective recombination reactions that involve electron transfers.[82,139] Within the Haberkorn master equation-based treatment of these reactions (discussed in Chapter 2), the details of the electron transfers are hidden. It is assumed that the influence of the electron transfer process on the spin dynamics can be accounted for by the

Haberkorn recombination operator. That is, the electron transfer process only introduces exponential decays of the singlet and triplet states at rates k_S and k_T and of the singlet-triplet coherences at a rate $(k_S + k_T)/2$. Whether this is valid will be explored in what follows and this will be carried out by explicitly treating both the spin dynamics and the dynamics of the electron transfer process for a model radical pair. Before this, a general description of electron transfer reactions will be presented.

In the following discussion, a system containing two molecules D, an electron donor, and A, an electron acceptor, embedded in a polarisable environment will be considered. An electron is free to transfer (reversibly) from the donor to the acceptor, and in doing so the system transitions from the reactant state, DA, to the product state, D^+A^-. This reaction leads to a significant rearrangement of the charge in the system and, as a consequence, it will be associated with a significant reorganisation of the surrounding environment.[91] The transition between distinct electronic states (electronic dynamics) is coupled to a motion of the environment (nuclear dynamics). Depending on the timescales involved in the electron transfer and nuclear dynamics processes, these can significantly influence each other, and in such a case it is necessary to treat the coupled dynamics of both electronic and nuclear degrees of freedom.

4.1.1 The Adiabatic Representation

The non-relativistic Hamiltonian for a general molecular system including electronic, $\boldsymbol{r}$, and nuclear, $\boldsymbol{q}$, degrees of freedom is[144–146]

$$\hat{H}(\boldsymbol{r}, \boldsymbol{q}) = \hat{T}_N(\boldsymbol{q}) + \hat{H}_e(\boldsymbol{r}; \boldsymbol{q}). \tag{4.1}$$

Here $\hat{T}_N$ is the kinetic energy operator associated with the N nuclear degrees of freedom, given by

$$\hat{T}_N = -\sum_{k=1}^{N} \frac{\hbar^2}{2M_k} \frac{\partial^2}{\partial q_k^2}, \tag{4.2}$$

and $\hat{H}_e(\boldsymbol{r};\boldsymbol{q})$ is the electronic Hamiltonian at a particular set of nuclear coordinates. This may be written in terms of the electronic kinetic energy operator and a potential energy operator, $\hat{V}_c(\boldsymbol{r};\boldsymbol{q})$, accounting for all interactions between the electrons and nuclei as

$$\hat{H}_e(\boldsymbol{r};\boldsymbol{q}) = \hat{T}_e(\boldsymbol{r}) + \hat{V}_c(\boldsymbol{r};\boldsymbol{q}). \tag{4.3}$$

The orthonormal eigenstates of the electronic Hamiltonian, $\psi_i(\boldsymbol{q};\boldsymbol{r})$, which satisfy

$$\hat{H}_e(\boldsymbol{r};\boldsymbol{q})\psi_i(\boldsymbol{r};\boldsymbol{q}) = E_i(\boldsymbol{q})\psi_i(\boldsymbol{r};\boldsymbol{q}) \tag{4.4}$$

where $E_i(\boldsymbol{q})$ represents the standard adiabatic potential energy surface, provide a convenient representation for the molecular wavefunction, $\Psi^{(a)}(\boldsymbol{r},\boldsymbol{q},t)$. Expanding the molecular wavefunction at the nuclear coordinate $\boldsymbol{q}$ in terms of products of the stationary electronic basis functions evaluated at $\boldsymbol{q}$ and time-dependent nuclear wavefunction (the Born-Huang expansion) gives[147]

$$\Psi^{(a)}(\boldsymbol{r},\boldsymbol{q},t) = \sum_i \chi_i^{(a)}(\boldsymbol{q},t)\psi_i(\boldsymbol{r};\boldsymbol{q}). \tag{4.5}$$

Here $\chi_i^{(a)}(\boldsymbol{q},t)$ accounts for the nuclear motion associated with the i-th adiabatic electronic state, $|\psi_i(\boldsymbol{q})\rangle$. Inserting this form for the wavefunction into the time-dependent Schrödinger equation, the vector of nuclear wavefunctions, $\boldsymbol{\chi}^{(a)}(\boldsymbol{q},t) = [\chi_1^{(a)}(\boldsymbol{q},t), \chi_2^{(a)}(\boldsymbol{q},t), \dots]^T$, evolves according to the equation[144,148]

$$\frac{\partial}{\partial t}\boldsymbol{\chi}^{(a)}(\boldsymbol{q},t) = -\frac{i}{\hbar}\left[\mathbf{T}^{(a)} + \mathbf{V}^{(a)}\right]\boldsymbol{\chi}^{(a)}(\boldsymbol{q},t). \tag{4.6}$$

In this adiabatic basis, $\mathbf{V}^{(a)}$ is a diagonal matrix of the adiabatic potential energy surface with matrix elements

$$V_{ij}^{(a)} = \delta_{ij}E_i(\boldsymbol{q}), \tag{4.7}$$

and $\mathbf{T}^{(a)}$ is the kinetic energy matrix

$$T_{ij}^{(a)} = \hat{T}_N\delta_{ij} + \langle\psi_i(\boldsymbol{r};\boldsymbol{q})|\hat{T}_N\psi_j(\boldsymbol{r};\boldsymbol{q})\rangle - \sum_{k=1}^{N}\frac{\hbar^2}{2M_k}\langle\psi_i(\boldsymbol{r};\boldsymbol{q})|\frac{\partial}{\partial q_k}\psi_j(\boldsymbol{r};\boldsymbol{q})\rangle\frac{\partial}{\partial q_k}, \tag{4.8}$$

which, in addition to the standard kinetic energy terms that give rise to evolution on the individual adiabatic potential energy surfaces, contains derivative and

second derivative coupling terms that lead to transitions between electron states. Since the adiabatic states are obtained as solutions of the electronic Schrödinger equation, their energies are directly available from standard electronic structure theory calculations.[149]

4.1.2 Nonadiabatic Effects

For a large number of chemical systems, the off-diagonal coupling between the electronic surfaces is small. The mass of an electron is significantly smaller than the mass of a typical nucleus and, as a result, electronic motion is often considerably faster than nuclear motion. As a consequence, it is often reasonable to treat the nuclei as fixed on the timescale of the electron dynamics.[148] This is the adiabatic (Born-Oppenheimer) approximation, which may be derived by treating the nuclear kinetic energy operator as a perturbation to the electronic Hamiltonian.[147,150] In this regime the molecular dynamics is described by evolution of the nuclei on individual, uncoupled adiabatic potential energy surfaces that are obtained by solving the electronic Schrödinger equation for each nuclear coordinate.

When the nuclear kinetic energy operator cannot be treated as a small perturbation, however, coupling between the electronic surfaces becomes important and it is necessary to include nonadiabatic transitions between the electronic states. In such a case the adiabatic representation is somewhat inconvenient.[146] The derivative coupling term significantly complicates the treatment of dynamics. For an example, at a conical intersection the derivative coupling becomes infinite.[151,152] As such, an alternative representation is often considered: the diabatic representation.[144,149]

4.1.3 The Diabatic Representation

In obtaining the adiabatic representation, the electronic states used to expand the molecular wavefunction were functions of the nuclear coordinates. As the nuclear position changed, the adiabatic electronic states changed constantly so as to remain eigenstates of the electronic Hamiltonian.[153] Within the diabatic representation

an alternative electronic basis is considered. Here, the molecular wavefunction at the nuclear coordinate $\boldsymbol{q}$ is expanded in terms of eigenstates of the electronic Hamiltonian obtained at some reference position, $\boldsymbol{q}_0$, as[144,151]

$$\Psi^{(d)}(\boldsymbol{r},\boldsymbol{q},t) = \sum_i \chi_i^{(d)}(\boldsymbol{q},t)\psi_i(\boldsymbol{r};\boldsymbol{q}_0), \tag{4.9}$$

where $\chi_i^{(d)}(\boldsymbol{q},t)$ accounts for the nuclear motion associated with the i-th diabatic electronic state, $|\psi_i(\boldsymbol{q_0})\rangle$. Proceeding as before, the vector of the nuclear wavefunctions, $\boldsymbol{\chi}^{(d)}(\boldsymbol{q},t) = [\chi_1^{(d)}(\boldsymbol{q},t), \chi_2^{(d)}(\boldsymbol{q},t), \dots]^T$, evolves according to the equation[151]

$$\frac{\partial}{\partial t}\boldsymbol{\chi}^{(d)}(\boldsymbol{q},t) = -\frac{i}{\hbar}\left[\mathbf{T}^{(d)} + \mathbf{V}^{(d)}\right]\boldsymbol{\chi}^{(d)}(\boldsymbol{q},t). \tag{4.10}$$

Within this representation the potential energy matrix, $\mathbf{V}^{(d)}$, is no longer diagonal and has matrix elements

$$V_{ij}^{(d)}(\boldsymbol{q}) = \langle\psi_i(\boldsymbol{r};\boldsymbol{q_0})|\,\hat{H}_e(\boldsymbol{r};\boldsymbol{q})\,|\psi_j(\boldsymbol{r};\boldsymbol{q_0})\rangle\,, \tag{4.11}$$

while the kinetic energy matrix, $\mathbf{T}^{(d)}$, is

$$T_{ij}^{(d)} = \delta_{ij}\hat{T}_N. \tag{4.12}$$

In the diabatic basis, the elements of the potential energy matrix are smooth functions of the nuclear coordinates.[154] The diagonal elements of this potential matrix are the diabatic potential energy surfaces. The off-diagonal coupling elements give rise to transitions between diabatic states. By diagonalising the diabatic potential energy matrix, the adiabatic potential energy surfaces can be obtained.[144] The relative magnitude of the off-diagonal diabatic coupling elements determines whether nonadiabatic effects are important. When these coupling elements are considerably larger than the thermal energy, k_BT, the adiabatic states are well separated and nonadiabatic transitions become less important.

For a sufficiently complete set of electronic basis functions, the two representations of the molecular wavefunction (equations 4.5 and 4.9) are equivalent.[146] In practice, given a set of adiabatic states it is not generally possible to construct a set of

diabatic states.[153] It is, therefore, generally easier to construct adiabatic potential energy surfaces and couplings;[149] approximate strategies are typically required when evaluating the equivalent terms in the diabatic basis.[151,153] However, in addition to having better behaved coupling elements, the diabatic representation provides a significant advantage over the adiabatic representation. Individual diabatic states do not change their physical character when the nuclear coordinates are changed.[149,153] That is, individual diabatic states may be constructed for a system such that they have a fixed spin state[155] or specific charge state,[153] independent of the nuclear coordinates. In contrast, since the adiabatic states are the eigenstates of the electronic Hamiltonian at each nuclear position their physical character will generally change as nuclei move. As a result, diabatic states are useful when describing electron transfer reactions as different diabats can be constructed to represent distinct charge transfer states.[153] In the next section, to avoid the issues associated with constructing diabatic potential energy surfaces for a real system, a model electron transfer system is constructed that specifies the diabatic potential energy surfaces and couplings.

4.2 Model Electron Transfer System

The Hamiltonian for a condensed phase direct-electron-transfer reaction between an electron donor, D, and an electron acceptor, A, embedded in a polarisable environment, can be written in the diabatic representation as[3,156]

$$\hat{H} = \hat{H}_0 \left|0\right\rangle \left\langle 0\right| + \hat{H}_1 \left|1\right\rangle \left\langle 1\right| + \hat{\Delta} \left|0\right\rangle \left\langle 1\right| + \hat{\Delta}^\dagger \left|1\right\rangle \left\langle 0\right|, \tag{4.13}$$

where $|0\rangle$ and $|1\rangle$ represent the reactant, DA, and product, D^+A^-, diabatic electronic states, respectively. The nuclear Hamiltonian for each diabat,

$$\hat{H}_i = \sum_{\nu=0}^{N_b} \frac{\hat{p}_\nu^2}{2m_\nu} + V_i(\hat{\boldsymbol{q}}), \tag{4.14}$$

with N_b+1 nuclear degrees of freedom and diabatic potential, $V_i(\hat{\boldsymbol{q}})$, accounts for the interactions between the system and environment when in either the reactant, $|0\rangle$, or product, $|1\rangle$, states. When the electron is on the donor (acceptor) the bath orients

to stabilise the electron on the donor (acceptor),[153] and this stabilisation is what is captured by the diabatic potentials. The transition of the electron is associated with a rearrangement of the bath, which is the dominant reaction coordinate for the electron transfer reaction.[153] The energy associated with this rearrangement of the bath is referred to as the reorganisation energy, Λ, and corresponds to the change in energy associated with altering the configuration of the bath while remaining on the reactant diabat (see figure 4.1).

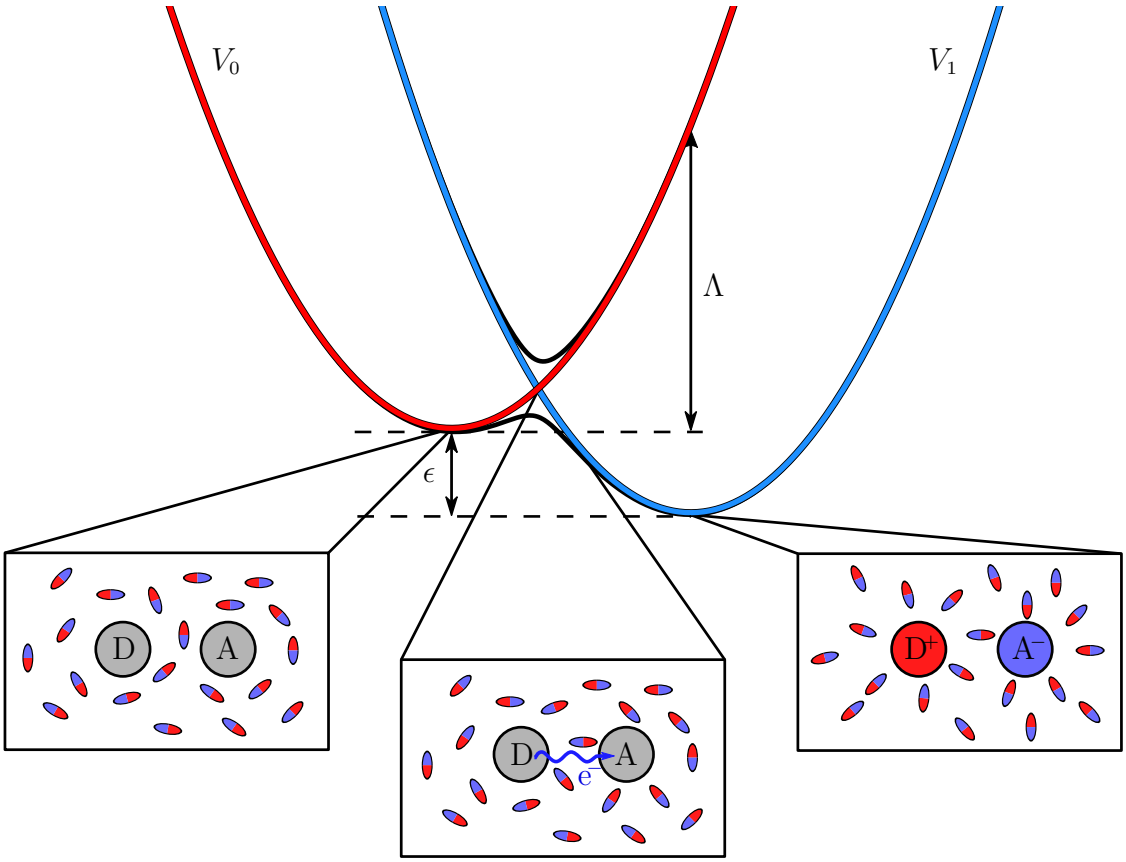

Figure 4.1: An illustration of the electron transfer system described by equation 5.110. When the electron is on the donor molecule D the bath orients itself to stabilise this system, this effect is accounted for by the diabatic potential, V_0. The diabatic potential V_1 accounts for the bath stabilising the charge transfer state D^+A^-. The black curves show the corresponding adiabatic potential energy surfaces. The electron transfer process is associated with a reorientation of the bath degrees of freedom and fluctuations in the bath allow for the transition to occur. The reorganisation energy, Λ, is the energy change in the reactant diabatic potential energy surface when the system configuration is changed from the minimum energy reactant to product configuration. The minima in the two diabatic potential energy surfaces are separated by an energy of ϵ, which is referred to as the bias of the reaction. For $|\epsilon| < \Lambda$ the reaction is in the Marcus normal regime, while $|\epsilon| > \Lambda$ is referred to as the Marcus inverted regime.

In equation 5.110, $\hat{\Delta}$ is the diabatic coupling operator accounting for the coupling between the reactant and product diabatic states. In general, since the electronic Hamiltonian depends on the nuclear coordinates so does the coupling between the diabatic states. In this model, only reactant and product diabats play a role in the reaction; the possibility of any energetically accessible intermediate electronic states facilitating the charge transfer process have been ignored.[91] A schematic of this model is shown in figure 4.1.

In principle, the dynamics of this system can be obtained by solving the time-dependent Schrödinger equation for all electronic and nuclear degrees of freedom. For small gas-phase systems, grid-based quantum mechanical methods (e.g. discrete variable representations) can be employed to solve the problem exactly.[157–159] However, for condensed phase electron transfer reactions with large numbers of nuclear degrees of freedom, the exponential scaling with system size of these grid-based methods precludes their use. Approximate methods are necessary for general diabatic potentials and electronic coupling operators. However, while approximate methods may provide reasonable descriptions for some chemical systems, they are not generally accurate.[149] As the aim here is to explore the validity of master equations developed for treating the spin dynamics of radical ion pairs, such methods are unsuitable. It would be challenging to ascertain whether deviations arise from inaccuracies in the master equation or from the dynamical method chosen for simulating the electron transfer reaction. As such, here, numerically exact simulations are performed on a simplified model for this electron transfer process. In what follows the spin-boson model, the prototypical nonadiabatic system for modelling electron transfer reactions in condensed phase environments,[160,161] is considered.

4.2.1 The Spin Boson Model

The spin-boson model is a commonly employed model for describing a molecule (system) interacting with a thermal environment (bath).[91] Within the context of electron transfer reactions, it provides a useful model for exploring how friction along the reaction coordinate that arises from coupling between this coordinate and other degrees of freedom of the environment, influences the dynamics of the electron transfer.[161] The environment (bath) is treated as a collection of harmonic oscillators that are coupled to the system through interactions that are linear in the bath coordinates.[162] The spin-boson Hamiltonian can be written as

$$\hat{H} = \hat{H}_0 \left|0\right\rangle \left\langle 0\right| + \hat{H}_1 \left|1\right\rangle \left\langle 1\right| + \Delta(\left|0\right\rangle \left\langle 1\right| + \left|1\right\rangle \left\langle 0\right|), \tag{4.15}$$

where $\hat{H}_0$ and $\hat{H}_1$ are the harmonic diabatic Hamiltonians. The coupling, Δ, between the states of the system, here representing the reactant, DA, and product, D^+A^-, diabats, is assumed to be independent of the environment coordinates (the Condon approximation[91]).

In the reaction coordinate form, the electronic degree of freedom for the system is only directly coupled to one bath degree of freedom. This reaction coordinate is itself coupled to the remaining bath degrees of freedom.[161] The diabatic potentials of this model are[161]

$$V_0 = \frac{1}{2}M\Omega^2 \left(\hat{q}_0 + \sqrt{\frac{\Lambda}{2M\Omega^2}}\right)^2 + \sum_{\alpha=1}^{N_b} \frac{1}{2} m_\alpha \omega_\alpha^2 \left(\hat{q}_\alpha - \frac{c_\alpha \hat{q}_0}{m_\alpha \omega_\alpha^2}\right)^2 \tag{4.16}$$

$$V_1 = \frac{1}{2}M\Omega^2 \left(\hat{q}_0 - \sqrt{\frac{\Lambda}{2M\Omega^2}}\right)^2 + \sum_{\alpha=1}^{N_b} \frac{1}{2} m_\alpha \omega_\alpha^2 \left(\hat{q}_\alpha - \frac{c_\alpha \hat{q}_0}{m_\alpha \omega_\alpha^2}\right)^2 - \epsilon, \tag{4.17}$$

where $\hat{q}_0$, M, and Ω are the reaction coordinate position operator, mass, and frequency, respectively. Additionally, $\hat{q}_\alpha$, m_α, and ω_α are the corresponding terms for the α-th bath mode, ϵ is a position-independent energy shift between the two diabats, and Λ is the Marcus-Hush theory reorganisation energy (see figure 4.1). Along the reaction coordinate the two diabatic potentials are shifted harmonic oscillators each with mass M, frequency Ω, and minima displaced by $\pm\sqrt{\frac{\Lambda}{2M\Omega^2}}$

depending on the diabat (+ for $|0\rangle$ and − for $|1\rangle$). This is closely related to the standard model employed in the Marcus-Hush theory treatment of electron transfer.[3,91,156,163–165]

In addition to the reaction coordinate, this model includes a bath of N_b harmonic oscillators that account for the remaining environment degrees of freedom. These oscillators are linearly coupled to the reaction coordinate (the second term in equation 4.16), which allows for transfer of energy between the reaction coordinate and the remainder of the bath. In the limit of an infinite dimensional classical bath, the effect of the bath can be interpreted as friction.[161] The bath modes may significantly influence the dynamics along the reaction coordinate and therefore the dynamics of the electron transfer process. The influence of the bath degrees of freedom on the reaction coordinate is fully accounted for by the associated spectral density,

$$J(\omega) = \frac{\pi}{2} \sum_{\alpha=1}^{N_b} \frac{c_\alpha^2}{m_\alpha \omega_\alpha} \delta(\omega - \omega_\alpha). \tag{4.18}$$

Typically this discrete spectral density is replaced with a continuous function of ω, which corresponds to taking the limit of an infinite bath of harmonic oscillators.[4,5,160] When doing so, it is useful to extend the spectral density to negative values of the frequency such that $J(-\omega) = -J(\omega)$.[91] Below a purely Ohmic spectral density is considered,

$$J(\omega) = \gamma M \omega. \tag{4.19}$$

For the Hamiltonian considered here, this spectral density gives rise to Langevin dynamics along the reaction coordinate with friction γ in the classical limit.[3,4,161] This model allows a variety of different regimes for the bath to be considered, depending on the values of the reaction coordinate frequency and friction coefficient. If $\gamma < 2\Omega$ the motion along the reaction coordinate is underdamped, if $\gamma = 2\Omega$ the motion is critically damped, and finally if $\gamma > 2\Omega$ it is overdamped. For underdamped reactions, in the classical limit, the dynamics along the reaction

coordinate appears ballistic, while in the strongly overdamped case it is diffusive.[161]

The coupling between the reaction coordinate and the bath modes complicates the evaluation of the dynamics of this system. It is beneficial to transform from the reaction coordinate form to the conventional form in which there are no interactions between different bath modes.[161] To do this it is useful to rewrite the spin-boson Hamiltonian in terms of contributions acting only on either the system, $\hat{H}_S$, or bath, $\hat{H}_B$, degrees of freedom, and a system-bath coupling term, $\hat{H}_{SB}$, as

$$\hat{H} = \hat{H}_S + \hat{H}_{SB} + \hat{H}_B. \tag{4.20}$$

For the spin-boson Hamiltonian considered here, the result can be written as

$$\hat{H}_S = \Delta\hat{\sigma}_x + \frac{\epsilon}{2}\hat{\sigma}_z \tag{4.21}$$

$$\hat{H}_{SB} = \sqrt{\frac{\Lambda M\Omega^2}{2}}\hat{q}_0\hat{\sigma}_z \tag{4.22}$$

$$\hat{H}_B = \frac{\hat{p}_0^2}{2m} + \frac{1}{2}m\Omega^2\hat{q}_0 + \sum_{\alpha=1}^{N_b}\left[\frac{\hat{p}_\alpha^2}{2m_\alpha} + \frac{1}{2}m_\alpha\omega_\alpha^2\left(\hat{q}_\alpha - \frac{c_\alpha\hat{q}_0}{m_\alpha\omega_\alpha^2}\right)^2\right], \tag{4.23}$$

where

$$\hat{\sigma}_x = |1\rangle\langle 0| + |0\rangle\langle 1| \qquad \hat{\sigma}_z = |0\rangle\langle 0| - |1\rangle\langle 1| \tag{4.24}$$

are the operators acting on the electronic degrees of freedom which, when represented in the diabatic basis, correspond to the Pauli spin matrices. In this definition of the Hamiltonian an unimportant energy shift of $(\Lambda - 2\epsilon)/4$ has been ignored.

4.2.2 Conventional Form

The spin-boson Hamiltonian in its conventional form describes a system that is linearly coupled to each mode of a bath of uncoupled harmonic oscillators. In order to obtain this form, it is necessary to perform a normal mode transformation on the bath coordinates.[161,166,167] On doing so, the system Hamiltonian remains unchanged,

while the system-bath coupling and bath Hamiltonians become[168]

$$\hat{\tilde{H}}_{SB} = \hat{\sigma}_z \sum_{\alpha=0}^{N_b} \tilde{c}_\alpha \hat{\tilde{q}}_\alpha \tag{4.25}$$

$$\hat{\tilde{H}}_B = \sum_{\alpha=0}^{N_b} \left[\frac{\hat{\tilde{p}}_\alpha^2}{2\tilde{m}_\alpha} + \frac{1}{2}\tilde{m}_\alpha \tilde{\omega}_\alpha^2 \hat{\tilde{q}}_\alpha^2 \right], \tag{4.26}$$

where $\hat{\tilde{q}}_\alpha$ is the α-th normal mode coordinate and $\hat{\tilde{p}}_\alpha$, $\tilde{m}_\alpha$, $\tilde{\omega}_\alpha$, and $\tilde{c}_\alpha$ are the corresponding transformed momentum operator, mass, frequency and coupling, respectively, and an unimportant energy shift of

$$\sum_{\alpha=0}^{N_b} \frac{\tilde{c}_\alpha^2}{2\tilde{m}_\alpha \tilde{\omega}_\alpha^2} \tag{4.27}$$

has been removed. As both representations of the spin-boson model correspond to a system (here the two diabatic states) linearly coupled to a harmonic bath, the influence of the bath can be fully captured through the spectral density.[169,170] All that is necessary to map between the two forms is the relation between the spectral density for the coupling of the nuclear coordinates and electronic states,

$$\tilde{J}(\omega) = \frac{\pi}{2} \sum_{\alpha=0}^{N_b} \frac{\tilde{c}_\alpha^2}{\tilde{m}_\alpha \tilde{\omega}_\alpha} \delta(\omega - \tilde{\omega}_\alpha), \tag{4.28}$$

and the spectral density, $J(\omega)$ (equation 4.18), for the coupling between the reaction coordinate and the remaining bath modes. The relationship between the two spectral densities may be obtained by comparing the time-dependent system-bath coupling operators,[161,166,167] which gives

$$\tilde{J}(\omega) = \frac{\Lambda}{2} \frac{\Omega^2 J(\omega)/M}{(\omega^2 - \Omega^2 + R(\omega))^2 + J^2(\omega)/M^2} \tag{4.29}$$

where

$$R(\omega) = \frac{2\omega^2}{M\pi} P \int_0^\infty \frac{J(\nu)\mathrm{d}\nu}{\nu\left(\nu^2 - \omega^2\right)} \tag{4.30}$$

and P denotes the Cauchy principle value. For the Ohmic spectral density given in equation 4.19 this becomes

$$\tilde{J}(\omega) \equiv J^{(B)}(\omega) = \frac{\Lambda}{2} \frac{\gamma \Omega^2 \omega}{\left(\omega^2 - \Omega^2\right)^2 + \gamma^2 \omega^2}, \tag{4.31}$$

which is known as the Brownian oscillator spectral density. The spectral density fully describes the influence of all bath degrees of freedom on the electron transfer

degrees of freedom. The reorganisation energy of the bath is readily extracted from the spectral density as

$$\Lambda = \frac{4}{\pi}\int_0^\infty \frac{\tilde{J}(\omega)}{\omega}\mathrm{d}\omega. \tag{4.32}$$

For the discrete spectral density defined in equation 4.28, this therefore gives

$$\Lambda = \sum_{\alpha=0}^{N_b} \frac{2\tilde{c}_\alpha^2}{\tilde{m}_\alpha \tilde{\omega}_\alpha^2}. \tag{4.33}$$

When written in the conventional form, the spin-boson model captures all of the same physics as is present in the reaction coordinate form. By varying the values of Ω and γ the different friction regimes can be explored. One commonly employed limit of this spectral density is the Debye (or Drude) spectral density, which describes an ideal solvent undergoing Debye relaxation.[166,171] The Debye spectral density can be obtained in the limit of a high frequency and strongly overdamped reaction coordinate. Defining $\omega_c = \Omega^2/\gamma$, the Brownian oscillator spectral density may be rewritten as

$$J^{(B)}(\omega) = \frac{\Lambda}{2}\frac{\omega_c\omega}{\left(\omega^2/\gamma - \omega_c\right)^2 + \omega^2}. \tag{4.34}$$

Taking the limit of a strongly overdamped reaction coordinate ($\gamma/2 \gg \Omega$), while keeping ω_c constant, gives[166]

$$J^{(D)}(\omega) = \frac{\Lambda}{2}\frac{\omega\omega_c}{\omega_c^2 + \omega^2}. \tag{4.35}$$

Alternatively, this spectral density is often considered as an approximation to the Ohmic spectral density (equation 4.19).[166] Expanding in powers of ω gives

$$J^{(D)}(\omega) = \frac{\Lambda}{2}\left(\frac{\omega}{\omega_c} - \frac{\omega^3}{\omega_c^3} + O(\omega^5)\right). \tag{4.36}$$

It is linear (Ohmic) at small frequencies with friction $\gamma = \Lambda/(2M\omega_c)$, while higher frequency contributions are damped by a lorentzian weight function. In the limit that $\omega_c \to \infty$ with the friction held constant, this reduces to the Ohmic spectral density.

The conventional form provides a significant advantage over the reaction coordinate form of the spin-boson Hamiltonian, in that all bath degrees of freedom are uncoupled. This dramatically simplifies the treatment of the dynamics of the model, and it is possible to exactly capture the effect of the bath on the dynamics of the system. This can be done using the hierarchical equations of motion (HEOM) approach, which provides an exact description of the dynamics of a quantum mechanical system linearly coupled to an uncoupled harmonic bath and will be discussed.

4.3 Hierarchical Equations of Motion: Preliminaries

The hierarchical equations of motion (HEOM) formalism, originally proposed by Tanimura and Kubo to treat a system interacting with a high temperature (classical) harmonic bath,[7] and extended by Ishizaki and Tanimura to include quantum mechanical effects in the bath,[8] is a numerically exact technique capable of describing the dynamics of an arbitrary quantum system linearly coupled to one or more harmonic baths. While it is one of the earliest approaches for treating such problems exactly, it remains one of the most powerful methods routinely applied to treat the dynamics of large systems.[172–174] Within this formalism, effects arising from the non-Markovian bath dynamics are captured through a hierarchy of auxiliary density operators (ADOs) that couple to the evolution of the system reduced density operator.[7,8]

In their standard form, the hierarchical equations of motion are suitable for computing the real time dynamics of an arbitrary quantum system coupled to M independent, infinite dimensional harmonic baths, where each bath is initially uncorrelated from the system and has a spectral density with the Debye form shown above.[8] However, because of its success in treating such systems, considerable effort has been dedicated towards extending its applicability. The approach has been extended to treat baths with arbitrary spectral densities,[175,176] initially correlated

baths,[177] imaginary time dynamics,[178] and fermionic baths.[179] Due to its ability to treat non-Markovian dynamics of a system coupled to a wide range of baths in a non-perturbative way, this approach has found widespread application for treating the dynamics of open quantum systems relevant to chemistry, biology and physics.[33,173,174,180–184]

While HEOM has found success in treating large systems, as the number of baths present or the strength of the system-bath coupling increases, the resultant equations of motion can become impractical to solve. A number of methods have been developed to overcome these limitations. These include alternative schemes for truncating the hierarchy of auxiliary density operators,[182,183,185] alternative (Padé approximant) representations of the bath correlation functions,[186,187] hybrid stochastic and hierarchical treatments of the influence of the bath on the system,[188] and matrix product state based solutions to the hierarchical equations of motion.[189] In Chapter 5, an approach closely related to that of the matrix product state treatment is discussed. In the remainder of this chapter the standard hierarchical equations of motion approach will be reviewed. However, before doing so it is necessary to fully specify the harmonic bath models to which the method will be applied.

4.3.1 Harmonic Bath Model

The model considered here consists of a general N-level quantum system linearly coupled to a set of harmonic baths. The system Hamiltonian, $\hat{H}_S$, is taken to be a completely general Hermitian operator acting on the space of the N system states. Each of the M independent harmonic baths has a Hamiltonian of the form

$$\hat{H}_{Bj} = \sum_{\alpha} \left[\frac{\hat{p}_{j\alpha}^2}{2m_{j\alpha}} + \frac{1}{2} m_{j\alpha} \omega_{j\alpha}^2 \hat{q}_{j\alpha}^2 \right], \tag{4.37}$$

where $\hat{q}_{j\alpha}$ is the coordinate associated with the α-th mode in the j-th bath, $\hat{p}_{j\alpha}$ is its momentum, $m_{j\alpha}$ its mass, and $\omega_{j\alpha}$ its frequency. Each bath couples to the

system with a system-bath Hamiltonian of the form

$$\begin{aligned}\hat{H}_{SBj} &= \hat{Q}_j \sum_\alpha c_{j\alpha}\hat{q}_{j\alpha} \\ &= \hat{Q}_j\hat{\eta}_j \end{aligned} \tag{4.38}$$

where $c_{j\alpha}$ is the coupling constant for the α-th mode of bath j, and $\hat{Q}_j$ is an arbitrary Hermitian operator that only acts on the system Hilbert space. The coupling constants and frequencies for each bath are defined by an associated spectral density (equation 4.28), which, in addition to the temperature of the thermal bath, T_j, uniquely describes the influence of the bath on the system dynamics. Here the infinite bath limit is taken, each spectral density is a continuous function of ω, taken to be a sum of an arbitrary number of Brownian oscillator, $J^{(B)}$ (equation 4.31), and Debye, $J^{(D)}$ (equation 4.35), spectral densities,

$$J_j(\omega) = \sum_{i=1}^{N_{Bj}} J_{ij}^{(B)}(\omega) + \sum_{i=1}^{N_{Dj}} J_{ij}^{(D)}(\omega). \tag{4.39}$$

The total Hamiltonian including all system and bath degrees of freedom is

$$\hat{H} = \hat{H}_S + \sum_{j=1}^{M}\left(\hat{H}_{SBj} + \hat{H}_{Bj}\right) \tag{4.40}$$

$$= \hat{H}_S + \hat{H}_{SB} + \hat{H}_B \tag{4.41}$$

4.3.2 Uncorrelated Initial Condition

The dynamics of the full N-level system and the M baths can be obtained by considering the evolution of the density operator accounting for all system and bath degrees of freedom, $\hat{\rho}(t)$. Here the system and bath will be taken to be initially uncorrelated with each bath, j, at thermal equilibrium with respect to the bath Hamiltonian, $\hat{H}_{Bj}$, at temperature T_j. For this initially uncorrelated system and bath, the density operator may be written as

$$\hat{\rho}(0) = \hat{\rho}_S(0)\hat{\rho}_B(0) = \hat{\rho}_S(0)\bigotimes_{j=1}^{M}\hat{\rho}_{Bj}(0), \tag{4.42}$$

where each of the initial bath density operators are given by

$$\hat{\rho}_{Bj}(0) = \frac{e^{-\beta_j\hat{H}_{Bj}}}{\mathrm{tr}\left[e^{-\beta_j\hat{H}_{Bj}}\right]_{Bj}}, \tag{4.43}$$

where $\beta_j = 1/(k_b T_j)$ is the inverse temperature associated with bath j, and $\mathrm{tr}\left[\cdot\right]_{Bj}$ denotes the partial trace over the degrees of freedom of the j-th bath. This condition is not strictly necessary to derive the hierarchical equations of motion[177]; however, it leads to significantly simplified expressions and is the case considered throughout the remainder of this thesis.

4.3.3 Dynamics in the Interaction Picture

The evolution of the full density operator is described by the standard Liouville-von Neumann equation[1]

$$\frac{\mathrm{d}}{\mathrm{d}t}\hat{\rho}(t) = -\frac{i}{\hbar}\left[\hat{H}, \hat{\rho}(t)\right] \tag{4.44}$$

$$= -\frac{i}{\hbar}\mathcal{L}\hat{\rho}(t), \tag{4.45}$$

where $\mathcal{L} = \left[\hat{H}, \cdot\right]$ is the Liouville space superoperator (Liouvillian) corresponding to the Hamiltonian. By dividing the full Hamiltonian into two parts:

$$\hat{H} = \hat{H}_S + \hat{H}_B + \hat{H}_{SB} \tag{4.46}$$

$$= \hat{H}_0 + \hat{H}_{SB} \tag{4.47}$$

equation 4.44 can be transformed into the interaction picture with respect to $\hat{H}_0$, giving

$$\frac{\mathrm{d}}{\mathrm{d}t}\tilde{\rho}(t) = -\frac{i}{\hbar}\left[\tilde{H}_{SB}(t), \tilde{\rho}(t)\right] \tag{4.48}$$

$$= -\frac{i}{\hbar}\tilde{\mathcal{L}}_{SB}(t)\tilde{\rho}(t). \tag{4.49}$$

Here $\tilde{O}(t)$ denotes the interaction Hamiltonian representation of an operator $\hat{O}$, which can be written as[91]

$$\tilde{O}(t) = e^{i\hat{H}_0 t/\hbar}\hat{O}e^{-i\hat{H}_0 t/\hbar}, \tag{4.50}$$

and evolves according to the equation of motion,

$$\frac{\mathrm{d}}{\mathrm{d}t}\tilde{O}(t) = \frac{i}{\hbar}\left[\hat{H}_0, \tilde{O}(t)\right]. \tag{4.51}$$

Integrating equation 4.48 with respect to time gives a recurrence relation for the density operator,

$$\tilde{\rho}(t) = \tilde{\rho}(0) - \frac{i}{\hbar}\int_0^t \mathrm{d}t_1 \tilde{\mathcal{L}}_{SB}(t_1)\tilde{\rho}(t_1). \tag{4.52}$$

Repeated application of this recursion relation gives an infinite series expansion for the density operator at time t,

$$\tilde{\rho}(t) = \sum_{m=0}^{\infty}\left(-\frac{i}{\hbar}\right)^m \int_0^t \mathrm{d}t_1 \cdots \int_0^{t_{m-1}} \mathrm{d}t_m \tilde{\mathcal{L}}_{SB}(t_1)\ldots\tilde{\mathcal{L}}_{SB}(t_m)\tilde{\rho}(0). \tag{4.53}$$

A general term of order m in this equation contains the action of the Liouvillian superoperator, $\tilde{\mathcal{L}}_{SB}(t)$, at different times. The fact that the Liouvillian superoperators evaluated at different times do not commute significantly complicates the evaluation of the expression. By inserting the definition of the Liouvillian into equation 4.53, a general term of order m may be written as a sum of the 2^m terms of the form

$$\tilde{H}_{SB}(t_{p_1})\ldots\tilde{H}_{SB}(t_{p_k})\tilde{\rho}(0)\tilde{H}_{SB}(t_{p_{k+1}})\ldots\tilde{H}_{SB}(t_{p_m}). \tag{4.54}$$

Here k is an arbitrary integer in the range $[0, m]$ and $\{p_1, \ldots, p_k, p_{k+1}\ldots p_m\}$ is a permutation of the integers from 1 to m with the first k indices satisfying $p_1 < p_2 < \cdots < p_k$, the remaining $m-k$ indices satisfy the condition $p_{k+1} > p_{k+2} > \cdots > p_m$, and there is no ordering between the indices in the two sets $\{p_1, \ldots, p_k\}$ and $\{p_{k+1}\ldots p_m\}$.

At this stage it is useful to introduce the chronological time-ordering operator $\mathcal{T}_{\leftarrow}$, which acts on products of time-dependent operators to order the time arguments so that they increase from right to left.[5] The time-ordered product of two time-dependent operators (acting on bosonic degrees of freedom) is

$$\mathcal{T}_{\leftarrow}\hat{A}(t_1)\hat{B}(t_2) = \hat{A}(t_1)\hat{B}(t_2)\Theta(t_1 - t_2) + \hat{B}(t_2)\hat{A}(t_1)\Theta(t_2 - t_1), \tag{4.55}$$

where $\Theta(t)$ is the Heaviside step function. Generalising this expression, the time-ordered product for a product of m operators may be written in terms of $m!$

contributions corresponding to all possible orderings of the operators. Using the time-ordering operator, equation 4.53 may be rewritten as[5]

$$\tilde{\rho}(t) = \sum_{m=0}^{\infty} \frac{1}{m!} \left(-\frac{i}{\hbar}\right)^m \mathcal{T}_{\leftarrow} \int_0^t \mathrm{d}t_1 \cdots \int_0^t \mathrm{d}t_m \tilde{\mathcal{L}}_{SB}(t_1) \ldots \tilde{\mathcal{L}}_{SB}(t_m) \tilde{\rho}(0) \tag{4.56}$$

$$= \mathcal{T}_{\leftarrow} \exp\left(-\frac{i}{\hbar} \int_0^t \tilde{\mathcal{L}}_{SB}(\tau) \mathrm{d}\tau\right) \tilde{\rho}(0), \tag{4.57}$$

where $\mathcal{T}_{\leftarrow} \exp$ denotes the time-ordered exponential.

While this expression is entirely general and describes the time-dependent state of an arbitrary system and bath, it is not practical. For the application considered here, the state of the system is the key quantity of interest. The details of the dynamics of the bath are unimportant, all that matters is its influence on the system dynamics. This can be fully accounted for by considering the system reduced density operator, $\tilde{\rho}_S(t)$, that can be obtained from equation 4.57 by evaluating the partial trace over the bath degrees of freedom

$$\tilde{\rho}_S(t) = \mathrm{tr}\left[\mathcal{T}_{\leftarrow} \exp\left(-\frac{i}{\hbar} \int_0^t \tilde{\mathcal{L}}_{SB}(\tau) \mathrm{d}\tau\right) \tilde{\rho}_B(0)\right]_B \tilde{\rho}_S(0) \tag{4.58}$$

$$= \left\langle \mathcal{T}_{\leftarrow} \exp\left(-\frac{i}{\hbar} \int_0^t \tilde{\mathcal{L}}_{SB}(\tau) \mathrm{d}\tau\right) \right\rangle_B \tilde{\rho}_S(0), \tag{4.59}$$

where $\langle \cdot \rangle_B$ denotes an average over the initial distribution of the bath, $\tilde{\rho}_B(0)$. The evaluation of the system reduced density operator therefore requires evaluation of the bath average of terms of the form given in equation 4.54 for arbitrary m. For general Hamiltonians this is impractical but for the quadratic bath Hamiltonians considered here it is possible.

4.3.4 Reduced System Dynamics

Time Evolved System-Bath Hamiltonian

As the system and bath Hamiltonians act on distinct Hilbert spaces, and hence commute, the interaction picture system-bath Hamiltonian, $\tilde{H}_{SB}(t)$, may be simplified

$$\begin{aligned}\tilde{H}_{SB}(t) &= \sum_{j=1}^{M} e^{i\left(\hat{H}_S+\hat{H}_B\right)t/\hbar}\hat{Q}_j\hat{\eta}_j e^{-i\left(\hat{H}_S+\hat{H}_B\right)t/\hbar} \\ &= \sum_{j=1}^{M} e^{i\hat{H}_S t/\hbar}\hat{Q}_j e^{-i\hat{H}_S t/\hbar}e^{i\hat{H}_B t/\hbar}\hat{\eta}_j e^{-i\hat{H}_B t/\hbar} \\ &= \sum_{j=1}^{M} \tilde{Q}_j(t)\tilde{\eta}_j(t). \end{aligned} \tag{4.60}$$

The time evolution of the collective bath coordinate,

$$\tilde{\eta}_j(t) = \sum_{\alpha} c_{j\alpha}\tilde{q}_{j\alpha}(t), \tag{4.61}$$

can be obtained by considering the time evolution of the bath position, $\tilde{q}_{j\alpha}(t)$, and momentum operators, $\tilde{p}_{j\alpha}(t)$, for each mode. Inserting these two operators into equation 4.51 leads to a set of coupled equations of motion,

$$\frac{\mathrm{d}}{\mathrm{d}t}\tilde{q}_{j\alpha} = \frac{i}{\hbar}\left[\hat{H}_B, \tilde{q}_{j\alpha}\right] = \frac{\tilde{p}_{j\alpha}}{m_{j\alpha}} \qquad \frac{\mathrm{d}}{\mathrm{d}t}\tilde{p}_{j\alpha} = \frac{i}{\hbar}\left[\hat{H}_B, \tilde{p}_{j\alpha}\right] = -m_{j\alpha}\omega_{j\alpha}^2\tilde{q}_{j\alpha}. \tag{4.62}$$

This system of equations describes simple harmonic motion and can be solved analytically to give[2]

$$\begin{aligned}\tilde{q}_{j\alpha}(t) &= \hat{q}_{j\alpha}\cos\left(\omega_{j\alpha}t\right) + \frac{\hat{p}_{j\alpha}}{m_{j\alpha}\omega_{j\alpha}}\sin\left(\omega_{j\alpha}t\right) \\ &= \sqrt{\frac{\hbar}{2m_{j\alpha}\omega_{j\alpha}}}\left(e^{i\omega_{j\alpha}t}\hat{a}_{j\alpha}^{\dagger} + e^{-i\omega_{j\alpha}t}\hat{a}_{j\alpha}\right), \end{aligned} \tag{4.63}$$

where

$$\hat{a}_{j\alpha}^{\dagger} = \sqrt{\frac{m_{j\alpha}\omega_{j\alpha}}{2\hbar}}\left(\hat{q}_{j\alpha} - \frac{i\hat{p}_{j\alpha}}{m_{j\alpha}\omega_{j\alpha}}\right) \tag{4.64}$$

and

$$\hat{a}_{j\alpha} = \sqrt{\frac{m_{j\alpha}\omega_{j\alpha}}{2\hbar}}\left(\hat{q}_{j\alpha} + \frac{i\hat{p}_{j\alpha}}{m_{j\alpha}\omega_{j\alpha}}\right) \tag{4.65}$$

are the harmonic oscillator creation and annihilation operators for mode (j,α).[2] The collective bath coordinate at time t is then given by[5]

$$\tilde{\eta}_j(t) = \sum_{\alpha}\sqrt{\frac{\hbar c_{j\alpha}^2}{2m_{j\alpha}\omega_{j\alpha}}}\left(e^{i\omega_{j\alpha}t}\hat{a}_{j\alpha}^{\dagger} + e^{-i\omega_{j\alpha}t}\hat{a}_{j\alpha}\right), \tag{4.66}$$

which is a linear function of time-independent bath creation and annihilation operators. This result allows significant simplification of the evaluation of the bath expectation value in equation 4.59.

Bath Averages

Expanding the time-ordered exponential in equation 4.59 gives

$$\tilde{\rho}_S(t) = \left[\sum_{m=0}^{\infty}\left(-\frac{i}{\hbar}\right)^m \int_0^t \mathrm{d}t_1 \cdots \int_0^{t_{m-1}} \mathrm{d}t_m \left\langle \tilde{\mathcal{L}}_{SB}(t_1)\ldots\tilde{\mathcal{L}}_{SB}(t_m)\right\rangle_B\right]\tilde{\rho}_S(0). \quad (4.67)$$

Each term with odd $m = 2k+1$ requires the evaluation of a bath average of the form

$$\left\langle \tilde{\mathcal{L}}_{SB}(t_1)\ldots\tilde{\mathcal{L}}_{SB}(t_{2k+1})\right\rangle_B. \quad (4.68)$$

Expanding this term allows it to be written as a sum of the bath expectation values of 2^m terms of the form given in equation 4.54. From equations 4.60 and 4.66, the system-bath Hamiltonian is a linear combination of the time-independent creation and annihilation operators acting on the bath. The product of the $m = 2k+1$ system-bath Hamiltonians results in a sum over terms each containing an odd number of creation and annihilation operators and, therefore, changes the total number of excitations in a given bath state. For the thermal bath distribution considered here (which is gaussian in terms of these operators), the bath expectation value of each of these is zero. All terms with odd m vanish from equation 4.59, and the reduced system density operator may be written as

$$\tilde{\rho}_S(t) = \mathcal{T}_{\leftarrow}\left\langle \exp\left(-\frac{1}{\hbar^2}\int_0^t \mathrm{d}t_1 \int_0^t \mathrm{d}t_2 \tilde{\mathcal{L}}_{SB}(t_1)\tilde{\mathcal{L}}_{SB}(t_2)\right)\right\rangle_B \tilde{\rho}_S(0). \quad (4.69)$$

All that remains now is to evaluate the bath averages of products of even numbers of system-bath Liouvillians — a task that is considerably more involved. In the standard derivation of the hierarchical equations of motion this is achieved using path integral techniques.[8] Here, a different approach will be employed, equation 4.69

will be evaluated using a cumulant expansion.[5,6,190–193] The time-ordered exponential in equation 4.69 may be expanded to give

$$\begin{aligned}\tilde{\rho}_S(t) &= \Big[1 - \frac{1}{\hbar^2}\int_0^t \mathrm{d}t_1 \int_0^{t_1} \mathrm{d}t_2 \left\langle \tilde{\mathcal{L}}_{SB}(t_1)\tilde{\mathcal{L}}_{SB}(t_2)\right\rangle_B \\ &\quad + \frac{1}{\hbar^4}\int_0^t \mathrm{d}t_1 \cdots \int_0^{t_3} \mathrm{d}t_4 \left\langle \tilde{\mathcal{L}}_{SB}(t_1)\tilde{\mathcal{L}}_{SB}(t_2)\tilde{\mathcal{L}}_{SB}(t_3)\tilde{\mathcal{L}}_{SB}(t_4)\right\rangle_B + \ldots \Big]\tilde{\rho}_S(0) \qquad (4.70)\\ &= \Big[1 - \tilde{\mathcal{X}}(t)\Big]\tilde{\rho}_S(0). \qquad (4.71)\end{aligned}$$

Differentiating this expression with respect to time gives a quantum master equation for the time-evolution of the system reduced density operator,

$$\begin{aligned}\frac{\mathrm{d}}{\mathrm{d}t}\tilde{\rho}_S(t) &= \Big[- \frac{1}{\hbar^2}\int_0^t \mathrm{d}t_1 \left\langle \tilde{\mathcal{L}}_{SB}(t)\tilde{\mathcal{L}}_{SB}(t_1)\right\rangle_B \\ &\quad + \frac{1}{\hbar^4}\int_0^t \mathrm{d}t_1 \int_0^{t_1} \mathrm{d}t_2 \int_0^{t_2} \mathrm{d}t_3 \left\langle \tilde{\mathcal{L}}_{SB}(t)\tilde{\mathcal{L}}_{SB}(t_1)\tilde{\mathcal{L}}_{SB}(t_2)\tilde{\mathcal{L}}_{SB}(t_3)\right\rangle_B + \ldots \Big]\tilde{\rho}_S(0). \end{aligned} \qquad (4.72)$$

By inverting equation 4.70 it is possible to obtain $\tilde{\rho}_S(0)$ as a function of $\tilde{\rho}_S(t)$, as

$$\begin{aligned}\tilde{\rho}_S(0) &= \Big[1 - \tilde{\mathcal{X}}(t)\Big]^{-1}\tilde{\rho}_S(t) \qquad (4.73)\\ &= \sum_{n=0}^{\infty} \tilde{\mathcal{X}}(t)^n \tilde{\rho}_S(t), \qquad (4.74)\end{aligned}$$

where it has been assumed that $\Big[1 - \tilde{\mathcal{X}}(t)\Big]^{-1}$ may be expanded as a geometric series.[5] Inserting equation 4.74 into 4.72, grouping together terms of the same order in the system-bath Liouvillian, and correctly time-ordering the integrals gives a master equation of the form

$$\frac{\mathrm{d}}{\mathrm{d}t}\tilde{\rho}_S(t) = \sum_{k=1}^{\infty} \tilde{\mathcal{K}}_{2k}(t)\tilde{\rho}_S(t). \qquad (4.75)$$

Here the functions $\tilde{\mathcal{K}}_{2k}(t)$ can be written in terms of the $2k$-th order ordered cumulants ($\langle\langle \ldots \rangle\rangle$) with respect to the bath density operator as[5,191,193]

$$\tilde{\mathcal{K}}_{2k}(t) = \left(-\frac{1}{\hbar^2}\right)^k \int_0^t \mathrm{d}t_1 \cdots \int_0^{t_{2k-2}} \mathrm{d}t_{2k-1} \left\langle\left\langle \tilde{\mathcal{L}}_{SB}(t)\tilde{\mathcal{L}}_{SB}(t_1)\ldots\tilde{\mathcal{L}}_{SB}(t_{2k-1})\right\rangle\right\rangle_B . \qquad (4.76)$$

These expressions are generally cumbersome to evaluate, however, for the system considered here this simplifies considerably. As the initial state of the system is gaussian with respect to the bath variables and the system-bath coupling operators are linear with respect to the bath variables, the cumulant expansion terminates

at second order. By using Wick's theorem for the bath operators[194,195] it can be shown that all higher order ordered cumulants are zero.[5,192,196] It is only necessary to evaluate the second-order ordered cumulant,

$$\left\langle\left\langle \tilde{\mathcal{L}}_{SB}(t_1)\tilde{\mathcal{L}}_{SB}(t_2)\right\rangle\right\rangle_B = \left\langle \tilde{\mathcal{L}}_{SB}(t_1)\tilde{\mathcal{L}}_{SB}(t_2)\right\rangle_B . \tag{4.77}$$

Inserting this into equation 4.75 gives

$$\frac{\mathrm{d}}{\mathrm{d}t}\tilde{\rho}_S(t) = -\frac{1}{\hbar^2}\int_0^t \mathrm{d}t_1 \left\langle \tilde{\mathcal{L}}_{SB}(t)\tilde{\mathcal{L}}_{SB}(t_1)\right\rangle_B \tilde{\rho}_S(t), \tag{4.78}$$

which is solved by

$$\tilde{\rho}_S(t) = \mathcal{T}_{\leftarrow}\exp\left(-\frac{1}{\hbar^2}\int_0^t \mathrm{d}t_1 \int_0^{t_1} \mathrm{d}t_2 \left\langle \tilde{\mathcal{L}}_{SB}(t_1)\tilde{\mathcal{L}}_{SB}(t_2)\right\rangle_B\right)\tilde{\rho}_S(0). \tag{4.79}$$

The influence of the bath on the dynamics of the system is thus fully accounted for by the autocorrelation function of the system-bath Liouvillian (equation 4.77).

The bath average of the system-bath Liouvillian autocorrelation function is a superoperator acting on the system Hilbert space. Its value can be readily obtained by acting it on an arbitrary system operator, $\tilde{O}_S$, which gives

$$\left\langle \tilde{\mathcal{L}}_{SB}(t_1)\tilde{\mathcal{L}}_{SB}(t_2)\right\rangle_B \tilde{O}_S = \mathrm{tr}\left[\left[\tilde{H}_{SB}(t_1),\left[\tilde{H}_{SB}(t_2),\hat{\rho}_B(0)\tilde{O}_s\right]\right]\right]_B . \tag{4.80}$$

On expanding the commutators, this becomes

$$\begin{aligned}\left\langle \tilde{\mathcal{L}}_{SB}(t_1)\tilde{\mathcal{L}}_{SB}(t_2)\right\rangle_B \tilde{O}_S = \sum_{j=1}^{M}\Big\{&\mathrm{tr}\left[\tilde{\eta}_j(t_1)\tilde{\eta}_j(t_2)\hat{\rho}_{Bj}(0)\right]_{Bj}\left[\tilde{Q}_j(t_1),\tilde{Q}_j(t_2)\tilde{O}_S\right]\\ &-\mathrm{tr}\left[\tilde{\eta}_j(t_2)\tilde{\eta}_j(t_1)\hat{\rho}_{Bj}(0)\right]_{Bj}\left[\tilde{Q}_j(t_1),\tilde{O}_S\tilde{Q}_j(t_2)\right]\Big\},\end{aligned} \tag{4.81}$$

where the cyclic permutation of the trace has been used to reorder the bath terms. Introducing the superoperators $\tilde{\mathcal{Q}}_j(t)$, $\tilde{\mathcal{Q}}_j^L(t)$, and $\tilde{\mathcal{Q}}_j^R(t)$ that are defined by their action on an arbitrary system operator,

$$\tilde{\mathcal{Q}}_j(t)\tilde{O}_s = \left[\tilde{Q}_j(t),\tilde{O}_s\right], \quad \tilde{\mathcal{Q}}_j^L(t)\hat{O} = \tilde{Q}_j(t)\hat{O}, \text{ and } \quad \tilde{\mathcal{Q}}_j^R(t)\hat{O} = \hat{O}\tilde{Q}_j(t), \tag{4.82}$$

the system-bath Liouvillian autocorrelation function may be written as

$$\left\langle \tilde{\mathcal{L}}_{SB}(t_1)\tilde{\mathcal{L}}_{SB}(t_2)\right\rangle_B = \sum_{j=1}^{M}\tilde{\mathcal{Q}}_j(t)\left[\left\langle\tilde{\eta}_j(t_1)\tilde{\eta}_j(t_2)\right\rangle_B\tilde{\mathcal{Q}}_j^L(t) - \left\langle\tilde{\eta}_j(t_2)\tilde{\eta}_j(t_1)\right\rangle_B\tilde{\mathcal{Q}}_j^R(t)\right]. \tag{4.83}$$

The correlation functions of the collective bath coordinate, $\langle\tilde{\eta}_j(t_1)\tilde{\eta}_j(t_2)\rangle_B$, may be evaluated by expanding them in terms of the individual bath modes,

$$\langle\tilde{\eta}_j(t_1)\tilde{\eta}_j(t_2)\rangle_B = \sum_\alpha c_\alpha^2 \langle\tilde{q}_{j\alpha}(t_1)\tilde{q}_{j\alpha}(t_2)\rangle_B . \tag{4.84}$$

Inserting equation 4.63 and evaluating the resultant expectation values of creation and annihilation operators gives

$$\langle\tilde{\eta}_j(t_1)\tilde{\eta}_j(t_2)\rangle_B = \sum_\alpha \frac{\hbar c_{j\alpha}^2}{2m_{j\alpha}\omega_{j\alpha}}\left[\coth\left(\frac{\beta_j\hbar\omega_{j\alpha}}{2}\right)\cos\left(\omega_{j\alpha}(t_1-t_2)\right) - i\sin\left(\omega_{j\alpha}(t_1-t_2)\right)\right]. \tag{4.85}$$

This is only a function of the difference between the two times, and so to simplify notation, the function $C_j(t_1-t_2) = \langle\tilde{\eta}_j(t_1)\tilde{\eta}_j(t_2)\rangle_B$ is introduced. This function may then be rewritten as

$$C_j(t) = \int_{-\infty}^{\infty}\sum_\alpha \frac{\hbar c_{j\alpha}^2}{2m_{j\alpha}\omega}\delta(\omega-\omega_{j\alpha})\left[\coth\left(\frac{\beta_j\hbar\omega}{2}\right)\cos\left(\omega t\right) - i\sin\left(\omega t\right)\right]\mathrm{d}\omega \tag{4.86}$$

$$= \frac{\hbar}{2\pi}\int_{-\infty}^{\infty} J_j(\omega)\left[\coth\left(\frac{\beta_j\hbar\omega}{2}\right)\cos\left(\omega t\right) - i\sin\left(\omega t\right)\right]\mathrm{d}\omega. \tag{4.87}$$

This may be simplified by inserting additional trigonometric functions into the integrand whose contributions vanish by symmetry to give,

$$C_j(t) = \frac{\hbar}{2\pi}\int_{-\infty}^{\infty} J_j(\omega)\left[\coth\left(\frac{\beta_j\hbar\omega}{2}\right) - 1\right]e^{i\omega t}\mathrm{d}\omega. \tag{4.88}$$

Inserting these expressions into equation 4.79 gives

$$\tilde{\rho}_S(t) = \mathcal{T}_{\leftarrow}\exp\Bigg(-\frac{1}{\hbar^2}\sum_{j=1}^{M}\int_0^t \mathrm{d}t_1\int_0^{t_1}\mathrm{d}t_2\,\tilde{\mathcal{Q}}_j(t_1)\Big[C_j(t_1-t_2)\tilde{\mathcal{Q}}_j^L(t_2) - C_j^*(t_1-t_2)\tilde{\mathcal{Q}}_j^R(t_2)\Big]\Bigg)\tilde{\rho}_S(0) \tag{4.89}$$

$$= \mathcal{T}_{\leftarrow}\tilde{\mathcal{G}}(t)\tilde{\rho}_S(0) \tag{4.90}$$

$$= \tilde{\mathcal{F}}(t)\tilde{\rho}_S(0).$$

The influence superoperator, $\tilde{\mathcal{F}}(t)$, fully encodes the influence of the bath on the system dynamics. It is uniquely determined by the temperatures of each bath, and their spectral densities and system-bath coupling operators. These properties uniquely determine the effect of the harmonic bath on the dynamics of the N-level system.

4.3.5 The Bath Correlation Functions

For the Debye and Brownian oscillator forms of the spectral densities, the bath correlation function (equation 4.88) can be evaluated through contour integration. Here only the final expressions are presented, the details of this contour integration can be found in appendix C.

The bath correlation function for the Brownian oscillator spectral density is given by

$$C(t) = F(t; 2\Omega/\gamma) + \frac{\lambda\gamma\Omega^2}{4\beta}\sum_{k=1}^{\infty}\frac{\nu_k e^{-\nu_k t}}{\gamma^2\nu_k^2 - \left(\nu_k^2 + \Omega^2\right)^2} \tag{4.91}$$

where $\lambda = \Lambda/4$ is the bath reorganisation energy, $\nu_k = 2\pi k/\beta\hbar$ is the k-th Matsubara frequency, β is the inverse temperature, and $F(t; 2\Omega/\gamma)$ is a function whose form depends on whether the dynamics along the reaction coordinate is overdamped, underdamped or critically damped:

- For an overdamped Brownian oscillator ($\gamma > 2\Omega$)

$$\begin{aligned} F(t; 2\Omega/\gamma < 1) &= \frac{\lambda\Omega^2\hbar}{2\kappa}\left[\left(\cot\left(\frac{\beta\hbar\nu_-}{2}\right) - i\right)e^{-\nu_- t} - \left(\cot\left(\frac{\beta\hbar\nu_+}{2}\right) - i\right)e^{-\nu_+ t}\right] \\ &= c_- e^{-\nu_- t} + c_+ e^{-\nu_+ t} \end{aligned} \tag{4.92}$$

  where $\kappa = \sqrt{(\gamma/2)^2 - \Omega^2} \in \mathbb{R}$ and $\nu_\pm = \gamma/2 \pm \kappa \in \mathbb{R}$.

- In the underdamped case ($\gamma < 2\Omega$)

$$\begin{aligned} F(t; 2\Omega/\gamma > 1) &= \frac{\lambda\Omega^2\hbar}{2\eta}\left[\left(\coth\left(\frac{i\beta\hbar\nu_-}{2}\right) - 1\right)e^{-\nu_- t} - \left(\coth\left(\frac{i\beta\hbar\nu_+}{2}\right) - 1\right)e^{-\nu_+ t}\right] \\ &= c_- e^{-\nu_- t} + c_+ e^{-\nu_+ t} \end{aligned} \tag{4.93}$$

  where $\eta = \sqrt{\Omega^2 - (\gamma/2)^2} \in \mathbb{R}$ and $\nu_\pm = \gamma/2 \pm i\eta \in \mathbb{C}$.

- In the critically damped case ($\gamma = 2\Omega$)

$$\begin{aligned} F(t; 2\Omega/\gamma = 1) &= \lambda\Omega\hbar\left[\left(\cot\left(\frac{\beta\hbar\Omega}{2}\right) - i\right)\Omega t e^{-\Omega t} + \frac{\beta\hbar\Omega}{2}\mathrm{cosec}^2\left(\frac{\beta\hbar\Omega}{2}\right)e^{-\Omega t}\right] \\ &= (c_t\Omega t + c_0)e^{-\Omega t}. \end{aligned} \tag{4.94}$$

The bath correlation function for the Debye spectral density is given by

$$C(t) = \lambda\omega_c\hbar\left[\cot\left(\frac{\beta\hbar\omega_c}{2}\right) - i\right]e^{-\omega_c t} + \frac{4\lambda\omega_c}{\beta}\sum_{k=1}^{\infty}\frac{\nu_k}{\nu_k^2 - \omega_c^2}e^{-\nu_k t}. \tag{4.95}$$

All four of these correlation functions contain an infinite sum over terms that decay exponentially with a Matsubara frequency, $\nu_k = 2\pi k/\beta\hbar$, that only depends on the temperature of the bath. These terms arise from the $\coth(\beta\hbar\omega/2)$ term in equation 4.88. In the classical limit, $\beta\hbar\omega \to 0$, this term becomes

$$\coth\left(\frac{\beta\hbar\omega}{2}\right) = \frac{2}{\beta\hbar\omega} \tag{4.96}$$

and no such Matsubara terms appear in the bath correlation functions. These Matsubara terms account for quantum mechanical corrections to the bath dynamics and are more important at lower temperatures.

The inclusion of the Matsubara terms is important for accurately capturing the influence of quantum mechanical effects in the bath on the dynamics of the system. However, this infinite series expansion is impractical. In order for the hierarchical equations of motion formalism to be practical it is necessary to truncate this contribution. Here this will be carried out using the standard approach based on a Markovian truncation of the Matsubara series.[8,195] The k-th term in the Matsubara expansion decays exponentially with rate $\nu_k = 2\pi k/\beta\hbar$. As k increases, the timescale over which the k-th Matsubara term contributions significantly to the correlation function decreases. For some value K, all Matsubara terms with $k > K$ will decay sufficiently quickly compared to the other timescales in the system that they may be treated as Markovian, they only contribute to the bath correlation function at $t = 0$. The Matsubara expansion may then be approximated by

$$\sum_{k=1}^{\infty} c_k\nu_k e^{-\nu_k t} \approx \sum_{k=1}^{K} c_k\nu_k e^{-\nu_k t} + \left(\sum_{k=K+1}^{\infty} c_k\right)\delta_+(t) \tag{4.97}$$

where $\delta_+(t)$ is the one-sided delta function. By increasing the value of K, this approximation can be made arbitrarily accurate.

Combining the above results, the bath correlation function arising from a spectral density of the form in Equation 4.39 can be approximated arbitrarily well by

$$C_j(t) = \Delta_j \delta_+(t) + \sum_{k=1}^{K_j^r} a_{jk} e^{-\zeta_{jk} t} + \sum_{k=1}^{K_j^c} \left(b_{jk}^+ e^{-\eta_{jk} t} + b_{jk}^- e^{-\eta_{jk}^* t} \right) + \sum_{k=1}^{K_j^l} c_{jk} \theta_{jk} t e^{-\theta_{jk} t} \quad (4.98)$$

with $\zeta_{jk}, \theta_{jk} \in \mathbb{R}$ and all coefficients and η_{jk}s arbitrary complex numbers.

4.4 Hierarchical Equations of Motion: Details

Introducing the superoperators

$$\tilde{\mathcal{V}}_j(t) = i\tilde{\mathcal{Q}}_j(t), \quad (4.99)$$

$$\tilde{\mathcal{U}}_j(t;\alpha,\beta) = i\Big[\alpha\tilde{\mathcal{Q}}_j^L(t) - \beta^*\tilde{\mathcal{Q}}_j^R(t)\Big], \quad (4.100)$$

and

$$\tilde{\mathcal{U}}_j(t;\alpha) = \tilde{\mathcal{U}}_j(t;\alpha,\alpha) = i\Big[\alpha\tilde{\mathcal{Q}}_j^L(t) - \alpha^*\tilde{\mathcal{Q}}_j^R(t)\Big], \quad (4.101)$$

and inserting the form of the bath correlation function given in equation 4.98 into equation 4.90 gives

$$\begin{aligned}\tilde{\rho}_S(t) = \mathcal{T}_{\leftarrow} \exp\Bigg\{ \frac{1}{\hbar^2} \sum_{j=1}^{M} \int_0^t \tilde{\mathcal{V}}_j(\tau) \Bigg[&\tilde{\mathcal{U}}_j(\tau;\Delta_j) + \sum_{k=1}^{K_j^r} \int_0^\tau \tilde{\mathcal{U}}_j(\tau';a_{jk}) e^{-\zeta_{jk}(\tau-\tau')} \mathrm{d}\tau' \\ &+ \sum_{k=1}^{K_j^c} \int_0^\tau \left(\tilde{\mathcal{U}}_j(t;b_{jk}^+,b_{jk}^-) e^{-\eta_{jk}(\tau-\tau')} + \tilde{\mathcal{U}}_j(t;b_{jk}^-,b_{jk}^+) e^{-\eta_{jk}^*(\tau-\tau')} \right) \mathrm{d}\tau' \\ &+ \sum_{k=1}^{K_j^l} \int_0^\tau \tilde{\mathcal{U}}_j(\tau';c_{jk}) \theta_{jk}(\tau-\tau') e^{-\theta_{jk}(\tau-\tau')} \mathrm{d}\tau' \Bigg] \mathrm{d}\tau \Bigg\} \tilde{\rho}_S(0). \end{aligned} \quad (4.102)$$

Alternatively, this can be written as

$$\tilde{\rho}_S(t) = \mathcal{T}_{\leftarrow} \prod_{j=1}^{M} \left[\tilde{\mathcal{G}}_j^{\delta}(t) \left(\prod_{k=1}^{K_j^r} \tilde{\mathcal{G}}_{jk}^r(t) \right) \left(\prod_{k=1}^{K_j^c} \tilde{\mathcal{G}}_{jk}^c(t) \right) \left(\prod_{k=1}^{K_j^l} \tilde{\mathcal{G}}_{jk}^l(t) \right) \right] \tilde{\rho}_S(0) \quad (4.103)$$

by introducing a set of superoperators, $\tilde{\mathcal{G}}_j^{\delta}$, $\tilde{\mathcal{G}}_{jk}^r$, $\tilde{\mathcal{G}}_{jk}^c$, and $\tilde{\mathcal{G}}_{jk}^l$, to account for terms arising from the different contributions to the bath correlation function. The first of these superoperators, accounting for the Markovian contributions, is defined by

$$\mathcal{T}_{\leftarrow} \tilde{\mathcal{G}}_j^{\delta}(t) = \mathcal{T}_{\leftarrow} \exp\left(\frac{1}{\hbar^2} \int_0^t \tilde{\mathcal{V}}_j(\tau) \tilde{\mathcal{U}}_j(\tau;\Delta_j) \mathrm{d}\tau \right) \quad (4.104)$$

with the remaining terms specified below.

In order to arrive at the final hierarchical equations of motion it is necessary to obtain an equation of motion for the system reduced density operator, $\tilde{\rho}_S(t)$. This requires the evaluation of derivatives of equation 4.102 with respect to time. This is a rather cumbersome process so here a set of auxiliary superoperators will be introduced to simplify the process.

4.4.1 Auxiliary Superoperators

Real Exponential Correlations

The contributions to equation 4.103 arising from the real exponential terms in the bath correlation function are given by

$$\mathcal{T}_{\leftarrow}\tilde{\mathcal{G}}^{r}_{jk}(t) = \mathcal{T}_{\leftarrow}\exp\left(\frac{1}{\hbar^2}\int_0^t \tilde{\mathcal{V}}_j(\tau)\int_0^\tau \tilde{\mathcal{U}}_j(\tau';a_{jk})e^{-\zeta_{jk}(\tau-\tau')}\mathrm{d}\tau'\mathrm{d}\tau\right) \tag{4.105}$$

$$= \mathcal{T}_{\leftarrow}\exp\left(-\frac{1}{\hbar}\int_0^t \tilde{\mathcal{V}}_j(\tau)\tilde{\mathcal{B}}^{r}_{jk}(\tau)\mathrm{d}\tau\right), \tag{4.106}$$

where the superoperator

$$\tilde{\mathcal{B}}^{r}_{jk}(\tau) = -\frac{1}{\hbar}\int_0^\tau \tilde{\mathcal{U}}_j(\tau';a_{jk})e^{-\zeta_{jk}(\tau-\tau')}\mathrm{d}\tau' \tag{4.107}$$

has been introduced to simplify the notation and will be referred to as the generating superoperator. Analogous generating superoperators will be required for the other contributions to the bath correlation function. Motivated by the form of this expression, a set of auxiliary influence superoperators for real exponential terms, indexed by a non-negative integer n, can be introduced

$$\mathcal{T}_{\leftarrow}\tilde{\mathcal{G}}^{r,n}_{jk}(t) = \mathcal{T}_{\leftarrow}\Big(\tilde{\mathcal{B}}^{r}_{jk}(t)^n\tilde{\mathcal{G}}^{r}_{jk}(t)\Big), \tag{4.108}$$

with $\tilde{\mathcal{G}}^{r}_{jk}(t) = \tilde{\mathcal{G}}^{r,0}_{jk}(t)$. Differentiating these superoperators with respect to time gives the equation of motion,

$$\mathcal{T}_{\leftarrow}\frac{\mathrm{d}}{\mathrm{d}t}\tilde{\mathcal{G}}^{r,n}_{jk}(t) = -\zeta_{jk}n\mathcal{T}_{\leftarrow}\tilde{\mathcal{G}}^{r,n}_{jk}(t) - \frac{n}{\hbar}\tilde{\mathcal{U}}_j(t;a_{jk})\mathcal{T}_{\leftarrow}\tilde{\mathcal{G}}^{r,n-1}_{jk}(t) - \frac{1}{\hbar}\tilde{\mathcal{V}}_j(t)\mathcal{T}_{\leftarrow}\tilde{\mathcal{G}}^{r,n+1}_{jk}(t), \tag{4.109}$$

where the time-ordered products have been partially expanded to take the $\tilde{\mathcal{U}}_j(t;a_{jk})$ and $\tilde{\mathcal{V}}_j(t)$ superoperator terms to the front. The time evolution of this superoperator with index n depends on its current value and the value of the superoperators with the index raised and lowered by one, $n \pm 1$.

Complex Exponential Correlations

In much the same manner as was done for real exponential correlations, we can define the superoperator arising from the conjugate pairs of complex exponentials by

$$\begin{aligned}\mathcal{T}_{\leftarrow}\tilde{\mathcal{G}}^{c}_{jk}(t) = \mathcal{T}_{\leftarrow}\exp\left\{\frac{1}{\hbar^2}\int_0^t \tilde{\mathcal{V}}_j(\tau)\int_0^\tau \Big(\tilde{\mathcal{U}}_j(t;b^+_{jk},b^-_{jk})e^{-\eta_{jk}(\tau-\tau')} \right.\\ \left. + \tilde{\mathcal{U}}_j(t;b^-_{jk},b^+_{jk})e^{-\eta^*_{jk}(\tau-\tau')}\Big)\mathrm{d}\tau'\mathrm{d}\tau\right\} \qquad (4.110)\end{aligned}$$

$$= \mathcal{T}_{\leftarrow}\exp\left(-\frac{1}{\hbar}\int_0^t \tilde{\mathcal{V}}_j(t)\Big(\tilde{\mathcal{B}}^{c+}_{jk}(\tau)+\tilde{\mathcal{B}}^{c-}_{jk}(\tau)\Big)\mathrm{d}\tau\right). \qquad (4.111)$$

At this stage it is again necessary to introduce a set of auxiliary superoperators, however here they are indexed by two non-negative integers, (n,m), defined by

$$\mathcal{T}_{\leftarrow}\tilde{\mathcal{G}}^{c,\{n,m\}}_{jk}(t) = \mathcal{T}_{\leftarrow}\Big(\tilde{\mathcal{B}}^{c+}_{jk}(t)^n\tilde{\mathcal{B}}^{c-}_{jk}(t)^m\tilde{\mathcal{G}}^{c}_{jk}(t)\Big). \qquad (4.112)$$

Differentiating these superators gives

$$\begin{aligned}\mathcal{T}_{\leftarrow}\frac{\mathrm{d}}{\mathrm{d}t}\tilde{\mathcal{G}}^{r,\{n,m\}}_{jk}(t) = &-\eta_{jk}n\mathcal{T}_{\leftarrow}\tilde{\mathcal{G}}^{c,\{n,m\}}_{jk}(t) - \frac{n}{\hbar}\tilde{\mathcal{U}}_j(t;b^+_{jk},b^-_{jk})\mathcal{T}_{\leftarrow}\tilde{\mathcal{G}}^{r,\{n-1,m\}}_{jk}(t)\\ &-\eta^*_{jk}m\mathcal{T}_{\leftarrow}\tilde{\mathcal{G}}^{c,\{n,m\}}_{jk}(t) - \frac{m}{\hbar}\tilde{\mathcal{U}}_j(t;b^-_{jk},b^+_{jk})\mathcal{T}_{\leftarrow}\tilde{\mathcal{G}}^{r,\{n,m-1\}}_{jk}(t)\\ &-\frac{1}{\hbar}\tilde{\mathcal{V}}_j(t)\mathcal{T}_{\leftarrow}\Big[\tilde{\mathcal{G}}^{r,\{n+1,m\}}_{jk}(t)+\tilde{\mathcal{G}}^{r,\{n,m+1\}}_{jk}(t)\Big],\end{aligned} \qquad (4.113)$$

the time derivatives of the superoperator with indices (n,m) depends on its value at time t and the values of the superoperators with indices $(n\pm1,m)$ and $(n,m\pm1)$.

4.4.2 Linear Exponential Correlations

A similar process can be performed to account for the remaining term in the bath correlation function (of the form $\gamma t e^{-\gamma t}$). The corresponding superoperator in

equation 4.103 is

$$\mathcal{T}_{\leftarrow}\tilde{\mathcal{G}}^{l}_{jk}(t) = \mathcal{T}_{\leftarrow}\exp\left(\frac{1}{\hbar^2}\int_0^t \tilde{\mathcal{V}}_j(\tau)\int_0^\tau \tilde{\mathcal{U}}_j(\tau';c_{jk})\theta_{jk}(\tau-\tau')e^{-\theta_{jk}(\tau-\tau')}\mathrm{d}\tau'\mathrm{d}\tau\right) \quad (4.114)$$

$$= \mathcal{T}_{\leftarrow}\exp\left(-\frac{1}{\hbar}\int_0^t \tilde{\mathcal{V}}_j(t)(\tau)\tilde{\mathcal{B}}^{l}_{jk}(\tau)\mathrm{d}\tau\right). \quad (4.115)$$

Now as the time derivative of the generating superoperator,

$$\tilde{\mathcal{B}}^{l}_{jk}(\tau) = -\frac{1}{\hbar}\int_0^\tau \tilde{\mathcal{U}}_j(\tau';c_{jk})\theta_{jk}(\tau-\tau')e^{-\theta_{jk}(\tau-\tau')}\mathrm{d}\tau', \quad (4.116)$$

is not just a multiple of itself or its integrand it is necessary to define a second generating superoperator,

$$\tilde{\mathcal{B}}^{lr}_{jk}(\tau) = -\frac{1}{\hbar}\int_0^\tau \tilde{\mathcal{U}}_j(\tau';c_{jk})e^{-\theta_{jk}(\tau-\tau')}\mathrm{d}\tau'. \quad (4.117)$$

A new set of auxiliary superoperators can be defined using these two generating superoperators, once again indexed by two non-negative integers (n, m), as

$$\mathcal{T}_{\leftarrow}\tilde{\mathcal{G}}^{l,\{n,m\}}_{jk}(t) = \mathcal{T}_{\leftarrow}\Big(\tilde{\mathcal{B}}^{l}_{jk}(t)^n\tilde{\mathcal{B}}^{lr}_{jk}(t)^m\tilde{\mathcal{G}}^{l}_{jk}(t)\Big). \quad (4.118)$$

The time-derivative of this operator may be evaluated giving

$$\begin{aligned}\mathcal{T}_{\leftarrow}\frac{\mathrm{d}}{\mathrm{d}t}\tilde{\mathcal{G}}^{l,\{n,m\}}_{jk}(t) = &-\theta_{jk}n\mathcal{T}_{\leftarrow}\tilde{\mathcal{G}}^{l,\{n,m\}}_{jk}(t) + \theta_{jk}n\mathcal{T}_{\leftarrow}\tilde{\mathcal{G}}^{l,\{n-1,m+1\}}_{jk}(t)\\ &-\theta_{jk}m\mathcal{T}_{\leftarrow}\tilde{\mathcal{G}}^{l,\{n,m\}}_{jk}(t) - \frac{m}{\hbar}\tilde{\mathcal{U}}_j(t;c_{jk})\mathcal{T}_{\leftarrow}\tilde{\mathcal{G}}^{l,\{n,m-1\}}_{jk}(t)\\ &-\frac{1}{\hbar}\tilde{\mathcal{V}}_j(t)\mathcal{T}_{\leftarrow}\tilde{\mathcal{G}}^{l,\{n+1,m\}}_{jk}(t).\end{aligned} \quad (4.119)$$

The resultant coupling pattern between these auxiliary superoperators is significantly different to those found before (i.e. in equations 4.109 and 4.113). The dynamics of the superoperator with indices (n, m) is directly coupled to the dynamics of the superoperators with indices $(n+1, m)$, $(n, m-1)$, and $(n-1, m+1)$. These auxiliary superoperators allow for a set of auxiliary density operators (ADOs) to be defined, whose dynamics couples to the dynamics of the system reduced density operators.

4.4.3 Auxiliary Density Operators

From these superoperators a set of auxiliary density operators (ADOs) can be defined with a similar functional form to the system reduced density operator in equation 4.103

$$\tilde{\sigma}_{\mathbf{n}}(t) = \mathcal{T}_{\leftarrow} \prod_{j=1}^{M} \left[\tilde{\mathcal{G}}_j^{\delta}(t) \left(\prod_{k=1}^{K_j^r} \tilde{\mathcal{G}}_{jk}^{r,\mathbf{n}_{jk}^r}(t) \right) \left(\prod_{k=1}^{K_j^c} \tilde{\mathcal{G}}_{jk}^{c\{\mathbf{n}_{jk}^c,\mathbf{m}_{jk}^c\}}(t) \right) \left(\prod_{k=1}^{K_j^l} \tilde{\mathcal{G}}_{jk}^{l\{\mathbf{n}_{jk}^l,\mathbf{m}_{jk}^l\}}(t) \right) \right] \tilde{\rho}_S(0). \tag{4.120}$$

Here $\mathbf{n} = \left\{ \mathbf{n}_1, \ldots \mathbf{n}_M \right\}$ is an array indexing the auxiliary density operators, with each element containing lists of indices for each bath. Each list of bath indices is given by

$$\mathbf{n}_j = \left\{ \mathbf{n}_j^r, \mathbf{n}_j^c, \mathbf{m}_j^c, \mathbf{n}_j^l, \mathbf{m}_j^l \right\} \tag{4.121}$$

$$= \left\{ n_{j1}^r, \ldots, n_{jK_j^r}^r, n_{j1}^c, m_{j1}^c, \ldots, n_{jK_j^c}^c, m_{jK_j^c}^c, n_{j1}^l, \ldots n_{jK_j^l}^l, m_{j1}^l, \ldots m_{jK_j^l}^l \right\}, \tag{4.122}$$

and contains the $K_j = K_j^e + 2K_j^l$ indices for the different auxiliary superoperator terms arising from the j-th bath correlation function, where $K_j^e = K_j^r + 2K_j^c$ is the total number of exponential terms in the bath correlation function. In the following discussion the notation n_{jk} will be used to correspond to the k-th element (or mode) of the flattened form, given in equation 4.122, of the list $\mathbf{n}_j$. By comparing the definition of these ADOs to the system reduced density operator given in equation 4.103, it can be seen that the ADO with all indices zero is the system reduced density operator

$$\tilde{\rho}_S(t) = \tilde{\sigma}_{\mathbf{0}}(t). \tag{4.123}$$

At $t = 0$, each of the generating superoperators ($\tilde{\mathcal{B}}_{jk}^r$, $\tilde{\mathcal{B}}_{jk}^c$, $\tilde{\mathcal{B}}_{jk}^l$, and $\tilde{\mathcal{B}}_{jk}^{lr}$) may be evaluated analytically, and are the zero superoperator. As such, all ADOs that are not the system reduced density operator are initially zero,

$$\tilde{\sigma}_{\mathbf{n}}(0) = 0. \tag{4.124}$$

4.4.4 Equations of Motion

Before obtaining the final equations of motion for these ADOs, it is useful to introduce three sets that account for the frequencies (exponents), coefficients, and complementary coefficients for each term in the bath correlation function. These sets each contain $K_j = K_j^r + 2K_j^c + K_j^l$ elements, and are given by

$$\boldsymbol{\nu}_j = \left\{\boldsymbol{\nu}_j^r, \boldsymbol{\nu}_j^c, \boldsymbol{\nu}_j^l\right\} = \left\{\zeta_{j1}, \ldots, \zeta_{jk}, \eta_{j1}, \eta_{j1}^*, \ldots, \eta_{jK_j^c}, \eta_{jK_j^c}^*, \theta_{j1}, \ldots, \theta_{jK_j^l}\right\} \tag{4.125}$$

$$\boldsymbol{\alpha}_j = \left\{\boldsymbol{\alpha}_j^r, \boldsymbol{\alpha}_j^c, \boldsymbol{\alpha}_j^l\right\} = \left\{a_{j1}, \ldots, a_{jk}, b_{j1}^+, b_{j1}^-, \ldots, b_{jK_j^c}^+, b_{jK_j^c}^-, c_{j1}, \ldots, c_{jK_j^l}\right\} \tag{4.126}$$

$$\overline{\boldsymbol{\alpha}}_j = \left\{\overline{\boldsymbol{\alpha}}_j^r, \overline{\boldsymbol{\alpha}}_j^c, \overline{\boldsymbol{\alpha}}_j^l\right\} = \left\{a_{j1}, \ldots, a_{jk}, b_{j1}^-, b_{j1}^+, \ldots, b_{jK_j^c}^-, b_{jK_j^c}^+, c_{j1}, \ldots, c_{jK_j^l}\right\}. \tag{4.127}$$

Differentiating equation 4.120 with respect to time and inserting the results obtained in Section 4.4.1 gives the hierarchical equations of motion in the interaction picture

$$\begin{aligned}
\frac{\mathrm{d}}{\mathrm{d}t}\tilde{\sigma}_{\mathbf{n}}(t) = \sum_{j=1}^{M}\Bigg\{ & \left[\frac{1}{\hbar^2}\tilde{\mathcal{V}}_j(t)\tilde{\mathcal{U}}_j(t;\Delta_j) - \sum_{k=1}^{K_j} n_{jk}\nu_{jk}\right]\tilde{\sigma}_{\mathbf{n}}(t) \\
& -\frac{1}{\hbar}\left[\tilde{\mathcal{V}}_j(t)\sum_{k=1}^{K_j^e}\tilde{\sigma}_{\uparrow_{\mathbf{n}}(n_{jk})}(t) + \sum_{k=1}^{K_j^e} n_{jk}\tilde{\mathcal{U}}_j(t;\alpha_{jk},\overline{\alpha}_{jk})\tilde{\sigma}_{\downarrow_{\mathbf{n}}(n_{jk})}(t)\right] \\
& -\frac{1}{\hbar}\left[\tilde{\mathcal{V}}_j(t)\sum_{k=1}^{K_j^l}\tilde{\sigma}_{\uparrow_{\mathbf{n}}(n_{jk}^l)}(t) + \sum_{k=1}^{K_j^l} m_{jk}^l\tilde{\mathcal{U}}_j(t;\alpha_{jk}^l)\tilde{\sigma}_{\downarrow_{\mathbf{n}}(m_{jk}^l)}(t)\right] \\
& +\sum_{k=1}^{K_j^l}\nu_{jk}^l n_{jk}^l\tilde{\sigma}_{\Vdash_{\mathbf{n}}(n_{jk}^l,m_{jk}^l)}(t)\Bigg\}.
\end{aligned} \tag{4.128}$$

Here the notation $\uparrow_{\mathbf{n}}\!\left(i\right)/\downarrow_{\mathbf{n}}\!\left(i\right)$, and $\Vdash_{\mathbf{n}}\!\left(i,j\right)$ denotes the set of indices obtained after incrementing/decrementing the element $i \in \mathbf{n}$, and the set of indices obtained after the element $i \in \mathbf{n}$ is decremented and the element $j \in \mathbf{n}$ is incremented. Converting to the Schrödinger picture and reintroducing the Hilbert space representation of these superoperators, gives the hierarchical equations of motion for a system coupled to M harmonic oscillator baths, each with a spectral density of the form

given in equation 4.39:[8,187,197]

$$\begin{aligned}\frac{\mathrm{d}}{\mathrm{d}t}\hat{\sigma}_{\mathbf{n}}(t) = &-\frac{i}{\hbar}\left[\hat{H}_S, \hat{\sigma}_{\mathbf{n}}(t)\right] - \sum_{j=1}^{M}\left\{\sum_{k=1}^{K_j}(n_{jk}\nu_{jk})\hat{\sigma}_{\mathbf{n}}(t) + \frac{1}{\hbar^2}\left[\hat{Q}_j, \left(\Delta_j\hat{Q}_j\hat{\sigma}_{\mathbf{n}}(t) - \Delta_j^*\hat{\sigma}_{\mathbf{n}}(t)\hat{Q}_j\right)\right]\right. \\ &-\frac{i}{\hbar}\sum_{k=1}^{K_j^e}\left(\left[\hat{Q}_j, \hat{\sigma}_{\uparrow_{\mathbf{n}}(\mathbf{n}_{jk})}(t)\right] + n_{jk}\alpha_{jk}\hat{Q}_j\hat{\sigma}_{\downarrow_{\mathbf{n}}(\mathbf{n}_{jk})}(t) - n_{jk}\overline{\alpha}_{jk}^*\hat{\sigma}_{\downarrow_{\mathbf{n}}(\mathbf{n}_{jk})}(t)\hat{Q}_j\right) \\ &-\frac{i}{\hbar}\sum_{k=1}^{K_j^l}\left(\left[\hat{Q}_j, \tilde{\sigma}_{\uparrow_{\mathbf{n}}(n_{jk}^l)}(t)\right] + m_{jk}^l\alpha_{jk}^l\hat{Q}_j\tilde{\sigma}_{\downarrow_{\mathbf{n}}(m_{jk}^l)}(t) - m_{jk}^l\overline{\alpha}_{jk}^{l*}\tilde{\sigma}_{\downarrow_{\mathbf{n}}(m_{jk}^l)}(t)\hat{Q}_j\right) \\ &\left.+\sum_{k=1}^{K_j^l}\nu_{jk}^l n_{jk}^l\tilde{\sigma}_{\|_{\mathbf{n}}(n_{jk}^l, m_{jk}^l)}(t)\right\}.\end{aligned} \tag{4.129}$$

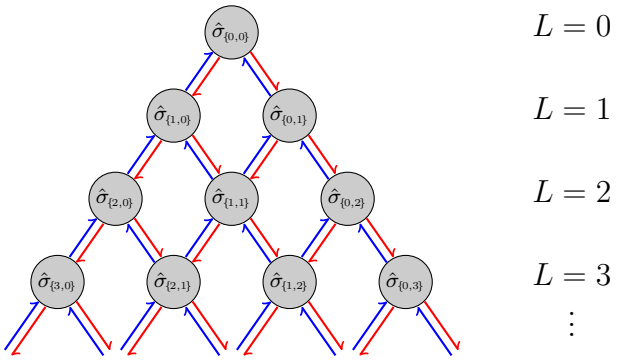

Figure 4.2: The coupling of auxiliary density operators arising from two exponential terms in the bath correlation function. There are two distinct types of coupling: the raising terms (depicted in red) describing the influence of an ADO in level L on ADOs in level $L+1$ and the lowering terms (depicted in blue) in which ADOs in level L influence the dynamics of ADOs in level $L-1$.

The terms on the first line of equation 4.129 account for the coherent evolution of the ADOs under the system Hamiltonian, an exponential decay (or exponentially damped oscillation) arising from the non-Markovian contributions to the bath correlation function, and the Markovian contribution to the dynamics, respectively. By considering the other terms in this equation the hierarchical nature becomes clear. An ADO indexed by $\mathbf{n}$ is in a given level of the hierarchy, defined by

$$L_{\mathbf{n}} = \sum_{j=1}^{M}\sum_{k=1}^{K_l} n_{jk}. \tag{4.130}$$

First, consider the terms in the second line of equation 4.129. These terms, arising from exponential contributions to the bath correlation function, introduce coupling between ADOs in different levels. The ADOs in level L are coupled to ADOs in levels $L-1$ and $L+1$ where one of the indices for the exponential coupling terms has been decremented or incremented by one. The first term on the second line accounts for the interaction of ADOs in level $L+1$ with those in level L, which will be referred to as lowering terms. The final two terms, describing the interaction of ADOs in level $L-1$ with those in level L, will be referred to as raising terms. This coupling scheme is illustrated in figure 4.2 for the case of two exponential terms in the bath correlation function.

The final two lines of equation 4.129 contain the terms arising from the linear exponential correlations that couple different ADOs. Here, there are three distinct contributions: the raising and lowering terms of the same form found for exponential correlations, and a transfer term (on the last line) that couples ADOs in the same level. For the linear exponential contributions to the bath correlation function, the lowering terms act only on the first index (n^l), while the raising terms act only on the second index (m^l). The ADOs with higher values of m only influence those with lower values indirectly through terms which lower the n index and transfer terms which lower the n index and raise the m index. This coupling scheme is illustrated in figure 4.3.

4.4.5 Truncation of the Hierarchy

In each level of the hierarchical expansion the total number of ADOs is given by

$$\binom{L+K-1}{L} = \frac{(L+K-1)!}{L!(K-1)!} \tag{4.131}$$

where $K = \sum_{j=1}^{M} K_j$ is the total number of integers required to index the ADO. This illustrates the importance of the Markovian truncation of the Matsubara series given in equation 4.97. The number of ADOs at layer $L = 1$ is K, if the Markovian truncation were not used then $K \to \infty$ and the dynamics of the reduced density

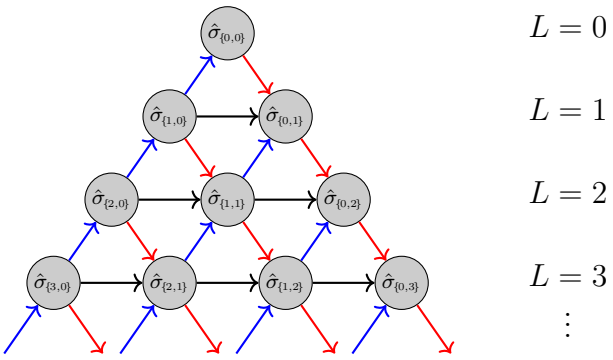

Figure 4.3: The coupling of auxiliary density operators arising from terms of the form $\gamma t e^{-\gamma t}$ in the bath correlation function. Here there are three distinct types of coupling: the raising (depicted in red) and lowering terms (depicted in blue) that were also seen for the case of an exponential bath correlation function and an additional transfer term (depicted by black arrows) in which ADOs on the same level interact.

operator is coupled to an infinite number of first level ADOs (each of which are themselves coupled to an infinite number of ADOs). This is clearly undesirable as the aim of this approach is to arrive at a practical numerical method. The parameter K can be considered as a convergence parameter that would ideally be as small as possible. As K increases, the number of ADOs increase rapidly and the resultant HEOM becomes computationally expensive. In what follows, K will be referred to as the number of modes of the HEOM, with each mode corresponding to a single index n_{jk} in bath j.

As presented here, the hierarchy continues to $L \to \infty$ and so equation 4.129 describes an infinite system of equations. As the goal is to obtain a practical method for simulating the dynamics of harmonic bath systems, this is undesirable and it is necessary to truncate the hierarchy. The standard truncation scheme is based on the observation that for deep enough layers of the hierarchy, $n_{jk}\nu_{jk}$ is large compared to the frequencies involved in the system Hamiltonian.[8,195] Equation 4.129 can be formally solved to give

$$\hat{\sigma}^{\mathbf{n}}(t) = \int_0^t \tilde{\mathcal{K}}^{\mathbf{n}}(t-\tau)\hat{Y}^{\mathbf{n}}(\tau)\mathrm{d}\tau, \tag{4.132}$$

where the memory kernel is given by

$$\tilde{\mathcal{K}}^{\mathbf{n}}(t-\tau)=\exp\left[-\left(\frac{i}{\hbar}\mathcal{L}_S+\sum_{j=1}^{M}\left(\sum_{k=1}^{K_j}n_{jk}\nu_{jk}+\frac{1}{\hbar^2}\tilde{\mathcal{Q}}_j\left[\Delta_j\tilde{\mathcal{Q}}_j^L-\Delta_j^*\tilde{\mathcal{Q}}_j^R\right]\right)\right)(t-\tau)\right], \tag{4.133}$$

and $\hat{Y}^{\mathbf{n}}(\tau)$ accounts for all terms in the final three lines of equation 4.129. In addition to the coherent evolution and Markovian truncation term, the memory kernel contains an exponential decaying contribution with rate

$$\nu^{\mathbf{n}}=\sum_{j=1}^{M}\sum_{k=1}^{K_j}n_{jk}\nu_{jk}. \tag{4.134}$$

If $\nu^{\mathbf{n}}$ is sufficiently large compared to the frequencies present in the system Liouvillian, then over the timescale of the system dynamics this term can be treated as Markovian,

$$\nu^{\mathbf{n}}e^{-\nu^{\mathbf{n}}(t-\tau)}\approx\delta_+(t-\tau). \tag{4.135}$$

Inserting this into equation 4.132, the integral over τ may now be evaluated to give

$$\hat{\sigma}^{\mathbf{n}}(t)=\hat{Y}^{\mathbf{n}}(t)/\nu^{\mathbf{n}}. \tag{4.136}$$

This may be inserted into equation 4.129 to give

$$\frac{\mathrm{d}}{\mathrm{d}t}\hat{\sigma}_{\mathbf{n}}(t)=-\frac{i}{\hbar}\left[\hat{H}_S,\hat{\sigma}_{\mathbf{n}}(t)\right]-\frac{1}{\hbar^2}\left[\hat{Q}_j,\left(\Delta_j\hat{Q}_j\hat{\sigma}_{\mathbf{n}}(t)-\Delta_j^*\hat{\sigma}_{\mathbf{n}}(t)\hat{Q}_j\right)\right]. \tag{4.137}$$

The dynamics of this auxiliary density operator does not depend on any of the others. As these auxiliary density operators are initially zero, they remain as such for all time.

The Markovian approximation discussed above is typically applied to all ADOs with $L>N$ for some value of N.[8,195] This truncates the hierarchical equations of motion at layer $L=N$. All ADOs with a larger L are zero for all time and, as a result, the raising terms no longer influence the dynamics of the ADOs in layer $L=N$. The resultant set of auxiliary density operators can be represented by lattice points in the $(K+1)$-simplex (the generalisation of the equilateral triangle, 2-simplex, and

regular tetrahedron, 3-simplex, to $K+1$ dimensions). This provides an easy scheme for indexing the ADOs that allows for an efficient implementation of the equations of motion (equation 4.129). However, whether or not a HEOM calculation is feasible depends strongly on the value of N required for the Markovian truncation to be valid. For a given value of N, the total number of ADOs in this expansion is given by

$$N_{ados}(N,K) = \sum_{L=0}^{N} \binom{L+K-1}{L} = \binom{N+K}{N} = \frac{(N+K)!}{N!K!}. \tag{4.138}$$

As a result, the number of ADOs required using this truncation scheme increases rapidly with N and even more so as the number of terms included in the bath correlation function, K, increases. Depending on the problem considered, the number of ADOs retained using this scheme may be infeasibly large, and alternative schemes are then required.

The Markovian truncation of the hierarchy employs the approximation given in equation 4.135, which is valid provided

$$\mathrm{Re}\left(\sum_{j=1}^{M}\sum_{k=1}^{K_j} n_{jk}\nu_{jk}\right) \gg \omega_S, \tag{4.139}$$

where ω_S is the largest frequency associated with the system dynamics. Within the standard truncation scheme the value N is typically chosen to ensure that[8,195]

$$\sum_{j=1}^{M}\sum_{k=1}^{K_l} n_{jk} \gg \frac{\omega_S}{|\min(\mathrm{Re}(\nu_{jk}))|}. \tag{4.140}$$

This is a sufficient condition to ensure that equation 4.139 is satisfied for all ADOs it is employed for but it is not necessary. As the ν_{jk} terms can vary considerably between the different modes, some ADOs will have memory kernels (equation 4.133) that are damped considerably more rapidly than others, and much more than required to apply the Markovian approximation. As a result, in many cases a large number of the ADOs are ~ 0 for all time and could have been excluded.

An alternative truncation scheme is suggested by equation 4.139. The Markovian truncation should be applied to all ADOs where

$$\mathrm{Re}\left(\sum_{j=1}^{M}\sum_{k=1}^{K_j} n_{jk}\nu_{jk}\right) > \Gamma \tag{4.141}$$

for some Γ that is large compared to the system Hamiltonian and system-bath coupling.[182] This truncation criterion can also be applied to the truncation of the Matsubara modes, and so rather than needing to specify the number of Matsubara modes and depth of the hierarchy only the Γ parameter is required. This scheme often results in considerably smaller hierarchies than the standard approach[182] and will be used in what follows.

Regardless of the truncation scheme employed, it is necessary to converge the resultant dynamics with respect to the truncation parameter. Once this truncation has been performed, the resultant system of first order linear differential equations can be solved using standard numerical integration schemes.

4.5 Application: Radical Pair Recombination Dynamics

The radical pair mechanism, which has been discussed in the previous two chapters, has found widespread use in explaining magnetic field effects arising in systems ranging from magnetoreceptors,[9,10] to organic semiconductors,[11,12] and molecular wires.[25] Within this model, a reaction proceeds via an intermediate radical pair that is formed with the electron spins in an initially correlated state. The electron spins evolve coherently due to magnetic interactions within the radicals (see Section 2.2.2), interconverting between singlet and triplet electron spin states. When in a singlet state the radical pair can recombine to form a singlet product with rate k_S, while when in a triplet state it can recombine to form a triplet product with rate k_T. The interplay between the coherent dynamics arising from the magnetic interactions and the incoherent recombination process allows for (potentially weak) magnetic fields to significantly alter the relative yields of these reactions.

Conventionally, the dynamics of radical pairs is modelled using the (phenomenological) Haberkorn master equation for the spin density operator,

$$\frac{\mathrm{d}}{\mathrm{d}t}\hat{\rho}_s(t) = -\frac{i}{\hbar}\left[\hat{H}_s, \hat{\rho}_s(t)\right] - \left\{\hat{K}, \hat{\rho}_s(t)\right\}. \tag{4.142}$$

Here $\hat{H}_s$ is the spin Hamiltonian, and $\hat{K}$ is the Haberkorn recombination operator (equation 2.63). Although this form of the master equation has found widespread use over the past 40 years, recently there has been some debate on whether it is the correct master equation for treating radical pair recombination, and a number of alternatives have been proposed.[46–49] These alternative master equations differ from the Haberkorn form in how they treat singlet-triplet coherences. As an example, the Jones-Hore master equation[46,47] introduces an additional singlet-triplet dephasing contribution to equation 4.142 of the form

$$\frac{k_S + k_T}{2}\left[\hat{P}_S\hat{\rho}(t)\hat{P}_T + \hat{P}_T\hat{\rho}(t)\hat{P}_S\right]. \tag{4.143}$$

As a result, the Jones-Hore master equation predicts dephasing of singlet-triplet coherences at a rate of $k_{ST} = k_S + k_T$, twice that of the Haberkorn treatment.

Recently Fay *et al.* have derived a series of quantum master equations (QMEs) starting from a microscopic model of a radical ion pair recombination reaction.[33] In the derivation of these equations a number of approximations were made. In the following discussion the validity of these approximations will be explored by considering the dynamics of a set of model radical ion pair recombination reactions obtained using the resultant QMEs and the numerically exact HEOM approach. Firstly, however, the model considered and the QMEs need to be discussed.

4.5.1 Model Radical Ion Pair

In reference [33], Fay *et al.* presented a microscopic model for the recombination dynamics of a radical ion pair that is closely related to the electron transfer model discussed above. A system consisting of an electron donor, D, and electron acceptor,

A, is excited to form the radical ion pair, $D^{\bullet+}A^{\bullet-}$. This radical ion pair is then free to undergo coherent interconverion between its singlet and triplet states and spin-selective electron transfer reactions to form singlet or triplet product states. This system can be described by considering two sets of diabatic electron states: $\{|0\rangle|S\rangle, |0\rangle|T_\alpha\rangle\}$, corresponding to singlet and triplet radical pair states which are assumed to be close in energy, and $\{|1\rangle|S\rangle, |1\rangle|T_\alpha\rangle\}$, corresponding to the singlet and triplet product states. To ensure conservation of spin in the electron transfer reactions only radical and product states with the same spin are coupled. The Hamiltonian describing this model,

$$\begin{aligned}\hat{H}_f = \hat{H}_0|0\rangle\langle 0| + \hat{H}_1|1\rangle\langle 1| + \Delta_S\hat{P}_S\Big(\hat{f}_S|0\rangle\langle 1| + \hat{f}_S^\dagger|1\rangle\langle 0|\Big) \\ + \Delta_T\hat{P}_T\Big(\hat{f}_T|0\rangle\langle 1| + \hat{f}_T^\dagger|1\rangle\langle 0|\Big)\end{aligned} \tag{4.144}$$

depends on all spin, electron and nuclear degrees of freedom for the system. Here the nuclear degrees of freedom refer to the nuclear positions and momenta, not the nuclear spins. In equation 4.144 $\hat{P}_S$ and $\hat{P}_T$ are the singlet and triplet projection operators, respectively; the $\hat{H}_i$ operators correspond to the combined spin and nuclear Hamiltonian for electronic state i, and the operators $\hat{f}_S$ and $\hat{f}_T$ are the diabatic coupling operators between the singlet and triplet radical pair and product states, respectively. In general, these operators are arbitrary functions of the nuclear degrees of freedom.[33] A schematic of this model is shown in figure 4.4.

The radical pair Hamiltonian, $\hat{H}_0$, can be decomposed into three terms

$$\hat{H}_0 = \hat{H}_{0s} + \hat{H}_{0n} + \hat{H}_{0ns} \tag{4.145}$$

corresponding to a spin term, a nuclear term, and a nuclear-spin coupling term, respectively. Following reference [33], the triplet recombination pathway will be ignored to simplify the treatment. In doing so, the product Hamiltonian can be written as

$$\hat{H}_1 = \hat{P}_S\hat{H}_{1n} \tag{4.146}$$

where $\hat{H}_{1n}$ acts only on the nuclear degrees of freedom.

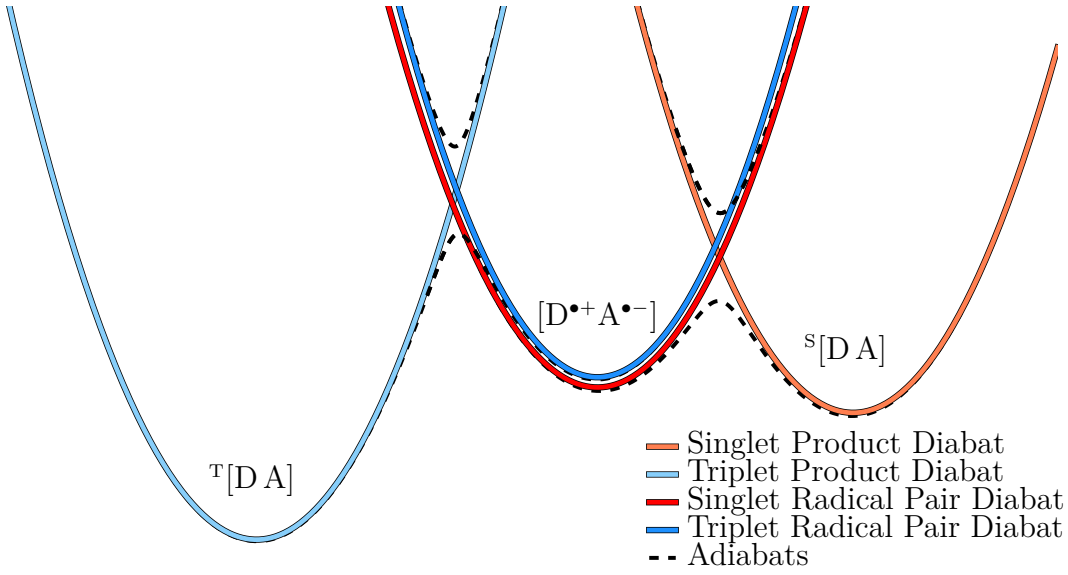

Figure 4.4: A schematic diabatic potential energy surface diagram for the radical ion pair system. The singlet and triplet radical pair diabats are very close in energy, while the singlet and triplet products states have minima at significantly different nuclear configurations. Transitions between the singlet and triplet radical pair diabats arise due to the spin interactions present. In order to ensure conservation of spin the singlet(triplet) radical pair diabat is only directly coupled to singlet(triplet) product diabat. The adiabatic potentials arising from this model are shown in black.

4.5.2 Quantum Master Equations

The dynamics of the ensemble of radical ion pairs can be described using the density operator for all spin, nuclear and electronic degrees of freedom, $\rho(t)$. However, evaluating the exact evolution of all degrees of freedom is typically impractical, and for many applications, unnecessary. In the context of radical pair recombination reactions it is typically only the dynamics of the radical pair electron spins and product states that are of interest.[15] Fay *et al.*[33] derived, by using standard projection operator techniques,[198,199] a series of quantum master equations (QMEs) describing the evolution of the reduced density operators for the spin degrees of freedom of the radical pair and product states for the model above. The final master equations, which are valid provided the spin dynamics is much slower than the nuclear dynamics (incoherent rate approximation), and the energy scale associated with $\hat{H}_{0s}$ is considerably smaller than that of $\hat{H}_{0n}$ (field independent rate approximation), were obtained by considering a perturbative expansion in the

diabatic coupling, Δ_S.

To second order in the diabatic coupling, the radical pair spin density operator, $\hat{\rho}_{0s}(t)$, and the product spin density operator, $\hat{\rho}_{1s}(t)$, evolve according to the master equations[33]

$$\begin{aligned}\frac{\mathrm{d}}{\mathrm{d}t}\hat{\rho}_{0s}(t) =& -\frac{i}{\hbar}\left[\hat{H}_{0s}, \hat{\rho}_{0s}(t)\right] - \frac{1}{2}\left\{k_f^{(2)}\hat{P}_S, \hat{\rho}_{0s}(t)\right\} \\ & - \frac{i}{\hbar}\left[-2J^{(2)}\hat{\boldsymbol{S}}_1\cdot\hat{\boldsymbol{S}}_2, \hat{\rho}_{0s}(t)\right] + k_b^{(2)}\hat{P}_S\hat{\rho}_{1s}(t)\hat{P}_S\end{aligned} \tag{4.147}$$

$$\frac{\mathrm{d}}{\mathrm{d}t}\hat{\rho}_{1s}(t) = k_f^{(2)}\hat{P}_S\hat{\rho}_{0s}(t)\hat{P}_S - k_b^{(2)}\hat{\rho}_{1s}(t). \tag{4.148}$$

The first term in the QME for the radical pair spin density operator accounts for the standard coherent evolution under the spin Hamiltonian. The second term is the Haberkorn recombination superoperator term with singlet recombination rate $k_S = k_f^{(2)}$ and triplet recombination rate $k_T = 0$. The third term describes an additional contribution to the coherent evolution arising from a reactive exchange coupling, $J^{(2)}$. The final term accounts for the back-reaction from the singlet product state, which occurs with rate $k_b^{(2)}$. If the product and radical pair states are sufficiently well separated in energy, the back-reaction terms can be ignored and these equations reduce to the Haberkorn master equation with an additional reactive exchange coupling interaction.[33]

Including all fourth order terms in the perturbative expansion in Δ_S gives the QME[33]

$$\begin{aligned}\frac{\mathrm{d}}{\mathrm{d}t}\hat{\rho}_{0s}(t) =& -\frac{i}{\hbar}\left[\hat{H}_{0s}, \hat{\rho}_{0s}(t)\right] - \frac{1}{2}\left\{k_f\hat{P}_S, \hat{\rho}_{0s}(t)\right\} - \frac{i}{\hbar}\left[-2J\hat{\boldsymbol{S}}_1\cdot\hat{\boldsymbol{S}}_2, \hat{\rho}_{0s}(t)\right] \\ & - k_d\left(\hat{P}_S\hat{\rho}_{0s}(t)\hat{P}_T + \hat{P}_T\hat{\rho}_{0s}(t)\hat{P}_S\right) + k_b\hat{P}_S\hat{\rho}_{1s}(t)\hat{P}_S\end{aligned} \tag{4.149}$$

$$\frac{\mathrm{d}}{\mathrm{d}t}\hat{\rho}_{1s}(t) = k_f\hat{P}_S\hat{\rho}_{0s}(t)\hat{P}_S - k_b\hat{\rho}_{1s}(t), \tag{4.150}$$

where $k_f = k_f^{(2)} + k_f^{(4)}$, $k_b = k_b^{(2)} + k_b^{(4)}$, $J = J^{(2)} + J^{(4)}$, and $k_d = k_d^{(4)}$ contain second and fourth order contributions. In addition to the terms found in the second order QME, the fourth order QME includes a singlet-triplet dephasing term with the same form as found in the Jones-Hore master equation.[46,47] When $k_d = (k_f^S + k_f^T)/2$, this becomes the Jones-Hore master equation; however, in general the dephasing

rate depends on the dynamics of the bath and the strength of the coupling between the adiabatic surfaces. In particular, in the nonadiabatic limit, the dephasing rate is 0, and this master equation reduces to the Haberkorn master equation with an additional reactive exchange coupling. For the second and fourth order master equations the recombination rates, dephasing rates, and reactive exchange coupling constant can be expressed in terms of time integrals of correlation functions of bath operators.[33] Including higher order terms in the perturbative expansion alters the form of the expressions for the rate constants and exchange coupling constant, it does not alter the form of the QME. That is, the QME obtained at arbitrary order in the diabatic couplings has the form given in equation 4.149.[33]

Three key approximations were made in the derivation of these QMEs: the incoherent recombination approximation, the field independent rate approximation, and a perturbative expansion. In order to explore the validity of these approximations, a simplified model is considered here for which numerically exact results can be obtained for comparison using the HEOM formalism.

4.5.3 Harmonic Bath Model

In general, it is infeasible to evaluate the dynamics arising from the Hamiltonian given by equation 4.144 for arbitrary diabatic potential energy surfaces and coupling operators. Here, a simplified model will be considered in which the diabatic potential energy surfaces (contained with $\hat{H}_{in}$) are treated as a set of uncoupled, displaced harmonic oscillators. Additionally, the Condon approximation will be made and so the diabatic coupling operators ($\hat{f}_S$ and $\hat{f}_T$) are taken to be independent of the nuclear coordinates.[91] Below, $\hat{f}_S$ will be taken to be the identity operator.

The nuclear Hamiltonians for each diabat is given by

$$\hat{H}_{0n} = \sum_{\alpha=1}^{N_b} \left[\frac{\hat{p}^2}{2m_\alpha} + \frac{1}{2} m_\alpha \omega_\alpha^2 \hat{q}_\alpha^2 + c_\alpha \hat{q}_\alpha \right] \tag{4.151}$$

$$\hat{H}_{1n} = \sum_{\alpha=1}^{N_b} \left[\frac{\hat{p}^2}{2m_\alpha} + \frac{1}{2} m_\alpha \omega_\alpha^2 \hat{q}_\alpha^2 - c_\alpha \hat{q}_\alpha \right] - \epsilon \tag{4.152}$$

where ϵ is the energy bias between the two diabats, $\hat{q}_\alpha$ and $\hat{q}_\alpha$ are the position and momentum operators for bath mode α, and m_α, ω_α, and c_α are the mass, angular frequency and coupling constant of this mode. Inserting this form for the diabatic nuclear Hamiltonian into equation 4.144, the full Hamiltonian may be written as a sum of a term acting on the system (electronic and spin) degrees of freedom, $\hat{H}_S$, a term acting on the bath (nuclear) degrees of freedom, $\hat{H}_B$, and a system-bath coupling term, $\hat{H}_{SB}$:

$$\hat{H}_S = \hat{H}_{0s} \left|0\right\rangle \left\langle 0\right| - \epsilon \hat{P}_S \left|1\right\rangle \left\langle 1\right| + \Delta_S \hat{P}_S \left(\left|0\right\rangle \left\langle 1\right| + \left|1\right\rangle \left\langle 0\right|\right) \tag{4.153}$$

$$\hat{H}_{SB} = \sum_{\alpha=1}^{N_b} \left(c_\alpha \hat{q}_\alpha \left|0\right\rangle \left\langle 0\right| - c_\alpha \hat{q}_\alpha \hat{P}_S \left|1\right\rangle \left\langle 1\right|\right) \tag{4.154}$$

$$\hat{H}_B = \sum_{\alpha=1}^{N_b} \left[\frac{\hat{p}^2}{2m_\alpha} + \frac{1}{2} m_\alpha \omega_\alpha^2 \hat{q}_\alpha^2\right]. \tag{4.155}$$

Here $\hat{H}_{0s}$ is a Hamiltonian acting only on spin degrees of freedom. In the limit of an infinite bath ($N_b \to \infty$), the spectral density that describes the influence of the bath on the system becomes a continuous function of frequency. This will be taken to be the Debye spectral density

$$J\left(\omega\right) = \frac{\Lambda}{2} \frac{\omega \omega_c}{\omega_c^2 + \omega^2}. \tag{4.156}$$

This model is a generalisation of the spin-boson model discussed in Section 4.2.1 that includes additional diabatic states that account for the different spin degrees of freedom. As such, the dynamics for this model can be obtained using the HEOM approach.

Initial Bath State

In deriving the QME given by equations 4.147 and 4.149, Fay *et al.* employed an uncorrelated initial condition for the density operator for the full system. It was assumed that there are no initial coherences between the electronic and nuclear states of the system, and that the nuclear degrees of freedom are in thermal equilibrium on each diabatic surface at inverse temperature, β. If the system is

initially in a radical pair state, with no population on the product states, the full density operator may be written as[33]

$$\hat{\rho}(0) = \hat{\rho}_{0s}(0) \otimes \hat{\rho}_{0n} \tag{4.157}$$

where

$$\hat{\rho}_{0n} = \frac{\exp\left(-\beta \hat{H}_{0n}\right)}{\mathrm{tr}\left[\exp\left(-\beta \hat{H}_{0n}\right)\right]_n}. \tag{4.158}$$

Within the HEOM formalism, the bath and system degrees of freedom are initially uncorrelated; however, the bath is initially in thermal equilibrium with respect to the bath Hamiltonian $\hat{H}_B$. This is a different initial condition, and it is therefore necessary to modify the model used for the HEOM so that the correct initial condition is used.

Having ignored the triplet product diabat, it is only necessary to consider the 3 diabatic states $|0\rangle|S\rangle$, $|0\rangle|T\rangle$, and $|1\rangle|S\rangle$. Working in this reduced diabatic basis, the identity operator on the diabatic states may be expressed as

$$\mathbf{1} = |0\rangle\langle 0| + \hat{P}_S |1\rangle\langle 1|. \tag{4.159}$$

Inserting this into the system-bath Hamiltonian 4.166 gives

$$\hat{H}_{SB} = \sum_{\alpha=1}^{N_b} \left(c_\alpha \hat{q}_\alpha \mathbf{1} - 2 c_\alpha \hat{q}_\alpha \hat{P}_S |1\rangle\langle 1| \right). \tag{4.160}$$

The first term in this expression is independent of the nuclear configuration and can therefore be treated as a contribution to the bath Hamiltonian (equation 4.155) giving

$$\hat{H}_B = \sum_{\alpha=1}^{N_b} \left[\frac{\hat{p}^2}{2m_\alpha} + \frac{1}{2} m_\alpha \omega_\alpha^2 \hat{q}_\alpha^2 + c_\alpha \hat{q}_\alpha \right]. \tag{4.161}$$

Completing the square and defining

$$\hat{\tilde{q}}_\alpha = \hat{q}_\alpha + \frac{c_\alpha}{m_\alpha \omega_\alpha^2}, \tag{4.162}$$

the system-bath and bath Hamiltonians may be rewritten as

$$\hat{H}_{SB} = \sum_{\alpha=1}^{N_b} \left(-2c_\alpha \hat{\tilde{q}}_\alpha + \frac{2c_\alpha^2}{m_\alpha \omega_\alpha^2} \right) \hat{P}_S \left|1\right\rangle \left\langle 1\right| \tag{4.163}$$

$$\hat{H}_B = \sum_{\alpha=1}^{N_b} \left[\frac{\hat{p}^2}{2m_\alpha} + \frac{1}{2} m_\alpha \omega_\alpha^2 \hat{\tilde{q}}_\alpha^2 - \frac{c_\alpha^2}{2m_\alpha \omega_\alpha^2} \right]. \tag{4.164}$$

The final term in the bath Hamiltonian is an unimportant energy shift and so may be ignored, while the newly introduced term in the system-bath coupling Hamiltonian is independent of the nuclear position and may be moved to the system Hamiltonian. Doing so and using the expression for the reorganisation energy given in equation 4.33, the overall Hamiltonian for the system may be written in terms of the new Hamiltonians

$$\hat{H}_S = \hat{H}_{0s} \left|0\right\rangle \left\langle 0\right| + (\Lambda - \epsilon) \hat{P}_S \left|1\right\rangle \left\langle 1\right| + \Delta_S \hat{P}_S \left(\left|0\right\rangle \left\langle 1\right| + \left|1\right\rangle \left\langle 0\right| \right) \tag{4.165}$$

$$\hat{H}_{SB} = -2 \sum_{\alpha=1}^{N_b} c_\alpha \hat{\tilde{q}}_\alpha \hat{P}_S \left|1\right\rangle \left\langle 1\right| \tag{4.166}$$

$$\hat{H}_B = \sum_{\alpha=1}^{N_b} \left[\frac{\hat{p}^2}{2m_\alpha} + \frac{1}{2} m_\alpha \omega_\alpha^2 \hat{\tilde{q}}_\alpha^2 \right]. \tag{4.167}$$

This Hamiltonian is, up to an arbitrary energy shift, the same as the Hamiltonian defined by equations 4.153-4.155, however here $\hat{H}_B = \hat{H}_{0n}$. As a result, HEOM calculations using this Haminltonian will now have an initial condition that corresponds to an uncorrelated system and bath, with the bath in thermal equilibrium with respect to the $\left|0\right\rangle$ diabatic state of the original problem. The transformed Hamiltonian corresponds to a system in which the product diabat is raised in energy by the reorganisation energy, Λ, and couples to the bath twice as strongly, while the radical pair diabats are uncoupled. By altering the form of the Hamiltonian an alternative definition of the auxiliary density operators has been obtained that allows for a different initial bath state to be considered. This approach can be applied to arbitrarily shift the initial bath equilibrium position. Unfortunately, this shifting gives rise to an increase in the coupling strength and as a result may lead to an increase in the size of the hierarchy required to obtain converged results.

Spin Systems

Here two model radical ion pairs will be considered, each with a different radical pair spin Hamiltonian and initial spin density operator.The first somewhat artificial model, model 1, consists of a radical pair with no spin interactions; that is with $\hat{H}_{0s} = 0$. The spin system is taken to initially be in a superposition of a singlet and triplet state, $\psi(0) = (|S\rangle + |T_0\rangle)/\sqrt{2}$, and therefore has an initial density operator given by

$$\hat{\rho}_{0s}(0) = \frac{1}{2}\left(|S\rangle\langle S| + |S\rangle\langle T_0| + |T_0\rangle\langle S| + |T_0\rangle\langle T_0|\right). \tag{4.168}$$

The absence of any spin interactions in this model allows for straightforward comparison between the dynamics of the singlet population, $\rho_{SS}(t) = \langle S|\,\hat{\rho}_{0s}(t)\,|S\rangle$, and singlet-triplet coherence, $\rho_{ST}(t) = \langle S|\,\hat{\rho}_{0s}(t)\,|T\rangle$, arising from the QMEs and HEOM approach for varying values of the diabatic coupling, Δ_S.

The second model, model 2, describes a radical pair interacting with an external magnetic field, B, and with a single hyperfine-coupled nuclear spin-$\frac{1}{2}$, with isotropic hyperfine coupling constant a, on one of the radicals. The spin Hamiltonian for this model is

$$\hat{H}_{0s} = \omega_0\hat{S}_{1z} + \omega_0\hat{S}_{2z} + a\hat{\boldsymbol{S}}_1 \cdot \hat{\boldsymbol{I}} \tag{4.169}$$

where $\hat{\boldsymbol{S}}_i$ is the vector spin operator for electron spin i, $\hat{\boldsymbol{I}}$ is the vector spin operator for the nuclear spin, and $\omega_0 = -\gamma_e B$ is the Zeeman frequency of the electron spin where γ_e is the gyromagnetic of a free electron. This radical pair system is chosen to be initially in a singlet state,

$$\hat{\rho}_{0s}(0) = \frac{1}{2}\hat{P}_S. \tag{4.170}$$

This model provides a more realistic description of a radical pair system. In what follows it will be used to explore whether the additional reactive exchange coupling can significantly influence the spin dynamics of a radical pair.

4.5.4 Simulation Details

A series of simulations were performed for both models using the HEOM approach, the QMEs presented in equations 4.147 and 4.149, and the Haberkorn master equation. For model 1 a number of simulations were performed for a range of different values of Λ and Δ, while for model 2 only a single set of parameters were considered. The parameters used for each model are given in table 4.1.

	T (K)	Λ (eV)	$\hbar\omega_c$ (meV)	ϵ (eV)	Δ (meV)	$a\hbar/\lvert\gamma_e\rvert$ (mT)	$\omega/\lvert\gamma_e\rvert$ (mT)
Model 1	300	$[0.125, 0.5]$	1.24	0	$[0.1, 25]$	–	–
Model 2	300	0.5	1.24	0.1	0.1	1.5	0.5

Table 4.1: The parameters used for the two model radical pair systems considered, for model 1 a range of Λ and Δ values were considered. Only the second model includes any terms accounting for spin interactions.

For both models, the hierarchical equations of motion were truncated using the frequency based truncation scheme (equation 4.141) described in Section 4.4.5. Results were obtained for increasing values of the truncation parameter, Γ, until convergence was observed. The final value of Γ required was strongly dependent on the reorganisation energy associated with the bath, and ranged between 250 ω_c and 1250 ω_c. In order to efficiently integrate the resultant linear system, an adaptive time step and order Taylor series integrator was used. This approach allows for small time steps to be made initially and so can accurately capture the short time bath dynamics, and larger time steps at longer times when the bath has reached equilibrium. The ADOs were scaled according to the scheme presented by Shi *et al.* to allow for efficient control of the errors in the integrator.[185]

For model 1, the QMEs 4.147 and 4.149 can be solved analytically. The resultant expressions for the matrix elements of the radical pair density operator of interest here are[33]

$$\rho_{SS}(t) = \langle S| \hat{\rho}_{1s}(t) |S\rangle = \frac{1}{2}\frac{k_b + k_f e^{-(k_f+k_b)t}}{k_f + k_b} \tag{4.171}$$

$$\rho_{ST_0}(t) = \langle S| \hat{\rho}_{1s}(t) |T_0\rangle = \frac{1}{2} e^{-2iJt/\hbar - (k_f/2 + k_d)t} \tag{4.172}$$

As the bias, ϵ, is zero for model 1, the forward and backward rates k_f and k_b are equal, wthis is not the case for model 2. The inclusion of the additional spin interactions in model 2 prevent an analytic solution of the resultant master equation. Here the resultant master equations are integrated numerically using standard techniques.[33]

Λ (eV)	ϵ (eV)	$\hbar^2 k_f^{(2)}/(2\Delta^2)$	$\hbar^2 k_b^{(2)}/(2\Delta^2)$	$2\hbar J^{(2)}/\Delta^2$
0.125	0	3.1088 ns	3.1088 ns	6.1149 ns
0.25	0	0.6609 ns	0.6609 ns	-3.3952 ns
0.375	0	0.1623 ns	0.1623 ns	-2.1633 ns
0.5	0	0.04229 ns	0.04229 ns	-1.5392 ns
0.5	0.1	0.2406 ns	0.0050270 ns	-2.0789 ns

Λ (eV)	ϵ (eV)	$\hbar^4 k_{f/b}^{(4)}/(2\Delta^4)$	$2\hbar^3 2\hbar^3 J^{(4)}/\Delta^4$	$\hbar^4 k_d^{(4)}/\Delta^4$
0.25	0	-1.0634$\times 10^5$ ps^3	2.4370$\times 10^{-6}$ ps^3	1.0447$\times 10^{-5}$ ps^3

Table 4.2: The second (top) and fourth (bottom) order rate constants obtained for the different parameter regimes considered for the two models. The second order rate constants used for model 1 were obtained with $\epsilon = 0$ eV and for $\Lambda = 0.125$, 0.25, 0.375, and 0.5 eV. Fourth order terms were only computed for $\Lambda = 0.25$ eV. For model 2 ($\Lambda = 0.5$ eV, $\epsilon = 0.1$ eV) only second order rate constants were considered.

The rate constants entering into the second and fourth order QME can be obtained by evaluating time integrals of bath correlation functions.[33] For the spin-boson model the required bath correlation functions can be evaluated analytically, the rate expressions cannot. In order to obtain the rate constants it is necessary to evaluate the integrals numerically. The rate constants obtained for the different sets of model parameters are given in table 4.2. In general, these rate constants depend on the form of the bath spectral density, and the bias between the potential energy surfaces. The Haberkorn and Jones-Hore master equations do not provide a connection between the microscopic description of the system and the recombination rates. As such, these rates must be obtained using an alternative approach. For model 1, the Haberkorn rate was obtained by fitting the analytic expression for $\hat{\rho}_{SS}(t)$ to the results obtained with the HEOM. For model 2, the Haberkorn rate was set to the second order rate constant.

4.5.5 Results

Model 1: Dynamics of Coherences

The dynamics of the singlet population, and the absolute value and imaginary component of the singlet-triplet coherence for model 1 with $\Lambda = 0.25$ eV, are shown in figure 4.5. For weak diabatic couplings, $\Delta_S = 0.1$ meV, both second and fourth order QMEs agree quantitatively with the HEOM results for all quantities considered. The Haberkorn master equation accurately describes the decay of the absolute value of the singlet-triplet coherence, $|\rho_{ST}(t)|$, but fails to capture the evolution of the imaginary part of the coherence, $\mathrm{Im}\,[\rho_{ST}(t)]$. This evolution arises due to the reactive exchange coupling contribution, and as such is not present in the Haberkorn treatment of recombination.

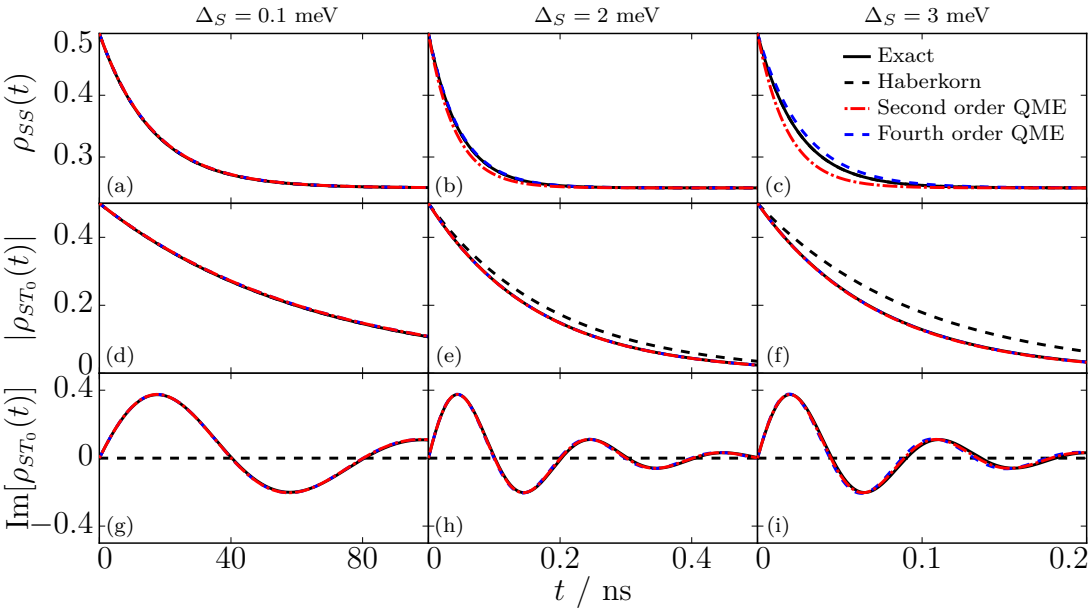

Figure 4.5: Comparison of the singlet population decay (a-c), absolute value of the singlet-triplet coherence (d-f), and imaginary part of the singlet-triplet coherence (g-i) obtained using HEOM calculations (exact), the Haberkorn master equation, and second and fourth order QMEs at different values of the diabatic coupling between singlet radical pair and product states. The diabatic couplings, Δ_S considered are 0.1 meV (a, d, g), 2 meV (b, e, h), and 3 meV (c, f, i).

For a diabatic coupling of $\Delta_S = 2$ meV, the fourth order QME still accurately captures the decay of the singlet population. In contrast, the second order QME

overestimates the decay rate. This indicates that the system is no longer in the nonadiabatic limit and higher order contributions (in Δ_S) are starting to influence the dynamics. In addition to the fourth order QME, somewhat surprisingly, the second order QME accurately captures the decay in $|\rho_{ST}(t)|$ and the oscillations in $\mathrm{Im}\left[\rho_{ST}(t)\right]$. The surprising accuracy of the second order QME can be attributed to a cancellation of errors. The singlet-triplet coherence decays at a rate $k_{ST} = k_S/2 + k_d$. The second order estimate for the singlet recombination rate, k_S, is too large, however this is almost perfectly offset by the absence of any additional dephasing contribution in the second order QME. As before, the Haberkorn master equation fails to capture the dynamics of $\mathrm{Im}\left[\rho_{ST}(t)\right]$, however now also fails to capture the decay of the singlet-triplet coherence. The Haberkorn master equation does not include any additional singlet triplet dephasing, and so it predicts $k_{ST} = k_S/2$.

On increasing the diabatic coupling to $\Delta_S = 3$ meV, both the second and fourth order QMEs predict an incorrect rate for the decay of the singlet population. The second order approach once again overestimates the decay, while the fourth order QME underestimates the decay. This is unsurprising given the use of perturbation theory in the derivation of these QMEs. For sufficiently large values of Δ_S, higher order terms become important. As a result, the second and fourth order approximations to the rate constants and exchange coupling are no longer accurate. The two master equations both capture the decay of the singlet-triplet coherence. This accuracy can, once again, be attributed to a cancellation of errors. The Haberkorn treatment fails to capture the decay of the singlet-triplet coherence, however, now by a more significant amount. This indicates that as Δ_S increases, the additional singlet-triplet dephasing contribution becomes more significant.

Upon further increasing the diabatic coupling to $\Delta_S = 25$ meV, as shown in figure 4.6, neither perturbative QME is able to capture the decay of the singlet population. The second order QME predicts much too rapid decay, while the fourth order form predicts a negative decay rate and, as a result, an unphysical exponential

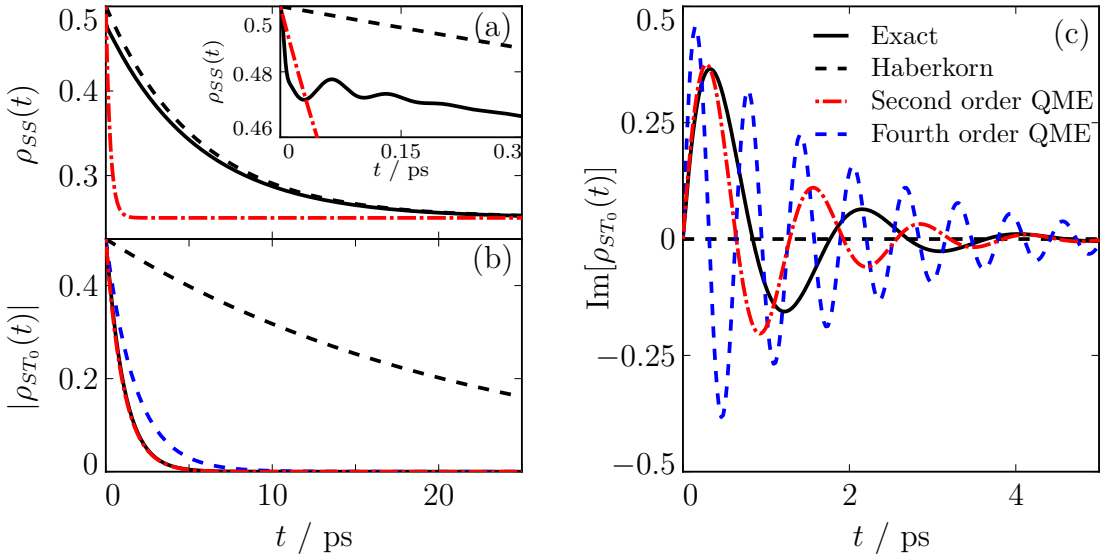

Figure 4.6: Comparison of the singlet population decay (a), absolute value of the singlet-triplet coherence (b), and imaginary part of the singlet-triplet coherence (c) obtained using HEOM calculations (exact), the Haberkorn master equation, and second and fourth order QMEs with $\Delta_S = 25$ meV. In panel a) the fourth order result increases exponentially with time and so is not observed on the range shown. The inset to panel a) shows the non-exponential dynamics occuring at short time.

growth in the singlet population. The second order QME is again able to capture the decay in the singlet-triplet coherence due to a fortuitous cancellation of errors but neither perturbative QME captures the timescale of the oscillations in the imaginary part of these coherence. This is not surprising, here Δ_S is large and as a result the system is far from the regime in which low order perturbation theory is expected to be accurate. This issue would likely be fixed by including higher order terms or by using the Padé approximant $k \approx k^{(2)}/(1-k^{(4)}/k^{(2)})$ for the rate constant.[171,200,201]

In contrast to the previous cases, the singlet population dynamics shown in figure 4.6 cannot be fitted by solutions to the Haberkorn master equation (or even by solutions to the general QME given in equation 4.149). The singlet population does not decay exponentially for all times; at short times there is a rapid non-exponential decrease in the singlet population (as shown in the inset in figure 4.6 panel a)). This non-exponential behaviour is a manifestation of a breakdown of the incoherent rate approximation. As the diabatic coupling increases the recombination dynamics

occurs over a shorter timescale. For sufficiently large diabatic coupling, the bath and recombination dynamics occur on comparable timescales. In this case non-Markovian effects in the bath become important and the QMEs discussed above can no longer capture the dynamics. At longer times, the bath has had sufficient time to equilibrate and the dynamics becomes rate-like.

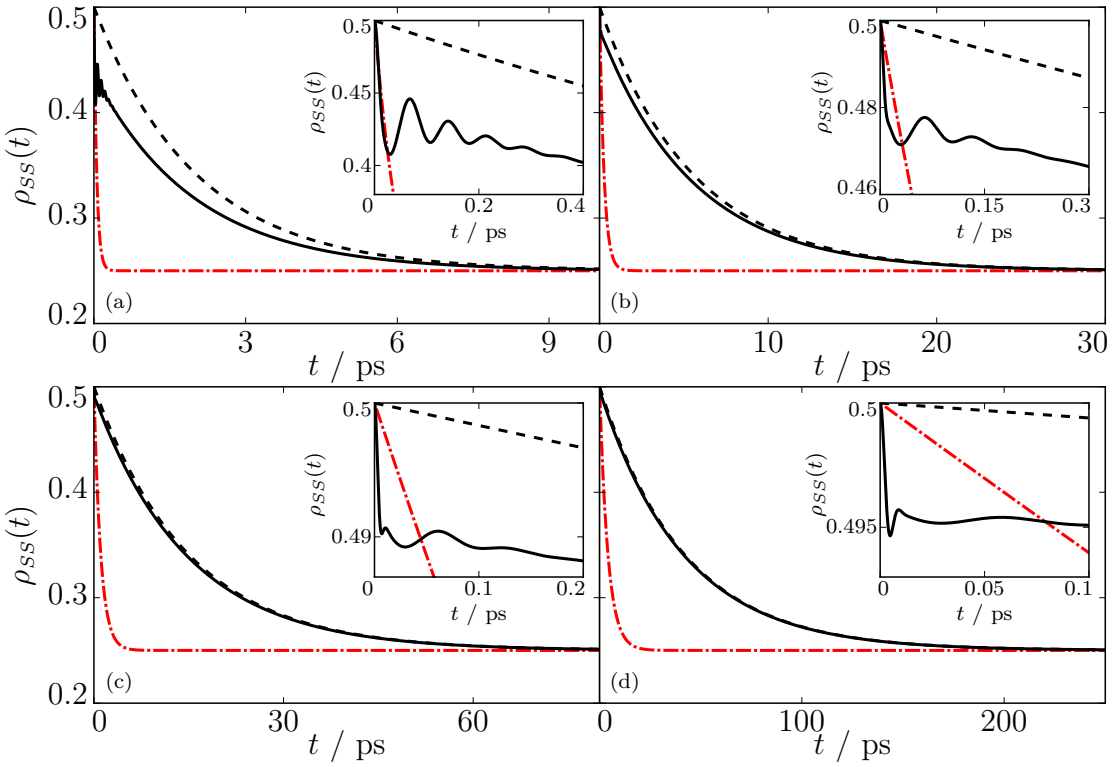

Figure 4.7: Singlet population dynamics obtained for model 1 with four different values for the bath reorganisation energy: a) $\Lambda = 0.125$ eV, b) $\Lambda = 0.25$ eV, c) $\Lambda = 0.375$ eV, and d) $\Lambda = 0.5$ eV. The insets show the short time non-exponential behaviour of the singlet population dynamics.

To explore this breakdown of the incoherent rate approximation further, the singlet population dynamics for model 1 obtained for four different values of the bath reorganisation energy ($\Lambda = 0.125$, 0.25, 0.375, and 0.5 eV) is shown in figure 4.7. For $\Lambda = 0.125$ eV (panel a), the non-exponential decay of the singlet population is considerably more pronounced than for the other values of Λ considered. The singlet population rapidly decays to ~ 0.4 following which exponential decay is observed. As the reorganisation energy decreases, the timescale on which the recombination

dynamics occurs becomes shorter, leading to non-Markovian effects being more important. Increasing the reorganisation energy to $\Lambda = 0.5$ eV (panel d), the non-Markovian effects play a significantly smaller role. While non-exponential decay is observed at very short time, it does not significantly alter the singlet population and the longer time decay can readily be fit using an exponential model.

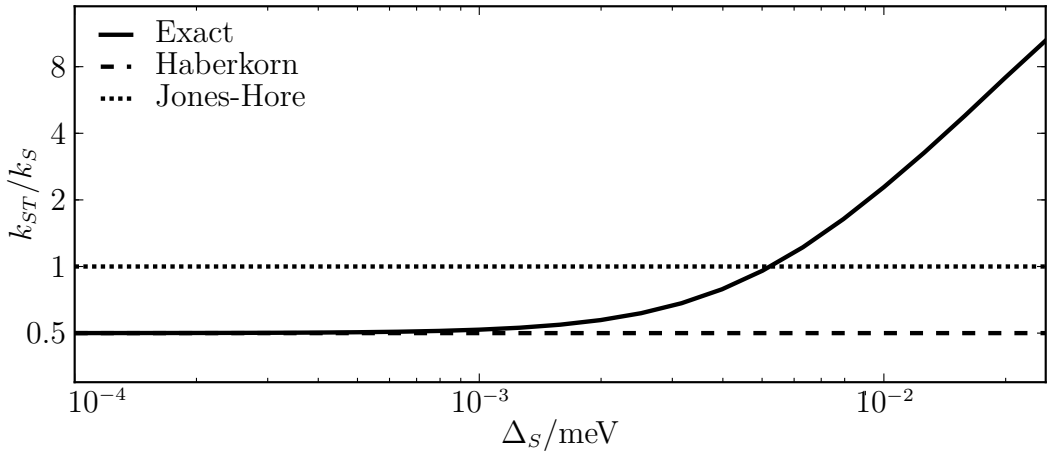

Figure 4.8: Comparison of the ratio of singlet-triplet dephasing rate to singlet recombination rate obtained from the HEOM approach, and the values arising for the Haberkorn and Jones-Hore master equations for varying values of Δ_S. For the larger values of Δ_S considered here, the electron transfer process is near the adiabatic regime.

As a final application of model 1 (with $\Lambda = 0.25$ eV), the ratio of the singlet-triplet coherence dephasing rate, k_{ST}, to the singlet recombination rate, k_S, is considered. In figure 4.8, the predictions made by the Haberkorn ($k_{ST}/k_S = 1/2$ for all Δ_S) and Jones-Hore master equations ($k_{ST}/k_S = 1$ for all Δ_S) are compared to the numerically exact HEOM calculations for a range of diabatic coupling constants, Δ_S. As expected, in the nonadiabatic limit ($\Delta_S \to 0$) the Haberkorn master equation accurately captures the exact result. In this limit, the second order QME, which also predicts $k_{ST}/k_S = 1/2$, is valid. In contrast, the Jones-Hore master equation overestimates the singlet-triplet decoherence rate in the nonadiabatic limit and underestimates it in the adiabatic regime (large Δ_S). It only agrees with the exact value for a single Δ_S at which the exact value varies rapidly. Moving towards

the adiabatic regime (large values of Δ_S) the value of k_{ST}/k_S obtained from the HEOM calculations increases rapidly with Δ_S. For large values of Δ_S the singlet dephasing rate, k_{ST} can become considerably larger than singlet recombination rate, k_S. In this case the singlet-triplet coherence are short lived compared to the lifetime of the radical pair state. When singlet-triplet dephasing is considerable, the interconversion between singlet and triplet states can be more accurately described using an incoherent kinetic model.[202] As such, these results suggest that, at least for this model, quantum mechanical effects may play less of a role in the spin dynamics of radical pairs undergoing adiabatic electron transfer reactions. Simple kinetic models may be sufficient to describe the recombination dynamics.

Model 2: Singlet Survival Probability

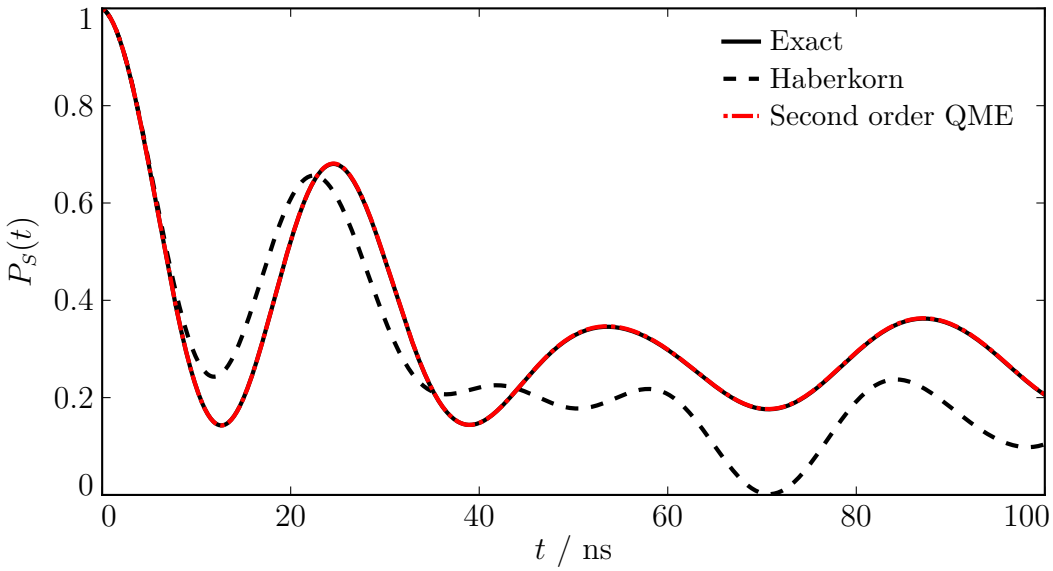

Figure 4.9: The radical pair singlet population as a function of time for model 2. Here second order QME and Haberkorn master equation results are compared against the exact HEOM results. The Haberkorn master equation uses the same rate constants as the second order QME but does not include any reactive exchange coupling.

The time-dependent radical pair singlet survival probability for model 2 is shown in figure 4.9. Here, results obtained using the Haberkorn master equation, the second order master equation, and HEOM approach are compared. The second order master equation agrees quantitatively with the numerically exact result over

the entire time frame considered. In comparison, the singlet survival probability obtained using the Haberkorn master equation deviates significantly from the exact result after $\sim$10ns. It fails to capture the frequency and magnitude of the oscillations observed in the singlet survival probability. The only difference between the second order QME and the Haberkorn master equation is the presence of the additional exchange coupling arising from the recombination process in the second order QME. In previous attempts to derive the Haberkorn master equation, this term has been assumed to be insignificant and was therefore discarded.[50] These results illustrate that there are regimes in which this exchange coupling can be significant, such as the case considered here where there is a significant difference between the singlet and triplet recombination rates.

4.6 Conclusion

In this chapter, the hierarchical equations of motion formalism, a numerically exact method for treating the dynamics of open quantum systems, has been discussed. This method is appropriate for treating arbitrary quantum mechanical systems linearly coupled to baths of Harmonic oscillators. A derivation of the approach was provided for the case of harmonic baths with spectral densities given by a sum of Debye and Brownian oscillator spectral densities. The equations of motion obtained describe the evaluation of an infinite hierarchy of auxiliary density operators that influence the dynamics of the system reduced density operator. In order to obtain a numerically efficient approach, it is necessary to truncate this hierarchy and two such truncation approaches were discussed.

Following this, a series of recently proposed quantum master equations for spin selective electron transfers of radical pairs were validated by comparison with numerically exact HEOM calculations for a simple radical pair model that was closely related to the spin-boson model, a commonly employed model of condensed

phase electron transfer. In the nonadiabatic limit, the QMEs reduce to the standard Haberkorn master equation with an additional electron spin coupling contribution arising from the recombination process. This additional term can be straightfowardly included in standard simulations of radical pairs, as exchange couplings are often included in models of radical pair reactions in any case (see Section 2.2.2). On moving away from the nonadiabatic limit, an additional contribution to the singlet-triplet dephasing is observed, which can become significant as the diabatic coupling constant becomes larger. This term complicates the treatment of radical pair recombination dynamics. Singlet-triplet dephasing does not preserve pure states and so the wavefunction-based approaches described in Chapter 2 cannot be applied directly. These results suggest that when modelling realistic radical pairs, exchange coupling and singlet-triplet dephasing terms should be included.

In the next chapter, the hierarchical equations of motion will be discussed further and an alternative approach for solving the equations will be presented that allows for considerably more challenging regimes to be treated.

5

Tree Tensor Network State Solution of the HEOM

Contents

5.1 Introduction

The hierarchical equations of motion (HEOM) formalism, originally presented by Tanimura and Kubo in 1987,[7] has found widespread success in treating the dynamics of open quantum systems. This approach makes no assumptions about the importance of quantum mechanical effects and explicitly accounts for non-Markovian effects arising from the dynamics of the bath, so can, in principle, treat arbitrary strength coupling between the system and bath degrees of freedom.[7,8,195,203] Additionally, this method is applicable to arbitrary systems that are linearly coupled to any number of Harmonic baths.[195] Owing to this fact, the HEOM formalism has been applied to a wide range of systems such as light harvesting complexes,[172,173] spin system,[174] electron transfer systems,[33,197,204,205] and proton-coupled-electron transfer systems,[184] as well as one-dimensional molecular crystals,[180] and molecular junctions.[206]

Within the HEOM formalism, the dynamics of the system reduced density operator is coupled to the dynamics of an infinite hierarchy of auxiliary density operators (ADOs). These ADOs account for the non-Markovian dynamics without employing any perturbative approximations.[7] In order to obtain a practical numerical method it is necessary to truncate the infinite hierarchy. This truncation is typically performed using a Markovian approximation to the dynamics of ADOs that are sufficiently far down the hierarchy.[195] In the previous chapter, two approaches for specifying which ADOs are included within the hierarchy were discussed. While these standard truncation schemes have previously been successful, as the number of baths present or the strength of the system-bath coupling increases, the number of elements in the hierarchy necessary to obtain converged results can become impractically large. To illustrate this, an application of the HEOM formalism to the dynamics of a two-level system coupled to a single Harmonic bath will be considered. The bath will be characterised by a Brownian oscillator spectral density,

$$J(\omega) = \frac{\Lambda}{2} \frac{\gamma \Omega^2 \omega}{\left(\omega^2 - \Omega^2\right)^2 + \gamma^2 \omega^2}, \tag{5.1}$$

where Λ is the reorganisation energy, Ω is the reaction coordinate frequency, and γ is the friction coefficient along the reaction coordinate (see Section 4.2.1). It will further be assumed that the bath is not critically damped and, as a result, the bath correlation function only contains exponential and Markovian contributions. The HEOM describing the dynamics of a system coupled to one such bath, with a Markovian contribution and K exponential contributions to the bath correlation function, can be written as

$$\begin{aligned}\frac{\mathrm{d}}{\mathrm{d}t}\hat{\sigma}_{\mathbf{n}}(t) = &-\frac{i}{\hbar}\left[\hat{H}_S, \hat{\sigma}_{\mathbf{n}}(t)\right] - \frac{1}{\hbar^2}\left[\hat{Q}, \left(\Delta\hat{Q}\hat{\sigma}_{\mathbf{n}}(t) - \Delta^*\hat{\sigma}_{\mathbf{n}}(t)\hat{Q}\right)\right] - \sum_{k=1}^{K} n_k\nu_k\hat{\sigma}_{\mathbf{n}}(t) \\ &-\frac{i}{\hbar}\sum_{k=1}^{K}\left(\left[\hat{Q}, \hat{\sigma}_{\uparrow_{\mathbf{n}}(\mathbf{n}_k)}(t)\right] + n_k\alpha_k\hat{Q}\hat{\sigma}_{\downarrow_{\mathbf{n}}(\mathbf{n}_k)}(t) - n_k\overline{\alpha}_k^*\hat{\sigma}_{\downarrow_{\mathbf{n}}(\mathbf{n}_k)}(t)\hat{Q}\right),\end{aligned} \tag{5.2}$$

where $\hat{Q}$ is the (time-independent) system component of the system-bath coupling operator and the notation $\hat{\sigma}_{\uparrow_{\mathbf{n}}(\mathbf{n}_k)}$ and $\hat{\sigma}_{\downarrow_{\mathbf{n}}(\mathbf{n}_k)}$ is defined in Section 4.4.4.

Figure 5.1 shows the population dynamics ($P(t) = \langle 0|\,\hat{\sigma}_0(t)\,|0\rangle$) of such a system for a range of reorganisation energies (Λ), a reaction coordinate frequency of $\beta\hbar\Omega = 4$, and friction coefficient of $\gamma = \Omega$. Here, the system is initially prepared in the $|0\rangle$ state and the bath degrees of freedom are initially in thermal equilibrium with respect to the diabatic potential energy surface associated with this state (see Section 4.3.2). This system evolves according to the spin-boson Hamiltonian, previously described in Section 4.2.2, with the driving force taken to be zero, $\beta\epsilon = 0$, and diabatic coupling constant taken to be $\Delta = \Lambda/60$.

For small values of the reorganisation energy, which correspond to weak system-bath coupling, use of the frequency-based truncation scheme (Section 4.4.5) leads to rapid convergence of the dynamics of this spin-boson model. For $\Lambda\beta = 20$, converged results are obtained with $\Gamma\beta\hbar = 40$, corresponding to a hierarchy containing $1,089$ ADOs. When $\Lambda\beta$ is increased to 40, the results obtained with $\Gamma\beta\hbar = 40$ show significant deviations from the converged results, obtained with $\Gamma\beta\hbar = 60$, past $t = 0.5\beta\hbar$. Further increasing Λ leads to considerably slower convergence of the

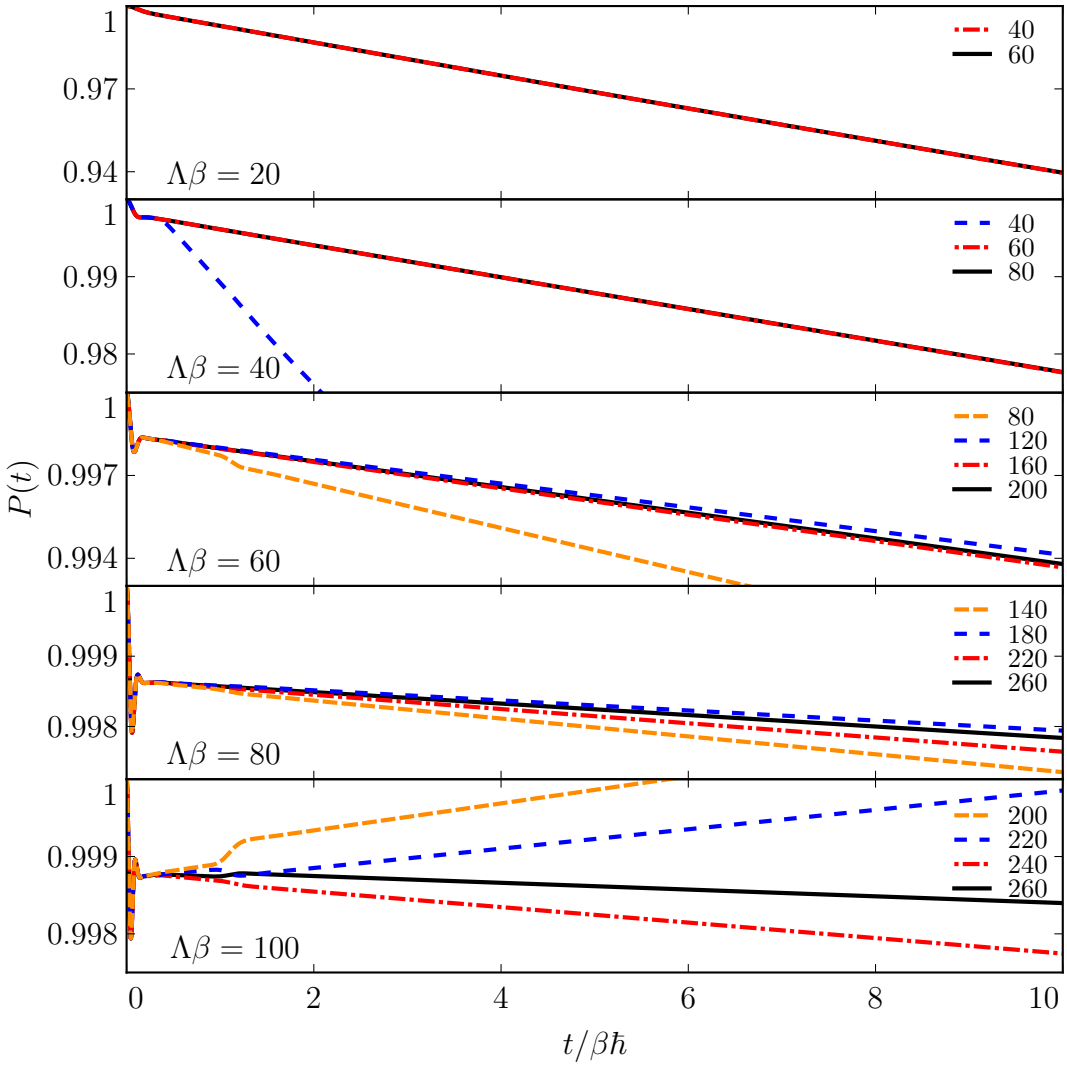

Figure 5.1: The time-dependent population in state $|0\rangle$ for a spin-boson model with a Brownian oscillator spectral density and various values of the reorganisation energy, Λ, (shown in each panel) reaction coordinate frequency $\beta\hbar\Omega = 4$, and friction coefficient $\gamma = \Omega$ and are obtained using the HEOM formalism with various values of the truncation parameter $\Gamma\beta\hbar$ (shown in the legend for each panel). Here, the system is initially prepared in state $|0\rangle$ and with the bath at thermal equilibrium with respect to the Hamiltonian associated with diabat, $|0\rangle$ (see Section 4.3.2).

dynamics with respect to the truncation parameter, Γ. For $\Lambda\beta = 60$, a significant unphysical feature is observed at $t \sim 1.2\beta\hbar$ for $\Gamma\beta\hbar = 80$, which vanishes as Γ is increased. As Γ increases, the timescale over which the dynamics is accurate also increases and the extent of the deviation decreases. To obtain converged results it is necessary to use $\Gamma\beta\hbar = 200$. For larger values of $\Lambda\beta$, converged results could not be obtained using this truncation scheme. For $\Lambda\beta = 80$, significant differences

in the long time decay are observed between the results obtained for all values of $\Gamma\beta\hbar$ considered here and, as such, it is not clear if the dynamics have converged. While for $\Lambda\beta = 100$, the dynamics obtained for $\Gamma\beta\hbar = 200$ show a significant unphysical feature at $t \sim 1\beta\hbar$ and gives rise to unphysical populations (> 1) in the $|0\rangle$ diabatic state at longer times. For $\Gamma\beta\hbar = 260$ this issue is no longer present but the dynamics is clearly not converged. This calculation employed a hierarchy containing $63,510,998$ ADOs and required ~ 50 gigabytes of memory to store the ADOs, as well as an indexing array that is necessary to efficiently implement the equations of motion. Further increasing the Γ parameter is not feasible. For example, if $\Gamma\beta\hbar = 300$ the calculation would require $\sim$250 gigabytes of memory and is unlikely to result in converged dynamics when $\Lambda\beta = 100$. At a temperature of 300 K, the reorganisation energy of $\Lambda\beta = 100$ is ~ 2.6 eV. This is comparable to the reorganisation energy observed experimentally for the symmetric electron transfer reaction V^{2+}-V^{3+} in water,[207] and therefore such a large system-bath coupling is chemically relevant. As such, it is desirable to be able to obtain converged HEOM results for such a problem.

A number of approaches have previously been developed for extending the HEOM to treat problems requiring larger hierarchies. The use of a filtering scheme, which removes ADOs that contribute little to the system dynamics, has allowed for large hierarchies including contributions from considerably more Matsubara modes than can be included within standard schemes to be treated.[185,205] Recently, an approach that employs a matrix product state representation of the auxiliary density operators has been proposed.[189] This method has been applied to the evaluation of the energy transfer dynamics of the Fenna-Matthews-Olson complex at low temperatures, $T = 77$ K, where it was observed to reduce the computational time required by a factor of 2 and give a factor of ~ 50 reduction in the memory required to obtain converged results.[189] A variant of this approach, in which a matrix product state representation for both the system's degrees of freedom and the ADOs is employed, has been successfully applied to treat the population dynamics of polaron models

linearly coupled to thermal baths.[208] In the remainder of this chapter, a closely related approach that exploits a more general tree tensor network state (TTNS) representation of the hierarchy of ADOs is presented. Before doing this, however, it is useful to provide an alternative representation of the HEOM given in equation 5.2.

5.1.1 The Hierarchical Equations of Motion

A useful interpretation of the hierarchical equations of motion given in equation 5.2 can be obtained by assigning a "bath mode" labelled by k to each of the indices represented by $\mathbf{n}$. Within this picture a given ADO, $\hat{\sigma}_{\mathbf{n}}$, has n_k "quanta" in the bath mode k, and equation 5.2 may be rewritten in terms of "creation" and "annihilation" operators acting on these bath modes. By introducing a Fock space for each of the bath modes, the hierarchy of ADOs can be treated as an element in the direct product space of the bath mode Fock spaces and the system Liouville space as

$$|\hat{\sigma}(t)\rangle = \sum_{\mathbf{n}} \hat{\sigma}_{\mathbf{n}(t)} \otimes |n_1\rangle_1 \otimes \cdots \otimes |n_K\rangle_K . \tag{5.3}$$

$\sum_{\mathbf{n}}$ denotes the sum over all values of $\mathbf{n} = \{n_1, \ldots, n_K\}$ indexing the ADOs, and $|n_k\rangle_k$ is the Fock space state of the k-th bath mode with n_k quanta. Within this representation, equation 5.2 may be written as

$$\frac{\mathrm{d}}{\mathrm{d}t}|\hat{\sigma}(t)\rangle = -\frac{i}{\hbar}\left(\mathcal{A}_S - \sum_{k=1}^{K}\left[-i\hbar\mathcal{N}_k + \left(\mathcal{Q}^-\left[\mathcal{B}_{-k} + \mathcal{B}^r_{+k}\right] + i\mathcal{Q}^+\mathcal{B}^i_{+k}\right)\right]\right)|\hat{\sigma}(t)\rangle , \tag{5.4}$$

where the superoperator

$$\mathcal{A}_S = \left[\mathcal{L}_S - \frac{i}{\hbar}\mathcal{Q}^-\left(\mathrm{Re}(\Delta)\mathcal{Q}^- + i\mathrm{Im}(\Delta)\mathcal{Q}^+\right)\right], \tag{5.5}$$

acting on the system degrees of freedom, has been introduced. In equation 5.5, $\mathcal{L}_S$ is the system Liouvillian, and the superoperators $\mathcal{Q}^-$ and $\mathcal{Q}^+$ act on an arbitrary system operator, $\hat{O}$, to give

$$\mathcal{Q}^-\hat{O} = \hat{Q}\hat{O} - \hat{O}\hat{Q} \qquad\qquad \mathcal{Q}^+\hat{O} = \hat{Q}\hat{O} + \hat{O}\hat{Q}. \tag{5.6}$$

Additionally, in equation 5.12 the operators, $\mathcal{N}_k$, $\mathcal{B}^r_{-k}$, $\mathcal{B}^i_{-k}$, and $\mathcal{B}_{+k}$, which act on the bath mode Fock spaces, have been introduced. These operators act on

a given state of bath k, $|n_k\rangle_k$, to give

$$\mathcal{N}_k |n_k\rangle_k = n_k \nu_k |n_k\rangle_k , \tag{5.7}$$

$$\mathcal{B}^r_{+k} |n_k\rangle_k = (n_k{+}1)\mathrm{Re}(\alpha_k) |n_k{+}1\rangle_k , \tag{5.8}$$

$$\mathcal{B}^i_{+k} |n_k\rangle_k = (n_k{+}1)\mathrm{Im}(\alpha_k) |n_k{+}1\rangle_k , \tag{5.9}$$

$$\mathcal{B}_{-k} |n_k\rangle_k = |n_k{-}1\rangle_k . \tag{5.10}$$

Finally, introducing the operator,

$$\mathcal{H} = \mathcal{A}_S - \sum_{k=1}^{K} \left[-i\hbar \mathcal{N}_k + \left(\mathcal{Q}^- \left[\mathcal{B}_{-k} + \mathcal{B}^r_{+k} \right] + i\mathcal{Q}^+ \mathcal{B}^i_{+k} \right) \right] , \tag{5.11}$$

acting on the system and bath modes, the HEOM may be rewritten as

$$\frac{\mathrm{d}}{\mathrm{d}t} |\hat{\sigma}(t)\rangle = -\frac{i}{\hbar} \mathcal{H} |\hat{\sigma}(t)\rangle . \tag{5.12}$$

This equation is entirely analogous to the equations of motion for a wavefunction (the state of the system and ADOs) evolving under a non-Hermitian Hamiltonian, $\mathcal{H}$. As such, it is possible to adapt approaches for computing the time-evolution of wavefunctions to solve the hierarchical equations of motion. In what follows, the use of a tree tensor network state representation of the hierarchy of ADOs to solve the HEOM will be considered.

5.2 ML-MCTDH and Tree Tensor Network States

Tree tensor networks have found considerable success in the field of molecular quantum dynamics. They have done so in the form of the multiconfiguration time-dependent Hartree (MCTDH)[209–212] method and its multilayer variant, the multilayer-multiconfiguration time-dependent Hartree (ML-MCTDH)[213–216] method. These approaches allow for the dynamics of a large molecular system to be computed in full dimensionality and with accurate potential energy surfaces. Applications of the ML-MCTDH method include: the computation of the IR spectrum of the Zundel cation ($H_5O_2^+$) on a potential energy surface obtained by fitting to electronic structure theory calculations,[217–220] the photoexcitation spectrum of pyrazine,[215,221]

condensed-phase proton transfers,[222] and the coupled electron and nuclear dynamics of the Fenna-Matthews-Olson complex with an arbitrary spectral density.[223] The multilayer implementation, in particular, allows for the dynamics of quantum mechanical systems with up to 1000 degrees of freedom to be treated routinely.[224–229]

Within standard approaches to quantum dynamics, the wavefunction, $|\Psi\rangle$, describing the state of the d-dimensional system is expanded in terms of a time-independent basis.[146,230] This basis is often chosen as a direct product of a set of $n_{\chi^{(k)}}$ orthonormal basis vectors for each mode, $\chi^{(k)}$, here represented by $\{|\chi^{(k)}_{\alpha_k}\rangle\}$. With respect to this basis, the wavefunction can be represented as

$$|\Psi(\boldsymbol{\chi},t)\rangle = \sum_{\alpha_1=1}^{n_{\chi^{(1)}}} \cdots \sum_{\alpha_d=1}^{n_{\chi^{(d)}}} \Psi_{\alpha_1\ldots\alpha_d}(t)\, |\chi^{(1)}_{\alpha_1}\rangle \otimes \cdots \otimes |\chi^{(d)}_{\alpha_d}\rangle \tag{5.13}$$

where $\Psi_{\alpha_1\ldots\alpha_d}(t) \equiv \Psi_{\boldsymbol{\alpha}}(t) = \left(\langle\chi^{(1)}_{\alpha_1}| \otimes \cdots \otimes \langle\chi^{(d)}_{\alpha_d}| \right) |\Psi(\boldsymbol{\chi},t)\rangle$ are the elements of a d-dimensional tensor (which for this application is simply a multidimensional array, $\Psi_{\boldsymbol{\alpha}} \in \mathbb{C}^{n_{\chi^{(1)}}\times\cdots\times n_{\chi^{(d)}}}$) of coefficients, Ψ; the combined index $\boldsymbol{\alpha} = \{\alpha_1,\ldots,\alpha_d\}$ has been introduced to simplify the notation. As the dimensionality, d, of the system increases, the number of elements in the coefficient tensor grows exponentially, and it rapidly becomes impractical to store the full tensor. As a result, approximate representations of this tensor are required.

Within the MCTDH and ML-MCTDH formalisms, the multidimensional wavefunction is written in terms of direct products of orthonormal, time-dependent functions that represent a subset of the physical modes.[209,210,213,214] The full multidimensional wavefunction can then be expressed as

$$|\Psi(\boldsymbol{\chi},t)\rangle = \sum_{i_{2;1}=1}^{n_{2;1}} \cdots \sum_{i_{2;m_1}=1}^{n_{2;m_1}} \mathcal{A}^1_{i_{2;1}\ldots i_{2;m_1}}(t) \bigotimes_{j=1}^{m_1} |\phi^{2;j}_{i_{2;j}}(\boldsymbol{\chi}^{(2;j)},t)\rangle\,, \tag{5.14}$$

where each $|\phi^{2;j}_{i_{2;j}}(\boldsymbol{\chi}^{(2;j)},t)\rangle$ is a time-dependent "single-particle" function representing a set of $d_{2;j}$ physical coordinates with $\boldsymbol{\chi}^{(2;j)} = \{\chi^{k_{(2;j),1}},\ldots,\chi^{k_{(2;j),d_{2;j}}}\} \subset \boldsymbol{\chi}$. The j-th mode single-particle function is therefore an element of a space with Hilbert space dimension $n_{\boldsymbol{\chi}^{(2;j)}} = n_{\chi^{(2;j,1)}} \ldots n_{\chi^{(2;j,d_{2;j})}}$. Within the MCTDH ansatz, the expansion

terminates at this step. Each of the $n_{2;j}$ time-dependent (second level) single-particle functions associated with the mode j are expanded in terms of the time-independent basis functions for these modes to give,[209,210]

$$|\phi_i^{2;j}(\boldsymbol{\chi}^{(2;j)},t)\rangle = \sum_{\alpha_1=1}^{n_{\chi^{(2;j,1)}}} \cdots \sum_{\alpha_{d_{2;j}}=1}^{n_{\chi^{(2;j,d_{2;j})}}} \mathcal{A}^{2;j}_{\alpha_1\ldots\alpha_{d_{2;j}}i}(t) \bigotimes_{k=1}^{d_{2;j}} |\chi^{(2;j,k)}_{\alpha_k}\rangle\,. \tag{5.15}$$

Within this representation, the multidimensional coefficient tensor of the full problem is approximated by

$$\Psi_{\boldsymbol{\alpha}}(t) = \sum_{i_{2;1}=1}^{n_{2;1}} \cdots \sum_{i_{2;m_1}=1}^{n_{2;m_1}} \left(\prod_{j=1}^{m_1} \mathcal{A}^{2;j}_{\alpha_{j;1}\ldots\alpha_{j;d_{2;j}}i_{2;j}}(t) \right) \mathcal{A}^{1}_{i_{2;1}\ldots i_{2;m_1}}(t), \tag{5.16}$$

which corresponds to a Tucker format tensor,[231] a special case of the tree tensor networks that will be considered below. The wavefunction coefficient tensor is thus represented as a tensor network involving a series of contractions (summations over the repeated indices) between a root tensor, $\mathcal{A}^1$, and m_1 leaf tensors, $\mathcal{A}^{2;j}$. If there is only one single-particle function for each set of physical coordinates, that is $n_{2;j} = 1$ for all $j = 1,\ldots,m_1$, then the MCTDH ansatz reduces to the time-dependent Hartree approximation,[211] and the wavefunctions for each set of physical coordinates evolve in the mean-field of the others. When more single-particle functions are included, the MCTDH ansatz corresponds to expanding a wavefunction in terms of a linear combination of Hartree products.[211] The MCTDH ansatz becomes exact upon increasing the number of single-particle functions in each mode to the Hilbert space dimension of the physical coordinates it represents, that is by setting $n_{2;j} = n_{\boldsymbol{\chi}^{(2;j)}}$t.

In the ML-MCTDH method this expansion is taken further. Rather than expanding the single-particle functions, $|\phi^{2;j}\rangle$, in terms of a set of time-independent basis functions, they are expanded in terms of $m_{2;j}$ new sets of single-particle functions, $\{|\phi_i^{3;j,k}\rangle\}$, with each set representing a further reduced set of the physical dimensions[213,214] ($\boldsymbol{\chi}^{(3;j,k)} \subset \boldsymbol{\chi}^{(2;j)}$ for $k = 1,\ldots,m_{2;j}$ such that $\boldsymbol{\chi}^{(3;j,k)} \cup \boldsymbol{\chi}^{(3;j,l)} = \varnothing$ if $k \neq l$ and $\boldsymbol{\chi}^{(3;j,1)} \cap \cdots \cap \boldsymbol{\chi}^{(3;j,m_{2;j})} = \boldsymbol{\chi}^{(2;j)}$). A general second-level single-particle function may be written as

$$|\phi_i^{2;j}(\boldsymbol{\chi}^{(2;j)},t)\rangle = \sum_{i_1=1}^{n_{\chi^{(2;j,1)}}} \cdots \sum_{i_{d_{2;j}}=1}^{n_{\chi^{(2;j,m_{2;j})}}} \mathcal{A}^{2;j}_{i_1\ldots i_{m_{2;j}}i}(t) \bigotimes_{k=1}^{m_{2;j}} |\phi_{i_k}^{3;j,k}(\boldsymbol{\chi}^{(3;j,k)},t)\rangle\,. \tag{5.17}$$

On further repeating this process, these (third level) single-particle functions may be expanded in terms of a new set of (fourth level) single-particle functions; again each representing a reduced set of physical dimensions. Generalising the above, an arbitary single-particle function at level l (labelled by the indices j_1, j_2, ..., j_{l-1}) can be expressed in terms of a coefficient tensor $\mathcal{A}$ and some set of single-particle functions for level $l+1$. Introducing a slightly modified form of the notation found in reference [224],

$$z = l; j_1, j_2, \ldots, j_{l-1} \qquad \text{and} \qquad z \circ j_l = l+1; j_1, j_2, \ldots, j_{l-1}, j_l, \tag{5.18}$$

a general single-particle function (which represents a set of d_z physical modes $\boldsymbol{\chi}^{(z)} = \{\chi^{k_{(z)1}}, \ldots, \chi^{k_{(z)d_z}}\}$) may be expanded as

$$|\phi^z_{i_z}(\boldsymbol{\chi}^{(z)}, t)\rangle = \sum_{i_{z\circ 1}=1}^{n_{z\circ 1}} \cdots \sum_{i_{z\circ m_z}=1}^{n_{z\circ m_z}} \mathcal{A}^z_{i_{z\circ 1},\ldots,i_{z\circ m_z} i_z}(t) \bigotimes_{j=1}^{m_z} |\phi^{z\circ j}_{i_{z\circ j}}(\boldsymbol{\chi}^{(z\circ j)}, t)\rangle \,. \tag{5.19}$$

On employing the Einstein summation convention (implicit summation over repeated indices), introducing the combined index $\boldsymbol{I}_z = \{i_{z\circ 1}, \ldots, i_{z\circ n_z}\}$, and implicitly defining the combined basis associated with the node z, $|\Phi^z\rangle$, equation 5.19 may be written in the compact form

$$|\phi^z_{i_z}(\boldsymbol{\chi}^{(z)}, t)\rangle = \mathcal{A}^z_{\boldsymbol{I}_z i_z}(t)\, |\Phi^z_{\boldsymbol{I}_z}(\boldsymbol{\chi}^{(z)}, t)\rangle \,. \tag{5.20}$$

This expansion continues until the single-particle functions acting on a single (potentially combined) physical degree of freedom, $\boldsymbol{\chi}^{(z)} = \{\chi^{(k)}\}$, are reached. The bottom level (leaf) single-particle functions can be written in terms of the time-independent basis functions for the physical modes as

$$|\phi^z_{i_z}(\chi^{(k)}, t)\rangle = \sum_{\alpha_k=1}^{n_k} \mathcal{A}^z_{\alpha_k i_z}(t)\, |\chi^{(k)}_{\alpha_k}\rangle = \sum_{\alpha_k=1}^{n_k} \mathcal{A}^z_{\alpha_k i_z}(t)\, |\Phi^z_{\alpha_k}(\boldsymbol{\chi}^z)\rangle \,, \tag{5.21}$$

where the combined bases associated with the leaf nodes, $|\Phi^z\rangle$, have been introduced. These equations provide a recursive definition for the ML-MCTDH ansatz for $\Psi_{\boldsymbol{\alpha}}$. While it is possible to work entirely with this recursive definition of the wavefunction, it is instructive to consider the expanded wavefunction. Unfortunately, expanding this recursive definition quickly becomes cumbersome as the number of layers in the expansion increases. As such, at this stage it is useful to introduce tensor network diagrams, as these provide simple diagrammatic representations of these expressions.

5.2.1 Tensor Network Diagrams

Tensor network diagrams are useful for discussing general tensor networks. In these diagrams a d-dimensional tensor is represented as a node with d outgoing lines, one for each index.[232] The basic building blocks of these network diagrams are depicted in figure 5.2.

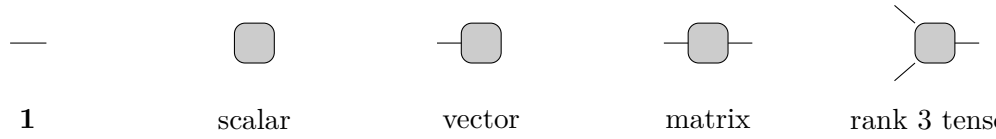

Figure 5.2: The basic elements of a tensor network diagram. A general d-dimensional tensor is represented by a node with d outgoing lines, a scalar is represented by a node, a vector by a node with one outgoing line, and a matrix by a node with two outgoing lines. A single line with no nodes represents an identity matrix.

Within this graphical representation, contractions of two tensors are represented by lines connecting the two nodes. A tensor network is a network constructed from a set of distinct tensors connected by contractions of the different indices of the tensors. Lines that are attached to only one node correspond to uncontracted indices, and the dimension of a tensor network is the number of uncontracted indices. Three tensor networks with their fully contracted results are shown in figure 5.3. The

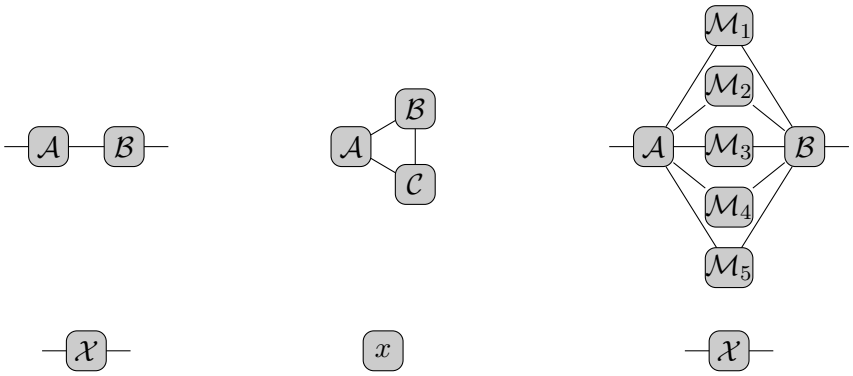

Figure 5.3: Three uncontracted tensor networks (top row) and the fully contracted result tensors (bottom row).

first of these networks corresponds to a contraction of two 2-dimensional tensors ($\mathcal{A}$

and $\mathcal{B}$), the result of which is, itself, a 2-dimensional tensor ($\mathcal{X}$). Such a network diagram can therefore represent a matrix-matrix product,

$$\mathbf{X} = \mathbf{AB}. \tag{5.22}$$

The second network represents a contraction of three 2-dimensional tensors ($\mathcal{A}$, $\mathcal{B}$, and $\mathcal{C}$), to give a scalar, x. This network diagram can represent the trace of a product of three matrices

$$x = \mathrm{tr}\left[\mathbf{ABC}\right]. \tag{5.23}$$

The final network represents the contraction of two 6-dimensional tensors with a series of 2-dimensional tensors to form a 2-dimensional tensor. A contraction of this form occurs often in the following discussion and can represent the matrix operation

$$\mathbf{X} = \mathbf{A}\left(\mathbf{M}_1 \otimes \cdots \otimes \mathbf{M}_5\right)\mathbf{B} \tag{5.24}$$

where $\mathbf{A}$ and $\mathbf{B}$ are matrix representations of the two 5-dimensional tensors and $\otimes$ denotes the Kronecker product. Each tensor in the tensor networks shown in figure 5.3 has been labelled for illustrative purposes, however in the following discussion the nodes of the tensor network will typically not be labelled. The labels and ordering of indices in tensor networks are entirely arbitrary and ultimately unimportant to the final implementation; all that matters is that the correct sequence of contractions is performed.

The diagrams provide a convenient representation of the ML-MCTDH ansatz discussed above. An example of a tensor network diagram representing an ML-MCTDH ansatz wavefunction for a 5-dimensional system is shown in figure 5.4. When fully contracted, this tensor network becomes the 5-dimensional tensor $\Psi_{\boldsymbol{\alpha}}$ with elements given by

$$\begin{aligned}\Psi_{\alpha_1\ldots\alpha_5} = \mathcal{A}^{1}_{i_{2;1},i_{2;2},i_{2;3}}&\left(\mathcal{A}^{2;1}_{i_{3;1,1}i_{3;1,2}i_{2;1}}\left(\mathcal{A}^{3;1,1}_{\alpha_1 i_{3;1,1}}\mathcal{A}^{3;1,2}_{\alpha_2 i_{3;1,2}}\right)\right)\\ &\left(\mathcal{A}^{2;2}_{i_{3;2,1}i_{3;2,2}i_{2;2}}\left(\mathcal{A}^{3;2,1}_{\alpha_3 i_{3;2,1}}\mathcal{A}^{3;2,2}_{\alpha_4 i_{3;2,2}}\right)\right)\\ &\left(\mathcal{A}^{2;3}_{\alpha_5 i_{2;3}}\right),\end{aligned} \tag{5.25}$$

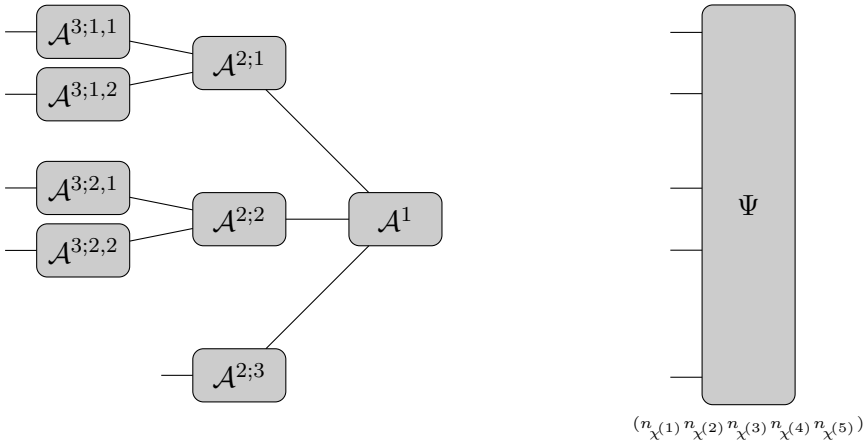

Figure 5.4: An example of a tree tensor network which, when fully contracted, corresponds to a 5-dimensional tensor.

where the Einstein summation convention has been employed. The ML-MCTDH ansatz corresponds to the approximation of the multidimensional coefficient tensor of a wavefunction using a general loop-free tensor network: a tree tensor network. The z index introduced in equation 5.18 uniquely describes the location of each of the tensors $\{\mathcal{A}^z\}$ in the tree tensor network. For the node with index z (at layer l), the nodes on the layer $l+1$, obtained by applying the concatenation operator (equation 5.18) once, are referred to as its children. Node z will be referred to as the parent of its children, and its children referred to as siblings of each other. In the following discussion, the tree tensor network represented by figure 5.4 will be used in order to provide explicit examples of the operations of interest.

A tree tensor networks may contain orders of magnitude fewer elements than the tensor it represents. In particular, if the number of single-particle functions included at each node is significantly smaller than the number of states it represents, then it will provide a compact representation of the fully contracted tensor. The ML-MCTDH method exploits this. By restricting the number of single-particle functions used to represent a wavefunction, an approximate solution to the full-dimensional time-dependent Schrödinger equation can be obtained. As the number of single-particle functions increases, the approximation becomes more accurate.[215,233]

The aim of the remaining discussion presented in this chapter is to obtain a set of equations describing the time-evolution of a tree tensor network approximation to the auxiliary density operators arising from the hierarchical equations of motion formalism. Within this approach, the system degrees of freedom and the bath modes will be analogous to the physical degrees of freedom, represented by the $\chi^{(k)}$s in the molecular dynamics context, while the Hamiltonian, $\hat{H}$, governing the dynamics is the non-Hermitian operator, $\mathcal{H}$, introduced earlier in Section 5.1.1 (see equation 5.11). In the following derivation, only the case of a Hamiltonian that is given as a sum of products of operators that act on each degree of freedom,

$$\hat{H} = \sum_r \hat{H}_r = \sum_r \bigotimes_{k=1}^{d} \hat{h}_r^{(k)}, \tag{5.26}$$

where $\hat{h}_r^{(k)}$ acts on the k-th degree of freedom, will be considered. This is a standard restriction employed when deriving the ML-MCTDH equations of motion,[213–216,224] and is also the case for the HEOM "Hamiltonian" given in equation 5.11.

5.2.2 Single Particle and Single Hole Functions

The single-particle functions, defined recursively by equation 5.20, are functions of some subset of the physical degrees of freedom. The representation of these functions, in terms of the basis functions, can be obtained by repeatedly expanding equation 5.20, (employing the Einstein summation convention) to give

$$|\phi_{i_z}^z(\boldsymbol{\chi}^{(z)}, t)\rangle = \phi^z_{\boldsymbol{\alpha}_{(z)} i_z}(t) \bigotimes_{k=1}^{d_z} |\chi^{(z)}_{\alpha_k}\rangle\,, \tag{5.27}$$

where $\boldsymbol{\alpha}_{(z)}$ is a combined index of the α_ks, and the single-particle coefficient tensor, $\phi^z_{\boldsymbol{\alpha}_{(z)} i_z}(t)$, is represented by a $(d_z + 1)$-dimensional tensor network containing the node, $\mathcal{A}^z$, and all child nodes of this tensor. Using equation 5.20, the single-particle function coefficient tensor can be obtained recursively in terms of the single-particle function coefficient tensor of the layer below as[215]

$$\phi^z_{\boldsymbol{\alpha}_z i_z}(t) = \mathcal{A}^z_{\boldsymbol{I}_z i_z}(t) \prod_{j=1}^{m_z} \phi^{z\circ j}_{\boldsymbol{\alpha}_{(z\circ j)} i_{z\circ j}}(t) \tag{5.28}$$

$$= \mathcal{A}^z_{\boldsymbol{I}_z i_z}(t) \Phi^z_{\boldsymbol{\alpha}_{(z)} \boldsymbol{I}_z}(t), \tag{5.29}$$

where, in the second line, the coefficient tensors for the basis functions for node z have been defined implicitly. This recurrence begins at the leaf nodes of the tree tensor network with

$$\phi^{z}_{\alpha i_z}(t) = \mathcal{A}^{z}_{\beta i_z}(t)\phi^{z\circ 1}_{\alpha\beta}, \tag{5.30}$$

where the single-particle functions associated with the layer below the leaf nodes have been introduced and are given by

$$\phi^{z\circ 1}_{\alpha\beta} = \langle \chi^{(k)}_{\alpha} | \chi^{(k)}_{\beta} \rangle = \delta_{\alpha\beta}, \tag{5.31}$$

where $\delta_{\alpha\beta}$ is the Kronecker delta function. Fully expanding these expressions to obtain a non-recursive set of equations is generally cumbersome, however, they have a rather simple tensor network diagram representation. The single-particle function associated with a node z in the tree tensor network is simply the subtree with root z, as illustrated in figure 5.5.

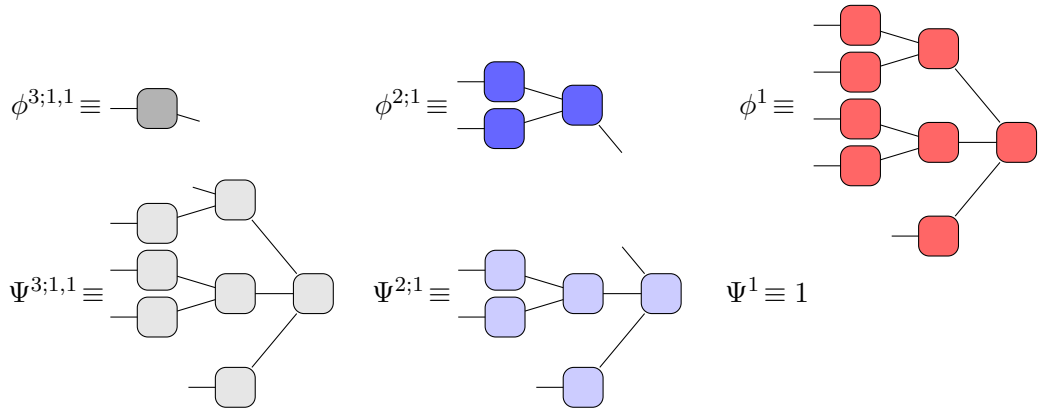

Figure 5.5: Graphical representation of the single-particle function coefficient tensors, ϕ^{z}, associated with the node z in the tree tensor network. In this figure the single-hole function coefficient tensors, Ψ^{z}, have been defined. These correspond to the remainder of the tensor network obtained after removing the single-particle functions.

The single-hole function coefficient tensors, Ψ^{z}, have been introduced in figure 5.5. The corresponding single-hole functions are defined by removing the single-particle functions associated with a node from the full wavefunction[224]

$$|\Psi\rangle = \sum_{i_z=1}^{n_z} |\phi^{z}_{i_z}(\boldsymbol{\chi}^{(z)}, t)\rangle \otimes |\Psi^{z}_{i_z}(\boldsymbol{\chi}^{(\backslash z)}, t)\rangle\,, \tag{5.32}$$

and they represent all degrees of freedom that the single-particle functions do not represent ($\boldsymbol{\chi}^{(\backslash z)} = \boldsymbol{\chi} \setminus \boldsymbol{\chi}^{(z)}$). The single-hole functions for a node z may be defined recursively in terms of the single-hole functions of its parent (the connected node with smaller l), and the single-particle functions of its siblings (all nodes, except the node z, that are connected to its parent in the same level l). This recurrence relation is given by[224]

$$|\Psi_m^{z\circ k}\rangle = |\Psi_j^z(\boldsymbol{\chi}^{(\backslash z)}, t)\rangle \otimes \left(\mathcal{A}^z_{\boldsymbol{I}^m_{z,k},j} \bigotimes_{\substack{j=1 \\ j\neq k}}^{m_z} |\phi^{z\circ j}_{i_{z\circ j}}(\boldsymbol{\chi}^{(z\circ j)}, t)\rangle \right) \tag{5.33}$$

where a new combined index $\boldsymbol{I}^m_{z,k} = \{i_{z\circ 1}, \ldots, i_{z\circ(k-1)}, m, i_{z\circ(k+1)}, \ldots, i_{z\circ m_z}\}$ has been introduced, and the recurrence begins with the root node, where $\Psi^1 = 1$ acts on no degrees of freedom. In what follows, the coefficient tensor associated with the single-hole functions, $|\Psi_j^z(\boldsymbol{\chi}^{(\backslash z)}, t)\rangle$, obtained by taking the inner product of the single-hole function with the time-independent basis states of the modes it represents, will be denoted by

$$\Psi^z_{\boldsymbol{\alpha}_{(\backslash z)}j}(t) \equiv \langle \boldsymbol{\chi}^{(\backslash z)}_{\boldsymbol{\alpha}_{(\backslash z)}} | \Psi_j^z(\boldsymbol{\chi}^{(\backslash z)}, t)\rangle \,, \tag{5.34}$$

where $\boldsymbol{\alpha}_{(\backslash z)}$ denotes a combined index for the time-independent basis states.

The single-particle and single-hole functions play an important role in evaluating the equations of motion for a tree tensor network representation wavefunction. The single-particle functions act as the basis states for the states in layers above, and the single-hole functions allow easy construction of the mean-field values of operators. Additionally, these functions allow for a convenient representation of the wavefunction in terms of the coefficient tensor associated with a given node z. Inserting equation 5.20 into equation 5.32, gives

$$|\Psi\rangle = \mathcal{A}^z_{\boldsymbol{I}_z i_z}(t)\, |\Phi^z_{\boldsymbol{I}_z}(\boldsymbol{\chi}^{(z)}, t)\rangle \otimes |\Psi^z_{i_z}(\boldsymbol{\chi}^{(\backslash z)}, t)\rangle \,, \tag{5.35}$$

where the Einstein summation convention has been used, and the coefficient tensor $\Psi_{\boldsymbol{\alpha}}$ may, therefore, be written as

$$\Psi_{\boldsymbol{\alpha}} = \mathcal{A}^z_{\boldsymbol{I}_z i_z}(t) \Phi^z_{\boldsymbol{\alpha}_{(z)}\boldsymbol{I}_z} \Psi^z_{\boldsymbol{\alpha}_{(\backslash z)} i_z}. \tag{5.36}$$

5.3 The ML-MCTDH Equations of Motion

For a general quantum mechanical system evolving under the Hamiltonian $\hat{H}$, the solutions, $|\Psi\rangle$, to the Schrödinger equation,

$$|\dot{\Psi}\rangle = -\frac{i}{\hbar}\hat{H}\,|\Psi\rangle\,, \tag{5.37}$$

can explore the full Hilbert space. By employing the ML-MCTDH ansatz with a fixed topology and number of single-particle functions in each node, the possible solutions that can be obtained are restricted to some manifold $\mathcal{M}$ in Hilbert space.[125,234] The ML-MCTDH equations of motion are a set of variational equations of motion that describe the evolution, under the Hamiltonian $\hat{H}$, of the wavefunction within this manifold.[213,214] Following the conventional approach, these equations of motion will be obtained through the use of the Dirac-Frenkel variational principle,[235,236]

$$\langle\delta\Psi|\,\frac{\partial}{\partial t} + \frac{i}{\hbar}\hat{H}\,|\Psi\rangle = 0. \tag{5.38}$$

which, while for general $|\Psi\rangle$ is not strictly a variational principle,[237,238] has found widespread use in numerical simulations of quantum dynamics. Here $\delta\Psi$ denotes all possible variations of the wavefunction, Ψ with respect to its parameters. Although originally presented for wavefunctions evolving under a Hermitian Hamiltonian,[235,236] this approach can be used to treat the dynamics of arbitrary bounded operators that act on a complex Hilbert space.[239] Furthermore, if all parameters are complex analytic, and as a result both $i\delta\Psi$ and $\delta\Psi$ are possible variations,[237] then the Dirac-Frenkel variational principle becomes equivalent to the McLachlan variational principle[238]

$$\delta\|\left(\frac{\partial}{\partial t} + \frac{i}{\hbar}\hat{H}\right)|\Psi\rangle\,\|^2 = 0. \tag{5.39}$$

The McLachlan variational principle determines the approximate solution, $\Psi(t)$, to the system of equations by imposing the condition that the time-derivative of

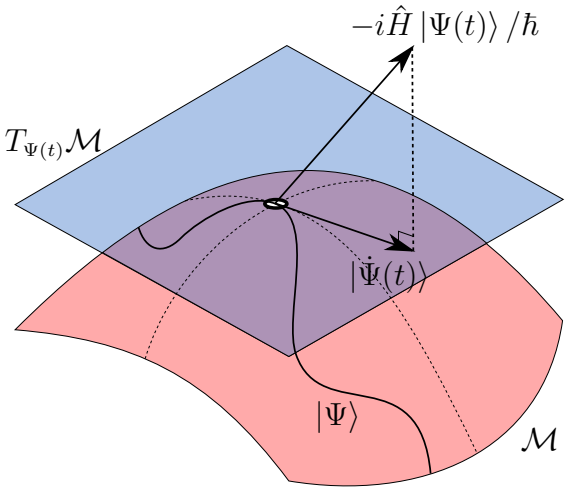

Figure 5.6: A graphical representation of the McLachlan variational principle. At each time t, the variational wavefunction, $\Psi(t)$, which is restricted to a manifold, $\mathcal{M}$, in the full Hilbert space, is obtained by using the best local approximation to the time-derivative $-i\hat{H}\,|\Psi(t)\rangle\,/\hbar$ at each point. This is carried out by taking the time-derivative of the variational wavefunction, $\dot{\Psi}(t)$, which lies in the tangent plane to $\mathcal{M}$ at the point $\Psi(t)$, $T_{\Psi(t)}\mathcal{M}$, to be equal to the projection of the true time-derivative onto this tangent plane.

the solution, which is a vector lying in the tangent plane, $T_{\Psi(t)}\mathcal{M}$, to the manifold at $\Psi(t)$, is chosen such that

$$\frac{\partial}{\partial t}\,|\Psi\rangle = |V\rangle\,, \qquad \text{where } |V \in T_{\Psi(t)}\mathcal{M}\rangle \text{ minimises} \qquad \|\,|V\rangle + \frac{i}{\hbar}\hat{H}\,|\Psi\rangle\,\|. \tag{5.40}$$

That is, it is the vector lying in the tangent plane that is the best local approximation to the true time-derivative $-i\hat{H}\,|\Psi(t)\rangle\,/\hbar$, as illustrated in figure 5.6. This best local approximation is simply the projection of $-i\hat{H}\,|\Psi(t)\rangle\,/\hbar$ into the tangent plane. The McLachlan variation principle gives rise to the equations of motion[125,234,240,241]

$$|\dot{\Psi}(t)\rangle = -\frac{i}{\hbar}P(\Psi(t))\hat{H}\,|\Psi(t)\rangle\,, \tag{5.41}$$

where $P(\Psi(t))$ is the $\Psi(t)$ dependent operator that projects an element of Hilbert space onto the tangent plane, $T_{\Psi(t)}\mathcal{M}$. For the case considered here, both variational principles are equivalent and, in what follows, the Dirac-Frenkel variational principle will be used. However, it is first necessary to impose some additional conditions on the ML-MCTDH ansatz representation of the wavefunction.

5.3.1 Gauge Condition

The ML-MCTDH ansatz representation for the wavefunction is not unique. An identity matrix may be inserted between any two tensors in the tensor network that are connected by a contraction without altering the value of the wavefunction. By expanding the identity product in terms of a general invertible matrix $\mathbf{M}$ and its inverse $\mathbf{M}^{-1}$, the value of the two tensors can be altered without changing the total tensor that the network represents. For the ML-MCTDH form of the wavefunction, the single-particle functions and coefficients at any node can be modified by an arbitrary invertible linear transform without altering the value of the wavefunction. As such, there is a redundancy (gauge freedom) in the ML-MCTDH form of the wavefunction. This gauge freedom of the tensor network prevents well-defined equations of motion being obtained and it is necessary to impose additional constraints on the tensor network to obtain uniquely defined equations of motion.[211]

Following the standard approach,[211,214,216] this ambiguity is removed by imposing the constraints

$$\langle \phi^z_{\alpha i}(\boldsymbol{\chi}^{(z)}, 0) | \phi^z_{\alpha j}(\boldsymbol{\chi}^{(z)}, 0) \rangle = \delta_{ij} \tag{5.42}$$

and

$$\langle \phi^z_{\alpha i}(\boldsymbol{\chi}^{(z)}, t) | \dot{\phi}^z_{\alpha j}(\boldsymbol{\chi}^{(z)}, t) \rangle = 0 \tag{5.43}$$

for the single-particle functions associated with all nodes except the root node ($z = 1$). These conditions ensure that at $t = 0$ the single-particle functions at each node are orthogonal and remain orthogonal for all time. By inserting the definition of single-particle functions given in equation 5.20 into equation 5.43, and evaluating the resultant expressions recursively from the leaf nodes upwards, this condition becomes

$$\langle \Phi^z_{\boldsymbol{I}_z}(\boldsymbol{\chi}^{(z)}, t) | \, \mathcal{A}^{z*}_{\boldsymbol{I}_z i}(t) \dot{\mathcal{A}}^z_{\boldsymbol{J}_z j}(t) \, | \Phi^z_{\boldsymbol{J}_z}(\boldsymbol{\chi}^{(z)}, t) \rangle = 0, \tag{5.44}$$

which can be represented by the tensor network diagram shown in figure 5.7, where the time-derivative of a tensor is represented by a diamond shaped node. The contraction of any subtree with root at z, and the same subtree with the node at

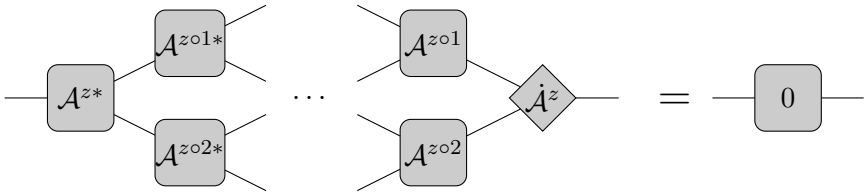

Figure 5.7: Tensor network diagram representation of the gauge condition given by equation 5.45. Here, and in the following discussion, diamond shape nodes are used to represent the time-derivative of a tensor. The inner product of any subtree with root at z, and the same subtree with the node at z replaced with its time-derivate, is zero.

z replaced with its time-derivate, is zero. On imposing the orthonormality of the single-hole functions, the gauge condition simplifies to

$$\mathcal{A}^{z*}_{\boldsymbol{I}_z i}(t)\dot{\mathcal{A}}^{z}_{\boldsymbol{I}_z j}(t) = 0, \tag{5.45}$$

By employing this additional constraint, it becomes possible to obtain a set of equations of motion for the ML-MCTDH ansatz.

5.3.2 The Equations of Motion

Using equation 5.36, the linear variations of the coefficients in the ML-MCTDH ansatz, $\delta\Psi$, may be written as

$$\delta\Psi_{\boldsymbol{\alpha}} = \left(\delta\mathcal{A}^{1}_{\boldsymbol{I}_1 i_1}\right)\Phi^{z}_{\boldsymbol{\alpha} i_1} + \sum_{j=1}^{m_1}\Phi^{2;j}_{\boldsymbol{\alpha}_{(2;j)}\boldsymbol{I}_{2;j}}\left(\delta\mathcal{A}^{2;j}_{\boldsymbol{I}_{2;j} i_{2;j}}\right)\Psi^{2;j}_{\boldsymbol{\alpha}_{(\setminus 2;j)} i_{2;j}} + \ldots \tag{5.46}$$

$$= \sum_{z\in\mathcal{N}(\Psi)}\Phi^{z}_{\boldsymbol{\alpha}_{(z)}\boldsymbol{I}_z}\delta\mathcal{A}^{z}_{\boldsymbol{I}_z i_z}\Psi^{z}_{\boldsymbol{\alpha}_{(\setminus z)} i_z} \tag{5.47}$$

where the Einstein summation convention has been employed for the sums over the indices $\boldsymbol{I}_z$ and i_z, and $\mathcal{N}(\Psi)$ denotes the set of all indices representing nodes in the tensor network Ψ. The time-derivative of the coefficient tensor, $\dot{\Psi}$, may be written as

$$\dot{\Psi}_{\boldsymbol{\alpha}} = \dot{\Phi}^{z}_{\boldsymbol{\alpha}_{(z)}\boldsymbol{I}_z}\mathcal{A}^{z}_{\boldsymbol{I}_z i_z}\Psi^{z}_{\boldsymbol{\alpha}_{(\setminus z)} i_z} + \Phi^{z}_{\boldsymbol{\alpha}_{(z)}\boldsymbol{I}_z}\dot{\mathcal{A}}^{z}_{\boldsymbol{I}_z i_z}\Psi^{z}_{\boldsymbol{\alpha}_{(\setminus z)} i_z} + \Phi^{z}_{\boldsymbol{\alpha}_{(z)}\boldsymbol{I}_z}\mathcal{A}^{z}_{\boldsymbol{I}_z i_z}\dot{\Psi}^{z}_{\boldsymbol{\alpha}_{(\setminus z)} i_z}, \tag{5.48}$$

for all $z \in \mathcal{N}(\Psi)$. The terms containing derivatives of the single-particle and single-hole functions may be expanded by applying the product rule to the recursive

definitions given in section 5.2.2. On doing so and simplifying the resulting expressions these two terms become

$$\dot{\Phi}^{z}_{\boldsymbol{\alpha}_{(z)}\boldsymbol{I}_z}\mathcal{A}^{z}_{\boldsymbol{I}_z i_z}\Psi^{z}_{\boldsymbol{\alpha}_{(\backslash z)} i_z} = \sum_{z'\in\mathcal{N}(\Phi^z)} \Phi^{z'}_{\boldsymbol{\alpha}_{(z')}\boldsymbol{I}_{z'}}\dot{\mathcal{A}}^{z'}_{\boldsymbol{I}_{z'} i_{z'}}\Psi^{z'}_{\boldsymbol{\alpha}_{(\backslash z')} i_{z'}} \tag{5.49}$$

and

$$\Phi^{z}_{\boldsymbol{\alpha}_{(z)}\boldsymbol{I}_z}\mathcal{A}^{z}_{\boldsymbol{I}_z i_z}\dot{\Psi}^{z}_{\boldsymbol{\alpha}_{(\backslash z)} i_z} = \sum_{z'\in\mathcal{N}(\Psi^z)} \Phi^{z'}_{\boldsymbol{\alpha}_{(z')}\boldsymbol{I}_{z'}}\dot{\mathcal{A}}^{z'}_{\boldsymbol{I}_{z'} i_{z'}}\Psi^{z'}_{\boldsymbol{\alpha}_{(\backslash z')} i_{z'}}, \tag{5.50}$$

respectively, where $\mathcal{N}(\Phi^z)$ and $\mathcal{N}(\Psi^z)$ denote the set of indices representing the nodes of the single-particle and single-hole function tensor networks Φ^z and Ψ^z. The total derivative may then be written as

$$\dot{\Psi}_{\boldsymbol{\alpha}} = \sum_{z'\in\mathcal{N}(\Psi)} \Phi^{z'}_{\boldsymbol{\alpha}_{(z')}\boldsymbol{I}_{z'}}\dot{\mathcal{A}}^{z'}_{\boldsymbol{I}_{z'} i_{z'}}\Psi^{z'}_{\boldsymbol{\alpha}_{(\backslash z')} i_{z'}} \tag{5.51}$$

Inserting equation 5.47 and 5.51 into equation 5.38, gives

$$\sum_{z\in\mathcal{N}(\Psi)} \delta\mathcal{A}^{z\dagger}_{\boldsymbol{I}_z i_z} \langle\Phi^{z}_{\boldsymbol{I}_z}|\otimes\langle\Psi^{z}_{i_z}| \left[\sum_{z'\in\mathcal{N}(\Psi)} \left(\dot{\mathcal{A}}^{z'}_{\boldsymbol{J}_{z'} j_{z'}}|\Phi^{z'}_{\boldsymbol{J}_{z'}}\rangle\otimes|\Psi^{z'}_{j_{z'}}\rangle\right) + \frac{i}{\hbar}\hat{H}\,|\Psi\rangle \right] = 0. \tag{5.52}$$

Now equation 5.52 holds for all allowed variations, and so by equating the coefficients this gives

$$\sum_{z'\in\mathcal{N}(\Psi)} \dot{\mathcal{A}}^{z'}_{\boldsymbol{J}_{z'} j_{z'}} \left(\langle\Phi^{z}_{\boldsymbol{I}_z}|\otimes\langle\Psi^{z}_{i_z}|\right)\left(|\Phi^{z'}_{\boldsymbol{J}_{z'}}\rangle\otimes|\Psi^{z'}_{j_{z'}}\rangle\right) = -\frac{i}{\hbar}\left(\langle\Phi^{z}_{\boldsymbol{I}_z}|\otimes\langle\Psi^{z}_{i_z}|\right)\hat{H}\,|\Psi\rangle\,, \tag{5.53}$$

for each $z \in \mathcal{N}(\Psi)$. On expanding $|\Psi\rangle$, the right hand side of equation 5.53, may be written as

$$\text{RHS} = -\frac{i}{\hbar}\left(\langle\Phi^{z}_{\boldsymbol{I}_z}|\otimes\langle\Psi^{z}_{i_z}|\right)\hat{H}\left(|\Phi^{z}_{\boldsymbol{J}_z}\rangle\otimes|\Psi^{z}_{j_z}\rangle\right)\mathcal{A}^{z}_{\boldsymbol{J}_z j_z}. \tag{5.54}$$

For each z, each of the terms in the sum of product operators form for the Hamiltonian, equation 5.26, may be split into a product of two components: the first $\hat{h}^z_r$, acting on the physical coordinates $\boldsymbol{\chi}^{(z)}$ that the single-particle functions act on and a component, $\hat{H}^z_r$, acting on the remaining coordinates $\boldsymbol{\chi}^{(\backslash z)}$ as

$$\sum_r \hat{H}_r = \sum_r \left(\bigotimes_{k\in k_{(z)}} \hat{h}^{(k)}_r\right)\otimes\left(\bigotimes_{k\in k_{(\backslash z)}} \hat{h}^{(k)}_r\right) \tag{5.55}$$

$$= \hat{h}^z_r \otimes \hat{H}^z_r \tag{5.56}$$

where $k \in k_{(\backslash z)}$ and $k \in k_{(z)}$ denote the values of k that index the physical modes $\boldsymbol{\chi}^{(\backslash z)}$ and $\boldsymbol{\chi}^{(z)}$, respectively. Inserting this form for the sum of product operator form for the Hamiltonian, equation 5.54 becomes

$$\text{RHS} = -\frac{i}{\hbar}\sum_r \langle \Phi^z_{\boldsymbol{I}_z}| \hat{h}^z_r |\Phi^z_{\boldsymbol{J}_z}\rangle \langle \Psi^z_{i_z}| \hat{H}^z_r |\Psi^z_{j_z}\rangle \mathcal{A}^z_{\boldsymbol{J}_z j_z} \tag{5.57}$$

$$= -\frac{i}{\hbar}\sum_r [h^z_r]_{\boldsymbol{I}_z \boldsymbol{J}_z} \langle H^z_r\rangle_{i_z j_z} \mathcal{A}^z_{\boldsymbol{J}_z j_z}. \tag{5.58}$$

Here the r-th contributions to the mean-field Hamiltonian

$$\langle H^z_r\rangle_{i_z j_z} = \langle \Psi^z_{i_z}| \hat{H}^z_r |\Psi^z_{j_z}\rangle, \tag{5.59}$$

and the single-particle Hamiltonian,

$$[h^z_r]_{\boldsymbol{I}_z \boldsymbol{J}_z} = \langle \Phi^z_{\boldsymbol{I}_z}| \hat{h}^z_r |\Phi^z_{\boldsymbol{J}_z}\rangle, \tag{5.60}$$

for node z have been introduced. Introducing the tensor representations of the Hamiltonian operators with respect to the underlying physical basis as

$$\mathfrak{h}^{(k)}_{r\alpha\beta} = \langle \chi^{(k)}_\alpha| \hat{h}^{(k)}_r |\chi^{(k)}_\beta\rangle \tag{5.61}$$

$$\mathfrak{h}^z_{r\boldsymbol{\alpha}\boldsymbol{\beta}} = \langle \boldsymbol{\chi}^{(z)}_{\boldsymbol{\alpha}}| \hat{h}^z_r |\boldsymbol{\chi}^{(z)}_{\boldsymbol{\beta}}\rangle \tag{5.62}$$

$$\mathcal{H}^z_{r\boldsymbol{\alpha}\boldsymbol{\beta}} = \langle \boldsymbol{\chi}^{(\backslash z)}_{\boldsymbol{\alpha}}| \hat{H}^z_r |\boldsymbol{\chi}^{(\backslash z)}_{\boldsymbol{\beta}}\rangle, \tag{5.63}$$

the single-particle and mean-field Hamiltonian operator tensors may be represented by the tensor network diagram shown in figure 5.8.

The left hand side (LHS) of equation 5.53 contains a sum over terms in which different nodes of the tree are differentiated. These terms can be grouped into whether they arise due to derivatives of the single-particle function, single-hole function, or coefficient tensor for node z. The LHS can alternatively be written as

$$\begin{aligned}\text{LHS} = {} & \langle \Phi^z_{\boldsymbol{I}_z}|\dot{\Phi}^z_{\boldsymbol{J}_z}\rangle \langle \Psi^z_{i_z}|\Psi^z_{j_z}\rangle \mathcal{A}^z_{\boldsymbol{J}_z j_z} + \langle \Phi^z_{\boldsymbol{I}_z}|\Phi^z_{\boldsymbol{J}_z}\rangle \langle \Psi^z_{i_z}|\Psi^z_{j_z}\rangle \dot{\mathcal{A}}^z_{\boldsymbol{J}_z j_z} \\ & + \langle \Phi^z_{\boldsymbol{I}_z}|\Phi^z_{\boldsymbol{J}_z}\rangle \langle \Psi^z_{i_z}|\dot{\Psi}^z_{j_z}\rangle \mathcal{A}^z_{\boldsymbol{J}_z j_z}.\end{aligned} \tag{5.64}$$

Imposing the gauge condition given in equation 5.43, the first term containing an inner product of single-particle functions with their derivatives is zero. As such, all

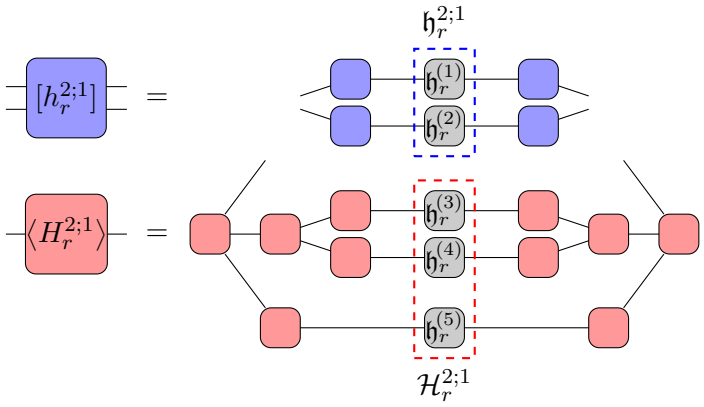

Figure 5.8: Tensor network diagram representations of the r-th contribution to the mean-field and single-particle Hamiltonians for node $z = 2;1$ of a wavefunction $|\Psi\rangle$ represented by the tree tensor network depicted in figure 5.4. The contributions to the mean-field Hamiltonian are obtained by taking the matrix elements of the Hamiltonian using the single-hole functions (red). The single-particle functions are the matrix elements obtained using the basis functions for the node (blue).

contribution to the LHS arising from equation 5.49 may be ignored. Imposing the orthonormality of the single-particle functions, this expression simplifies further to give

$$\text{LHS} = \delta_{\boldsymbol{I}_z \boldsymbol{J}_z} \langle \Psi^z_{i_z} | \Psi^z_{j_z} \rangle \dot{\mathcal{A}}^z_{\boldsymbol{J}_z j_z} + \delta_{\boldsymbol{I}_z \boldsymbol{J}_z} \langle \Psi^z_{i_z} | \dot{\Psi}^z_{j_z} \rangle \mathcal{A}^z_{\boldsymbol{J}_z j_z}. \tag{5.65}$$

Evaluation of the contribution arising from the time derivative of the single-hole functions (the final term in equation 5.65) is more involved. Expanding the time-derivative there are two distinct terms depending on the node z considered and which node (z') the time-derivative is acting on. These are show in figure 5.9. If the time-derivative acts on a node that is in a different branch of the tree, as shown in panel a) of figure 5.9, then the tensor network contains a contraction of the form given by equation 5.45. In this case, the total network is zero and these terms contribute nothing to the sum. If however, the time-derivative acts on a z or an ancestor (parents, parents of parents, etc) of z, then no such contraction is found in the resultant network and the result is, in general, non-zero.

If z corresponds to the root node index, that is $z = 1$, then all contributions but one are zero by equation 5.45. In the remaining term the time-derivative acts on the root node; this can be evaluated trivially by exploiting the orthogonality

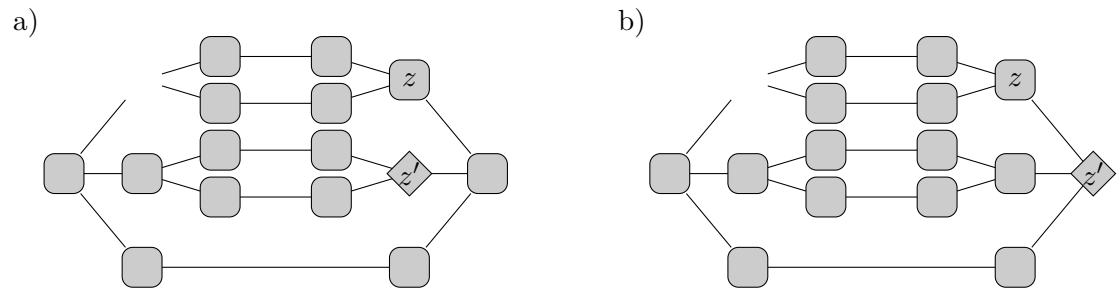

Figure 5.9: Tensor network diagrams of the two distinct types of terms arising on the left hand side of equation 5.53 for $z = 2;1$. In a), the node $z' = 2;2$, which has been differentiated with respect to time, is on a distinct branch of the tree to z, and by equation 5.45 is zero. In b), the node which is differentiated ($z' = 1$) is an ancestor of z, and no contraction of the form given by equation 5.45 is present in the network.

of the single-particle functions. As such, the equation of motion for the root node coefficients is[213,214,216]

$$\dot{\mathcal{A}}^1_{\boldsymbol{I}} = -\frac{i}{\hbar} \sum_r [h^1_r]_{\boldsymbol{IJ}} \, \mathcal{A}^1_{\boldsymbol{J}}. \tag{5.66}$$

For general $z \neq 1$ the left hand side of equation 5.53 is the sum of multiple terms. At this stage, in order to simplify the equations of motion, it is useful to introduce the projection tensor, P^z, with elements

$$P^z_{IJ} = \mathcal{A}^z_{Im} \mathcal{A}^{z*}_{Jm}. \tag{5.67}$$

Applying this projection tensor to the remaining terms in the left hand side (LHS) of equation 5.65 gives rise to one of two situations. For the case where $z' = z$, applying the projection tensor yields a tensor network of the form shown in a) of figure 5.10. The section of the tensor network contained within the red rectangle is then of the form shown in figure 5.7, and is zero due to the gauge condition, equation 5.45. This holds regardless of the network topology, and so, in general, the projection tensor given in equation 5.67 projects out the contributions to the LHS with $z' = z$.

When $z' \neq z$, which corresponds to the components arising from derivatives of the single-hole functions, the component of the tensor network contained within the

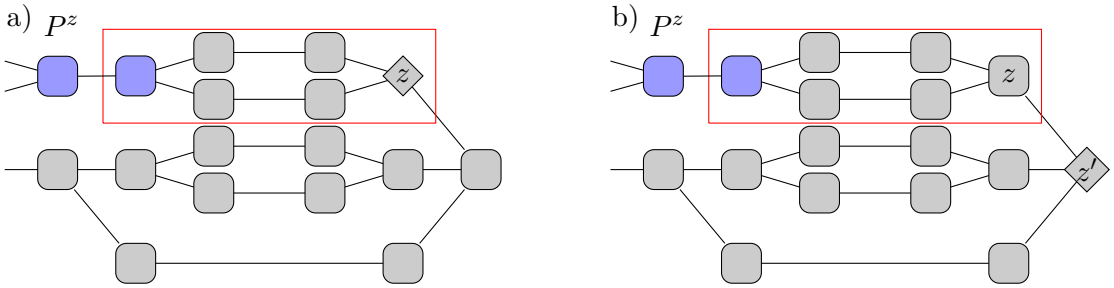

Figure 5.10: Tensor network diagrams showing the action of the projection tensor given by equation 5.67 (shown in blue) on the distinct types of terms that provide non-zero contributions to the left hand side of equation 5.53. The network can be simplified by evaluating the contractions over the nodes contained within the red rectangles.

red rectangle involves an inner product of single-particle functions with themselves. From the two gauge conditions, these single-particle functions are orthogonal for all time and, as such, this reduces to the identity matrix. The network can be further simplified by evaluating the contraction of the first index of the identity matrix with the m index of the remaining contribution to the projection tensor, $\mathcal{A}^z_{Im}$. In doing so, and exploiting the fact that the single-particle functions are orthogonal for all time, it can be seen that this tensor network returns to its original form, shown in b) in figure 5.9. This argument can be applied to an arbitrary tensor network and $z' \neq z$.

If the projection tensor P^z is applied to equation 5.53, the component arising from derivatives of the coefficient tensor at nodes z vanish, and an equation of motion for the single-hole functions is obtained

$$\langle \Psi^z_i | \dot{\Psi}^z_j \rangle \mathcal{A}^z_{\boldsymbol{I}j} = -\frac{i}{\hbar} \sum_r P^z_{\boldsymbol{IJ}} \left[h^z_r\right]_{\boldsymbol{JK}} \langle H^z_r \rangle_{ij} \mathcal{A}^z_{\boldsymbol{K}j}. \tag{5.68}$$

Alternatively, applying the projection tensor $\mathbf{1} - P^z$, where $\mathbf{1}$ is the identity operator, projects out the contributions from the derivatives of the single-hole function tensor to give

$$\langle \Psi^z_i | \Psi^z_j \rangle \dot{\mathcal{A}}^z_{\boldsymbol{I}j} = -\frac{i}{\hbar} \sum_r \left(\delta_{\boldsymbol{IJ}} - P^z_{\boldsymbol{IJ}}\right) \left[h^z_r\right]_{\boldsymbol{JK}} \langle H^z_r \rangle_{ij} \mathcal{A}^z_{\boldsymbol{K}j}. \tag{5.69}$$

By defining the single-particle density matrix for node z, $\boldsymbol{\rho}^z$, whose matrix elements are

$$\rho^z_{ij} = \langle \Psi^z_i | \Psi^z_j \rangle , \tag{5.70}$$

equation 5.69 may be rearranged, assuming ρ^z is invertible, to give an equation of motion for the coefficients at an arbitrary non-root node z,[216,224]

$$\dot{\mathcal{A}}^z_{\boldsymbol{I}i} = -\frac{i}{\hbar} \sum_r \left(\delta_{\boldsymbol{IJ}} - P^z_{\boldsymbol{IJ}}\right) \left[h^z_r\right]_{\boldsymbol{JK}} \left(\boldsymbol{\rho}^z\right)^{-1}_{ij} \left\langle H^z_r \right\rangle_{jk} \mathcal{A}^z_{\boldsymbol{K}k}. \tag{5.71}$$

This and equation 5.66 are the ML-MCTDH equations of motion, which may be written compactly in terms of the matrix representation (the matrix obtained by treating each combined index as a single index) of each tensor as

$$\dot{\boldsymbol{\mathcal{A}}}^1 = -\frac{i}{\hbar} \sum_r \left[\boldsymbol{h}^1_r\right] \boldsymbol{\mathcal{A}}^1 \tag{5.72}$$

$$\dot{\boldsymbol{\mathcal{A}}}^z = -\frac{i}{\hbar} \sum_r \left(\mathbf{1} - \boldsymbol{P}^z\right) \left[\boldsymbol{h}^z_r\right] \boldsymbol{\mathcal{A}}^z \left(\left(\boldsymbol{\rho}^z\right)^{-1} \left\langle \boldsymbol{H}^z_r \right\rangle\right)^T. \tag{5.73}$$

This system of nonlinear differential equations describes the evolution of each of the coefficient tensors in the tree tensor network. The equations for each value of z are coupled due to the presence of the single-particle and single-hole Hamiltonians.

5.4 Integration of the Equations of Motion

The ML-MCTDH equations of motion, equations 5.72 and 5.73, provide a means for constructing a time-dependent tree tensor network approximation to the solution of the time-dependent Schrödinger equation

$$|\dot{\Psi}\rangle = -\frac{i}{\hbar} \hat{H} \, |\Psi\rangle \,, \tag{5.74}$$

where $\hat{H}$ is the Hamiltonian governing the dynamics of the quantum system. In the derivation of these equations of motion the only restriction on the operator $\hat{H}$ was that it could be represented by the sum of product operators form given in equation 5.26 — it does not need to be a Hermitian operator. As such, by treating each of the "bath modes" of the HEOM as the physical modes of a problem these equations can be directly applied to solve the hierarchical equations of motion given in Section 5.1.1. These coupled ordinary differential equations (ODE) may then be solved using standard ODE integrators or through the use of special integrators developed for treating these equations of motion.[211,242] In practice, however, these

equations are highly unstable and need to be modified in order for their evaluation to be practical. The first issue arises from the application of the projector matrix, $\boldsymbol{P}^z = \boldsymbol{\mathcal{A}}^z \boldsymbol{\mathcal{A}}^{z\dagger}$, in equation 5.73. This projector ensures that the single-particle functions remain orthonormal at all times.[211,216] A build-up of numerical error throughout the integration of these equations may result in a loss in orthonormality of the single-particle functions, in which case the operator $\boldsymbol{P}^z$ is no longer a valid projection matrix.[211] Once this occurs, the orthonormality of the single-particle functions is lost rapidly, even if the equations of motion are integrated exactly. A number of strategies have been proposed to overcome this issue.[211,216] Here, following the procedure given in reference [211], it is handled by replacing the projector with

$$\boldsymbol{P}^z = \boldsymbol{\mathcal{A}}^z \left(\boldsymbol{\mathcal{A}}^{z\dagger} \boldsymbol{\mathcal{A}}^z \right)^{-1} \boldsymbol{\mathcal{A}}^{z\dagger}. \tag{5.75}$$

While the single-particle functions are orthonormal, this approach does not alter the definition of $\boldsymbol{P}^z$ at all. However, if the build up of numerical errors leads to a loss of orthonormality of the single-particle functions, this definition ensures that $\boldsymbol{P}^z$ is a valid projection operator and helps to overcome further rapid loss of orthonormality.

The second numerical difficulty is significantly more severe. In deriving equation 5.71 it was assumed that the single-particle density matrices for each node z, $\boldsymbol{\rho}^z$, were invertible. These single-particle density matrices depend on the current state of the tree tensor network and so, in general, $\boldsymbol{\rho}^z$ is not invertible. If the state of the system can be represented with fewer single-particle functions at a given node z than are present, then there are linear combinations of the single-particle functions which do not contribute to the total wavefunction. In this case, the single-particle density matrix will have eigenvalues that are zero and will therefore not be invertible.[243] This difficulty is particularly problematic when attempting to apply this integration scheme to the hierarchical equations of motion. The initial state of the hierarchy of auxiliary density operators is given by

$$\hat{\sigma}_{\mathbf{n}}(0) = \begin{cases} \hat{\rho}_S(0) & \mathbf{n} = 0 \\ 0 & \text{otherwise} \end{cases} \tag{5.76}$$

where $\hat{\rho}_S(0)$ denotes the initial system reduced density operator. This function is exactly represented by a single Hartree product state:

$$\hat{\sigma}_{\mathbf{n}}(0) = \hat{\rho}_S(0) \otimes |0\rangle_1 \otimes \cdots \otimes |0\rangle_K \,, \tag{5.77}$$

and can therefore be represented by a tree tensor network with one single-particle function at each node. As the HEOM couple the different Matsubara modes to the system state, at later times the HEOM state cannot be represented by a single Hartree product. At later times it is necessary to include more than one single-particle function for each node in order to obtain accurate results. However, on doing so, all single-particle density matrices are initially singular, and equation 5.73 is therefore ill-defined.

A number of possible methods have been presented for overcoming this difficulty. In the standard approach, the inverse of the single-particle density matrix is replaced with a regularised form[209–211,216,244] giving

$$\dot{\boldsymbol{\mathcal{A}}}^z = -\frac{i}{\hbar} \sum_r \left(\mathbf{1} - \boldsymbol{P}^z\right) \left[\boldsymbol{h}_r^z\right] \boldsymbol{\mathcal{A}}^z \left(\left(\boldsymbol{\rho}_\epsilon^z\right)^{-1} \langle \boldsymbol{H}_r^z \rangle \right)^T . \tag{5.78}$$

where

$$\boldsymbol{\rho}_\epsilon^z = \boldsymbol{\rho}^z + \epsilon \exp\left(-\boldsymbol{\rho}^z/\epsilon\right) \tag{5.79}$$

and ϵ is a positive number. The regularised equations of motion can then be solved numerically to obtain an approximation to the ML-MCTDH treatment of the dynamics of the system.[211] By decreasing the value of the regularisation parameter, ϵ, the dynamics can, in principle, be converged towards that of the original equations of motion. However, in addition to there being some concerns about the mathematical validity of the regularised ML-MCTDH equations of motion,[233] a number of practical issues limit the efficiency and robustness of this approach. This regularisation perturbs the dynamics obtained. For any non-zero value of ϵ the dynamics of weakly populated single-particle functions is significantly altered by the regularisation,[211] and hence it is necessary to check convergence of the dynamics obtained as ϵ is decreased. As ϵ is decreased, however, the resultant equations of motion become

significantly more challenging to integrate, since they become considerably more stiff. At short times when many single-particle functions are weakly occupied, the computation cost associated with integrating the regularised equations of motion scales inversely with the regularisation parameter, ϵ, and the resultant system of equations may become sufficiently ill-behaved that converged results cannot be obtained.[212,224] This was found to be the case for the HEOM considered here. The standard regularisation scheme was insufficient to obtain converged results and so two alternative approaches for handling the regularisation of the equations of motion are instead considered. The first of these employs an alternative regularisation scheme,[212,224] while the second reformulates the ML-MCTDH equations of motion to avoid the need for regularisation entirely.[231,234,240]

5.4.1 Alternative Regularisation Scheme

The standard regularisation scheme discussed above involves a regularisation of the single-particle density matrix. Recently, an alternative approach has been proposed by Wang and Meyer, originally for the MCTDH ansatz[212] and later extended to the ML-MCTDH ansatz,[224] in which the single-hole functions are regularised instead of the single-particle density matrices. Regularisation of the single-hole functions in turn leads to regularisation of the single-particle density matrices, and has been observed to lead to improved numerical stability of the resultant equations of motion.[212,224]

On inserting the definition of the single-particle density matrix and mean-field Hamiltonian matrices, equation 5.73 may be rewritten as

$$\dot{\boldsymbol{\mathcal{A}}}^{z} = -\frac{i}{\hbar}\sum_{r}\left(\mathbf{1}-\boldsymbol{P}^{z}\right)\left[\boldsymbol{h}_{r}^{z}\right]\boldsymbol{\mathcal{A}}^{z}\left(\left(\boldsymbol{\Psi}^{z\dagger}\boldsymbol{\Psi}^{z}\right)^{-1}\boldsymbol{\Psi}^{z\dagger}\boldsymbol{\mathcal{H}}_{r}^{z}\boldsymbol{\Psi}^{z}\right)^{\mathrm{T}}, \tag{5.80}$$

where $\boldsymbol{\Psi}^{z}$ and $\boldsymbol{M}_{r}^{z}$ are the matrix representations of the single-hole function coefficients, and Hamiltonian operator acting on the single-hole function degrees of freedom (equation 5.63). Following the approaches given in references [212]

and [224], the single-hole function coefficients may be rewritten in terms of their singular values decomposition

$$\boldsymbol{\Psi}^z = \boldsymbol{U}^z \boldsymbol{S}^z \boldsymbol{V}^{z\dagger}, \tag{5.81}$$

where $\boldsymbol{U}$ is, in general, a rectangular matricx with orthonormal columns, $\boldsymbol{V}$ is a unitary matrix, and $\boldsymbol{S}$ is a diagonal matrix containing the real, non-negative, singular values of $\boldsymbol{\Psi}^z$.[224] Using this decomposition, the single-particle density matrix becomes

$$\boldsymbol{\rho}^z = \boldsymbol{V}^z \left(\boldsymbol{S}^z\right)^2 \boldsymbol{V}^{z\dagger}. \tag{5.82}$$

Similarly, equation 5.80 may be rewritten in terms of the singular value decomposition of $\boldsymbol{\Psi}^z$ to give

$$\dot{\boldsymbol{\mathcal{A}}}^z = -\frac{i}{\hbar} \sum_r \left(\mathbf{1} - \boldsymbol{P}^z\right) \left[\boldsymbol{h}_r^z\right] \boldsymbol{\mathcal{A}}^z \left(\left(\boldsymbol{V}^z \left(\boldsymbol{S}^z\right)^2 \boldsymbol{V}^{z\dagger} \right)^{-1} \boldsymbol{V}^z \boldsymbol{S}^z \boldsymbol{U}^{z\dagger} \boldsymbol{\mathcal{H}}_r^z \boldsymbol{\Psi}^z \right)^{\mathrm{T}}. \tag{5.83}$$

Within the standard regularisation scheme, at this stage the inverse of the single-particle density matrix would be replaced with its regularised form, or equivalently the $\boldsymbol{S}^z$ matrices in equation 5.82 would be replaced with their regularised form[212,224]

$$\boldsymbol{S}_\epsilon^z = \boldsymbol{S}^z + \epsilon^{1/2} \exp\left(-\boldsymbol{S}^z/\epsilon^{1/2}\right). \tag{5.84}$$

In doing so, equation 5.83 becomes

$$\dot{\boldsymbol{\mathcal{A}}}^z = -\frac{i}{\hbar} \sum_r \left(\mathbf{1} - \boldsymbol{P}^z\right) \left[\boldsymbol{h}_r^z\right] \boldsymbol{\mathcal{A}}^z \left(\boldsymbol{V}^z \left(\boldsymbol{S}_\epsilon^z\right)^{-2} \boldsymbol{S}^z \boldsymbol{U}^{z\dagger} \boldsymbol{\mathcal{H}}_r^z \boldsymbol{\Psi}^z \right)^{\mathrm{T}}. \tag{5.85}$$

The standard regularisation scheme leads to a system of equations where both regularised and unregularised forms of the $\boldsymbol{S}^z$ matrix are present.

Alternatively, further simplifying equation 5.83 gives

$$\dot{\boldsymbol{\mathcal{A}}}^z = -\frac{i}{\hbar} \sum_r \left(\mathbf{1} - \boldsymbol{P}^z\right) \left[\boldsymbol{h}_r^z\right] \boldsymbol{\mathcal{A}}^z \left(\boldsymbol{V}^z \left(\boldsymbol{S}^z\right)^{-1} \boldsymbol{U}^{z\dagger} \boldsymbol{\mathcal{H}}_r^z \boldsymbol{\Psi}^z \right)^{\mathrm{T}}, \tag{5.86}$$

which is still, in general, singular. A singularity-free equation of motion may be obtained by replacing the inverse of the diagonal matrix $\boldsymbol{S}^z$ with its regularised inverse to give

$$\dot{\boldsymbol{\mathcal{A}}}^z = -\frac{i}{\hbar} \sum_r \left(\mathbf{1} - \boldsymbol{P}^z\right) \left[\boldsymbol{h}_r^z\right] \boldsymbol{\mathcal{A}}^z \left(\boldsymbol{V}^z \left(\boldsymbol{S}_\epsilon^z\right)^{-1} \boldsymbol{U}^{z\dagger} \boldsymbol{\mathcal{H}}_r^z \boldsymbol{\Psi}^z \right)^{\mathrm{T}}. \tag{5.87}$$

This may be written in the form of equation 5.73 as

$$\dot{\boldsymbol{\mathcal{A}}}^{z} = -\frac{i}{\hbar}\sum_{r}\left(\mathbf{1}-\boldsymbol{P}^{z}\right)\left[\boldsymbol{h}_{r}^{z}\right]\boldsymbol{\mathcal{A}}^{z}\left(\left(\boldsymbol{\rho}_{\epsilon}^{z}\right)^{-1}\boldsymbol{\Psi}_{\epsilon}^{z\dagger}\boldsymbol{\mathcal{H}}_{r}^{z}\boldsymbol{\Psi}^{z}\right)^{\mathrm{T}} \tag{5.88}$$

where $\boldsymbol{\rho}_{\epsilon}^{z}$ is the regularised single-particle density matrix given in equation 5.79, and

$$\boldsymbol{\Psi}_{\epsilon}^{z\dagger} = \boldsymbol{U}^{z}\boldsymbol{S}_{\epsilon}^{z}\boldsymbol{V}^{z\dagger} \tag{5.89}$$

is a regularised form of the single-hole function coefficient tensor. This small modification to the standard regularisation scheme has been previously found to improve the robustness of the ML-MCTDH approach to changes in the regularisation parameter.[212,224] This approach has been shown to significantly reduce the number of integration steps required to obtain converged results, compared with the standard regularisation schemes, and as a result has allowed the dynamics of spin-boson models with challenging parameters to be obtained.[224]

In the form presented above, this regularisation scheme requires the evaluation of the singular value decomposition of the single-hole function coefficient tensor. Generally, the single-hole function matrices are very large, and for the leaf nodes of the tree tensor network they can have comparable numbers of elements as occurs in the full Hilbert space. As a result, the formation of the single-hole function matrices is often impractical, and, as such, so too is the evaluation of their singular value decomposition. Fortunately, however, it is possible to obtain recursive expressions for all terms in equation 5.88 that avoid the explicit construction of these very large matrices.[224] The singular value decomposition of the single-hole functions may be constructed recursively from the singular value decompositions of the coefficient tensors, which are much more manageable matrices. By employing recursive definitions of these operations, the numerical cost associated with this approach is comparable to the standard approach.[224] In the following discussion this approach will be referred to as the ML-MCTDH integrator.

5.4.2 Projector-Splitting Integrator

An alternative approach for handling the singular equations of motion was proposed by Lubich in 2015, in the context of the MCTDH equations of motion.[240] This alternative integration scheme, obtained from the McLachlan variational principle by inserting an explicit form for the tangent space projector into equation 5.41,[231,240,241] exploits an alternative representation of the MCTDH equation of motion that avoids the inversion of any singular matrices. This approach may be generalised to the multilayer case, that is, to ML-MCTDH. In what follows, this will be carried out by starting from the ML-MCTDH equations of motion obtained in Section 5.3.2.

First, the matrix representation of the total coefficient tensor given in equation 5.36 will be considered:

$$\boldsymbol{\Psi} = \boldsymbol{\Phi}^{z} \boldsymbol{\mathcal{A}}^{z} \boldsymbol{\Psi}^{z\mathrm{T}}, \tag{5.90}$$

where $\boldsymbol{\Psi}$ is a vector representation of the coefficient tensor $\Psi_{\boldsymbol{\alpha}}$. The single-hole function matrix, $\boldsymbol{\Psi}^{z}$, may be decomposed into the form

$$\boldsymbol{\Psi}^{z} = \boldsymbol{U}^{z} \boldsymbol{R}^{z}, \tag{5.91}$$

where $\boldsymbol{U}^{z}$ is a rectangular matrix with orthonormal columns and $\boldsymbol{R}^{z}$ is a square matix. Using the singular value decomposition given in equation 5.81, gives

$$\boldsymbol{R}^{z} = \boldsymbol{S}^{z} \boldsymbol{V}^{z\dagger}. \tag{5.92}$$

The decomposition given by equation 5.91 is not unique, there is a gauge freedom analogous to that discussed in Section 5.3.1. As such, it is necessary to impose a gauge condition to ensure uniquely defined equations of motion, here chosen to be[231,240,241]

$$\boldsymbol{U}^{z\dagger} \dot{\boldsymbol{U}}^{z} = 0, \tag{5.93}$$

for all nodes in the tree except the root node ($z = 1$). Inserting the decomposed form of the single-hole matrix into equation 5.36 gives

$$\boldsymbol{\Psi} = \boldsymbol{\Phi}^z \left(\boldsymbol{\mathcal{A}}^z \boldsymbol{R}^{z\mathrm{T}}\right) \boldsymbol{U}^{z\mathrm{T}} \tag{5.94}$$

$$= \boldsymbol{\Phi}^z \tilde{\boldsymbol{\mathcal{A}}}^z \tilde{\boldsymbol{\Psi}}^{z\mathrm{T}}. \tag{5.95}$$

In the following discussion $\tilde{\boldsymbol{\mathcal{A}}}^z$ and $\tilde{\boldsymbol{\Psi}}^{z\mathrm{T}}$ will be referred to as the modified coefficient and single-hole matrix for node z (other than the root node), respectively. This provides an alternative representation of the wavefunction, in which the single-hole matrices at each node are orthogonal for all time.[231,240,241,245] Differentiating the modified coefficient tensor with respect to time gives

$$\dot{\tilde{\boldsymbol{\mathcal{A}}}}^z = \dot{\boldsymbol{\mathcal{A}}}^z \boldsymbol{R}^{z\mathrm{T}} + \boldsymbol{\mathcal{A}}^z \dot{\boldsymbol{R}}^{z\mathrm{T}}. \tag{5.96}$$

The first of these two contributions to the equation of motion for the modified coefficient tensor may be obtained by inserting equation 5.91 into the matrix representation of equation 5.69, which gives

$$\dot{\boldsymbol{\mathcal{A}}}^z (\boldsymbol{R}^{z\dagger} \boldsymbol{R}^z)^{\mathrm{T}} = -\frac{i}{\hbar} \sum_r (\mathbf{1} - \boldsymbol{P}^z) [\boldsymbol{h}_r^z] \boldsymbol{\mathcal{A}}^z \boldsymbol{R}^{z\mathrm{T}} \left(\boldsymbol{U}^{z\dagger} \boldsymbol{\mathcal{H}}_r^z \boldsymbol{U}^z\right)^{\mathrm{T}} \boldsymbol{R}^{z*}, \tag{5.97}$$

where $\boldsymbol{R}^{z*}$ denotes the element-wise complex conjugate of the matrix $\boldsymbol{R}^z$. On introducing the modified mean-field Hamiltonian,

$$\left\langle \tilde{\boldsymbol{H}}_r^z \right\rangle = \tilde{\boldsymbol{\Psi}}^{z\dagger} \boldsymbol{\mathcal{H}}_r^z \tilde{\boldsymbol{\Psi}}^z, \tag{5.98}$$

this equation becomes,

$$\dot{\boldsymbol{\mathcal{A}}}^z \boldsymbol{R}^{z\mathrm{T}} \boldsymbol{R}^{z*} = -\frac{i}{\hbar} \sum_r (\mathbf{1} - \boldsymbol{P}^z) [\boldsymbol{h}_r^z] \tilde{\boldsymbol{\mathcal{A}}}^z \left\langle \tilde{\boldsymbol{H}}_r^z \right\rangle^{\mathrm{T}} \boldsymbol{R}^{z*}. \tag{5.99}$$

The second contribution may be obtained by considering the equation of motion for the standard single-hole functions given in equation 5.68, which has the matrix representation:

$$\boldsymbol{\mathcal{A}}^z \left(\boldsymbol{\Psi}^{z\dagger} \dot{\boldsymbol{\Psi}}^z\right)^{\mathrm{T}} = -\frac{i}{\hbar} \sum_r \boldsymbol{P}^z [\boldsymbol{h}_r^z] \boldsymbol{\mathcal{A}}^z \left(\boldsymbol{\Psi}^{z\dagger} \boldsymbol{\mathcal{H}}_r^z \boldsymbol{\Psi}^z\right)^{\mathrm{T}}. \tag{5.100}$$

Inserting equation 5.91 and expanding the derivative, this becomes

$$\boldsymbol{\mathcal{A}}^{z}\left(\boldsymbol{R}^{z\dagger}\boldsymbol{U}^{z\dagger}\dot{\boldsymbol{U}}^{z}\boldsymbol{R}^{z}+\boldsymbol{R}^{z\dagger}\dot{\boldsymbol{R}}^{z}\right)^{\mathrm{T}}=-\frac{i}{\hbar}\sum_{r}\boldsymbol{P}^{z}\left[\boldsymbol{h}_{r}^{z}\right]\tilde{\boldsymbol{\mathcal{A}}}^{z}\left\langle\tilde{\boldsymbol{H}}_{r}^{z}\right\rangle\left(\boldsymbol{R}^{z\dagger}\right)^{\mathrm{T}}, \tag{5.101}$$

Applying the gauge condition given in equation 5.93, the first term on the left hand side of equation 5.101 vanishes to give

$$\boldsymbol{\mathcal{A}}^{z}\dot{\boldsymbol{R}}^{z\mathrm{T}}\boldsymbol{R}^{z*}=-\frac{i}{\hbar}\sum_{r}\boldsymbol{P}^{z}\left[\boldsymbol{h}_{r}^{z}\right]\tilde{\boldsymbol{\mathcal{A}}}^{z}\left\langle\tilde{\boldsymbol{H}}_{r}^{z}\right\rangle\boldsymbol{R}^{z*}. \tag{5.102}$$

Adding equation 5.102 to equation 5.99, therefore, gives

$$\dot{\tilde{\boldsymbol{\mathcal{A}}}}^{z}\boldsymbol{R}^{z*}=-\frac{i}{\hbar}\sum_{r}\left[\boldsymbol{h}_{r}^{z}\right]\tilde{\boldsymbol{\mathcal{A}}}^{z}\left\langle\tilde{\boldsymbol{H}}_{r}^{z}\right\rangle\boldsymbol{R}^{z*}. \tag{5.103}$$

This uniquely defines the equation of motion for $\tilde{\boldsymbol{\mathcal{A}}}^{z}$ whenever $\boldsymbol{R}^{z*}$ is non-singular, to give

$$\dot{\tilde{\boldsymbol{\mathcal{A}}}}^{z}=-\frac{i}{\hbar}\sum_{r}\left[\boldsymbol{h}_{r}^{z}\right]\tilde{\boldsymbol{\mathcal{A}}}^{z}\left\langle\tilde{\boldsymbol{H}}_{r}^{z}\right\rangle. \tag{5.104}$$

The matrix $\boldsymbol{R}^{z*}$ is non-singular whenever $\boldsymbol{\Psi}^{z}$ is non-singular and, in this case, the equations of motion given in equation 5.104 are equivalent to the standard ML-MCTDH equations of motion (equation 5.71). When $\boldsymbol{\Psi}^{z}$ is singular, the dynamics arising from equation 5.104 correctly describes the evolution of the occupied single-particle functions[231]; however, the dynamics of unoccupied single-particles is not necessarily accurate. The projector-splitting integrator provides an alternative treatment of the dynamics of the unoccupied single-particle functions than the regularised approaches do, although it is not known *a priori* which of the schemes is more accurate. In order to address this issue, it is necessary to go beyond the Dirac-Frenkel variational principle and treat higher order variations.[231,243] Such an approach is considerably more complicated and will not be considered here. While this alternative integration scheme does not overcome this difficulty it has one key advantage over the standard ML-MCTDH equations of motion, that is equation 5.104 is still well defined when $\boldsymbol{\Psi}^{z}$ is singular and therefore provides a practical means for evolving the coefficients tensors through these singular regions of the manifold, $\mathcal{M}$.

Below, a multilayer generalisation of the MCTDH projector-splitting integration scheme described in reference [243] will be employed. Variants of this integration scheme have been applied to obtain variational approximations to the time-dependent Schrödinger equation employing a number of different tensor network representations of wavefunctions, including a matrix product state representation,[246] a multi-set matrix product state representation,[247] and a tree tensor network state representation.[248] Within this approach, each of the coefficient tensors $\tilde{\boldsymbol{\mathcal{A}}}^{z}$ are evolved through a time step with all other coefficient tensors held constant. As such, this algorithm closely resembles the constant mean-field integrator employed for the standard MCTDH equations of motion.[211,242] Importantly, this method only requires the evaluation of terms with a similar form to those present in the alternative regularisation scheme of Wang and Meyer, and therefore has a comparable numerical cost per integration step. In the remainder of this thesis this integration scheme will be referred to as the tree tensor network state (TTNS) integrator.

5.4.3 Comparison of the Integration Schemes

The two integration schemes described above provide alternative strategies for handling the singularities in the ML-MCTDH equations of motion (equations 5.66 and 5.71). The first, an alternative regularisation scheme proposed by Wang and Meyer[212,224] (which will be referred to as the ML-MCTDH integrator), employs a regularisation of the standard equations of motion to remove the singularity. In contrast, the projector-splitting method of Lubich[240] (the TTNS integrator), uses an alternative representation for the ML-MCTDH equations of motion that does not require the inverse of a singular matrix (equation 5.104). If all single-particle density matrices are non-singular for all time, the standard ML-MCTDH equations of motion and the projector-splitting equations of motion are equivalent. These approaches differ in how they treat the unoccupied single-particle functions that give rise to singular single-particle density matrices.[212,243] It is not clear *a priori* which of the two approaches is more accurate or stable in such a case, and so a comparison of these two approaches with an exact solution of the hierarchical

equations of motion will be presented here.

As a first test of the TTNS-based approach to solving the hierarchical equations of motion, the reduced system dynamics arising for a spin-boson model will be considered. The Hamiltonian describing this model can be written in terms of system and bath terms, and a system-bath coupling term as

$$\hat{H} = \hat{H}_S + \hat{H}_{SB} + \hat{H}_B \tag{5.105}$$

$$= \Delta\hat{\sigma}_x + \frac{\epsilon}{2}\hat{\sigma}_z + \hat{\sigma}_z \sum_{\alpha=0}^{N_b} c_\alpha \hat{q}_\alpha + \sum_{\alpha=0}^{N_b} \left[\frac{\hat{p}_\alpha^2}{2m_\alpha} + \frac{1}{2} m_\alpha \omega_\alpha^2 \hat{q}_\alpha^2 \right], \tag{5.106}$$

where the $\hat{\sigma}_x$ and $\hat{\sigma}_z$ are Pauli spin matrices acting on the system degrees of freedom, here represented using two states $|0\rangle$, $|1\rangle$. The system Hamiltonian therefore includes a coupling between the states of the two-level system with strength, Δ, and an energy bias (driving force) between the two states of ϵ. For the model considered here, these parameters are taken to be $\beta\Delta = 0.25$ and $\beta\epsilon = 0$, where β is the reciprocal temperature. The operators $\hat{q}_\alpha$ and $\hat{p}_\alpha$ are the position and momentum operators for the α-th mode of the bath, and m_α, ω_α, and c_α are the corresponding mass, frequency and coupling, respectively. The mass, frequency, and coupling parameters may be determined from the bath spectral density. Here, a Brownian oscillator spectral density (equation 5.1) with a Marcus-Hush reorganisation energy of $\Lambda\beta = 20$, a reaction coordinate frequency of $\beta\hbar\Omega = 4$, and a friction coefficient of $\beta\hbar\gamma = 2$ will be used to describe the bath.

Within the HEOM formalism, the dynamics of the system density operator for the spin-boson model may be obtained by considering an infinite hierarchy of equations of motion. Truncating this infinite hierarchy leads to an equation of motion of the form given in equation 5.12, which can then be solved directly or by using the TTNS-based approaches discussed above. The hierarchy is truncated using the frequency-based criterion given by equation 4.141 with $\beta\hbar\Gamma = 100$. The truncated hierarchy includes contributions from 17 terms in the bath correlation function and a total of $282,526$ included auxiliary density operators, and the system dynamics

is well converged with respect to the size of the hierarchy. In order to apply the two ML-MCTDH approaches to solve these equations of motion it is necessary to specify a TTNS representation of the hierarchy. The topology of the tensor network used is shown in figure 5.11. Here, a constant number of single-particle functions, n_{spf} was used in each node. Rather than treating each of the 18 individual modes of the HEOM (the 17 "bath modes" and the system mode) separately, the leaf nodes $\mathcal{L}^1$ to $\mathcal{L}^5$ each represented a combined set of the modes, as shown in the table in figure 5.11. Combining modes that are strongly coupled can significantly improve the efficieny of the TTNS representation. When two modes are strongly coupled, a single Hartree product will provide a poor description of the state of the system on long timescales and it becomes necessary to include many single-particle functions to capture the coupling of these two modes. If instead the modes are combined into one, the coupling is treated within the single-particle functions and fewer of these combined functions are required. In the calculations presented here, these combined modes were truncated using the level-based truncation scheme (equation 4.139) with L (shown in the table in figure 5.11) chosen so that all $282,526$ ADOs present in the original hierarchy were included. For a combined mode containing a set of bath modes $\{b_i, \ldots, b_j\}$, L was chosen as

$$L = \left\lfloor \frac{\Gamma}{\min\limits_{k\in\{i,\ldots,j\}}(\text{Re}(\nu_k))} \right\rfloor, \tag{5.107}$$

where $\min\limits_{k\in\{i,\ldots,j\}}(\text{Re}(\nu_k)))$ is the smallest of the real components of the frequencies associated with the bath modes $\{b_i, \ldots, b_j\}$. This approach leads to a considerably larger hierarchy than is used in the standard HEOM calculations. As an example for the problem considered here, the TTNS includes contributions from $902,210,400$ ADOs (the product of the number of ADOs, N_{ados}, shown in figure 5.11) compared to the $282,526$ ADOs included using the standard truncation scheme. As such, while this approach is related to the standard frequency-based truncation scheme, it is not equivalent. In general, the hierarchy arising from the standard frequency-based truncation scheme cannot be written as a direct product of functions for the different "bath modes" and so cannot be used directly within the TTNS representation. In the

following discussion, all results obtained using the TTNS integrator were obtained with a fixed time step. In contrast, due to the wide range of timescales arising from the regularised ML-MCTDH equations of motion, a variable time step integrator (an adaptive stepsize Runge-Kutta Cash-Karp integrator[138,249]) was used. All results presented were converged with respect to the time step (for the TTNS integrator) or integrator tolerance parameter (for the ML-MCTDH integrator).

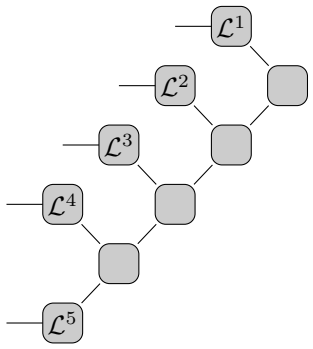

Node	Modes	L	N_{ados}
$\mathcal{L}^1$	$\{\text{sys}, b_1, b_2\}$	25	351
$\mathcal{L}^2$	$\{b_3, b_4\}$	15	136
$\mathcal{L}^3$	$\{b_5, b_6\}$	5	21
$\mathcal{L}^4$	$\{b_7, b_8, b_9\}$	3	20
$\mathcal{L}^5$	$\{b_{10}, \ldots, b_{17}\}$	2	45

Figure 5.11: The tree tensor network representation for the auxiliary density operators used to obtain the results given in figure 5.12. Each of the leaf nodes, $\mathcal{L}^x$, act on the subset of HEOM "modes" shown in the table, where b_i corresponds to the i-th "bath mode".

The time-dependent population on state $|0\rangle$ is shown in figure 5.12 for this spin-boson model with initial density operator

$$\hat{\rho}(0) = |0\rangle\langle 0| \otimes e^{-\beta \hat{H}_B} / \text{tr}\left[e^{-\beta \hat{H}_B}\right]_B, \tag{5.108}$$

where β is the inverse temperature of the bath and $\text{tr}\,[\cdot]_B$ denotes the partial trace over bath degrees of freedom. The results shown were obtained using the exact HEOM approach (Exact) and using the ML-MCTDH and TTNS integration schemes for varying numbers of single-particle functions, n_{spf}. For $n_{\text{spf}} = 1$, the population dynamics obtained using the two approximate methods agree well with each other for all times, but fail to capture the exact evolution after $t \sim 2\beta\hbar$. When $n_{\text{spf}} = 1$, the tree tensor network reduces to a single Hartree product and, as a result, the ADOs associated with a given combined mode evolve in the mean field of the others. Consequently, only the influence of the first two bath modes (b_1 and b_2)

on the system degrees of freedom is captured accurately, with the system degrees of freedom evolving in the mean-field of the remaining modes. As modes b_1 and b_2, which account for the dynamics in the classical limit, are the most strongly coupled modes, the approximate dynamics is reasonably accurate. However, it is necessary to more accurately capture the influence of the Matsubara modes (modes b_3 to b_{17}) in order to obtain quantitatively accurate dynamics.

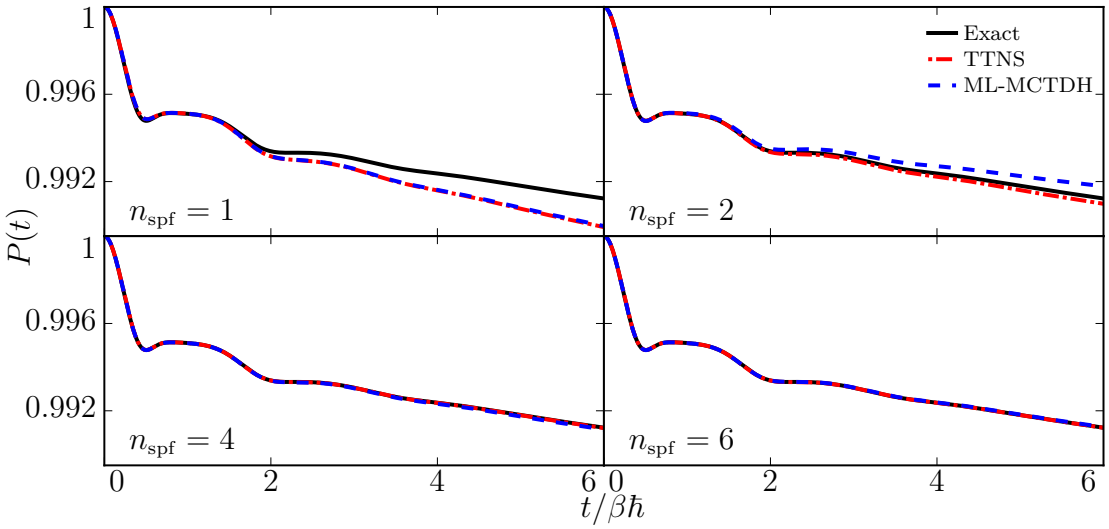

Figure 5.12: The time-dependent population on state $|0\rangle$ of a spin-boson model with a Brownian oscillator spectral density with $\beta\Lambda = 20$, $\beta\hbar\Omega = 4$, and $\beta\hbar\gamma = 2$, obtained using the alternative regularisation scheme (ML-MCTDH), projector-splitting integrator (TTNS), and an exact solution of the hierarchical equations of motion (Exact). Here the system is initially prepared in state $|0\rangle$ with the bath initially at thermal equilibrium with respect to the bath Hamiltonian. The different panels show the results obtained for different numbers of single-particle functions, n_{spf}, (shown in each panel) in the tensor network representation of the auxiliary density operator hierarchy, shown in figure 5.11.

Increasing n_{spf} to 2 leads to a moderate improvement in the accuracy of the result obtained using the ML-MCTDH integrator, and a significant improvement in the accuracy of the result obtained using the TTNS integrator. Here, in contrast to the $n_{\mathrm{spf}} = 1$ case, the dynamics obtained using the two approaches differs. When $n_{\mathrm{spf}} = 2$, the initial state of the hierarchy of ADOs, which can be exactly represented using a single Hartree product, gives rise to singular single-particle density matrices. While the dynamics of the occupied single-particle functions arising from these

two approaches should be the same, they give rise to different dynamics for the unoccupied single-particle functions. At later times when these initially unoccupied single-particle functions become occupied they are different and, as seen here, may yield different dynamics. However, this issue may be overcome by further increasing the number of single-particle functions. For $n_{\mathrm{spf}} = 4$ the dynamics obtained using the TTNS integrator has converged to the exact results within graphical accuracy, while only minor deviations are observed in the ML-MCTDH result at longer times. Further increasing n_{spf} to 6, both approximate methods have converged to graphical accuracy.

All results obtained using the regularised ML-MCTDH equations of motion required convergence with respect to the ϵ parameter used to regularise the single-hole functions (equation 5.84). Following reference [212], the convergence with respect to ϵ was monitored by considering the cumulative deviation between a reference calculation, $P_{\mathrm{ref}}(\tau)$, and the calculation at a given ϵ, $P_{\epsilon}(t)$, defined by,

$$\Delta_{\mathrm{ref}} = \frac{1}{t}\int_0^t |P(\tau) - P_{\mathrm{ref}}(\tau)|\mathrm{d}\tau, \tag{5.109}$$

where t is the time period of the simulation. Here, two reference calculations are used: the numerically exact result obtained from direct HEOM calculations, and the results obtained for the smallest ϵ parameter considered for each value of n_{spf}. The cumulative deviations from these references, Δ_{exact} and Δ_{ref}, measure convergence towards the exact results and convergence towards the limit of no regularisation for a given n_{spf}, respectively.

The cumulative deviation obtained for the ML-MCTDH calculations with different values of ϵ and for the TTNS calculations for $n_{\mathrm{spf}} = 2$, and 6, as well as the number of time steps required to obtain these results are shown in table 5.1. For $n_{\mathrm{spf}} = 2$ the number of integration steps required to obtain results is relatively insensitive to the regularisation parameter for all $\epsilon < 10^{-10}$, consistent with the results obtained by Wang and Meyer.[224] However, in contrast to their results where the

$n_{\mathrm{spf}} = 2$			
$\log_{10}(\epsilon)$	N_{step}	Δ_{exact}	Δ_{ref}
-8	-	-	-
-10	4311	2.1×10^{-4}	3.8×10^{-5}
-12	4202	2.4×10^{-4}	7.6×10^{-6}
-16	4416	2.4×10^{-4}	7.5×10^{-7}
-20	4541	2.4×10^{-4}	7.0×10^{-8}
-24	4633	2.4×10^{-4}	ref
TTNS	600	9.7×10^{-5}	

$n_{\mathrm{spf}} = 6$			
$\log_{10}(\epsilon)$	N_{step}	Δ_{exact}	Δ_{ref}
-12	-	-	-
-16	13288	1.2×10^{-5}	1.2×10^{-6}
-16.8	14624	1.3×10^{-5}	ref
-20	-	-	-
-24	-	-	-
TTNS	600	9.2×10^{-8}	

Table 5.1: The convergence of the tree tensor network state (of the form given in figure 5.11) solution to the hierarchical equations of motion using the alternative regularisation scheme and the projector-splitting integrator for different numbers of single-particle functions, as well as the number of time steps required to obtain the results over a time period of $t = 6\beta\hbar$. Failure of the integration scheme to provide results over this time period is indicated by a "-". For the alternative regularisation scheme the result obtained depends on a regularisation parameter, ϵ, and here two sets of cumulative deviations of the regularised results are provided. The first compares the value obtained with a given value of ϵ against the exact HEOM result, while the second compares against a reference calculation obtained with the smallest ϵ parameter for which results were obtained. For the projector-splitting integrator (TTNS), only the deviation from the exact results is presented as this approach does not involve a regularisation parameter.

integration scheme was stable over the entire range of the regularisation parameter they considered, here the integration scheme fails for $\epsilon = 10^{-8}$. On increasing n_{spf} to 6, this issue becomes considerably more problematic; there is only a narrow region of ϵ values for which converged results could be obtained. The integration scheme fails for both small and large values of the regularisation parameter. This failure may be attributed to the non-unitary nature of dynamics arising from the HEOM. The final term in equation 5.11 ($i\mathcal{Q}^{+}\mathcal{B}^{i}_{-k}$) gives rise to rapid growth in the norms of the auxiliary density operators far down the hierarchy. As a result, very small errors arising from the integration of the initially stiff regularised equations of motion can grow rapidly with time, and ultimately results in failure of the integrator. It is possible that an alternative choice of integrator (such as a constant mean-field integrator[211,242]), an alternative rescaling of the HEOM,[185] and/or an alternative implementation of the regularisation of the single-hole functions may alleviate these numerical issues, but these options are not considered here. In contrast to the ML-MCTDH integrator, the TTNS integrator exhibited no such numerical issues. Converged results were readily obtained using a total of 600 fixed sized integration

steps for all values of n_{spf} considered. This corresponds to a factor of ~ 24 reduction in the number of integration steps required when $n_{\mathrm{spf}} = 6$, and the cumulative deviation of these results from the exact HEOM dynamics was over two orders of magnitude smaller than the best ML-MCTDH results. Due to this, in the following discussion only the projector-splitting integrator will be considered.

5.4.4 A More Challenging Regime

The spin-boson model considered in figure 5.12 does not correspond to a particularly challenging problem; converged results may be obtained using the HEOM with the frequency-based truncation with $\hbar\beta\Gamma = 40$ and can therefore be obtained routinely. As such, a more challenging set of parameters for the spin-boson model will now be considered. The TTNS method will be applied to the population dynamics of a series of spin-boson models each with a Brownian oscillator spectral density. A range of reorganisation energies will be treated, $\beta\Lambda = 20$, 40, 60, 80, and 100, and in all cases the reaction coordinate frequency and friction coefficient will be taken to be $\beta\hbar\Omega = 4$ and $\beta\hbar\gamma = 4$, respectively. These parameters are the same as those considered in figure 5.1, where the standard HEOM approach was unable to provide converged results for large reorganisation energies.

A comparison of the results obtained using the TTNS approach to treat the HEOM are compared with the standard HEOM results (previously shown in figure 5.1) in figure 5.13 for $\beta\Lambda = 20$, 40, and 60. For these values of Λ the standard HEOM approach could be converged with respect to the truncation parameter, Γ, and all TTNS results have converged onto the standard HEOM results. In obtaining these TTNS results a tree tensor network, with a similar structure to that presented in figure 5.11, was used. It contained significantly more layers and included contributions from considerably more HEOM modes. For each value of Λ the TTNS results were converged with respect to the number of single-particle functions. The final converged results were obtained with $n_{\mathrm{spf}} = 6$, 8, and 10 for $\beta\Lambda = 20$, 40, and 60, respectively.

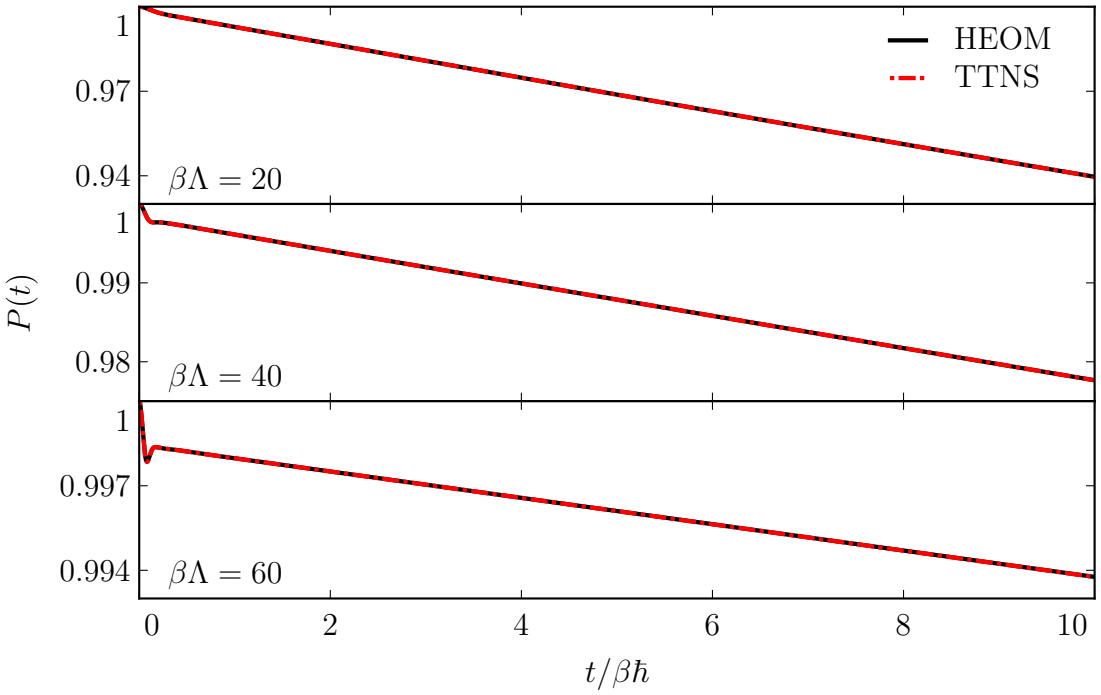

Figure 5.13: The time-dependent population in state $|0\rangle$, $P(t) = \langle 0|\,\hat{\rho}(t)\,|0\rangle$, for a spin-boson model with a Brownian oscillator spectral density with various values of the reorganisation energy, Λ, (shown in each panel) reaction coordinate frequency $\beta\hbar\Omega = 4$, and friction coefficient $\gamma = \Omega$, obtained using the TTNS-based approximation to the HEOM (TTNS) and the standard HEOM formalism (HEOM). Here, the system is initially prepared in state $|0\rangle$ with the bath initially at thermal equilibrium with respect to the Hamiltonian associated with diabat, $|0\rangle$ (see Section 4.3.2).

For both methods the calculation performed for $\beta\Lambda = 60$ was the most computationally expensive. In order to obtain converged results using the standard HEOM it was necessary to use a truncation parameter of $\beta\hbar\Gamma = 200$. The resultant hierarchy contained $7,327,766$ auxiliary density operators, and the calculation required 5.4 gigabytes of memory to store the ADOs and the indexing array necessary for an efficient implementation of the equations of motion. Despite using a larger hierarchy, the converged TTNS-based calculation obtained with n_{spf} used a total of 26 megabytes of memory — a factor of $\sim$200 reduction in the memory requirements. These results indicate that not only is the TTNS approach able to reproduce results

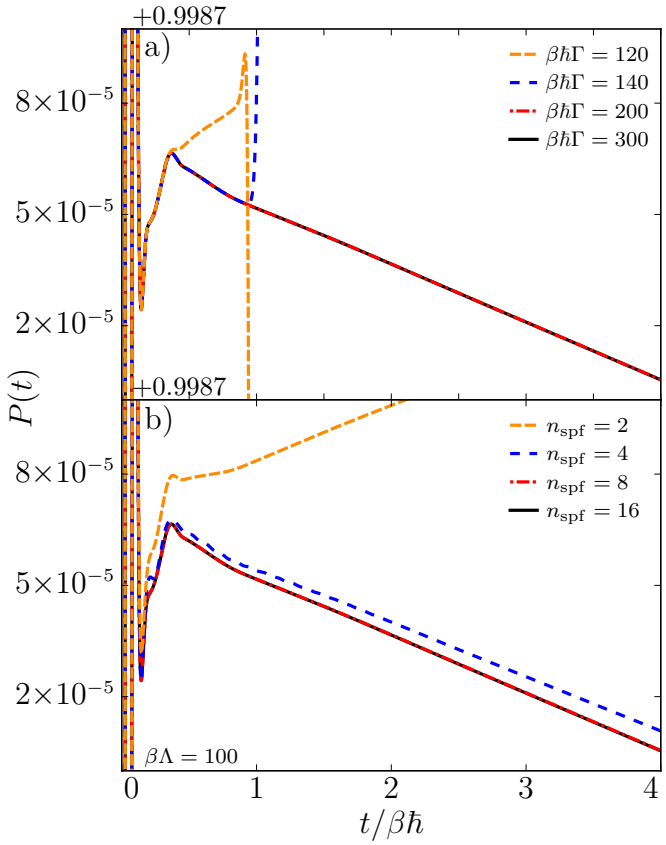

$\beta\hbar\Gamma$	Δ_{ref}	N_{ados}
120	1.3	2.4×10^{11}
140	5.3×10^{-3}	3.8×10^{12}
160	5.6×10^{-6}	2.1×10^{14}
180	9.7×10^{-8}	6.9×10^{14}
200	5.4×10^{-8}	2.7×10^{14}
220	2.5×10^{-8}	2.1×10^{17}
250	1.1×10^{-8}	2.4×10^{18}
300	ref	2.1×10^{20}

n_{spf}	Δ_{ref}
1	2.5×10^{-3}
2	1.5×10^{-4}
4	6.3×10^{-6}
8	1.5×10^{-7}
12	9.7×10^{-8}
16	1.3×10^{-8}
20	ref

Figure 5.14: Convergence of the time-dependent population in state $|0\rangle$, $P(t) = \langle 0|\,\hat{\rho}(t)\,|0\rangle$, for a spin-boson model with a Brownian oscillator spectral density with a reorganisation energy of $\beta\Lambda = 100$, a reaction coordinate frequency $\beta\hbar\Omega = 4$, and a friction coefficient $\gamma = \Omega$ obtained using the TTNS approximation of the HEOM as a function of the number the truncation parameter Γ (a) and number of single-particle functions n_{spf} (b). The results in panel a) were obtained with $n_{\mathrm{spf}} = 12$, and the results obtained in panel b) are for $\beta\Gamma\hbar = 200$. The tables on the right present the cumulative deviation (obtained between $t = 0$ and $t = 10\beta\hbar$) from the most converged results obtained with $\beta\hbar\Gamma = 300$ and $n_{\mathrm{spf}} = 20$, respectively, for a larger set of results than are shown in the accompanying figure. Additionally, in the first of the two tables the total number of auxiliary density operators N_{ados} that are included in each calculation are shown.

obtained using the standard HEOM approach, it is able to do so considerably more efficiently and may therefore be able to treat parameter regimes inaccessible to the standard HEOM approach. To illustrate this, the TTNS integrator is now applied to this model with $\beta\Lambda = 80$ and 100, where converged results could not be obtained using the standard approach. The population dynamics obtained using the TTNS integrator with $\beta\Lambda = 100$ are shown in figure 5.14. Here, convergence of the dynamics with respect to the number of auxiliary density operators included (parameterised by

the Γ parameter discussed earlier in this chapter) and with respect to the number of single-particle functions (n_{spf}) included in each node of the TTNS are shown in panels a) and b), respectively. For small values of the truncation parameter ($\beta\hbar\Gamma = 120$) the population dynamics is only accurate for short timescales. Past $t \sim 0.4\beta\hbar$ the dynamics starts to deviate from the converged results and at $t \sim 0.9\beta\hbar$ it exhibits a rapid decay that at longer time gives rise to unphysical, negative populations on state $|0\rangle$ (not shown). However, as Γ increases the dynamics converges rapidly. By $\beta\hbar\Gamma = 200$ the dynamics obtained has a cumulative deviation from the reference calculation obtained with $\beta\hbar\Gamma = 300$ of 5.4×10^{-7}, and has converged to within the graphical accuracy shown. With $\beta\hbar\Gamma = 200$ a total of $\sim 2.7\times10^{14}$ auxiliary density operators are included within the hierarchy, which, if stored explicitly using double precision complex numbers (as is required for the standard calculation), would require ~ 17 petabytes of storage, compared to the 92 megabytes used for the entire calculation shown here. As shown in panel b) of figure 5.14, this result, obtained with $n_{\mathrm{spf}} = 12$, has a cumulative deviation of $\sim 10^{-7}$ from the results obtained with $n_{\mathrm{spf}} = 20$ and is therefore sufficiently well converged with respect to the number of single-particle functions. Thus, these results indicate that the TTNS approach is able to provide converged results even in this considerably more challenging regime.

The converged TTNS results obtained with $\beta\Lambda = 80$ and 100 are compared in figure 5.15 with the results obtained using the standard HEOM approach with a range of different truncation parameters Γ. For both values of Λ the standard HEOM results agree well with the TTNS results at very short times ($t < 0.2\beta\hbar$) for all values of Γ, however, at longer times deviations are observed. As expected, for a given value of Γ, the population dynamics obtained using the standard HEOM approach with $\beta\Lambda = 80$ agrees more closely with the TTNS results than when $\beta\Lambda = 100$. However, none of the results obtained using the standard approach show convergence for either reorganisation energy. For $\beta\Lambda = 80$, the standard HEOM results deviate slightly from those of the TTNS at longer times. The dynamics obtained is qualitatively correct, however, the standard approach fails to capture

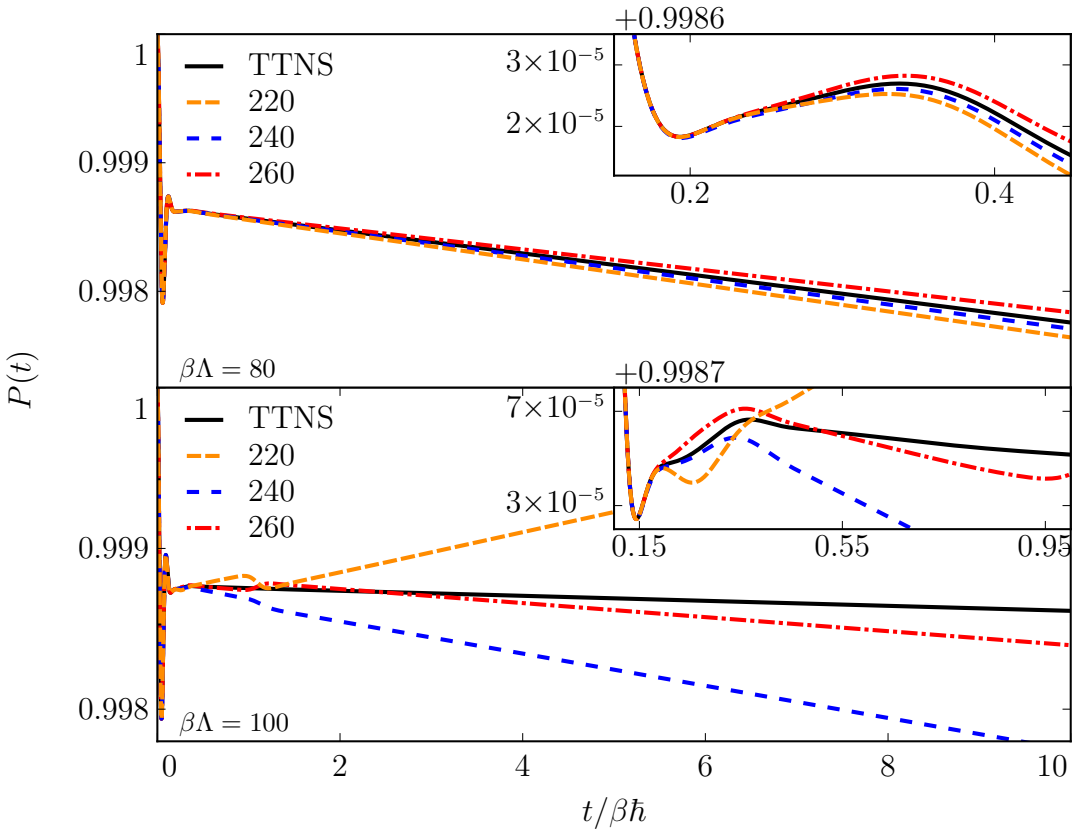

Figure 5.15: The time-dependent population in state $|0\rangle$, $P(t) = \langle 0|\,\hat{\rho}(t)\,|0\rangle$, for a spin-boson model with a Brownian oscillator spectral density for two values of the reorganisation energy, Λ, (shown in each panel), a reaction coordinate frequency of $\beta\hbar\Omega = 4$ and a friction coefficient of $\gamma = \Omega$, obtained using the TTNS-based approximation to the HEOM (TTNS) and the standard HEOM formalism employing a range of different truncation parameters Γ. The inset shows the time period in which the standard HEOM results begin to deviate from the converged TTNS results.

the rate of decay of the population in state $|0\rangle$. In contrast, for $\beta\Lambda = 100$, the HEOM results obtained using the standard truncation scheme fail to capture the dynamics even qualitatively. An unphysical kink is observed in all of the standard HEOM results at $t \sim 1\beta\hbar$. At longer times the standard HEOM approach fails to capture the rate of the decay of the population in state $|0\rangle$ (for any computationally feasible value of Γ).

The standard HEOM calculations, given in figure 5.15, were performed using larger values for the frequency-based truncation parameter Γ than required to obtain the converged TTNS results shown in figure 5.14 ($\beta\hbar\Gamma \sim 180$). This suggests that, while

the frequency-based truncation scheme may provide a more efficient approach than the standard level-based truncation scheme,[182] it is still not optimal. Using this approach, ADOs that contribute little to the dynamics are included (such as those with $n_1 > 50$ and all other indices 0, which are not included in the TTNS simulations) while other ADOs that do significantly influence the dynamics are not included. In the case of $\beta\Lambda = 100$, this leads to considerable increases in the computational cost of the simulations in going from $\beta\hbar\Gamma = 220$ to 260, without significant improvement in the timescale on which the simulation is accurate, as is shown in the inset in figure 5.15. In contrast, using the truncation scheme employed for the TTNS approach, an increase in the Γ parameter leads to results that are converged over longer time periods. While the resultant hierarchies contain considerably more elements and, as a result, cannot be treated using the standard approach, but their time-evolution can readily be evaluated using the TTNS integrator. These results suggest that this TTNS approach, with the truncation scheme described above, provides an efficient method for evaluating the dynamics of open quantum systems and allows for sigificantly larger system-bath couplings to be treated than is feasible using the standard HEOM formalism. In the remainder of this chapter, an application of this approach, which will from now on be referred to as the HEOM-TN method, to the evaluation of electron transfer rates will be presented.

5.5 Application: Electron Transfer Rates

Electron transfer processes play an important role in many chemical reactions.[163,165] In these reactions the electron transfer gives rise to a significant rearrangement of the charge distribution within the system, which leads to a significant reorganisation of the surrounding environment.[91] Depending on the timescales involved in the transition between the distinct electronic states (electronic dynamics) and the motion of the the environment (nuclear dynamics), they may significantly influence each other. In such a case, it is no longer valid to make the Born-Oppenheimer approximation and, as such, it is necessary to treat the coupled dynamics of electronic and nuclear degrees of freedom.

The Hamiltonian for a condensed phase electron-transfer reaction can be written in the diabatic representation as[3,156]

$$\hat{H} = \hat{H}_0 \left|0\right\rangle \left\langle 0\right| + \hat{H}_1 \left|1\right\rangle \left\langle 1\right| + \Delta \left(\left|0\right\rangle \left\langle 1\right| + \left|1\right\rangle \left\langle 0\right|\right), \tag{5.110}$$

where $|0\rangle$ and $|1\rangle$ are the reactant, DA, and product, D^+A^-, diabatic electronic states, respectively, $\hat{H}_i$ is the nuclear Hamiltonian associated with each diabat, and Δ is the diabatic coupling constant between the two states. This Hamiltonian determines the dynamics of the populations on the two states, $|0\rangle$ and $|1\rangle$, from which a wide range of properties may be obtained. In particular, the quantum mechanical rate for the electron transfer process may be obtained by considering how the system, initially at thermal equilibrium in the reactant diabat (that is with initial density operator

$$\hat{\rho}(0) = \left|0\right\rangle \left\langle 0\right| \otimes e^{-\beta \hat{H}_0} / \mathrm{tr}\left[e^{-\beta \hat{H}_0}\right], \tag{5.111}$$

where β is the inverse temperature), returns to equilibrium. This initial density operator evolves in time according to the Liouville-von Neumann equation (equation 4.44), and from it the time-dependent populations of the two states may be obtained using

$$P_i(t) = \left\langle i\right| \hat{\rho}(t) \left|i\right\rangle. \tag{5.112}$$

Assuming that the dynamics can be described by a kinetic process in the long-time limit, the time-dependent populations of the two states will eventually, after some transient behaviour, satisfy the kinetic equations[181,205]

$$\dot{P}_0(t) = -k_f P_0(t) + k_b P_1(t) \tag{5.113}$$

$$\dot{P}_1(t) = -k_b P_1(t) + k_f P_0(t). \tag{5.114}$$

Here, k_f and k_b are the forward (from state $|0\rangle$ to state $|1\rangle$) and backward rate constants, and as these are the only two states involved in the dynamics, $P_0(t) + P_1(t) = 1$. Inserting this into equation 5.114, gives

$$\dot{P}_1(t) = k_f - (k_f + k_b) P_1(t) = (k_f + k_b)(\langle P_1 \rangle - P_1(t)), \tag{5.115}$$

where in the second step the steady state population on state $|1\rangle$,

$$\langle P_1 \rangle = \lim_{t\to\infty} P_1(t) = \frac{k_f}{k_f + k_b}, \tag{5.116}$$

has been introduced. The analogous definition for state $|0\rangle$,

$$\langle P_0 \rangle = \lim_{t\to\infty} P_0(t) = \frac{k_b}{k_f + k_b}, \tag{5.117}$$

is such that the two steady state populations satisfy microscopic reversibility, $\langle P_1 \rangle / \langle P_0 \rangle = k_f/k_b$. Rearranging equation 5.115, the forward rate constant may be obtained as[222]

$$k_f = \frac{\dot{P}_1(t)}{1 - P_1(t)/\langle P_1 \rangle} \tag{5.118}$$

where t corresponds to a time after the transient behaviour has subsided.[181] Unfortunately, the diabatic potential energy surfaces for a general condensed-phase electron transfer reaction can be arbitrary (anharmonic) functions of the nuclear coordinates. In such a case a direct solution of the Liouville-von Neumann, and therefore evaluation of the time-dependent populations, is intractable and approximate approaches are required.

Marcus-Hush theory, which assumes that the system is in the nonadiabatic (Fermi golden rule) limit, is the most widely used method for predicting the rates of electron transfer reactions.[163,164,250] However, this theory employs a classical description for the nuclear motion in the system and, as a consequence, may not be accurate when nuclear quantum effects are important. This is often the case in the "inverted regime", in which the driving force is larger than the reorganisation energy, where tunnelling through the reaction barrier can lead to orders of magnitude increases in electron transfer rates.[251] Imaginary time path integral approaches may be used to include nuclear quantum effects in the description of nonadiabatic electron transfers.[252,253] Such approaches can be applied to treat nonadiabatic electron transfers with arbitrary numbers of nuclear degrees of freedom and with arbitrary diabatic potential energy surfaces,[254,255] in both the normal and inverted regimes.[253]

However, these approaches are only applicable in the nonadiabatic limit, and as the diabatic coupling, Δ, becomes larger they are no longer applicable.

In the large Δ (adiabatic) limit, the diabatic potential energy surfaces become energetically well separated and the Born-Oppenheimer approximation becomes valid. In this regime, ring polymer molecular dynamics (RPMD) reaction rate theory[256–258] provides an efficient scheme for computing thermal reaction rates.[259,260] This approach accurately captures tunnelling and zero point energy effects, and can routinely be applied to atomistic models of condensed phase reactions with arbitrary numbers of degrees of freedom and general Born-Oppenheimer potential energy surfaces.[258–260]

Owing to the success of RPMD in the adiabatic limit, there has been considerable interest in generalising it to the intermediate coupling regime.[261–264] However, despite some successful applications[265] of these generalisations, all of the methods that have been proposed so far have issues that limit their applicability or practicality.[181] Recently, Lawrence *et al.* have proposed a simple approach for evaluating electron transfer rates in the intermediate regime that avoids the need to generalise RPMD.[181] Within this approach, the electron transfer rate at an arbitrary value of Δ is obtained using the simple interpolation formula[181]

$$k(\Delta) \approx \frac{k_{\mathrm{N}}(\Delta)k_{\mathrm{A}}(\Delta)}{k_{\mathrm{N}}(\Delta) + k_{\mathrm{A}}(\Delta = 0)}, \tag{5.119}$$

where $k_{\mathrm{N}}(\Delta)$ and $k_{\mathrm{A}}(\Delta)$ are the Δ-dependent electron transfer rates obtained using approaches valid in the nonadiabatic and adiabatic limits, respectively. Both of these can be calculated for systems with arbitrary numbers of degrees of freedom and general potential energy surfaces using well-established imaginary time path integral methods.[252,253,256–258] In the following discussion, the validity of the interpolation formula in equation 5.119 will be explored over a wide range of physically relevant regimes. This will be done by comparing the electron transfer rates obtained using the interpolation formula for a series of spin-boson models against the numerically exact rates obtained using the hierarchical equations of motion.

5.5.1 Simulation Details

To test the validity of the interpolation formula of Lawrence *et al.*,[181] rates computed using the interpolation formula were compared against those obtained using the HEOM-TN approach for a series of 9 spin-boson models, spanning a wide range of physical regimes. Each of these spin-boson models was described by the Hamiltonian given in equation 5.106, and with a Brownian oscillator spectral density (equation 5.1). A reorganisation energy of $\beta\Lambda = 60$, which at 300 K gives $\Lambda \sim 1.5$ eV, was used for all models. By varying the remaining parameters a wide range of physical regimes can be considered. Varying the bath reaction coordinate frequency, Ω, alters the importance of nuclear quantum effects. For large values of Ω nuclear quantum effects should be important. Varying the driving force, ϵ, alters the nature of the electron transfer. For $0 \leq \epsilon < \Lambda$ the reaction is in the normal regime, while for for $\epsilon > \Lambda$ it is in the inverted regime. Finally the solvent friction determines how significantly the other bath degrees of freedom influence dynamics along the reaction coordinate. The model parameters considered here are shown in table 5.2. The first 8 spin-boson models represent systems with low and high reaction coordinate frequency, symmetric and asymmetric electron transfers in the normal regime, and low (underdamped) and high (overdamped) bath friction. The final model describes a system in the inverted regime.

Model	$\beta\hbar\Omega$	γ	$\beta\epsilon$	$\beta\Delta$	Model	$\beta\hbar\Omega$	γ	$\beta\epsilon$	$\beta\Delta$
a)	4	Ω	0	$[0.1, 10]$	e)	0.5	Ω	0	$[0.1, 10]$
b)	4	16Ω	0	$[0.1, 10]$	f)	0.5	16Ω	0	$[0.1, 10]$
c)	4	Ω	15	$[0.1, 10]$	g)	0.5	Ω	15	$[0.1, 10]$
d)	4	16Ω	15	$[0.1, 10]$	h)	0.5	16Ω	15	$[0.1, 10]$
i)	4	Ω	120	$[0.1, 100]$					

Table 5.2: The reaction coordinate frequency, Ω, friction coefficient, γ, driving force, ϵ, and diabatic coupling constants used for the 9 different spin-boson models. At 300 K the two reaction coordinate frequencies of $\beta\hbar\Omega = 0.5$ and 4 correspond to $\Omega \sim 100$ and 830 cm^{-1}, respectively.

For all models in the normal regime, a range of diabatic couplings between $\beta\Delta = 0.1$

and $\beta\Delta = 10$ were considered. Over this range, the transition from the nonadiabatic limit to adiabatic limit could be observed and at each value of Δ, a well defined rate could be obtained. As Δ is increased further, the barrier between reactant and product states decreases. For sufficiently large values of Δ, no barrier is observed and it is no longer possible to treat the population dynamics using the kinetic equations 5.113 and 5.114. In the inverted regime, the electron transfer rate is still well defined for considerably larger values of the diabatic couplings. Here, diabatic coupling constants between $\beta\Delta = 0.1$ and $\beta\Delta = 100$ were considered.

The HEOM-TN approach was used to obtain the population dynamics for these model systems. In all of these HEOM-TN simulations, the system was initially prepared in the reactant state, $|0\rangle$, with an uncorrelated bath. This bath was initially at thermal equilibrium with respect to the $|0\rangle$ diabatic potential energy surface at an inverse temperature, β (see Section 4.3.2 for further details). Following an initial transient period, the population dynamics could be described by the kinetic equations 5.113 and 5.114. Electron transfer rates could then be obtained from the population dynamics according to equation 5.118. The time period over which the transient was observed depended strongly on the parameters considered. For the high frequency spin-boson models (models a)-d) and i)) the transient was considerably shorter lived than for the low frequency spin-boson models (models e)-h)). For all models, the population dynamics was calculated for a sufficiently long timescale to capture the long-time kinetic behaviour.

While it may have been possible to treat models a), c) and e) using the standard HEOM approach, as the bath parameters are the same as those considered in the last panel in figure 5.13, the HEOM-TN approach provided a considerably more efficient way to evaluate the population dynamics. Additionally, for the overdamped model it was not possible to obtain converged results using the standard HEOM approach, while the calculations were routine using the HEOM-TN approach. All HEOM-TN calculations are converged with respect to the number of single-particle

functions and number of ADOs included in the hierarchy. A time step of $5{\times}10^{-4}\beta\hbar$ was sufficient to obtain converged results for all calculations.

The interpolation formula rates for models a)-h), which were obtained using RPMD rate theory[256–258] and Wolynes theory[252,253] to obtain the adiabatic and nonadiabatic rates, respectively, were taken from reference [181]. Additionally, to demonstrate the importance of nuclear quantum effects in the rates all rates are compared with the rate given by the Zusman equation,[266] an analytical result for the rate constant that extends Marcus-Hush theory to include the effect of friction along the reaction coordinate. For the spin-boson models considered here, the Zusman equation is given by[181,266,267]

$$k_Z(\Delta) = \frac{\frac{\beta\Delta^2}{\hbar}\frac{\Omega^2}{4\gamma}\left(1-\frac{\epsilon^2}{\Lambda^2}\right)e^{-\beta(\Lambda-\epsilon)^2/4\Lambda}}{\frac{\Delta^2}{\hbar}\sqrt{\frac{\pi\beta}{\Lambda}}+\frac{\Omega^2}{4\gamma}\sqrt{\frac{\beta\Lambda}{\pi}}\left(1-\frac{\epsilon^2}{\Lambda^2}\right)}. \tag{5.120}$$

5.5.2 Results and Discussion

The electron transfer rates obtained for models a)-d) using the interpolation formula, the Zusman formula, and the HEOM-TN approach are shown in figure 5.16. For all models considered here, the interpolation formula agrees well with the numerically exact results obtained using the HEOM-TN approach. For small values of the diabatic coupling, Δ, the interpolation formula agrees quantitatively with the numerically exact results obtained using the HEOM-TN approach. Here, the Δ dependence of the exact rate is dominated by the nonadiabatic (Fermi golden rule) limit, increasing $\propto \Delta^2$. As such the accuracy of the interpolation formula result in this regime simply reflects the accuracy of Wolynes theory.

For larger values of Δ, the results obtained using the interpolation formula show small deviations from the exact rates. The largest deviation of $\sim 30\%$ is observed for models b) and d) and at intermediate diabatic coupling strengths, $\beta\Delta \sim 1.8$. In contrast the interpolation formula is exceptionally accurate for models a) and c)

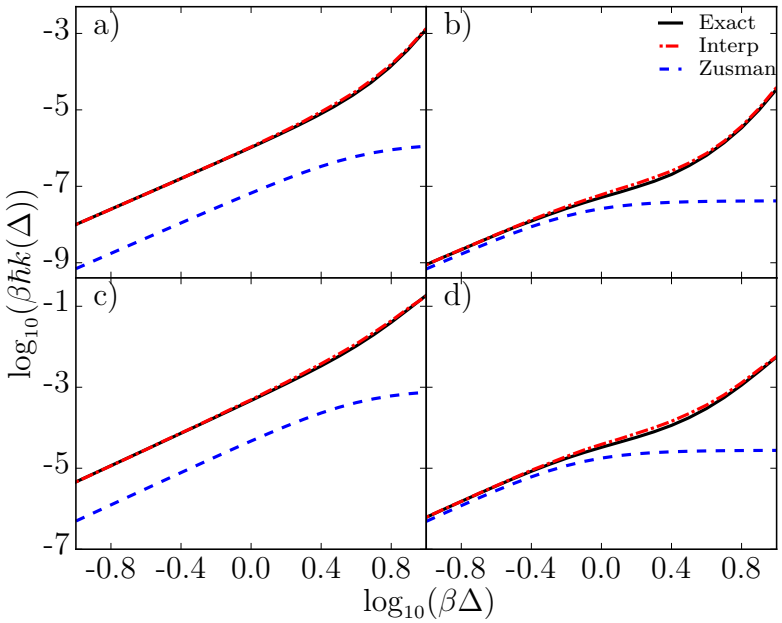

Figure 5.16: A comparison of the electron transfer rates, $k(\Delta)$, obtained using the interpolation formula proposed by Lawrence *et al.*[181] (red), the Zusman formula given in equation 5.120 (blue), and the HEOM-TN method (black) for the four spin-boson models (a-d) with a Brownian oscillator spectral density and parameters given in table 5.2. All interpolation theory results were taken from reference [181].

at intermediate diabatic coupling strengths. This difference can be attributed to the effect of solvent friction which can drive a reaction away from the nonadiabatic limit even for small values of Δ.[161,171,266,268] Models b) and d) are in the overdamped (high solvent friction) regime and as a result the exact electron transfer rate begins to deviate from the non-adiabatic limit for smaller values of the diabatic coupling ($\beta\Delta \sim 0.4$) than for models a) and c) ($\beta\Delta \sim 2$). As a consequence, in models b) and c) there is a larger region of Δ for which neither adiabatic nor diabatic rates are accurate, and the interpolation formula is less accurate in this regime. For larger values of $\beta\Delta$ the deviations observed in the interpolation formula results become smaller as the exact rate tends towards the Born-Oppenheimer (adiabatic) limit. In this regime a rapid (exponential) increase in the rate is observed associated with a decrease in the barrier on the Born-Oppenheimer adiabatic potential energy surface with increasing Δ.[267] This behaviour is observed for both symmetric ($\beta\epsilon = 0$) and asymmetric ($\beta\epsilon = 15$) electron transfers (models a) and b), and models c) and d), respectively).

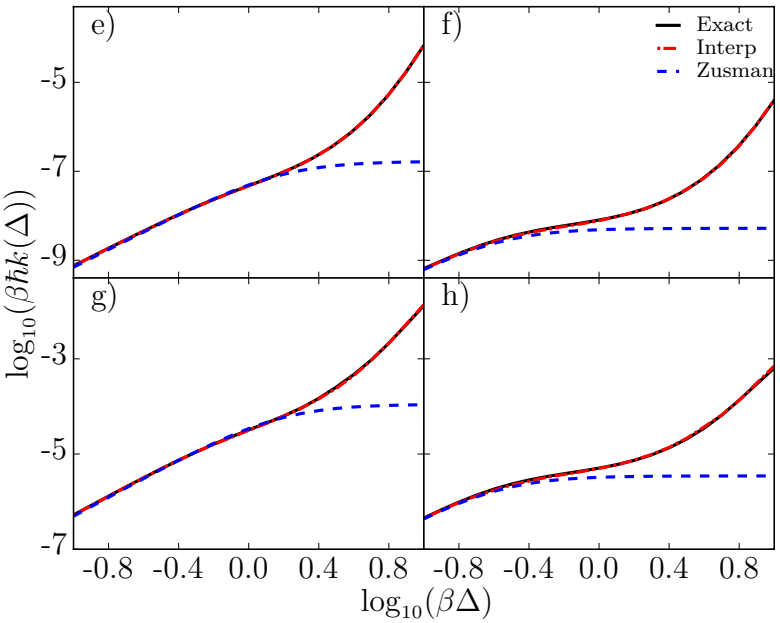

Figure 5.17: A comparison of the electron transfer rates, $k(\Delta)$, obtained using the interpolation formula proposed by Lawrence *et al.*[181] (red), the Zusman formula given in equation 5.120 (blue), and the HEOM-TN method (black) for the four spin-boson models (e-h) with a Brownian oscillator spectral density and parameters given in table 5.2. All interpolation theory results were taken from reference [181].

For models a) and c), significant quantum effects are observed. In the nonadiabatic limit the electron transfer rates obtained using the HEOM-TN approach are approximately an order of magnitude larger than the rates obtained using the classical Zusman theory. As Wolynes theory, the nonadiabatic limit used in the interpolation formula, includes nuclear quantum effects, the interpolation formula is able to accurately capture this increase in the rate. For models b) and d), nuclear quantum effects are significantly less important. While the nonadiabatic limit rates obtained using the HEOM-TN approach are larger than the classical Zusman formula rates, the difference is significantly less pronounced than in models a) and c). This difference arises due to the increased friction along the reaction coordinate which reduces tunneling rates.[167]

When the reaction coordinate frequency is decreased to $\beta\hbar\Omega = 0.5$, nuclear quantum effects become significantly less important. This is illustrated in figure 5.17, where

the Zusman formula rates agree quantitatively with the HEOM-TN rates in the nonadiabatic limit. In this figure, the electron rates obtained for models e)-f) using the interpolation formula are compared with the benchmark rates obtained using the HEOM-TN approach. Once again, the interpolation formula agrees excellently with the exact rates for all values of the solvent friction and bias considered. For these models the interpolation formula agrees with the numerically exact rates with graphical accuracy over the entire range of diabatic couplings.

These results, obtained for a wide range of electron transfer reactions in the normal regime, are clearly very promising. They indicate that the interpolation formula of Lawrence *et al.* is capable of accurately predicting condensed-phase electron transfer rates over a wide range of physical parameter regimes. While small deviations of $\sim 30\%$ are observed in the intermediate coupling regimes, these are comparable to the deviations observed in RPMD rate theory in the Born-Oppenheimer limit and in Wolynes theory in the nonadiabatic limit, suggesting that other generalisations of RPMD to this regime are unlikely to do better. When used with RPMD rate theory and Wolynes theory, the interpolation formula can be straightforwardly applied to realistic models of chemical reactions involving anharmonic, multidimensional potential energy surfaces.

5.5.3 Inverted Regime

The Δ-dependent electron transfer rates obtained for model i), which has a driving force of $\epsilon = 2\Delta$, using the HEOM-TN approach are shown in figure 5.18. As was the case in the normal regime, the rate is well described by the golden rule (increasing $\propto \Delta^2$) for small values of Δ. This is not surprising as Wolynes theory provides an accurate description of nonadiabatic electron transfer reactions even in the inverted regime.[253] In contrast to the rates obtained for all other models, as Δ increases a maximum in the rate is observed at $\beta\Delta \sim 8$, following which the rate decreases with increasing Δ.

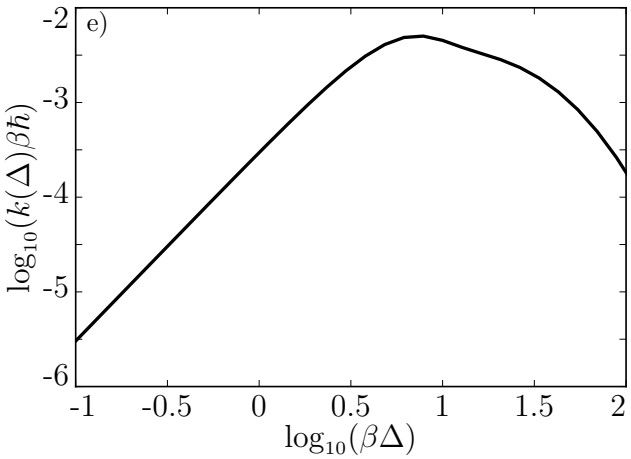

Figure 5.18: The Δ-dependent electron transfer rate, $k(\Delta)$, obtained using the HEOM-TN approach for a spin-boson model (model e) in the inverted regime.

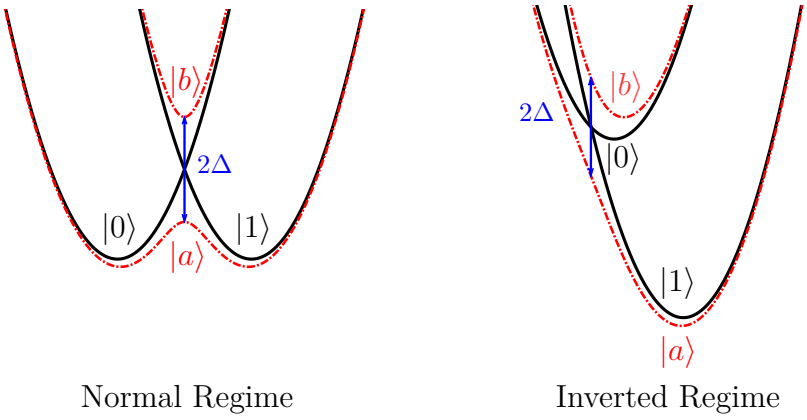

Figure 5.19: Schematic reaction coordinate diabatic and adiabatic potential energy surfaces for electron transfer reactions in the normal and inverted regimes with large diabatic coupling Δ. The potential energy surfaces for the two diabatic states, $|0\rangle$ and $|1\rangle$ representing the reactant and product states, respectively, are shown in black. The potential energy surfaces for the two adiabatic states, $|a\rangle$ and $|b\rangle$, are shown in red.

The qualitatively different behaviour observed in the normal and inverted regimes may be understood by considering the reaction coordinate diabatic and adiabatic potential energy surfaces in the two regimes for large values of Δ, schematics of which are shown in figure 5.19. In the adiabatic limit and normal regime the electron transfer process between diabatic states $|0\rangle$ and $|1\rangle$ is well described by evolution on the adiabatic potential energy surface associated with state $|a\rangle$. As Δ increases further the barrier seperating the two wells decreases and as a consequence the rate increases. In the inverted regime, on the other hand, the large Δ limit of the

electron transfer process no longer corresponds to dynamics on a single adiabatic potential energy surface. The electron transfer process involves a transfer from the adiabatic state $|b\rangle$ to the state $|a\rangle$. As Δ is increased the seperation between these adiabatic states increases, and as a result there is a reduction in the electron transfer rate.[269] Importantly, in order to provide an accurate description of the electron transfer process in this regime, it is necessary to capture transitions between distinct electronic states far from the nonadiabatic limit. RPMD rate theory, which can only treat reactions that proceed on a single Born-Oppenheimer potential energy surface clearly cannot do this, and so while the the nonadiabatic limit rate, $k_N(\Delta)$ may be obtained using Wolynes theory, RPMD rate theory cannot provide the adiabatic limit rate, $k_A(\Delta)$. As a consequence, this type of system cannot be treated using the interpolation formula in equation 5.119.

5.6 Conclusion and Future Work

In this chapter, a tree tensor network-based method for solving the hierarchical equations of motion has been presented. Within this approach a tree tensor network state-based representation of the hierarchy of auxiliary density operators is time-evolved according to a variational set of equations of motion. Under certain conditions these equations of motion require the evaluation of the inverses of singular matrices (the single-particle density matrices). This leads to considerable numerical difficulty. In this chapter, two approaches for overcoming this were considered. The first, an alternative regularisation scheme originally proposed by Wang and Meyer,[212,224] can be used to obtain results in some cases. However, in some parameter regimes it suffers from severe numerical issues, which greatly restrict its practicality. The second approach, a projector-splitting integrator that was originally proposed by Lubich[240] and employs an alternative representation of the equations of motion, was found to be considerably more reliable. Using this approach it was possible to obtain converged results even when the other integration scheme failed completely. As such, this method was employed for all further calculations.

The tree tensor network-based method with the projector-splitting integrator (HEOM-TN) was then applied to a series of spin-boson models with varying ranges of system-bath coupling. It was found to reproduce standard HEOM results, in regimes where these results could be obtained, and was demonstrated to converge in regimes for which the standard calculations were impractical. The approach was then applied to the calculation of numerically exact electron transfer rates for a series of spin-boson models with parameters spanning a wide range of physically relevant regimes. The resulting HEOM-TN rates were used to validate a newly proposed interpolation formula[181] and highlight the regimes in which it could be applied.

In this chapter, only applications of the HEOM-TN to spin-boson models have been considered. However, the method is by no means restricted to the case. The generalisation to more baths, and to the spectral density given in equation 4.39, provided none of the contributions are critically damped Brownian oscillators, is straightforward. Additional baths and more complicated spectral densities simply add additional bath modes that can be treated readily within the TTNS approach. This generalisation has been implemented with the aim of applying the method to treat the electron transfer dynamics in more complicated systems, such as those arising in the cryptochrome system considered in Section 2.4 (which includes three or four consecutive electron transfers).

Treating critically damped Brownian oscillator spectral densities is more involved. It alters the form of the HEOM by introducing the transfer term present in equation 4.129 and, as such, the equations of motion cannot be written in the form given by equation 5.12. However, this term can be expressed in terms of a product of operators acting on three degrees of freedom: the system and two bath degrees of freedom. The total HEOM "Hamiltonian" can still be expressed in a sum of product operators form. Critically damped Brownian oscillator spectral densities can be treated by this approach with only slight modification.

Extension to even more general spectral densities is also possible. The extended HEOM formalism,[175] which makes use of an orthogonal polynomial decomposition of the bath correlation function and its derivative, provides a similar, hierachical set of equations of motion for the reduced system density operator that can treat baths with arbitrary spectral density. Applications of this method are typically limited by the large number of orthogonal polynomials required to represent the bath correlation function, each of which contribute two modes to the hierarchy.[175] As a result of this, long-time calculations are incredibly challenging within this formalism.[175] In view of this it would be interesting to extend the HEOM-TN method, which can readily include arbitrarily large number of modes, to treat this formalism.

6 Conclusions

For systems that are embedded in a condensed-phase environment, interactions with the environment can significantly alter the system dynamics. In order to capture these effects it is generally necessary to include the degrees of freedom for both the system and its environment (bath). As such, an accurate description of the system dynamics may require the explicit treatment of a very large number of degrees of freedom. In this thesis, the dynamics of quantum mechanical systems interacting with large numbers of bath degrees of freedom were considered in two contexts:

1. Small spin systems interacting with one or more large baths of spins, such as those that arise in models of radical pair recombination reactions, and in the hyperfine-induced decoherence of the spin of an electron confined within a quantum dot.

2. Two-level systems interacting with harmonic oscillator baths, which occur in models of electron transfer reactions.

6.1 Spin Dynamics

The standard quantum mechanical and semiclassical treatments of radical pair recombination reactions were presented in Chapter 2. A direct quantum mechanical

treatment is straightforward for radical pairs containing few nuclear spins. However, due to the exponential scaling of Hilbert space dimension with the systems size, quantum mechanical approaches rapidly becomes infeasible. In an effort to overcome this, a number of semiclassical methods have previously been proposed for treating radical pair recombination. In Section 2.3, two such approachs, Schulten-Wolynes theory[60] and an improved semiclassical theory,[61,62] were discussed. The accuracy of these semiclassical methods was assessed by considering two model radical pairs ($FAD^{\bullet-}Z^{\bullet}$ and $FAD^{\bullet-}TrpH^{\bullet+}$) based on the photochemistry of cryptochrome proteins. The semiclassical methods were found to be accurate for these models in the absence of electron spin coupling interactions, however, all semiclassical methods were inaccurate in the presence of a realistic amount of electron spin coupling. Even with a relatively large number of nuclear spins it is not immediately obvious if semiclassical approaches are suitable. As such, there is still a need to develop either more accurate semiclassical methods or more efficient quantum mechanical methods for treating large radical pair systems where all spin interactions are non-perturbative.

Motivated by the results obtained in Chapter 2, in Chapter 3 a new quantum mechanical approach for treating the dynamics of spin systems coupled to spin baths was proposed. This new method, the moment-fitting method, was initially presented in the context of the central spin model, which is a model that arises when describing the hyperfine-induced decoherence of electron spins confined within quantum dots. The moment-fitting method treats the dynamics of large central spin models by considering a series of simpler problems that are designed to capture the influence of the bath spins on the central spin. This method readily captures the dynamics of two special cases of the central spin model, for which the exact dynamics can be obtained without running into the exponential scaling problem. These are the cases of homogeneous coupling and the Schulten-Wolynes theory limit. Additionally, as the complexity of the approximate Hamiltonians was increased, the dynamics obtained was observed to converge onto the exact dynamics for a

number of different central spin models with large numbers of spins (between 49 and 1000). This was demonstrated in Section 3.6 by comparison with results that had previously been obtained using the time-dependent density matrix renormalisation group (t-DMRG) and algebraic Bethe ansatz (ABA) methods, for two central spin models. The converged results obtained using the moment-fitting method were observed to agree with those obtained using these approaches; however, they were found to be applicable to longer time than the t-DMRG approach and did not suffer from the statistical errors observed using the ABA method.

The results obtained using the moment-fitting method were sufficiently accurate over long-enough timescales that they were able to provide a stringent test of the semiclassical methods that were discussed in Section 2.3. The results of these comparisons are reported in Section 3.6.3, where it was observed that even for a very large nuclear spin bath containing $N = 999$ nuclear spins, none of the semiclassical methods considered could quantitatively describe the central spin dynamics. These results further highlight the importance of efficient quantum mechanical methods for large systems. Exact quantum mechanical methods, suitable for treating large spin systems, provide a useful tool for benchmarking approximate methods. Previously semiclassical methods have been benchmarked by comparison with small quantum mechanical simulations.[61] The semiclassical methods fail to capture the quantum coherence present in small radicals, however, these are rapidly damped as the number of nuclear spins increases and the semiclassical methods become accurate. Using the moment-fitting methods, it is possible to treat considerably larger spin systems for which coherence effects are considerably less important. As such, using this approach it is possible to determine whether there are other sources of inaccuracies present in the semiclassical methods. In particular, the comparisons performed in Section 3.6.3 identified that the semiclassical methods considered here are unable to capture the long-time decay of the central spin correlation functions. For smaller spin systems, these effects are less noticeable as other sources of error, such as the lack of quantum coherence effects in the semiclassical methods, dominate.

The moment-fitting method makes no approximations concerning operators acting solely on the central spin Hilbert space and this approach can be readily generalised to treat more complicated spin systems interacting with a bath. This was carried out in Section 3.7, in which an extension of the moment-fitting method was used to treat the recombination dynamics of a carotenoid-porphyrin-fullerene (CPF) radical pair. This radical pair contains a total of 47 spins and, as a result, only semiclassical calculations have previously been employed to treat the dynamics of the system in its full dimensionality.[62] In Section 3.7, the validity of semiclassical treatments of the recombination dynamics of the CPF radical pair were explored. In the presence of a ~ 1 mT magnetic field, the earlier semiclassical theory of Schulten and Wolynes[60] was found to provide a considerably better description of the radical pair survival probability than the semiclassical method of Lewis *et al.*.[62] However, Schulten-Wolynes theory predicted considerable undamped oscillations in the fraction of singlet radical pairs arising due to the approximation of a fixed nuclear spin bath. Additionally, in the absence of a magnetic field Schulten-Wolynes theory gave rise to qualitatively incorrect dynamics. The semiclassical method of Lewis *et al.* was able to capture the damping of the oscillation in the singlet fraction observed quantum mechanically, and it did not show a sudden failure at low field. In the case of symmetric recombination, it showed excellent agreement with the moment-fitting method results. However, in the presence of asymmetric recombination, the semiclassical method was far from quantitative suggesting that its ad hoc treatment of the recombination dynamics can give rise to inaccuracies.

When taken together, the results presented in Chapters 2 and 3 indicate that care should be taken when applying semiclassical methods to treat the dynamics of radical pair recombination reactions.

6.2 Dynamics of Electron Transfer Reactions

The dynamics of electron transfer reactions of radical ion pairs was considered in Chapter 4. Within the standard treatment of these radical pairs (discussed in chapter 2), the recombination reaction is entirely described using a superoperator acting on the spin density operator. It is assumed that this fully captures the influence of the electron transfer process on the spin dynamics. In order to explore the validity of this, the coupled electronic, nuclear, and spin dynamics of a series of simple models of radical ion pairs were evaluated using the hierarchical equations of motion (HEOM) formalism.[7,8] The HEOM formalism provides numerically exact equations of motion for the reduced density operator describing an arbitrary quantum system that is linearly coupled to one or more harmonic baths. This is done by employing an infinite series of auxiliary density operators (ADOs), whose dynamics couples to the dynamics of the reduced density operator. The ADOs also fully account for non-Markovian effects arising from the bath dynamics. A derivation of the hierarchical equations of motion as well as a discussion of implementation details necessary to obtain an efficient method was provided in sections 4.3 and 4.4.

Following the above, the validity of a series of recently proposed quantum master equations (QMEs) for spin selective electron transfers of radical pairs was explored for a simple radical ion pair model. In order to do this, the dynamics obtained using the QMEs was compared against numerically exact HEOM calculations treating the coupled dynamics of all electronic, nuclear, and spin degrees of freedom for this model. The QMEs, which in the nonadiabatic limit reduce to the standard Haberkorn master equation with an additional reactive electron spin coupling contribution, were found to accurately capture the spin dynamics in this limit. On moving away from the nonadiabatic limit, an additional singlet-triplet dephasing contribution, captured by the fourth order form of these newly proposed QMEs, is observed, and becomes more significant on moving towards the adiabatic limit. These results suggest that when modelling realistic radical pairs, exchange coupling

and singlet-triplet dephasing terms should be included. However, the singlet-triplet dephasing term complicates the treatment of radical pair recombination dynamics. Singlet-triplet dephasing does not preserve pure states. In this case, the wavefunction-based approaches described in Chapters 2 and 3 cannot be applied directly. The singlet-triplet dephasing term may be rewritten in Lindblad form[5,91] as

$$-k_d\left(\hat{P}_S\hat{\rho}_{0s}(t)\hat{P}_T+\hat{P}_T\hat{\rho}_{0s}(t)\hat{P}_S\right)=2k_d\left(\hat{P}_S\hat{\rho}_{0s}(t)\hat{P}_S-\frac{1}{2}\left\{\hat{P}_S^\dagger\hat{P}_S,\hat{\rho}_{0s}(t)\right\}\right) \quad (6.1)$$

by using $\hat{P}_T=\hat{\mathbf{1}}-\hat{P}_S$, and that $\hat{P}_S^\dagger\hat{P}_S=\hat{P}_S$. In the absence of any additional non-unitary contributions to the dynamics, this term can be treated within a wavefunction-based approach using the quantum jump trajectory method.[270–272] It would be interesting to see whether an analogous approach could be developed to include the non-unitary contributions that arise from asymmetric recombination in the radical pair recombination process.

While the HEOM method is, in principle, applicable to arbitrary systems with arbitrarily strong system-bath coupling, as the strength of the system bath coupling increases the number of auxiliary density operators needed to obtain converged results may become infeasibly large. A tree tensor network state-based approach for solving the hierarchical equations of motion was presented in Chapter 5. This approach (HEOM-TN) was demonstrated to reproduce standard HEOM results in regimes where these results could be obtained. Further, it could be used to obtain converged results in regimes for which the standard calculations were impractical. Finally, the HEOM-TN method was applied to the calculation of numerically exact electron transfer rates for a series of spin-boson models with parameters spanning a wide range of physically relevant regimes. These rates were used to validate a newly proposed interpolation formula for electron transfer rates[181] and highlight the regimes in which it could be applied. While, in Chapter 5, the HEOM-TN approach was only applied to treat the dynamics of spin-boson models, it is by no means limited to these systems. The extension of the HEOM-TN method to more general systems and baths is currently underway.

Appendices

A

Hyperfine Coupling Constants

The hyperfine coupling tensor that were used in the simulations of the cryptochrome-based radical pairs presented in section 2.4 are shown in tables A.1 and A.2. These hyperfine coupling tensors were taken from reference [83].

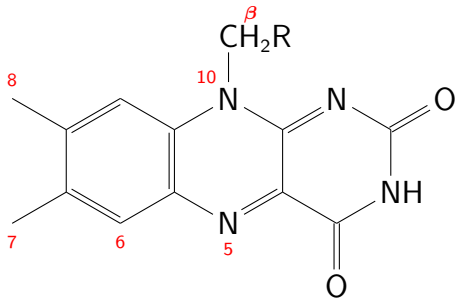

Nucleus		**A**		Nucleus		**A**	
N5	-0.0989	0.0039	0	N10	-0.0190	-0.0048	0
	0.0039	-0.0881	0		-0.0048	-0.0196	0
	0	0	1.7569		0	0	0.6046
H6	-0.2569	-0.1273	0	3×H8	0.4399	0	0
	-0.1273	-0.4711	0		0	0.4399	0
	0	0	-0.4336		0	0	0.4399
2×Hβ	0.4070	0	0	3×H7	-0.1416	0	0
	0	0.4070	0		0	-0.1416	0
	0	0	0.4070		0	0	-0.1416

Table A.1: The hyperfine coupling tensors of the 11 nuclear spins included in simulations of radical pairs containing the flavin adenine dinucleotide radical ($FAD^{\bullet -}$).

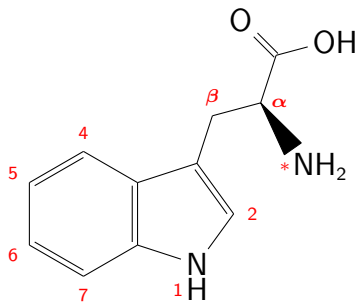

Nucleus		**A**		Nucleus		**A**	
N1	-0.0336	0.0924	-0.1354	H1	-0.9920	-0.2091	-0.2003
	0.0924	0.3303	-0.5318		-0.2091	-0.2631	0.2803
	-0.1354	-0.5318	0.6680		-0.2003	0.2803	-0.5398
H2	-0.2843	0.1757	0.1525	H4	-0.5596	-0.1956	-0.1657
	0.1757	-0.2798	0.0975		-0.1956	-0.4020	0.0762
	0.1525	0.0975	-0.2699		-0.1657	0.0762	-0.5021
H6	-0.0506	0.0622	0.0889	H7	-0.4355	-0.1541	-0.1239
	0.0622	-0.3100	-0.0297		-0.1541	-0.2777	0.0864
	0.0889	-0.0297	0.2642		-0.1239	0.0864	-0.3770
Hβ1	1.5808	-0.0453	-0.0506	Hα	-0.0601	0.0037	0.0331
	-0.0453	1.5575	0.0988		0.0037	-0.0251	0.0111
	-0.0506	0.0988	1.6752		0.0331	0.0111	-0.1940
N$*$	0.1295	-0.0134	0.0075	Hβ2	0.1634	-0.0230	-0.0064
	-0.0134	0.1729	-0.0249		-0.0230	-0.0082	0.0158
	0.0075	-0.0249	0.1371		-0.0064	0.0158	-0.0182
H5	0.0051	0.0616	0.0694				
	0.0616	-0.0665	0.0391				
	0.0694	0.0391	-0.0586				

Table A.2: The hyperfine coupling tensors of the 11 nuclear spins included in simulations of radical pairs containing the tryptophan radical ($TrpH^{\bullet+}$).

B

Derivation of Schulten-Wolynes Theory

In this appendix a derivation of the semiclassical theory of Schulten and Wolynes will be presented.[60] This theory is based on the assumption that when there are a sufficiently large number of bath spins, the hyperfine-weighted sum of nuclear spin operators,

$$\hat{\boldsymbol{K}} = \sum_{k=1}^{N} a_k \hat{\boldsymbol{I}}_k, \tag{B.1}$$

can be treated as a constant vector, $\boldsymbol{K}$. This approximation becomes exact in the $N \to \infty$ provided a few constraints are place on the distribution of hyperfine coupling constants. To shown this, a central spin problem containing N bath spins each coupled to the central spin with a hyperfine coupling constant, $a_k(N)$, that is a function of N, will be considered. Schulten-Wolynes theory becomes exact provided,

$$\lim_{N\to\infty} \sqrt{N} a_k(N) = \widetilde{a}_k \tag{B.2}$$

where each $\widetilde{a}_k$ is independent of N. The Hamiltonian governing the dynamics of this central spin problem can be written as

$$\hat{H}_N = \omega_\alpha \hat{S}_\alpha + \frac{1}{\sqrt{N}} \sum_{k=1}^{N} \widetilde{a}_k \hat{S}_\alpha \hat{I}_{k\alpha} \tag{B.3}$$

where the Einstein summation convention (implicit summation over repeated indices) has been adopted for all greek indices. Introducing the bath operator of order n,

$$\hat{\boldsymbol{K}}^{[n]} = \sum_{k=1}^{N} a_k^n \hat{\boldsymbol{I}}_k = N^{-n/2} \sum_{k=1}^{N} \widetilde{a}_k^n \hat{\boldsymbol{I}}_k, \tag{B.4}$$

equation B.3 may be rewritten as

$$\hat{H}_N = (\omega_\alpha + \hat{K}^{[1]}_\alpha)\hat{S}_\alpha. \tag{B.5}$$

where here $\hat{K}^{[1]}_\alpha$, is the α-th component of the first order bath operator.

In the Heisenberg picture the central spin operators,

$$\hat{S}_\alpha(t) = e^{i\hat{H}_N t/\hbar}\hat{S}_\alpha e^{-i\hat{H}_N t/\hbar}, \tag{B.6}$$

are analytic functions of time and, therefore, may be expanded as a Taylor series around $t = 0$ to give

$$\hat{S}_\alpha(t) = \sum_{n=0}^{\infty} \hat{S}^{(n)}_\alpha(0)\frac{t^n}{n!}, \tag{B.7}$$

where $\hat{S}^{(n)}_\alpha(0)$ is the n-th order time derivative of $\hat{S}_\alpha(t)$ evaluated at $t = 0$. The spin operators evolve according to the Heisenberg equation of motion, so inserting equation B.5 gives

$$\hat{S}^{(1)}_\alpha(t) = \frac{i}{\hbar}\left[\hat{H}_N, \hat{S}_\alpha(t)\right] \tag{B.8}$$

$$= \epsilon_{\alpha\beta\gamma}(\omega_\beta + \hat{K}^{[1]}_\beta(t))\hat{S}_\gamma(t). \tag{B.9}$$

Using the generalised Leibniz rule,[273] the n-th order time derivate of $\hat{S}_\alpha(t)$ is found to be,

$$\hat{S}^{(n)}_\alpha(t) = \frac{\mathrm{d}^{n-1}}{\mathrm{d}t^{n-1}}\hat{S}^{(1)}_\alpha(t) \tag{B.10}$$

$$= \epsilon_{\alpha\beta\gamma}\left[(\omega_\beta + \hat{K}^{[1]}_\beta(t))\hat{S}^{(n-1)}_\gamma(t) + \sum_{k=1}^{n-1}\binom{n-1}{k}(\hat{K}^{[1](k)}_\beta(t))\hat{S}^{(n-(k+1))}_\gamma(t)\right]. \tag{B.11}$$

This expression provides a recurrence relation for the n-th time derivative of $\hat{S}_\alpha(t)$ in terms of all lower-order time derivatives of the central spin and bath operators. The time derivatives of the bath operators can similarly be obtained from the Heisenberg equation of motion. The time derivative of the first order bath operator $\hat{K}^{[1]}_\alpha(t)$,

$$\hat{K}^{[1](1)}_\alpha(t) = \frac{i}{\hbar}\hat{S}_\beta(t)\sum_{k=1}^{N}\sum_{k'=1}^{N} a_k a_{k'}\left[\hat{I}_{k\beta}(t), \hat{I}_{k'\alpha}(t)\right] \tag{B.12}$$

$$= \epsilon_{\alpha\beta\gamma}\hat{S}_\beta(t)\sum_{k=1}^{N} a_k^2\hat{I}_{k\gamma}(t) = \epsilon_{\alpha\beta\gamma}\hat{S}_\beta(t)\hat{K}^{[2]}_\gamma(t), \tag{B.13}$$

depends on the bath operator of order 2. For a bath operator of arbitrary order, $\hat{K}_{\beta}^{[n]}(t)$, this can be generalised to give,

$$\hat{K}_{\alpha}^{[n]\,(1)}(t) = \epsilon_{\alpha\beta\gamma}\hat{S}_{\beta}(t)\hat{K}_{\gamma}^{[n+1]}(t). \tag{B.14}$$

Within, the Schulten-Wolynes theory approximation the details of the bath dynamics are unimportant, it is only the influence of the bath on the dynamics of the central spin that is of interest, and therefore it is useful to evaluate the trace over the bath degrees of freedom. Taking an expectation value over the initial bath density operator $\hat{\rho}_B = \frac{1}{Z}\mathbb{1}_B$, the mean field central spin operators,

$$\left\langle \hat{S}_{\alpha} \right\rangle_B(t) = \frac{1}{Z}\mathrm{tr}\left[\hat{S}_{\alpha}(t)\right]_B = \sum_{n=0}^{\infty}\frac{1}{Z}\mathrm{tr}\left[\hat{S}_{\alpha}^{(n)}(0)\right]_B\frac{t^n}{n!}, \tag{B.15}$$

are obtained. To evaluate these operators it is now necessary to evaluate the bath expectation value of the arbitrary order time derivatives of the central spin operators. From equations B.10 and B.14, it is clear that these n-th order time derivatives will in general depend on products of up to n bath operators.

B.1 Bath Expectation Values

As all components of the vector spin angular momentum operator have zero trace, the expectation value of the n-th order bath operator is

$$\frac{1}{Z}\mathrm{tr}\left[\hat{K}_{\alpha}^{[n]}(t)\right]_B = \left\langle \hat{K}_{\alpha}^{[n]}(t)\right\rangle_B = \sum_{i=1}^{N}\frac{a_i^n}{Z}\mathrm{tr}\left[\hat{I}_{i\alpha}(t)\right]_B = 0 \tag{B.16}$$

The bath expectation value of the product of any two bath operators is

$$\begin{aligned}\left\langle \hat{K}_{\alpha_1}^{[n_1]}(t)\hat{K}_{\alpha_2}^{[n_2]}(t)\right\rangle_B &= \sum_{i=1}^{N}\sum_{j=1}^{N}a_i^{n_1}a_j^{n_2}\left\langle \hat{I}_{i\alpha_1}(t)\hat{I}_{j\alpha_2}(t)\right\rangle_B \\ &= \sum_{i=1}^{N}a_i^{n_{12}}\left\langle \hat{I}_{i\alpha_1}(t)\hat{I}_{i\alpha_2}(t)\right\rangle_B \\ &= \sum_{i=1}^{N}\frac{a_i^{n_{12}}I_i(I_i+1)}{3}\delta_{\alpha_1\alpha_2}.\end{aligned} \tag{B.17}$$

where the notation $n_{i_1 \ldots i_n} = \sum_{i=1}^{N} n_i$ has been introduced. Rewriting this in terms of the $\widetilde{a}_k$ variables gives

$$\left\langle \hat{K}_{\alpha_1}^{[n_1]}(t) \hat{K}_{\alpha_2}^{[n_2]}(t) \right\rangle_B = \sum_{i=1}^{N} N^{\text{-}n_{12}/2} \frac{\widetilde{a}_i I_i (I_i+1)}{3} \delta_{\alpha_1 \alpha_2}, \tag{B.18}$$

and therefore

$$N^{1\text{-}n_{12}/2} \min_i \left(\frac{\widetilde{a}_i I_i (I_i+1)}{3} \right) \delta_{\alpha_1 \alpha_2} \leq \left\langle \hat{K}_{\alpha_1}^{[n_1]}(t) \hat{K}_{\alpha_2}^{[n_2]}(t) \right\rangle_B \leq N^{1\text{-}n_{12}/2} \max_i \left(\frac{\widetilde{a}_i I_i (I_i+1)}{3} \right) \delta_{\alpha_1 \alpha_2}.$$

For $n_{12} = n_1 + n_2 > 2$, terms of this form vanish in the limit that $N \to \infty$. So equation B.17 becomes,

$$\lim_{N\to\infty} \left\langle \hat{K}_{\alpha}^{[n]}(t) \hat{K}_{\beta}^{[m]}(t) \right\rangle_B = \lim_{N\to\infty} \sum_{i=1}^{N} \frac{a_k I_i (I_i+1)}{3} \delta_{\alpha\beta} \delta_{n1} \delta_{m1}. \tag{B.19}$$

As such, the only products of two generalised bath operators that have non-zero expectation value are the three $\hat{K}_{\alpha}^{[1]} \hat{K}_{\alpha}^{[1]}$ terms.

For a product of three spin operators, all terms containing a trace of a single spin operator have zero expectation value and so the only terms that remain are

$$\left\langle \hat{K}_{\alpha_1}^{[n_1]}(t) \hat{K}_{\alpha_2}^{[n_2]}(t) \hat{K}_{\alpha_3}^{[n_3]}(t) \right\rangle_B = \sum_{i=1}^{N} a_i^{n_{123}} \left\langle \hat{I}_{i\alpha_1}(t) \hat{I}_{i\alpha_2}(t) \hat{I}_{i\alpha_3}(t) \right\rangle_B. \tag{B.20}$$

As the average of 3 spin operators is independent of the number of spins, in the limit that $N \to \infty$, this becomes,

$$\lim_{n\to\infty} \left\langle \prod_{i=1}^{3} \hat{K}_{\alpha_i}^{[n_i]}(t) \right\rangle_B = \lim_{n\to\infty} \sum_{i=1}^{N} \widetilde{a}_i^{n_{123}} N^{\text{-}n_{123}/2} \left\langle \hat{I}_{i\alpha_1}(t) \hat{I}_{i\alpha_2}(t) \hat{I}_{i\alpha_3}(t) \right\rangle_B \tag{B.21}$$

$$\leq \lim_{n\to\infty} \max_k (\widetilde{a}_i^{n_{123}} \left\langle \hat{I}_{i\alpha_1}(t) \hat{I}_{i\alpha_2}(t) \hat{I}_{i\alpha_3}(t) \right\rangle) N^{1\text{-}n_{123}/2} = 0, \tag{B.22}$$

and so all products of three generalised bath operators have a zero expectation value. As a final explicit example, consider the products of four bath operators:

$$\begin{aligned} \left\langle \prod_{i=1}^{4} \hat{K}_{\alpha_i}^{[n_i]}(t) \right\rangle_B &= \sum_{i=1}^{N} a_i^{n_{1234}} \left\langle \hat{I}_{i\alpha_1}(t) \hat{I}_{i\alpha_2}(t) \hat{I}_{i\alpha_3}(t) \hat{I}_{i\alpha_4}(t) \right\rangle_B \\ &+ \sum_{i=1}^{N} \sum_{j\neq i}^{N} \Bigg(a_i^{n_{12}} a_j^{n_{34}} \left\langle \hat{I}_{i\alpha_1}(t) \hat{I}_{i\alpha_2}(t) \right\rangle_B \left\langle \hat{I}_{j\alpha_3}(t) \hat{I}_{j\alpha_4}(t) \right\rangle_B \\ &\quad + a_i^{n_{13}} a_j^{n_{24}} \left\langle \hat{I}_{i\alpha_1}(t) \hat{I}_{i\alpha_3}(t) \right\rangle_B \left\langle \hat{I}_{j\alpha_2}(t) \hat{I}_{j\alpha_4}(t) \right\rangle_B \\ &\quad + a_i^{n_{14}} a_j^{n_{23}} \left\langle \hat{I}_{i\alpha_1}(t) \hat{I}_{i\alpha_4}(t) \right\rangle_B \left\langle \hat{I}_{j\alpha_2}(t) \hat{I}_{j\alpha_3}(t) \right\rangle_B \Bigg). \end{aligned} \tag{B.23}$$

The contribution of the first term to this expectation value scales as $\mathcal{O}(N^{1-n_{1234}/2})$, and therefore tends to zero as $N \to \infty$. This expression may therefore be rewritten as

$$\begin{aligned}\left\langle \prod_{i=1}^{4} \hat{K}_{\alpha_i}^{[n_i]}(t) \right\rangle_B = \sum_{i=1}^{N}\sum_{j=1}^{N} \Big(& a_i^{n_{12}} a_j^{n_{34}} \left\langle \hat{I}_{i\alpha_1}(t)\hat{I}_{i\alpha_2}(t)\right\rangle_B \left\langle \hat{I}_{j\alpha_3}(t)\hat{I}_{j\alpha_4}(t)\right\rangle_B \\ & + a_i^{n_{13}} a_j^{n_{24}} \left\langle \hat{I}_{i\alpha_1}(t)\hat{I}_{i\alpha_3}(t)\right\rangle_B \left\langle \hat{I}_{j\alpha_2}(t)\hat{I}_{j\alpha_4}(t)\right\rangle_B \\ & + a_i^{n_{14}} a_j^{n_{23}} \left\langle \hat{I}_{i\alpha_1}(t)\hat{I}_{i\alpha_4}(t)\right\rangle_B \left\langle \hat{I}_{j\alpha_2}(t)\hat{I}_{j\alpha_3}(t)\right\rangle_B \Big) + \mathcal{O}\left(N^{-n_{1234}/2}\right),\end{aligned} \tag{B.24}$$

where the missing terms in the double sum, whose contribution scales as $\mathcal{O}(N^{1-n_{1234}/2})$, have been reintroduced. Taking the limit as $N \to \infty$ this expression becomes

$$\begin{aligned}\lim_{N\to\infty} \left\langle \prod_{i=1}^{4} \hat{K}_{\alpha_i}^{[n_i]}(t) \right\rangle_B = \lim_{N\to\infty} \Big(& \left\langle \hat{K}_{\alpha_1}^{[n_1]}(t)\hat{K}_{\alpha_2}^{[n_2]}(t)\right\rangle_B \left\langle \hat{K}_{\alpha_3}^{[n_3]}(t)\hat{K}_{\alpha_4}^{[n_4]}(t)\right\rangle_B \\ & + \left\langle \hat{K}_{\alpha_1}^{[n_1]}(t)\hat{K}_{\alpha_3}^{[n_3]}(t)\right\rangle_B \left\langle \hat{K}_{\alpha_2}^{[n_2]}(t)\hat{K}_{\alpha_4}^{[n_4]}(t)\right\rangle_B \\ & + \left\langle \hat{K}_{\alpha_1}^{[n_1]}(t)\hat{K}_{\alpha_4}^{[n_4]}(t)\right\rangle_B \left\langle \hat{K}_{\alpha_2}^{[n_2]}(t)\hat{K}_{\alpha_3}^{[n_3]}(t)\right\rangle_B \Big);\end{aligned} \tag{B.25}$$

the expectation value of products of four bath spin operators can be written in terms of all possible sums of products of the expectation values of two bath operator expectation values.[274]

This argument may be generalised to the product of an arbitrary numbers, m, of the bath operators, $\hat{K}_{\alpha_i}^{[n_i]}(t)$. On doing so, it is found that for all odd values of m,[117,274]

$$\lim_{N\to\infty} \left\langle \prod_{i=1}^{m} \hat{K}_{\alpha_i}^{[n_i]}(t) \right\rangle_B = 0, \tag{B.26}$$

while for even values of m,

$$\lim_{N\to\infty} \left\langle \prod_{i=1}^{m} \hat{K}_{\alpha_i}^{[n_i]}(t) \right\rangle_B = \lim_{N\to\infty} \sum \prod \left\langle \hat{K}_{\alpha_i}^{[n_i]}(t)\hat{K}_{\alpha_j}^{[n_j]}\right\rangle_B \delta_{(n_1+\ldots n_m)n}, \tag{B.27}$$

where $\sum\prod$ denotes the sum over all $(m-1)!!$ distinct ways of partitioning these m operators into pairs $m/2$ pairs.[275] For all $n_i = 1$, where $\delta_{(n_1+\ldots n_m)n} = 1$, this result is equivalent to Wick's theorem for three uncorrelated classical normal variates(K_x, K_y, K_z),[275–278] each with zero mean and variance

$$\sigma^2 = \lim_{N\to\infty} \sum_{k=1}^{N} \frac{a_k I_k (I_k+1)}{3}. \tag{B.28}$$

B.2 Central Spin Dynamics

In the $N \to \infty$ limit, the bath average of equation B.11 becomes

$$\lim_{N\to\infty} \left\langle \hat{S}_\alpha^{(n)}(t) \right\rangle_B = \epsilon_{\alpha\beta\gamma} \lim_{N\to\infty} \left\langle (\omega_\beta + \hat{K}_\beta^{[1]}(t)) \hat{S}_\gamma^{(n-1)}(t) \right\rangle_B \tag{B.29}$$

where contributions from the time derivatives of the bath operators, which can be expressed in terms of higher order bath operators (see equation B.14), have been excluded as they tend to 0 in this limit. Repeatedly applying this recurrence relation gives an explicit expression for the n-th derivative of the mean field central spin operator

$$\lim_{N\to\infty} \left\langle \hat{S}_\alpha^{(n)}(t) \right\rangle_B = \left(\epsilon_{\alpha j_1 i_1} \prod_{k=1}^{n-1} \epsilon_{i_k j_k i_{k+1}} \right) \left\langle \prod_{k=1}^{n} (\omega_{j_k} + \hat{K}_{j_k}^{[1]}(t)) \right\rangle_B \hat{S}_{i_n}(t). \tag{B.30}$$

At $t = 0$, this expression depends only on the bath operators $\hat{K}_\alpha^{[1]}$, which satisfy Wick's theorem for classical gaussian distributed variables. The trace over the bath can therefore be replaced with a gaussian weighted integral over the uncorrelated classical variables, $\mathrm{K} = (K_x, K_y, K_z)$,[117]

$$\lim_{n\to\infty} \left\langle \prod_{i=1}^{n} \hat{K}_{\alpha_i}^{[1]}(t) \right\rangle_B \to \int \prod_{i=1}^{n} K_{\alpha_i} P(\boldsymbol{K}) \mathrm{d}\boldsymbol{K}. \tag{B.31}$$

where

$$P(\boldsymbol{K}) = \frac{1}{(2\pi)^{\frac{3}{2}}\sigma^3} e^{-\boldsymbol{K}^2/(2\sigma^2)}. \tag{B.32}$$

Collecting together all terms in the Taylor series expansion of the central spin operators gives

$$\lim_{N\to\infty} \left\langle \hat{\boldsymbol{S}} \right\rangle(t) = \int \hat{\boldsymbol{S}}(\boldsymbol{K}, t) P(\boldsymbol{K}) \mathrm{d}\boldsymbol{K}, \tag{B.33}$$

where $\hat{\boldsymbol{S}}(\boldsymbol{K}, t)$ is the time-dependent central spin operator obtained for a given realisation of the classical hyperfine field vector. The elements of this central spin operator evolve according to

$$\frac{\mathrm{d}}{\mathrm{d}t} \hat{S}_\alpha(\boldsymbol{K}, t) = \epsilon_{\alpha\beta\gamma} (\omega_\beta + K_\beta) \hat{S}_\gamma(\boldsymbol{K}, t). \tag{B.34}$$

These are just the Heisenberg equation of motion for a central spin operator precessing around a fixed magnetic field. This is Schulten-Wolynes theory for the

central spin problem.[60,61,94] As shown here, Schulten-Wolynes theory is exact for any finite amount of time in the limit of an infinite number of hyperfine-coupled bath spins provided equation B.2 is satisfied. For a finite N, the leading order error of each coefficient in the Taylor series of the spin operator is $\mathcal{O}(N^{-1/2})$, and so Schulten-Wolynes theory is accurate for large number of spins and for short times.

C

Evaluation of Bath Correlation Functions

A number of different methods exist for evaluating the correlation function

$$C(t) = \frac{\hbar}{2\pi}\int_{-\infty}^{\infty} J(\omega)\left[\coth\left(\frac{\beta\hbar\omega}{2}\right) - 1\right] e^{i\omega t}\mathrm{d}t \tag{C.1}$$

associated with a bath with spectral density, $J(\omega)$, that arises as one of the key quantities in the hierarchical equations of motion. This correlation function fully describes the influence of the bath on the system dynamics. The standard approach makes use of an infinite (Matsubara) series expansion of the integral.[8,195] Here this approach will be employed to derive a general expression for the bath correlation function for any spectral density that may be written as

$$J(\omega) = \omega F(\omega) \tag{C.2}$$

where $F(\omega)$ is an analytic function of ω except at some finite set of points $\{z_1, \ldots, z_M\}$, none of which lie on the real axis, and $F(z)$ decays more rapidly than $1/z$ as $|z| \to \infty$. Further it will be assumed that the poles of $F(\omega)$ in the upper half plane, which will be taken as the first N poles $\{z_1, z_2, \ldots, z_N\}$, do not coincide with the poles of $\omega\coth(\beta\hbar\omega/2)$ lying in the upper half plane, $\{i\nu_1, i\nu_2, \ldots, i\nu_k, \ldots\}$ where

$$\nu_k = \frac{2\pi k}{\beta\hbar} \tag{C.3}$$

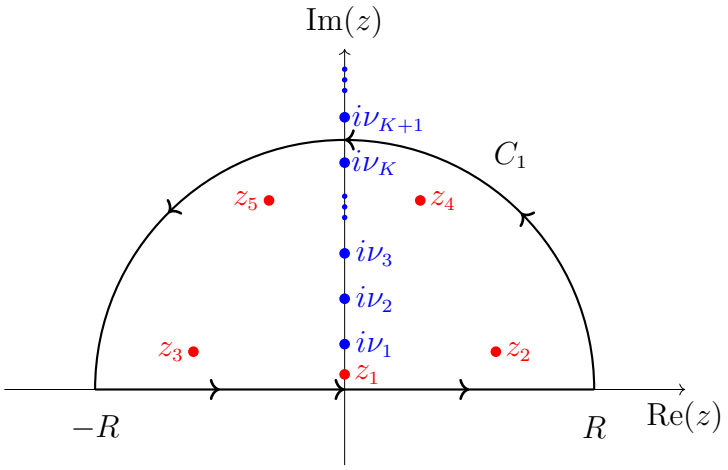

Figure C.1: The contour, C, used to evaluate the bath correlation function. The poles of $\omega \coth(\beta\hbar\omega/2)$ and $F(w)$ lying in the upper half plane are shown in blue and red, respectively.

are the Matsubara frequencies. While this is not strictly required it considerably simplifies the treatment that will be presented below. The bath correlation function of this spectral density may be evaluated by considering the contour shown in figure C.1.

Introducing the function

$$G(z) = F(z)z\left[\coth\left(\frac{\beta\hbar z}{2}\right) - 1\right] \tag{C.4}$$

and taking

$$R = \frac{2\pi(K+1/2)}{\beta\hbar} \tag{C.5}$$

sufficiently large such that the contour C encloses all poles of $F(z)$ lying in the upper half plane, then by Cauchy's residue theorem[279]

$$\frac{\hbar}{2\pi}\oint_C G(z)e^{izt}\mathrm{d}z = \frac{\hbar}{2\pi}\left[\int_{C_1} G(z)e^{izt}\mathrm{d}z + \int_{-R}^{R} G(\omega)e^{i\omega t}\mathrm{d}\omega\right] \tag{C.6}$$

$$= i\hbar\left[\sum_{i=1}^{N}\mathrm{Res}\left(G(z)e^{izt}, z_i\right) + \sum_{k=1}^{K}\mathrm{Res}\left(G(z)e^{izt}, i\nu_k\right)\right]. \tag{C.7}$$

where $\mathrm{Res}\left(f(z), z_k\right)$ denotes the residue of $f(z)$ at z_k, which for an n-th order pole is given by[279]

$$\mathrm{Res}\left(f(z), z_k\right) = \frac{1}{(n-1)!}\lim_{z\to z_k}\frac{\mathrm{d}^{n-1}}{\mathrm{d}z^{n-1}}\left[(z-z_k)^n f(z)\right]. \tag{C.8}$$

Taking the limit as $K \to \infty$, the integral over C_1 vanishes by Jordan's Lemma[279] and this expression becomes

$$C(t) = i\hbar \left[\sum_{i=1}^{N} \mathrm{Res}\left(G(z)e^{izt}, z_i\right) + \sum_{k=1}^{\infty} \mathrm{Res}\left(G(z)e^{izt}, i\nu_k\right) \right] \tag{C.9}$$

As the poles of the functions $F(z)$ and $z\coth(\beta\hbar z/2)$ do not concide, this may be rewritten as

$$C(t) = i\hbar \Big[\sum_{j=1}^{N} \mathrm{Res}\left(G(z)e^{i\omega t}, z_j\right) + \sum_{k=1}^{\infty} \mathrm{Res}\left(\coth\left(\frac{\beta\hbar z}{2}\right), i\nu_k \right) i\nu_k F(i\nu_k) e^{-\nu_k t} \Big] \tag{C.10}$$

$$= i\hbar \Big[\sum_{j=1}^{N} \mathrm{Res}\left(G(z)e^{i\omega t}, z_j\right) + \sum_{k=1}^{\infty} \frac{2i\nu_k}{\beta\hbar} F(i\nu_k) e^{-\nu_k t} \Big]. \tag{C.11}$$

This expression holds for all $F(\omega)$ satisfying the conditions discussed above, two examples of which are the Debye and Brownian oscillator spectral densities. In what follows their bath correlation functions will be obtained explicitly.

C.1 Debye Spectral Density

The Debye spectral density

$$J(\omega) = \frac{\Lambda}{2} \frac{\omega\omega_c}{\omega^2 + \omega_c^2}, \tag{C.12}$$

where Λ is the reorganisation energy and ω_c is the bath cutoff frequency, may be rewritten as $J(\omega) = \omega F(\omega)$ with

$$F(\omega) = \frac{\Lambda\omega_c}{2} \frac{1}{(\omega + i\omega_c)(\omega - i\omega_c)}. \tag{C.13}$$

As such, $F(\omega)$, has two simples poles at $\omega = \pm i\omega_c$ with residues

$$\mathrm{Res}(F(\omega), \pm i\omega_c) = \pm \frac{\Lambda}{4i}. \tag{C.14}$$

Only one of these $(i\omega_c)$ lies in the upper half plane and so the bath correlation function for the Debye spectral density is given by

$$C(t) = \frac{i\Lambda\omega_c\hbar}{4} \left[\coth\left(\frac{i\beta\hbar\omega_c}{2}\right) - 1 \right] e^{-\omega_c t} + \sum_{k=1}^{\infty} \frac{\Lambda\omega_c}{\beta} \frac{\nu_k}{\nu_k^2 - \omega_c^2} e^{-\nu_k t} \tag{C.15}$$

Introducing the bath reorgansiation energy $\lambda = \Lambda/4$ and using that $i\coth(iz) = \cot(z)$, this expression can be written as

$$C(t) = \lambda\omega_c\hbar \left[\cot\left(\frac{\beta\hbar\omega_c}{2}\right) - i \right] e^{-\omega_c t} + \sum_{k=1}^{\infty} \frac{\lambda\omega_c}{4\beta} \frac{\nu_k}{\nu_k^2 - \omega_c^2} e^{-\nu_k t}. \tag{C.16}$$

C.2 Brownian Oscillator Spectral Density

The Brownian Oscillator spectral density

$$J(\omega) = \frac{\Lambda}{2} \frac{\gamma \Omega^2 \omega}{(\omega^2 - \Omega^2)^2 + \gamma^2 \omega^2} \tag{C.17}$$

where Λ is the reorganisation energy, Ω is the reaction coordinate frequency, and γ is the friction coefficient along the reaction coordinate, may be written in the form $J(\omega) = \omega F(\omega)$ with

$$F(\omega) = \frac{1}{2} \frac{\Lambda \gamma \Omega^2}{(\omega + i\nu_+)(\omega + i\nu_-)(\omega - i\nu_+)(\omega - i\nu_-)} \tag{C.18}$$

where

$$\nu_\pm = \frac{\gamma}{2} \pm \sqrt{\gamma^2/4 - \Omega^2} \tag{C.19}$$

$$= \frac{\gamma}{2} \pm \kappa. \tag{C.20}$$

Provided the poles of $F(\omega)$ do not coincide with the Matsubara frequencies, the Matsubara frequency contributions to the bath correlation function may be evaluated for all values of γ and Ω as

$$i\hbar \sum_{k=1}^{\infty} \frac{2i\nu_k}{\beta\hbar} F(i\nu_k) e^{-\nu_k t} = \frac{\Lambda \gamma \Omega^2}{\beta} \sum_{k=1}^{\infty} \frac{\nu_k}{\gamma^2 \nu_k^2 - (\nu_k^2 + \Omega^2)^2} e^{-\nu_k t}, \tag{C.21}$$

The number of poles of $F(\omega)$ depends on the values of γ and Ω, as illustrated in figure C.2. In the overdamped and underdamped cases there are four simple poles, two of which are in the upper half plane, while in the critically damped case there are two second order poles, one of which lies in the upper half plane. As a result, the form of the contribution to the bath correlation function arising from the poles of $F(\omega)$, which will be denoted by $F(t; 2\Omega/\gamma)$, is dependent on the regime considered.

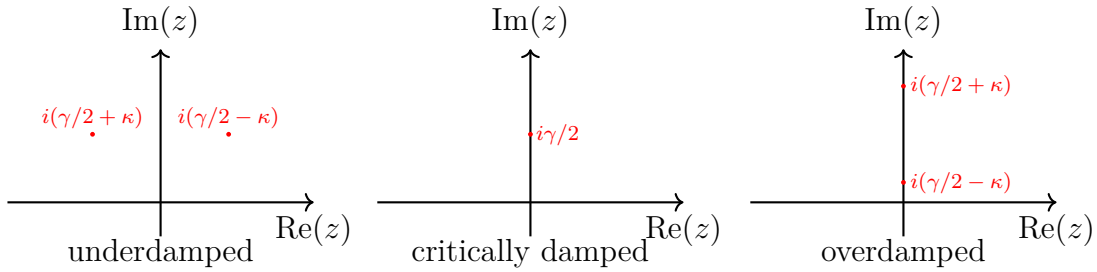

Figure C.2: The poles of the Brownian oscillator spectral density for different values of the reaction coordinate frequency, Ω, and friction coefficient, γ. In the underdamped regime, there are a conjugate pair of simple poles in the upper half plane. In the critically damped, these two poles coalesce to give a single second order pole on the imaginary axis. In the overdamped case, there are once again two simple poles, however, both now lying on the imaginary axis.

C.2.1 The Underdamped and Overdamped Regimes

In the underdamped and overdamped regimes, the contribution to the bath correlation function arising from the poles of $F(\omega)$ may be written as

$$\begin{aligned} F(t;2\Omega/\gamma) = &-\nu_+\hbar\mathrm{Res}\left(F(z),i\nu_+\right)\left[\coth\left(\frac{i\beta\hbar\nu_+}{2}\right)-1\right]e^{-\nu_+ t} \\ &-\nu_-\hbar\mathrm{Res}\left(F(z),i\nu_-\right)\left[\coth\left(\frac{i\beta\hbar\nu_-}{2}\right)-1\right]e^{-\nu_- t}. \end{aligned} \tag{C.22}$$

and evaluating the residue at each of these points, this becomes

$$F(t;2\Omega/\gamma) = -\frac{i\Lambda\Omega^2\hbar}{8\kappa}\left(\left[\coth\left(\frac{i\beta\hbar\nu_+}{2}\right)-1\right]e^{-\nu_+ t}-\left[\coth\left(\frac{i\beta\hbar\nu_-}{2}\right)-1\right]e^{-\nu_- t}\right). \tag{C.23}$$

In the overdamped case $\kappa = \sqrt{\gamma^2/4-\Omega^2}$ is a real number and so equation C.23 can be simplified to give

$$F(t;2\Omega/\gamma<1) = -\frac{\Lambda\Omega^2\hbar}{8\kappa}\left(\left[\cot\left(\frac{\beta\hbar\nu_+}{2}\right)-i\right]e^{-\nu_+ t}-\left[\cot\left(\frac{\beta\hbar\nu_-}{2}\right)-i\right]e^{-\nu_- t}\right). \tag{C.24}$$

In the underdamped case equation C.23 may be simplified to

$$F(t;2\Omega/\gamma>1)=-\frac{\Lambda\Omega^2\hbar}{8\eta}\left(\left[\coth\left(\frac{i\beta\hbar\nu_+}{2}\right)-1\right]e^{-\nu_+ t}-\left[\coth\left(\frac{i\beta\hbar\nu_-}{2}\right)-1\right]e^{-\nu_- t}\right), \tag{C.25}$$

where $\eta = \sqrt{\Omega^2-\gamma^2/4} \in \mathbb{R}$.

C.2.2 The Critically Damped Regime

In the critically damped regime ($\gamma = 2\Omega$) the two simple poles at ν_+ and ν_- coalesce to give a single second order pole at $z = \gamma/2 = \Omega$. The contribution to the bath correlation function arising from the poles of $F(\omega)$ may, therefore, be written as

$$F(t;2\Omega/\gamma=1)=i\hbar\mathrm{Res}\left(G(z)e^{i\omega t},i\Omega\right) \tag{C.26}$$

$$=i\hbar\lim_{z\to i\Omega}\frac{\mathrm{d}}{\mathrm{d}z}\left[(z+i\Omega)^2G(z)e^{izt}\right]. \tag{C.27}$$

Inserting the definition of $G(z)$ and simplifying this gives

$$F(t;2\Omega/\gamma=1)=\frac{i\Lambda\gamma\Omega^2\hbar}{2}\lim_{z\to i\Omega}\frac{\mathrm{d}}{\mathrm{d}z}\left[\frac{z}{(z+i\Omega)^2}\left[\coth\left(\frac{\beta\hbar z}{2}\right)-1\right]e^{izt}\right]. \tag{C.28}$$

In order to proceed it is necessary to evaluate the derivative with respect to z, giving

$$\begin{aligned}\frac{\mathrm{d}}{\mathrm{d}z}\left[(z+i\Omega)^2G(z)e^{izt}\right]=\Bigg[&\left(1-2\frac{z}{z+i\Omega}+izt\right)\left[\coth\left(\frac{\beta\hbar z}{2}\right)-1\right]\\&-\frac{\beta\hbar z}{2}\mathrm{cosech}^2\left(\frac{\beta\hbar z}{2}\right)\Bigg]\frac{e^{izt}}{(z+i\Omega)^2}.\end{aligned} \tag{C.29}$$

Inserting this into equation C.26 and simplifying gives

$$F(t;2\Omega/\gamma=1)=\frac{\Lambda\Omega^2\hbar}{4}\left[\left(\cot\left(\frac{\beta\hbar\Omega}{2}\right)-i\right)te^{-\Omega t}+\frac{\beta\hbar}{2}\mathrm{cosec}^2\left(\frac{\beta\hbar\Omega}{2}\right)e^{-\Omega t}\right]. \tag{C.30}$$

References

(1) J. von Neumann, *Mathematical Foundations of Quantum Mechanics*, trans. by R. T. Beyer, Princeton University Press, 1955.

(2) J. J. Sakurai, *Modern Quantum Mechanics*, Addison-Wesley Publishing Company, 1994.

(3) R. Zwanzig, *Nonequilibrium statistical mechanics*, Oxford University Press, 2001.

(4) U. Weiss, *Quantum Dissipative Systems*, World Scientific Publishing Company, 4th edn., 2012.

(5) H.-P. Breuer and F. Petruccione, *The Theory of Open Quantum Systems*, Oxford University Press, 2002.

(6) S. Mukamel, *Principles of Nonlinear Optical Spectroscopy*, Oxford University Press, 1995.

(7) Y. Tanimura and R. Kubo, *J. Phys. Soc. Jpn.*, 1989, **58**, 101–114.

(8) A. Ishizaki and Y. Tanimura, *J. Phys. Soc. Jpn.*, 2005, **74**, 3131–3134.

(9) K. Maeda, K. B. Henbest, F. Cintolesi, I. Kuprov, C. T. Rodgers, P. A. Liddell, D. Gust, C. R. Timmel and P. J. Hore, *Nature*, 2008, **453**, 387–390.

(10) C. T. Rodgers and P. J. Hore, *Proc. Natl. Acad. Sci. U. S. A.*, 2009, **106**, 353–360.

(11) J. M. Lupton, D. R. McCamey and C. Boehme, *ChemPhysChem*, 2010, **11**, 3040–3058.

(12) B. Hu, L. Yan and M. Shao, *Adv. Mater.*, 2009, **21**, 1500–1516.

(13) N. J. Turro, M. F. Chow, C. J. Chung and C. H. Tung, *J. Am. Chem. Soc.*, 1983, **105**, 1572–1577.

(14) C. T. Rodgers, *Pure Appl. Chem.*, 2009, **81**, 19–43.

(15) U. E. Steiner and T. Ulrich, *Chem. Rev.*, 1989, **89**, 51–147.

(16) A. L. Buchachenko, A. P. Orlov, D. A. Kuznetsov and N. N. Breslavskaya, *Nucleic Acids Res.*, 2013, **41**, 8300.

(17) P. Atkin and R. Friedman, *Molecular Quantum Mechanics*, Oxford University Press, 5th edn., 2011.

(18) R. N. Zare, *Angular Momentum, Understanding Spatial Aspects in Chemistry and Physics*, John Wiley & Sons, 1987.

(19) J. A. Weil and J. R. Bolton, *Electron Paramagnetic Resonance: Elementary Theory and Practical Applications*, John Wiley & Sons, 2nd edn., 2006.

(20) K. McLauchlan and U. Steiner, *Mol. Phys.*, 1991, **73**, 241–263.

(21) C. P. Slichter, *Prinpicles of Magnetic Resonance*, Springer-Werlag, 3rd edn., 1996.

(22) A. Carrington and A. D. McLachlan, *Introduction to Magnetic Resonance With Application To Chemistry and Cheimcal Physics*, Harper and Row, 1967.

(23) J. E. Harriman, *Theoretical Foundations of Electron Spin Resonance*, Academic Press, 1978.

(24) P. H. Reiger, *Electron Spin Resonance: Analysis and Interpretation*, Royal Society of Chemistry, 2007.

(25) T. P. Fay, A. M. Lewis and D. E. Manolopoulos, *J. Chem. Phys*, 2017, **147**, 064107.

(26) D. R. Kattnig, J. K. Sowa, I. A. Solov'yov and P. J. Hore, *New J. Phys.*, 2016, **18**, 063007.

(27) W. Heitler and F. London, *Z. Phys.*, 1927, **44**, 455–472.

(28) J. H. V. Vleck, *The Theory of Electric and Magnetic Susceptibilities*, Oxford University Press, 1st edn., 1932.

(29) P. W. Anderson, *Phys. Rev.*, 1950, **79**, 350–356.

(30) P. W. Anderson, *Phys. Rev.*, 1959, **115**, 2–13.

(31) H. Kramers, *Physica*, 1934, **1**, 182 –192.

(32) Y. Kobori, T. Yago, K. Akiyama, S. Tero-Kubota, H. Sato, F. Hirata and J. R. Norris, *J. Phys. Chem. B*, 2004, **108**, 10226–10240.

(33) T. P. Fay, L. P. Lindoy and D. E. Manolopoulos, *J. Chem. Phys*, 2018, **149**, 064107.

(34) E. Fermi, *Z. Phys.*, 1930, **60**, 320–333.

(35) W. Kutzelnigg, *Theor. Chem. Acc.*, 1988, **73**, 173–200.

(36) J. D. Jackson, *Classical Electrodynamics*, John Wiley & Sons, 2nd edn., 1975.

(37) A. Abragram, *The Principles of Nuclear Magnetism*, Oxford University Press, 1961.

(38) W. Weltner, Jr., *Magnetic Atoms and Molecules*, Van Nostrand Reinhold, 1983.

(39) R. Kubo, *J. Phys. Soc. Jpn.*, 1969, **26**, 1–5.

(40) J. H. Freed, G. V. Bruno and C. F. Polnaszek, *J. Phys. Chem.*, 1971, **75**, 3385–3399.

(41) A. G. Redfield, *IBM J. Res. Dev.*, 1957, **1**, 19–31.

(42) M. Goldman, *J. Magn. Reson.*, 2001, **149**, 160–187.

(43) J. H. Freed, *J. Chem. Phys.*, 1968, **49**, 376–391.

(44) T. P. Fay, L. P. Lindoy and D. E. Manolopoulos, *J. Chem. Phys*, 2019, **151**, 154117.

(45) R. Haberkorn, *Mol. Phys.*, 1976, **32**, 1491–1493.

(46) J. Jones and P. Hore, *Chem. Phys. Lett.*, 2010, **488**, 90 –93.

(47) J. Jones, K. Maeda and P. Hore, *Chem. Phys. Lett.*, 2011, **507**, 269 –273.

(48) I. K. Kominis, *Phys. Rev. E*, 2009, **80**, 056115.

(49) P. Purtov, *Chem. Phys. Lett.*, 2010, **496**, 335 –338.

(50) K. L. Ivanov, M. V. Petrova, N. N. Lukzen and K. Maeda, *J. Phys. Chem. A*, 2010, **114**, 9447–9455.

(51) J. Jones, K. Maeda, U. Steiner and P. Hore, *Chem. Phys. Lett.*, 2011, **508**, 184 –185.

(52) M. Tiersch, U. E. Steiner, S. Popescu and H. J. Briegel, *J. Phys. Chem. A*, 2012, **116**, 4020–4028.

(53) K. Maeda, P. Liddell, D. Gust and P. J. Hore, *J. Chem. Phys*, 2013, **139**, 234309.

(54) A. Weiße, G. Wellein, A. Alvermann and H. Fehske, *Rev. Mod. Phys.*, 2006, **78**, 275–306.

(55) A. M. Lewis, T. P. Fay and D. E. Manolopoulos, *J. Chem. Phys*, 2016, **145**, 244101.

(56) E. H. Lieb, *Commun. Math. Phys.*, 1973, **31**, 327–340.

(57) J. M. Radcliffe, *J. Phys. A*, 1971, **4**, 313–323.

(58) J. M. Hammersley and D. C. Handscomb, *Monte Carlo Methods*, Methuen & Co, 1964.

(59) B. Urbaszek, X. Marie, T. Amand, O. Krebs, P. Voisin, P. Maletinsky, A. Högele and A. Imamoglu, *Rev. Mod. Phys.*, 2013, **85**, 79–133.

(60) K. Schulten and P. G. Wolynes, *J. Chem. Phys*, 1978, **68**, 3292–3297.

(61) D. E. Manolopoulos and P. J. Hore, *J. Chem. Phys*, 2013, **139**, 124106.

(62) A. M. Lewis, D. E. Manolopoulos and P. J. Hore, *J. Chem. Phys*, 2014, **141**, 044111.

(63) S. I. Erlingsson and Y. V. Nazarov, *Phys. Rev. B*, 2004, **70**, 205327.

(64) G. Chen, D. L. Bergman and L. Balents, *Phys. Rev. B*, 2007, **76**, 045312.

(65) B. Fauseweh, P. Schering, J. Hüdepohl and G. S. Uhrig, *Phys. Rev. B*, 2017, **96**, 054415.

(66) C. T. Rodgers, Ph.D. Thesis, Oxford University, 2007.

(67) A. Lewis, *Spin Dynamics in Radical Pairs*, Spinger, 2018.

(68) T. Ritz, S. Adem and K. Schulten, *Biophys. J.*, 2000, **78**, 707 –718.

(69) K. Schulten, C. Swenberg and A. Weiler, *Z. Phys. Chem.*, 1978, **111**, cited By 195, 1–5.

(70) P. J. Hore and H. Mouritsen, *Annu. Rev. Biophys.*, 2016, **45**, 299–344.

(71) W. Wiltschko and R. Wiltschko, *Science*, 1972, **176**, 62–64.

(72) W. Wiltschko, *J. Ornithol.*, 1974, **115**, 1–7.

(73) T. Ritz, P. Thalau, J. B. Phillips, R. Wiltschko and W. Wiltschko, *Nature*, 2004, **429**, 177–180.

(74) T. Ritz, R. Wiltschko, P. Hore, C. T. Rodgers, K. Stapput, P. Thalau, C. R. Timmel and W. Wiltschko, *Biophys. J.*, 2009, **96**, 3451 –3457.

(75) S. Engels, N.-L. Schneider, N. Lefeldt, C. M. Hein, M. Zapka, A. Michalik, D. Elbers, A. Kittel, P. J. Hore and H. Mouritsen, *Nature*, 2014, **509**, 353 EP –.

(76) H. Hiscock, Ph.D. Thesis, Oxford University, 2018.

(77) S. Schwarze, N.-L. Schneider, T. Reichl, D. Dreyer, N. Lefeldt, S. Engels, N. Baker, P. J. Hore and H. Mouritsen, *Front. Behav. Neurosci.*, 2016, **10**, 55.

(78) H. G. Hiscock, H. Mouritsen, D. E. Manolopoulos and P. Hore, *Biophys. J.*, 2017, **113**, 1475 –1484.

(79) W. Wiltschko and R. Wiltschko, *J. Comp. Physiol. A*, 1995, **177**, 363–369.

(80) R. Wiltschko, K. Stapput, H.-J. Bischof and W. Wiltschko, *Front. Zool.*, 2007, **4**, 5.

(81) R. Wiltschko, K. Stapput, P. Thalau and W. Wiltschko, *J. Royal Soc. Interface*, 2010, **7**, S163–S177.

(82) K. Maeda, A. J. Robinson, K. B. Henbest, H. J. Hogben, T. Biskup, M. Ahmad, E. Schleicher, S. Weber, C. R. Timmel and P. J. Hore, *Proc. Natl. Acad. Sci. U. S. A.*, 2012, **109**, 4774–4779.

(83) H. G. Hiscock, S. Worster, D. R. Kattnig, C. Steers, Y. Jin, D. E. Manolopoulos, H. Mouritsen and P. J. Hore, *Proc. Natl. Acad. Sci. U. S. A.*, 2016, **113**, 4634–4639.

(84) A. A. Lee, J. C. S. Lau, H. J. Hogben, T. Biskup, D. R. Kattnig and P. J. Hore, *J. Royal Soc. Interface*, 2014, **11**, 20131063.

(85) H. J. Hogben, O. Efimova, N. Wagner-Rundell, C. R. Timmel and P. Hore, *Chem. Phys. Lett.*, 2009, **480**, 118 –122.

(86) I. A. Solov'yov and K. Schulten, *Biophys. J.*, 2009, **96**, 4804 –4813.

(87) D. R. Kattnig and P. J. Hore, *Sci. Rep.*, 2017, **7**, 11640.

(88) D. R. Kattnig, *J. Phys. Chem. B*, 2017, **121**, 10215–10227.

(89) T. P. Fay, L. P. Lindoy, D. E. Manolopoulos and P. J. Hore, *Faraday Discuss.*, 2020, **221**, 77–91.

(90) O. Efimova and P. Hore, *Biophys. J.*, 2008, **94**, 1565 –1574.

(91) A. Nitzan, *Chemical Dynamics in Condensed Phases, Relaxation, Transfer, and Reactions in Condensed Molecular Systems*, Oxford University Press, 2006.

(92) S. I. Erlingsson and Y. V. Nazarov, *Phys. Rev. B*, 2004, **70**, 205327.

(93) P. J. Hore, *Proc. Natl. Acad. Sci. U. S. A.*, 2012, **109**, 1357–1358.

(94) I. A. Merkulov, A. L. Efros and M. Rosen, *Phys. Rev. B*, 2002, **65**, 205309.

(95) A. Khaetskii, D. Loss and L. Glazman, *Phys. Rev. B*, 2003, **67**, 195329.

(96) V. V. Dobrovitski and H. A. De Raedt, *Phys. Rev. E*, 2003, **67**, 056702.

(97) W. A. Coish and D. Loss, *Phys. Rev. B*, 2004, **70**, 195340.

(98) P.-F. Braun, X. Marie, L. Lombez, B. Urbaszek, T. Amand, P. Renucci, V. K. Kalevich, K. V. Kavokin, O. Krebs, P. Voisin and Y. Masumoto, *Phys. Rev. Lett.*, 2005, **94**, 116601.

(99) K. A. Al-Hassanieh, V. V. Dobrovitski, E. Dagotto and B. N. Harmon, *Phys. Rev. Lett.*, 2006, **97**, 037204.

(100) G. Chen, D. L. Bergman and L. Balents, *Phys. Rev. B*, 2007, **76**, 045312.

(101) E. Barnes, L. Cywiński and S. Das Sarma, *Phys. Rev. Lett.*, 2012, **109**, 140403.

(102) A. Faribault and D. Schuricht, *Phys. Rev. Lett.*, 2013, **110**, 040405.

(103) D. Stanek, C. Raas and G. S. Uhrig, *Phys. Rev. B*, 2013, **88**, 155305.

(104) J. R. Petta, A. C. Johnson, J. M. Taylor, E. A. Laird, A. Yacoby, M. D. Lukin, C. M. Marcus, M. P. Hanson and A. C. Gossard, *Science*, 2005, **309**, 2180–2184.

(105) R. Hanson, L. P. Kouwenhoven, J. R. Petta, S. Tarucha and L. M. K. Vandersypen, *Rev. Mod. Phys.*, 2007, **79**, 1217–1265.

(106) M. Pioro-Ladrière, T. Obata, Y. Tokura, Y.-S. Shin, T. Kubo, K. Yoshida, T. Taniyama and S. Tarucha, *Nat. Phys.*, 2008, **4**, 776–779.

(107) J. M. Elzerman, R. Hanson, L. H. Willems van Beveren, B. Witkamp, L. M. K. Vandersypen and L. P. Kouwenhoven, *Nature*, 2004, **430**, 431–435.

(108) A. C. Johnson, J. R. Petta, J. M. Taylor, A. Yacoby, M. D. Lukin, C. M. Marcus, M. P. Hanson and A. C. Gossard, *Nature*, 2005, **435**, 925–928.

(109) F. H. L. Koppens, C. Buizert, K. J. Tielrooij, I. T. Vink, K. C. Nowack, T. Meunier, L. P. Kouwenhoven and L. M. K. Vandersypen, *Nature*, 2006, **442**, 766–771.

(110) F. H. L. Koppens, K. C. Nowack and L. M. K. Vandersypen, *Phys. Rev. Lett.*, 2008, **100**, 236802.

(111) D. Loss and D. P. DiVincenzo, *Phys. Rev. A*, 1998, **57**, 120–126.

(112) J. Levy, *Phys. Rev. Lett.*, 2002, **89**, 147902.

(113) M. A. Nielson and I. L. Chuang, *Quantum Computation and Quantum Information*, Cambridge University Press, 2000.

(114) C. Kloeffel and D. Loss, *Annu. Rev. Condens. Matter Phys.*, 2013, **4**, 51–81.

(115) D. Gammon, A. L. Efros, T. A. Kennedy, M. Rosen, D. S. Katzer, D. Park, S. W. Brown, V. L. Korenev and I. A. Merkulov, *Phys. Rev. Lett.*, 2001, **86**, 5176–5179.

(116) J. Schliemann, A. Khaetskii and D. Loss, *J. Phys. Condens. Matter*, 2003, **15**, R1809–R1833.

(117) R. Röhrig, P. Schering, L. B. Gravert, B. Fauseweh and G. S. Uhrig, *Phys. Rev. B*, 2018, **97**, 165431.

(118) B. Pal, S. Y. Verbin, I. V. Ignatiev, M. Ikezawa and Y. Masumoto, *Phys. Rev. B*, 2007, **75**, 125322.

(119) B. Fauseweh, P. Schering, J. Hüdepohl and G. S. Uhrig, *Phys. Rev. B*, 2017, **96**, 054415.

(120) H.-P. Breuer, D. Burgarth and F. Petruccione, *Phys. Rev. B*, 2004, **70**, 045323.

(121) W. A. Coish, J. Fischer and D. Loss, *Phys. Rev. B*, 2010, **81**, 165315.

(122) J. Jing and L.-A. Wu, *Sci. Rep.*, 2018, **8**, 1471.

(123) D. Stanek, C. Raas and G. S. Uhrig, *Phys. Rev. B*, 2014, **90**, 064301.

(124) A. Faribault and D. Schuricht, *Phys. Rev. B*, 2013, **88**, 085323.

(125) Gaudin, M., *J. Phys. France*, 1976, **37**, 1087–1098.

(126) M. Gaudin, *The Bethe wavefunction*, Cambridge University Press, 2014.

(127) M. Bortz, S. Eggert and J. Stolze, *Phys. Rev. B*, 2010, **81**, 035315.

(128) A. Faribault, O. El Araby, C. Sträter and V. Gritsev, *Phys. Rev. B*, 2011, **83**, 235124.

(129) T. D. Kieu and C. J. Griffin, *Phys. Rev. E*, 1994, **49**, 3855–3859.

(130) S. R. White and A. E. Feiguin, *Phys. Rev. Lett.*, 2004, **93**, 076401.

(131) U. Schollwöck, *Rev. Mod. Phys.*, 2005, **77**, 259–315.

(132) U. Schollwöck, *Ann. Phys. (N. Y.)*, 2011, **326**, January 2011 Special Issue, 96 –192.

(133) D. Stanek, Ph.D. Thesis, Technischen Universität Dortmund, 2013.

(134) P. Calabrese and J. Cardy, *J. Stat. Mech.: Theory Exp.*, 2005, **2005**, P04010.

(135) D. Gobert, C. Kollath, U. Schollwöck and G. Schütz, *Phys. Rev. E*, 2005, **71**, 036102.

(136) M. Bortz and J. Stolze, *J. Stat. Mech.: Theory Exp.*, 2007, **2007**, P06018–P06018.

(137) L. P. Lindoy and D. E. Manolopoulos, *Phys. Rev. Lett.*, 2018, **120**, 220604.

(138) W. H. Press, S. A. Teukolsky, W. T. Vetterling and B. P. Flannery, *Numerical recipes in fortran*, Cambridge University Press, 2nd edn., 1992.

(139) G. Kodis, P. A. Liddell, A. L. Moore, T. A. Moore and D. Gust, *J. Phys. Org. Chem.*, 2004, **17**, 724–734.

(140) K. Maeda, C. J. Wedge, J. G. Storey, K. B. Henbest, P. A. Liddell, G. Kodis, D. Gust, P. J. Hore and C. R. Timmel, *Chem. Commun.*, 2011, **47**, 6563–6565.

(141) C. Kerpal, S. Richert, J. G. Storey, S. Pillai, P. A. Liddell, D. Gust, S. R. Mackenzie, P. J. Hore and C. R. Timmel, *Nat. Commun.*, 2019, **10**, 3707.

(142) A. M. Lewis, T. P. Fay, D. E. Manolopoulos, C. Kerpal, S. Richert and C. R. Timmel, *J. Chem. Phys*, 2018, **149**, 034103.

(143) M. R. Wasielewski, *J. Org. Chem.*, 2006, **71**, 5051–5066.

(144) N. E. Henriksen and F. Y. Hansen, *Theories of Molecular Reaction Dynamics, The Microscopic Foundation of Chemical Kinetics*, Oxford University Press, 2008.

(145) J. N. Murrell and S. D. Bosanac, *Introduction to the Theory of Atomic and Molecular Collisions*, John Wiley & Sons, 1989.

(146) J. Z. H. Zhang, *Theory and Application of Quantum Molecular Dynamics*, World Scientific Publishing Company, 1999.

(147) M. Born and K. Huang, *Dynamical Theory of Crystal Lattices*, Oxford University Press, 1954.

(148) K. Takatsuka, T. Yonehara, K. Hanasaki and Y. Arasaki, *Chemical Theory beyond the Born-Oppenheimer Paradigm, Nonadiabatic Electronic and Nuclear Dynamics in Chemical Reactions*, World Scientific Publishing Company, 2015.

(149) J. C. Tully, *J. Chem. Phys*, 2012, **137**, 22A301.

(150) M. Born and R. Oppenheimer, *Ann. Phys. (Berl.)*, 1927, **389**, 457–484.

(151) T. Pacher, L. S. Cederbaum and H. Köppel, *J. Chem. Phys*, 1988, **89**, 7367–7381.

(152) B. H. Lengsfield, P. Saxe and D. R. Yarkony, *J. Chem. Phys*, 1984, **81**, 4549–4553.

(153) T. Van Voorhis, T. Kowalczyk, B. Kaduk, L.-P. Wang, C.-L. Cheng and Q. Wu, *Annu. Rev. Phys. Chem.*, 2010, **61**, 149–170.

(154) U. Manthe and H. Köppel, *J. Chem. Phys*, 1990, **93**, 1658–1669.

(155) G. Granucci, M. Persico and G. Spighi, *J. Chem. Phys*, 2012, **137**, 22A501.

(156) *Electron Transfer: From Isolated Molecules to Biomolecules: Part One*, ed. J. Jortner and M. Bixon, John Wiley & Sons, 1999.

(157) J. C. Light and Z. Bačić, *J. Chem. Phys*, 1987, **87**, 4008–4019.

(158) H. Kamisaka, W. Bian, K. Nobusada and H. Nakamura, *J. Chem. Phys*, 2002, **116**, 654–665.

(159) C. Petrongolo, *J. Chem. Phys*, 1988, **89**, 1297–1308.

(160) A. Caldeira and A. Leggett, *Ann. Phys. (N. Y.)*, 1983, **149**, 374 –456.

(161) A. Garg, J. N. Onuchic and V. Ambegaokar, *J. Chem. Phys*, 1985, **83**, 4491–4503.

(162) A. J. Leggett, S. Chakravarty, A. T. Dorsey, M. P. A. Fisher, A. Garg and W. Zwerger, *Rev. Mod. Phys.*, 1987, **59**, 1–85.

(163) R. Marcus and N. Sutin, *Biochim. Biophys. Acta, Bioenerg.*, 1985, **811**, 265 –322.

(164) N. S. Hush, *J. Chem. Phys*, 1958, **28**, 962–972.

(165) R. A. Marcus, *Annu. Rev. Phys. Chem.*, 1964, **15**, 155–196.

(166) M. Thoss, H. Wang and W. H. Miller, *J. Chem. Phys*, 2001, **115**, 2991–3005.

(167) A. J. Leggett, *Phys. Rev. B*, 1984, **30**, 1208–1218.

(168) S. Chakravarty and A. J. Leggett, *Phys. Rev. Lett.*, 1984, **52**, 5–8.

(169) R. Feynman and F. Vernon, *Ann. Phys. (N. Y.)*, 1963, **24**, 118 –173.

(170) R. P. Feynman and A. R. Hibbs, *Quantum Mechanics and Path Integrals*, McGraw-Hill Book Company, 1965.

(171) M. Sparpaglione and S. Mukamel, *J. Chem. Phys*, 1988, **88**, 3263–3280.

(172) J. Strümpfer and K. Schulten, *J. Chem. Theory Comput.*, 2012, **8**, 2808–2816.

(173) C. Kreisbeck, T. Kramer and A. Aspuru-Guzik, *J. Chem. Theory Comput.*, 2014, **10**, 4045–4054.

(174) M. Tsuchimoto and Y. Tanimura, *J. Chem. Theory Comput.*, 2015, **11**, 3859–3865.

(175) Z. Tang, X. Ouyang, Z. Gong, H. Wang and J. Wu, *J. Chem. Phys*, 2015, **143**, 224112.

(176) H. Rahman and U. Kleinekathöfer, *J. Chem. Phys*, 2019, **150**, 244104.

(177) Y. Tanimura, *J. Chem. Phys*, 2014, **141**, 044114.

(178) Y. Tanimura, *J. Chem. Phys*, 2015, **142**, 144110.

(179) J. Jin, X. Zheng and Y. Yan, *J. Chem. Phys*, 2008, **128**, 234703.

(180) L. Chen, Y. Zhao and Y. Tanimura, *J. Phys. Chem. Lett.*, 2015, **6**, 3110–3115.

(181) J. E. Lawrence, T. Fletcher, L. P. Lindoy and D. E. Manolopoulos, *J. Chem. Phys*, 2019, **151**, 114119.

(182) A. G. Dijkstra and V. I. Prokhorenko, *J. Chem. Phys*, 2017, **147**, 064102.

(183) L. Chen and Q. Shi, *J. Chem. Phys*, 2009, **130**, 134505.

(184) K. Song and Q. Shi, *J. Chem. Phys*, 2017, **146**, 184108.

(185) Q. Shi, L. Chen, G. Nan, R.-X. Xu and Y. Yan, *J. Chem. Phys*, 2009, **130**, 084105.

(186) J. Hu, M. Luo, F. Jiang, R.-X. Xu and Y. Yan, *J. Chem. Phys*, 2011, **134**, 244106.

(187) J.-J. Ding, R.-X. Xu and Y. Yan, *J. Chem. Phys*, 2012, **136**, 224103.

(188) J. M. Moix and J. Cao, *J. Chem. Phys*, 2013, **139**, 134106.

(189) Q. Shi, Y. Xu, Y. Yan and M. Xu, *J. Chem. Phys*, 2018, **148**, 174102.

(190) R. Kubo, *J. Phys. Soc. Jpn.*, 1962, **17**, 1100–1120.

(191) N. V. Kampen, *Physica*, 1974, **74**, 239 –247.

(192) H.-P. Breuer and F. Petruccione, *Phys. Rev. A*, 2001, **63**, 032102.

(193) R. Doll, D. Zueco, M. Wubs, S. Kohler and P. Hänggi, *Chem. Phys.*, 2008, **347**, Ultrafast Photoinduced Processes in Polyatomic Molecules, 243 –249.

(194) D. Kohen, C. C. Marston and D. J. Tannor, *J. Chem. Phys*, 1997, **107**, 5236–5253.

(195) A. Ishizaki and G. R. Fleming, *J. Chem. Phys*, 2009, **130**, 234111.

(196) S. Mukamel, *Phys. Rev. E*, 2003, **68**, 021111.

(197) Y. Tanimura, *J. Chem. Phys*, 2012, **137**, 22A550.

(198) S. Nakajima, *Prog. Theor. Phys.*, 1958, **20**, 948–959.

(199) R. Zwanzig, *J. Chem. Phys*, 1960, **33**, 1338–1341.

(200) M. G. Mavros, D. Hait and T. Van Voorhis, *J. Chem. Phys*, 2016, **145**, 214105.

(201) A. A. Golosov and D. R. Reichman, *J. Chem. Phys*, 2001, **115**, 9848–9861.

(202) T. P. Fay and D. E. Manolopoulos, *J. Chem. Phys*, 2019, **150**, 151102.

(203) Y. Tanimura, *Phys. Rev. A*, 1990, **41**, 6676–6687.

(204) M. Tanaka and Y. Tanimura, *J. Phys. Soc. Jpn.*, 2009, **78**, 073802.

(205) Q. Shi, L. Chen, G. Nan, R. Xu and Y. Yan, *J. Chem. Phys*, 2009, **130**, 164518.

(206) L. Song and Q. Shi, *Phys. Rev. B*, 2017, **95**, 064308.

(207) K. M. Rosso and J. R. Rustad, *J. Phys. Chem. A*, 2000, **104**, 6718–6725.

(208) R. Borrelli, *J. Chem. Phys*, 2019, **150**, 234102.

(209) H.-D. Meyer, U. Manthe and L. Cederbaum, *Chem. Phys. Lett.*, 1990, **165**, 73 –78.

(210) U. Manthe, H.-D. Meyer and L. S. Cederbaum, *J. Chem. Phys.*, 1992, **97**, 3199–3213.

(211) M. Beck, A. Jäckle, G. Worth and H.-D. Meyer, *Phys. Rep.*, 2000, **324**, 1 –105.

(212) H.-D. Meyer and H. Wang, *J. Chem. Phys.*, 2018, **148**, 124105.

(213) H. Wang and M. Thoss, *J. Chem. Phys.*, 2003, **119**, 1289–1299.

(214) U. Manthe, *J. Chem. Phys.*, 2008, **128**, 164116.

(215) O. Vendrell and H.-D. Meyer, *J. Chem. Phys.*, 2011, **134**, 044135.

(216) H. Wang, *J. Phys. Chem. A*, 2015, **119**, 7951–7965.

(217) O. Vendrell, F. Gatti, D. Lauvergnat and H.-D. Meyer, *J. Chem. Phys.*, 2007, **127**, 184302.

(218) O. Vendrell, F. Gatti and H.-D. Meyer, *J. Chem. Phys.*, 2007, **127**, 184303.

(219) O. Vendrell, M. Brill, F. Gatti, D. Lauvergnat and H.-D. Meyer, *J. Chem. Phys.*, 2009, **130**, 234305.

(220) O. Vendrell, F. Gatti and H.-D. Meyer, *J. Chem. Phys.*, 2009, **131**, 034308.

(221) A. Raab, G. A. Worth, H.-D. Meyer and L. S. Cederbaum, *J. Chem. Phys.*, 1999, **110**, 936–946.

(222) I. R. Craig, M. Thoss and H. Wang, *J. Chem. Phys.*, 2007, **127**, 144503.

(223) J. Schulze, M. F. Shibl, M. J. Al-Marri and O. Kühn, *J. Chem. Phys.*, 2016, **144**, 185101.

(224) H. Wang and H.-D. Meyer, *J. Chem. Phys.*, 2018, **149**, 044119.

(225) D. Mendive-Tapia, E. Mangaud, T. Firmino, A. de la Lande, M. Desouter-Lecomte, H.-D. Meyer and F. Gatti, *J. Phys. Chem. B*, 2018, **122**, 126–136.

(226) H. Wang and M. Thoss, *J. Phys. Chem. A*, 2007, **111**, 10369–10375.

(227) I. Kondov, M. Čížek, C. Benesch, H. Wang and M. Thoss, *J. Phys. Chem. C*, 2007, **111**, 11970–11981.

(228) H. Wang and M. Thoss, *New J. Phys.*, 2008, **10**, 115005.

(229) J. Zheng, Y. Xie, S. Jiang and Z. Lan, *J. Phys. Chem. C*, 2016, **120**, 1375–1389.

(230) J. C. Light and T. Carrington Jr., in *Advances in Chemical Physics*, John Wiley & Sons, 2007, pp. 263–310.

(231) B. Kloss, I. Burghardt and C. Lubich, *J. Chem. Phys.*, 2017, **146**, 174107.

(232) S. Montangero, *Introduction to Tensor Network Methods, Numerical Simulations of Low-Dimensional Many-Body Quantum Systems*, Springer, 2018.

(233) Conte, Dajana and Lubich, Christian, *ESAIM: Math. Modell. Numer. Anal.*, 2010, **44**, 759–780.

(234) C. Lubich, *Math. Comp*, 2005, 765–779.

(235) P. A. M. Dirac, *Math. Proc. Cambridge Philos. Soc.*, 1930, **26**, 376–385.

(236) J. Frenkel, *Wave Mechanics, advanced general theory*, Clarendon Press, 1934.

(237) J. Broeckhove, L. Lathouwers, E. Kesteloot and P. V. Leuven, *Chem. Phys. Lett.*, 1988, **149**, 547 –550.

(238) A. McLachlan, *Mol. Phys.*, 1964, **8**, 39–44.

(239) A. Raab, *Chem. Phys. Lett.*, 2000, **319**, 674 –678.

(240) C. Lubich, *Appl. Math. Res. Express*, 2015, **2015**, 311–328.

(241) M. Bonfanti and I. Burghardt, *Chem. Phys.*, 2018, **515**, 252 –261.

(242) M. Beck and H.-D. Meyer, *Z. Phys. D: At., Mol. Clusters*, 1997, **42**, 113–129.

(243) U. Manthe, *J. Chem. Phys.*, 2015, **142**, 244109.

(244) G. A. Worth, M. H. Beck, A. Jäckle and H.-D. Meyer, *The MCTDH Package*, Version 8.2, (2000). H.-D. Meyer, Version 8.3 (2002), Version 8.4 (2007). See http://mctdh.uni-hd.de Current version: 8.4.18 (2019).

(245) C. Lubich, T. Rohwedder, R. Schneider and B. Vandereycken, *SIAM J. Matrix Anal. Appl.*, 2013, **34**, 470–494.

(246) J. Haegeman, C. Lubich, I. Oseledets, B. Vandereycken and F. Verstraete, *Phys. Rev. B*, 2016, **94**, 165116.

(247) B. Kloss, D. R. Reichman and R. Tempelaar, *Phys. Rev. Lett.*, 2019, **123**, 126601.

(248) F. A. Y. N. Schröder, D. H. P. Turban, A. J. Musser, N. D. M. Hine and A. W. Chin, *Nat. Commun.*, 2019, **10**, 1062.

(249) J. R. Cash and A. H. Karp, *ACM Trans. Math. Softw.*, 1990, **16**, 201–222.

(250) R. A. Marcus, *J. Chem. Phys.*, 1956, **24**, 966–978.

(251) P. Siders and R. A. Marcus, *J. Am. Chem. Soc.*, 1981, **103**, 748–752.

(252) P. G. Wolynes, *J. Chem. Phys.*, 1987, **87**, 6559–6561.

(253) J. E. Lawrence and D. E. Manolopoulos, *J. Chem. Phys.*, 2018, **148**, 102313.

(254) C. Zheng, J. McCammon and P. G. Wolynes, *Chem. Phys.*, 1991, **158**, 261 –270.

(255) J. S. Bader, R. A. Kuharski and D. Chandler, *J. Chem. Phys.*, 1990, **93**, 230–236.

(256) I. R. Craig and D. E. Manolopoulos, *J. Chem. Phys.*, 2005, **122**, 084106.

(257) I. R. Craig and D. E. Manolopoulos, *J. Chem. Phys.*, 2005, **123**, 034102.

(258) R. Collepardo-Guevara, I. R. Craig and D. E. Manolopoulos, *J. Chem. Phys.*, 2008, **128**, 144502.

(259) S. Habershon, D. E. Manolopoulos, T. E. Markland and T. F. Miller, *Annu. Rev. Phys. Chem.*, 2013, **64**, PMID: 23298242, 387–413.

(260) J. E. Lawrence and D. E. Manolopoulos, *Faraday Discuss.*, 2020, –.

(261) P. Shushkov, R. Li and J. C. Tully, *J. Chem. Phys.*, 2012, **137**, 22A549.

(262) N. Ananth, *J. Chem. Phys.*, 2013, **139**, 124102.

(263) J. O. Richardson and M. Thoss, *J. Chem. Phys.*, 2013, **139**, 031102.

(264) A. R. Menzeleev, F. Bell and T. F. Miller, *J. Chem. Phys.*, 2014, **140**, 064103.

(265) J. S. Kretchmer, N. Boekelheide, J. J. Warren, J. R. Winkler, H. B. Gray and T. F. Miller, *Proc. Natl. Acad. Sci. U. S. A.*, 2018, **115**, 6129–6134.

(266) L. Zusman, *Chem. Phys.*, 1980, **49**, 295 –304.

(267) L. Hartmann, I. Goychuk and P. Hänggi, *J. Chem. Phys.*, 2000, **113**, 11159–11175.

(268) I. Rips and J. Jortner, *J. Chem. Phys.*, 1987, **87**, 2090–2104.

(269) *Electron Transfer: From Isolated Molecules to Biomolecules: Part Two*, ed. J. Jortner and M. Bixon, John Wiley & Sons, 1999.

(270) K. Mølmer, Y. Castin and J. Dalibard, *J. Opt. Soc. Am. B*, 1993, **10**, 524–538.

(271) J. Dalibard, Y. Castin and K. Mølmer, *Phys. Rev. Lett.*, 1992, **68**, 580–583.

(272) M. B. Plenio and P. L. Knight, *Rev. Mod. Phys.*, 1998, **70**, 101–144.

(273) P. J. Olver, *Application of Lie Groups to Differential Equations*, Springer, 2000.

(274) L. Cywiński, W. M. Witzel and S. Das Sarma, *Phys. Rev. B*, 2009, **79**, 245314.

(275) J. V. Michalowicz, J. M. Nichols, F. Bucholtz and C. C. Olson, *J. Stat. Phys.*, 2009, **136**, 89–102.

(276) L. Isserlis, *Biometrika*, 1916, **11**, 185–190.

(277) L. Isserlis, *Biometrika*, 1918, **12**, 134–139.

(278) G. C. Wick, *Phys. Rev.*, 1950, **80**, 268–272.

(279) G. B. Arfken, H. J. Weber and F. E. Harris, *Mathematical Methods for Physicists*, Elsevier, 2013.